

HABILITATIONSSCHRIFT

Nanoscience on Surfaces

eingereicht an der

Technischen Universität Wien
Fakultät für Physik

von

Dipl.-Ing. Dr. techn. Ilse-Christine Gebeshuber
Auhofstrasse 92/6a, 1130 Wien

Wien, im April 2008

.....

Contents

LIST OF ABBREVIATIONS	4
PREFACE.....	5
INTRODUCTION.....	5
1 SCANNING PROBE MICROSCOPY: FROM LIVING CELLS TO THE SUBATOMIC RANGE.....	6
1.1 INTRODUCTION	6
1.2 CELLS IN VIVO AS EXEMPLIFIED BY DIATOMS	7
1.2.1 <i>Introduction to diatoms</i>	7
1.2.2 <i>SPM of diatoms</i>	9
1.3 INTERACTION OF LARGE ORGANIC MOLECULES.....	14
1.4 NANODEFFECTS ON ATOMICALLY FLAT SURFACES.....	19
1.4.1 <i>Ion bombardment of highly oriented pyrolytic graphite</i>	20
1.4.2 <i>Bombardment of insulator single crystal surfaces with multicharged ions</i>	25
1.4.3 <i>Nanodefects generated on Al₂O₃ single crystal surfaces via bombardment with multicharged ions</i>	26
1.4.4 <i>Bombardment of single crystal CaF₂ surfaces via with multicharged ¹²⁹Xe ions reveal a potential energy threshold for nanodefects generation</i>	29
1.5 CONCLUSIONS AND OUTLOOK	35
2 DIATOM TRIBOLOGY	36
REFERENCES.....	39
LIST OF FIGURES	44
APPENDIX A: PUBLICATIONS SELECTED FOR REVIEW.....	47
A.1 SCANNING PROBE MICROSCOPY: FROM LIVING CELLS TO THE SUBATOMIC RANGE	47
A.2 PROBING PROTEIN-PROTEIN INTERACTIONS IN REAL TIME.....	75
A.3 ATOMIC FORCE MICROSCOPY STUDY OF LIVING DIATOMS IN AMBIENT CONDITIONS	80
A.4 IN VIVO NANOSCALE ATOMIC FORCE MICROSCOPY INVESTIGATION OF DIATOM ADHESION PROPERTIES ...	90
A.5 AFM SEARCH FOR SLOW MCI-PRODUCED NANODEFFECTS ON ATOMICALLY CLEAN MONOCRYSTALLINE INSULATOR SURFACES	95
A.6 NANOSCOPIC SURFACE MODIFICATION BY SLOW ION BOMBARDMENT	103
A.7 SURFACE NANOSTRUCTURES INDUCED BY SLOW HIGHLY CHARGED IONS ON CaF ₂ SINGLE CRYSTALS ...	112
A.8 POTENTIAL ENERGY THRESHOLD FOR NANOHILLOCK FORMATION BY IMPACT OF SLOW HIGHLY CHARGED IONS ON A CaF ₂ (111) SURFACE.....	117
A.9 DIATOM BIONANOTRIBOLOGY - BIOLOGICAL SURFACES IN RELATIVE MOTION: THEIR DESIGN, FRICTION, ADHESION, LUBRICATION AND WEAR.....	123
A.10 MICROMECHANICS IN BIOGENIC HYDRATED SILICA: HINGES AND INTERLOCKING DEVICES IN DIATOMS.	134
APPENDIX B: PUBLICATION LIST.....	145
JOURNAL ARTICLES.....	145
INVITED BOOK CHAPTERS	147
PAPERS RESULTING FROM PRESENTATIONS AT INTERNATIONAL CONFERENCES	148
PAPERS SUBMITTED AND IN PREPARATION:.....	151

APPENDIX C: CURRICULUM VITAE	152
EDUCATION.....	152
EMPLOYMENT	152
RESEARCH VISITS.....	153
CURRENT RESEARCH INTERESTS	153
TEAM MEMBER IN RESEARCH PROJECTS	153
RESEARCH PROJECT MANAGEMENT	154
RESEARCH PROJECT ACQUISITION.....	154
INVITED, PLENARY AND KEYNOTE TALKS AT INTERNATIONAL CONFERENCES.....	155
TEACHING EXPERIENCE.....	156
PUPILS AND STUDENTS FROM UNIVERSITIES OF APPLIED SCIENCES, DOING AN INTERNSHIP	157
UNDERGRADUATE STUDENTS, DOING THE PROJECT WORK “INTERACTIONS WITH SURFACES” (8 HOURS PER WEEK, FOR ONE SEMESTER):	157
SUMMER STUDENTS	159
IAESTE (INTERNATIONAL ASSOCIATION FOR THE EXCHANGE OF STUDENTS FOR TECHNICAL EXPERIENCE) STUDENTS	159
DIPLOMA STUDENTS	160
GRADUATE STUDENTS (WORKING FOR DR. TECHN.).....	160
POSTDOC	160
POPULAR SCIENCE / OUTREACH ACTIVITIES	161
PUBLICITY.....	163
EDUCATION AND TRAINING OF PHYSICS TEACHERS	163
HONORS AND AWARDS	164
COMMITTEE POSITIONS.....	164
EDITORIAL BOARD MEMBERSHIPS.....	165
OTHER SCIENTIFIC COMMUNITY SERVICES.....	165
REVIEWING WORK (PEER-REVIEWED JOURNALS, BOOKS)	166
ACKNOWLEDGEMENTS	167

List of abbreviations

AFM	atomic force microscopy
ATP	adenosine triphosphate
CDOS	charge density-of-states
ESD	electron stimulated desorption
HOPG	highly oriented pyrolytic graphite
ID	interstitial defect
MCI	multiply charged ion
MEMS	microelectromechanical system
NEMS	nanoelectromechanical systems
PS	potential sputtering
PSD	photon stimulated desorption
rms	root mean square
SEM	scanning electron microscopy
SPM	scanning probe microscopy
UHV	ultra-high vacuum
VD	vacancy defect

Preface

This is a cumulative habilitation thesis.

The connection between the publications is explained in the introduction.

Introduction

This habilitation thesis has two main chapters.

The first chapter deals with scanning probe microscopy (SPM) on various samples ranging from living cells to single atoms. SPM of diatoms, real-time interaction of single molecules and nanodefects on atomically flat surfaces are presented. The basis for the first chapter is an invited chapter published in the book „Applied Scanning Probe Methods III – Characterization” by Springer Verlag in 2006 as part of the book series „Nanoscience and Technology” [**Publication A1 in Appendix A**]. Here this book chapter is extended and actualized. **Publications A1 to A8 in Appendix A** are the corresponding publications selected for review.

The second chapter deals with diatom tribology, a new field that was initiated by Gebeshuber and Drack in 1994. **Publications A9 and A10 in Appendix A** are the corresponding publications selected for review.

In **Appendix A**, the publications selected for review are attached, followed by **Appendix B** (publication list) and **Appendix C** (curriculum vitae).

1 Scanning Probe Microscopy: From living cells to the subatomic range

1.1 Introduction

In this chapter the reader will be introduced to scanning probe microscopy of samples varying by seven orders of magnitude in size (**Figure 1**). The largest samples presented are living cells, measuring some hundreds of micrometers. Small units of life, biomolecules with only some tens of nanometers, are the next sample. They are investigated interacting with each other in real-time. Finally, small ion induced defects on atomically flat crystals represent structures in the nanometer regime. New data storage devices might result from such investigations.

These versatile investigations demand methods such as scanning tunneling and atomic force microscopy (STM/AFM) at ultra- high vacuum (10^{-11} mbar) and atomic force microscopy (AFM) at ambient conditions.

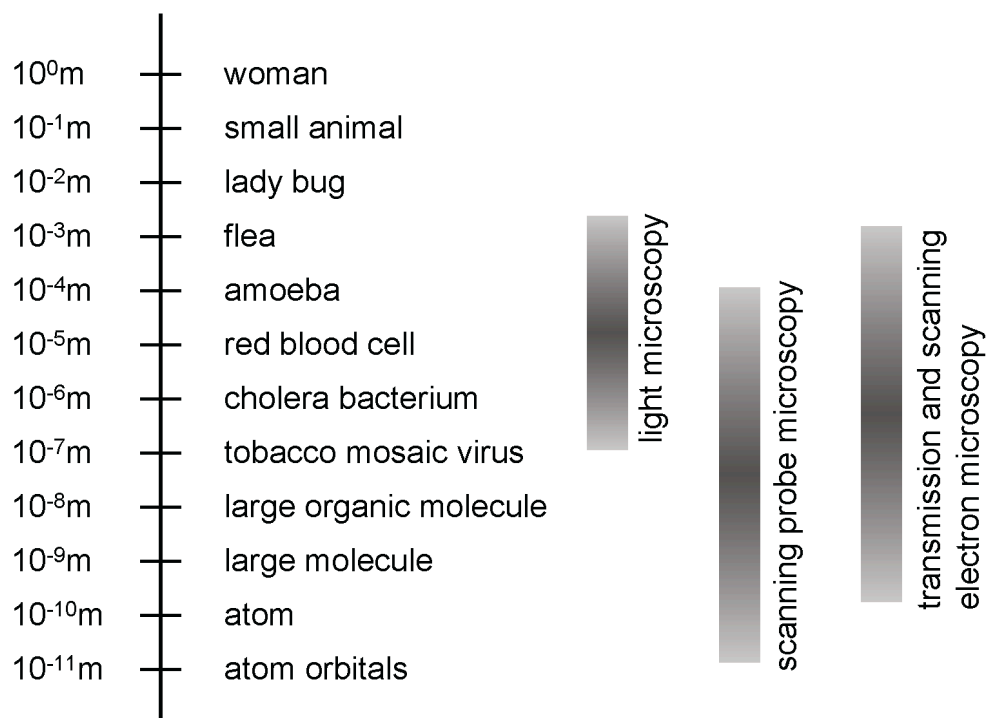


Figure 1: The major types of microscopy cover at least eight orders of magnitude in sample size. Common examples for every scale are given. Note that scanning probe microscopy covers seven orders of magnitude in length.

1.2 Cells in vivo as exemplified by diatoms

Dvorak gives an excellent overview on the investigation of living vertebrate cells by atomic force microscopy [1]. Below, we present the extension of the types of living cells imaged by the atomic force microscope with organisms called diatoms, i.e. single celled algae with biogenic silica shells.

1.2.1 Introduction to diatoms

Diatoms [2] are unicellular microalgae with a cell wall consisting of a siliceous skeleton enveloped by an organic case essentially composed of polysaccharides and proteins [3].

Diatoms are small, mostly easy to cultivate, highly reproductive and, since many of them are transparent, they are accessible by different kinds of optical microscopy methods.

The cell walls form a pillbox-like shell (siliceous exoskeleton). This shell consists of two valves and a series of girdle bands. Diatoms vary greatly in shape, ranging from box-shaped to cylindrical; they can be symmetrical as well as asymmetrical and exhibit an amazing diversity of nanostructured frameworks (**Figure 2**).

These naturally nanostructured surfaces gained the attention of nanoscientists, and diatom nanotechnology developed as a new interdisciplinary field of research [4].

Diatoms are found in freshwater, brackish and marine environments, as well as in moist soils, and on other regularly moist surfaces. They are either freely floating (planktonic forms) or attached to a substratum (benthic forms), and some species may form colonies in the form of chains of cells of varying length. Individual diatoms range from two micrometers up to several millimeters in size, although only few species are larger than 200 micrometers. Diatoms as a group are very diverse with 12000 to 60000 species reported [5][6].

These unicellular organisms are interesting from the point of materials science and biomimetic studies, since they master challenges as diverse as building nanostructured glass shells with high load capacity (a problem interesting for lightweight structures architecture) and engineering strong and robust adhesives that are stable in wet environments (most man-made adhesives fail to bond in wet conditions, owing to chemical modification of the adhesive or its substrate). Furthermore, diatoms excel at preventing dissolution of their silica shells in water owing to a covering layer (up-to-date technology is currently facing the problem that man made glass fiber reinforced polymers show rapid deterioration when used in water).

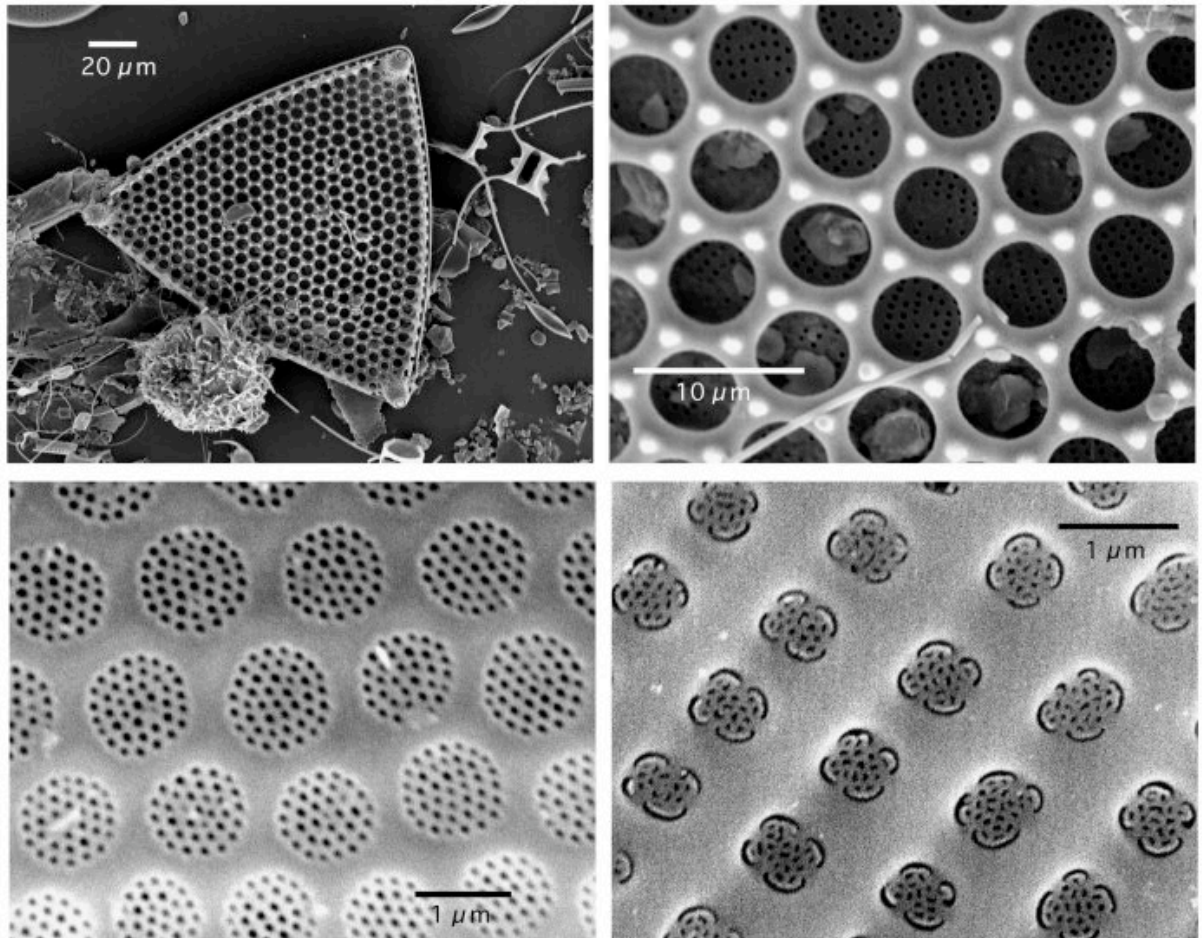


Figure 2: Siliceous exoskeletons of three diatom species imaged with scanning electron microscopy. **Top:** *Tricaeratum favus*, whole cell (**left**), detail (**right**). **Bottom:** *Roperia tessellata* (**left**) and *Achnathes brevipes* (**right**). From [7], **Publication A4 in Appendix A**, © 2002 IoM Communications Ltd.

Currently, human chemical synthesis cannot produce siliceous structures with the hierarchical structural detail of the diatom frustules nor can ordered siliceous structures be produced synthetically under the benign conditions of diatom biomineralization. Biosilicification occurs at ambient temperatures and pressures, whereas artificial chemical synthesis of silica-based materials (e.g. resins, molecular sieves and catalysts) requires extreme conditions of temperature, pressure and pH.

1.2.2 SPM of diatoms

The first AFM study of diatoms was presented in 1992 [8]. In this study, the surface structures of six different diatom species collected from a mud sample were imaged after the cells had been briefly rinsed with ethanol to kill, clean and immobilize them.

Almquist *et al* reported topography and micromechanical properties like elasticity and hardness of dead diatom cells in 2001 [9].

Additionally to these AFM images of dead cells, topography and micromechanical properties (such as viscoelastic properties, adhesion forces and hardness) of the surface of the living diatom cell have been investigated (e.g. [7], **Publication A4 in Appendix A**, [10]-[13]).

Lee and co-workers combined scanning electrochemical microscopy and scanning optical microscopy to obtain simultaneous electrochemical and optical images of living diatoms in a constant-current mode [14]. This kind of microscopy might prove useful in mapping the biochemical activity of a living cell.

Hamm and co-workers investigated the defense potential of the diatom shell by measuring their strength [15]. It was found that diatoms are remarkably strong by virtue of their architecture and the material properties of the diatom silica.

In 2004 Arce and co-workers used the AFM to compare the adhesion of diatoms to several surfaces. Tipless AFM cantilevers were functionalized with live diatom cells, and the surfaces investigated were tested with the same diatom bioprobe [16].

1.2.2.1 Diatom topography as investigated with AFM

Owing to the poor adhesion to the substrate, it is impossible to obtain stable images of most living diatom species with the AFM.

AFM-compatible diatom species can be selected from a large sample by following a simple and effective strategy: Freshwater aquarium plants covered with benthic diatoms are placed in a jar filled with water, as well as two left-handed European freshwater snail species, *Physa fontinalis* and *Planorbarius corneus*, and some glass slides. In the following weeks, the diatoms will colonize the jar and the glass slides. The snails will feed on the diatoms, predominantly leaving the species behind, which obviously strongly attach to the substrate.

By this strategy, Gebeshuber and co-workers selected three different diatom species: *Eunotia sudetica*, *Navicula seminulum* and a yet unidentified species, and subsequently imaged them in contact mode AFM (**Figure 3**, [11]).

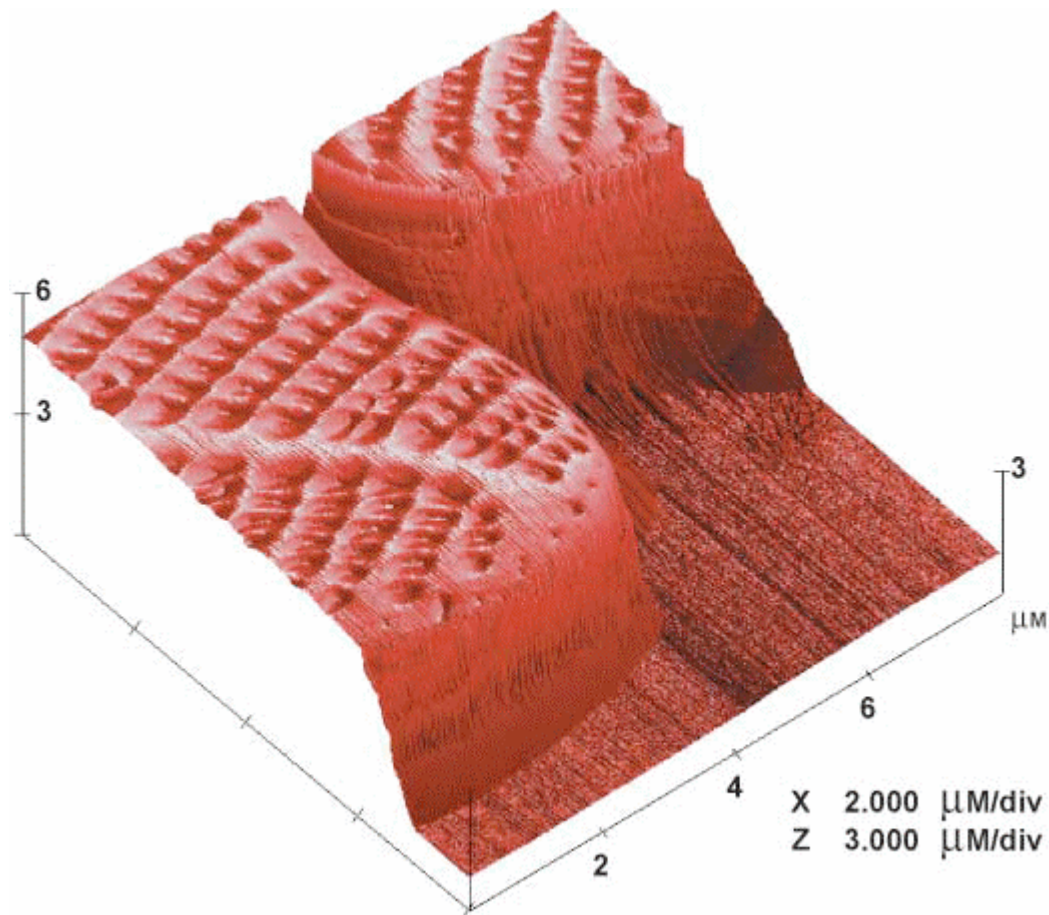


Figure 3: AFM image of parts of two living diatom cells of the species *Navicula seminulum* growing on a glass slide. Note that the flat area does not correspond to the surface of the glass slide, but is determined by the maximum possible extension of the z-piezo of the microscope. Image acquired using AFM contact-mode imaging in water, imaging parameter topography, scan size $8 \times 8 \mu\text{m}^2$, scanning frequency 1 Hz. From [11], **Publication A3 in Appendix A**, © 2003, The Royal Microscopical Society.

The natural adhesives of these diatoms, which attach them to the substrate as well as to each other (all of them are colonial forms), prove to be sufficiently strong that stable AFM imaging conditions are achieved without further sample preparation.

The cells are imaged in their culture medium or in tap water while they are still growing on the glass slides. Tapping-mode as well as contact mode imaging is easy to achieve as long as engaging the cantilever takes place on the cell surface.

Navicula seminulum grows in stacks of cells pointing out from the glass slide. These chains of cells can be about 10 cells high, as investigated by scanning electron microscopy (SEM, data not shown). **Figure 3** reveals detailed surface patterning of the top valve faces of two adjacent cells of *Navicula seminulum*.

The chains of *Eunotia sudetica* and of the yet unidentified species grow with the valve faces perpendicular to the surface of the glass slide, allowing for AFM investigation of the girdle bands.

The cells are alive and continue to divide after imaging.

1.2.2.2 Diatom adhesives investigated by SPM

Most man-made adhesives fail to bond in wet conditions, owing to chemical modification of the adhesive or its substrate. Engineering strong and robust underwater adhesives that are stable in wet environments are a challenge to current technology. Diatoms produce excellent adhesives that are stable and robust in wet environments.

Phase images depict the phase delay between the drive and response of the cantilever. These images contain information about the energy dissipated during the interaction of the AFM tip with the sample, and can help us to understand the viscoelastic and adhesion properties of the surfaces investigated, specifically of the organic material responsible for diatom adhesion

Because phase imaging highlights edges and is not affected by large-scale height differences, it provides clearer observation of fine features that might otherwise be hidden by rough topography (**Figure 4**). To investigate the natural adhesives utilized to attach cells to each other and to the substratum, it was tried to probe the cleft between two connected diatom cells with the AFM. In the yet unidentified species, the cleft at the cell-cell interface proved too deep. In this region, even the use of electron-beam-deposited AFM tips with high aspect ratio merely results in tip imaging. Phase imaging reveals slight differences (2°) in viscoelastic and adhesion properties of the two adjacent valves. *Eunotia sudetica*, by contrast, is very convenient for *in situ* investigation of the diatom adhesive at the cell interface, because there is barely any cleft between adjacent cells and valve undulations are less pronounced than in the other species investigated (**Figure 4**). The diatom adhesive is apparent as small topographic features at the cell interface. The bead-like structures are 10-20 nm high, have lateral dimensions of about 1 μm and are about 1 μm apart.

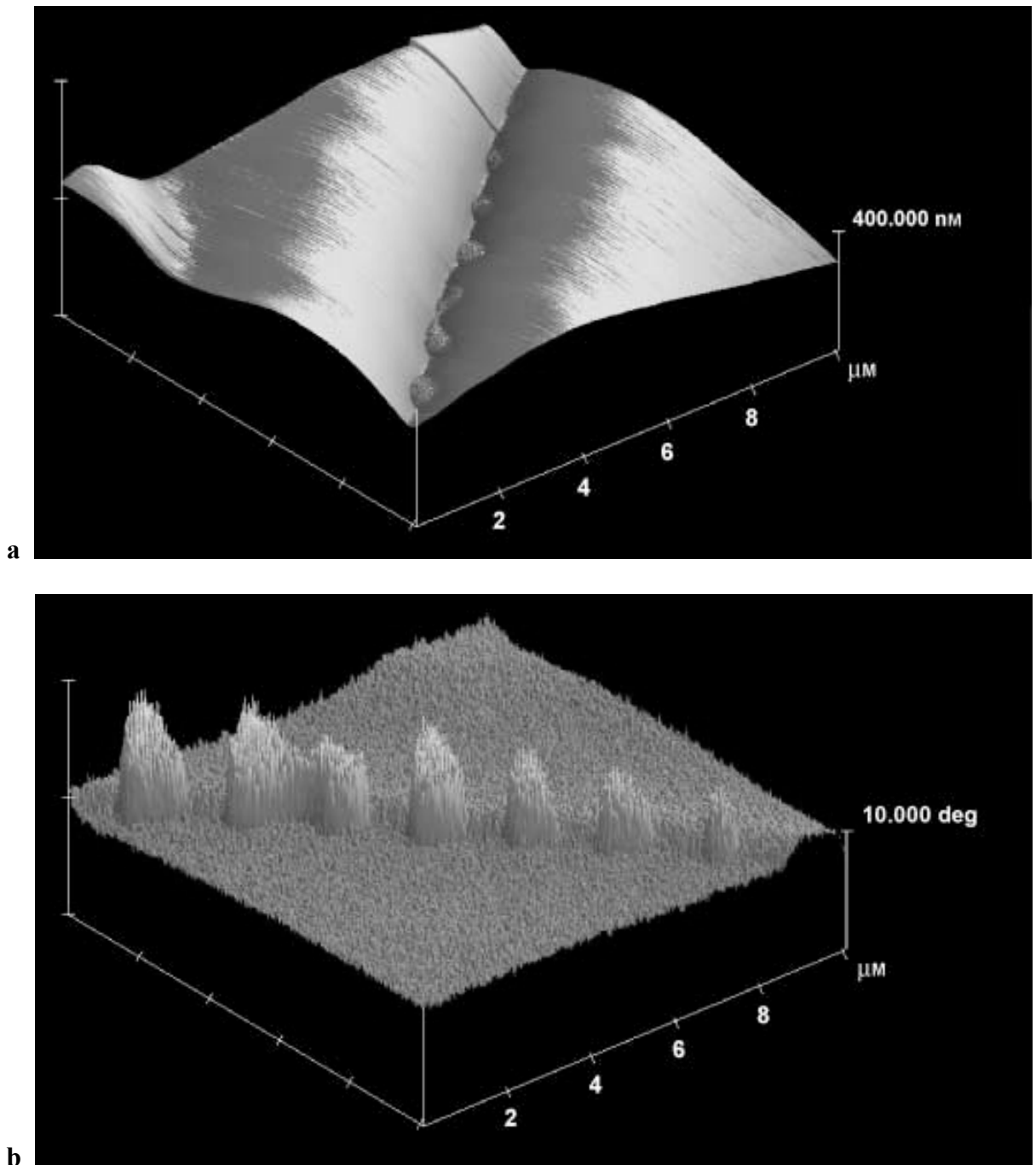


Figure 4: (a) The adhesives in the contact region of two cells of *Eunotia sudetica* are apparent as small topographic features on the slightly undulated cell interface. The corrugation of the bead-like structures is between 10 and 20 nm, and their lateral dimension and spacing is about 1 μm. (b) In the phase image these features are far more striking. The diatom adhesive causes a phase lag of about 10 degrees compared with the rest of the frustule surfaces, where on a single frustule it is within 1 degree. Note the 2-degree interfrustule phase step, which reveals slightly different viscoelastic properties of the two neighbouring valves. Tapping mode, topography and phase, scan size 10*10 μm², scan rate 5 Hz. Note that for better view (b) is rotated clockwise by 90 degrees as compared with (a). From [11], **Publication A3 in Appendix A**, © 2003, The Royal Microscopical Society.

The phase image clearly depicts the altered viscoelastic properties of these structures: the diatom adhesive causes a phase difference of up to 10 degrees compared with the phase difference on the rest of each of the two frustules, where it is within 1 degree on each, apart from a 2 degree phase difference between the two adjacent valves, a feature which also appears in the other species, where the adhesives are not accessible because of deep clefts between the single organisms.

Force-distance curves on the surface and on the adhesive of *Eunotia sudetica* reveal basic differences in adhesion properties (**Figure 5**). On the diatom surface, no adhesion force can be detected (**Figure 5 left**). The diatom adhesive, by contrast, is strong and robust in the wet environment. To gain reproducible access to this natural adhesive, a chain of *Eunotia sudetica* that was embedded in a densely packed field of *Navicula seminulum* was scraped away from the glass slide with a scanning tunnelling microscopy tip mounted on a three-dimensional micromanipulator. Over a period of several hours, force-distance curves were taken on the adhesive molecules that had attached the diatom cells to the glass slide (**Figure 5 right**). No change in the basic shape of the force-distance curves can be detected within hours of repetitive pulling in the area where the colony was located. Typically, several debonding events occur until the natural adhesive molecules finally debond at a tip-surface separation of about 600 nm. For a detailed description of this study, see ([7][11], **Publications A3 and A4 in Appendix A**).

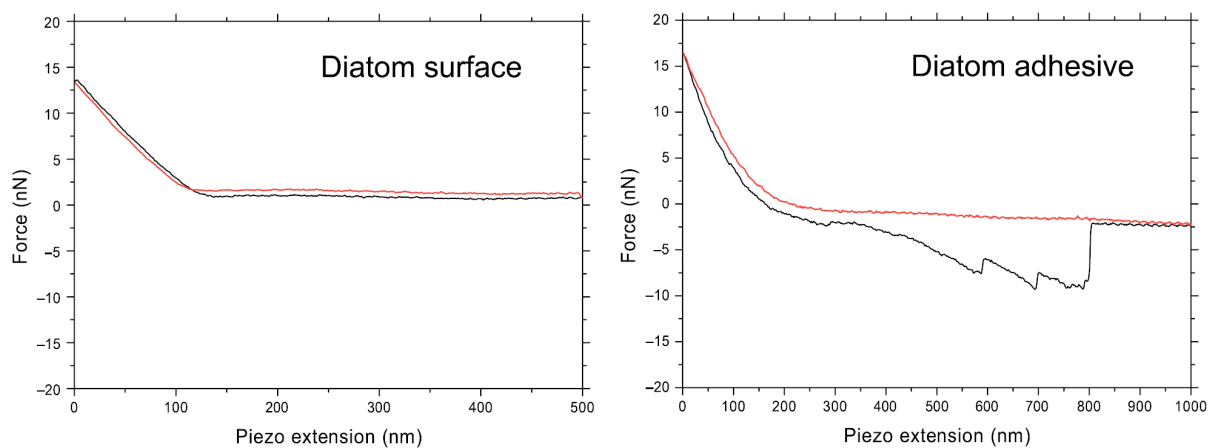


Figure 5: Force-distance curves. **Left:** No adhesion can be recognized on the diatom surface. **Right:** Representative data for the diatom adhesive that attaches *Eunotia sudetica* to the substrate. Several debonding events occur. From [11], **Publication A3 in Appendix A**, © 2003, The Royal Microscopical Society.

1.3 Interaction of large organic molecules

Conformational diseases such as Parkinson's disease, Alzheimer's disease, kuru, scrapie, BSE and vCJD (variant Creutzfeldt-Jakob Disease) result from misfolded proteins aggregating into detrimental structures such as amyloid fibers [17]-[19].

The amount of protein involved in such diseases ranges from scarcely detectable to kilograms. Partial unfolding might expose significant regions of the polypeptide chain to the outside world, allowing the protein to aggregate and convert into amyloid fibrils. Once formed, the strong hydrogen bonding between molecules can make this process effectively irreversible.

As with crystallization, the formation of amyloid fibrils is "seeded" by pre-formed aggregates, a phenomenon that might also be responsible for the rapid progression of sporadic diseases such as Alzheimer's once the symptoms become evident. BSE for example has almost undoubtedly resulted from the highly unnatural practice of feeding young cows on the remains of old ones, with the disease then being transmitted to humans as vCJD. Both kuru and BSE have virtually disappeared as a result of effective action taken once their origins were understood.

The proteins that have emerged under evolutionary pressure are normally robust enough to resist reversion to aggregated states. Evolutionary processes have selected sequences of amino acids with the remarkable ability to form monomeric structures in which the main chain is folded in a unique way within the mass of close-packed side chains, preventing it from interacting with other molecules.

Furthermore, "chaperone" proteins help to protect against such changes. Chaperones are proteins whose function is to assist other proteins in achieving proper folding: They prevent protein aggregation by providing encapsulated hydrophobic environments that allow the protein to fold properly.

Many chaperones are heat or cold shock proteins, that is, proteins expressed in heat or cold shock conditions. The reason for this behavior is that protein folding is severely affected by extreme temperatures. Chaperones act to counteract the potential damage. Although most proteins can fold in absence of chaperones, a minority strictly requires them.

A large number of chaperones need adenosine triphosphate (ATP) for proper function. Chaperones recognize unfolded proteins by the hydrophobic residues these expose to the solvent. Exposed hydrophobic residues are unusual for properly folded proteins.

Since the environment of the cell is characterized by hydrophilic groups (mostly water), incompletely folded or misfolded proteins, with exposed hydrophobic groups have a tendency to aggregate to larger structures, where again, the hydrophobic residues would be hidden from the surrounding. Chaperonins are a subset of chaperone proteins found in prokaryotes, mitochondria and plastids.

The AFM has proven to be a useful tool for studying proteins at the single molecule level. For a review on single molecule techniques in biomedicine and pharmacology see [20]. Many of the single molecule studies with the AFM have been restricted by noise and speed limitations.

The first protein-protein interactions on the single molecule level imaged in real time were presented in 2000 [21, **Publication A2 in Appendix A**]. This study demonstrated the enormous contributions AFM can make to molecular biology. Bulk results are interesting, but there are many valuable properties that can only be investigated on the single molecule level.

This work was enabled by the development of small cantilevers [22]-[24]. Small cantilevers allow for faster imaging and force spectroscopy of single biopolymers because they have higher resonant frequencies and lower coefficients of viscous damping. A new generation of AFMs using small cantilevers will enable the study of biological processes with greater time resolution, possibly at video refresh rates. Furthermore, because of the possibility to perform faster force spectroscopy, small cantilever AFMs allow to narrow the gap in observation time between results from force spectroscopy experiments and molecular dynamics calculations.

The small cantilevers used in this study are fabricated out of low stress silicon nitride. They are ten micrometers long, have widths of 3–5 μm , and their thickness is about 75 nm. These cantilevers can measure smaller forces than larger cantilevers with the same spring constant because they have lower coefficients of viscous damping.

The prototype small AFM detects the motion of small cantilevers by using high numerical aperture optics to focus a laser beam onto the cantilever and then measuring angular changes in the reflected light beam.

This microscopy was used to observe, in real time, the interactions between individual molecules of the *Escherichia coli* chaperonin protein GroES binding to and then dissociating from individual *E. coli* GroEL proteins that were immobilized on a mica support.

Both X-ray crystallography and cryoelectron microscopy studies have been used to resolve the structures of GroEL and the GroEL-GroES complex in different stages of the folding cycle (**Figure 6**, e.g. [25]-[30]).

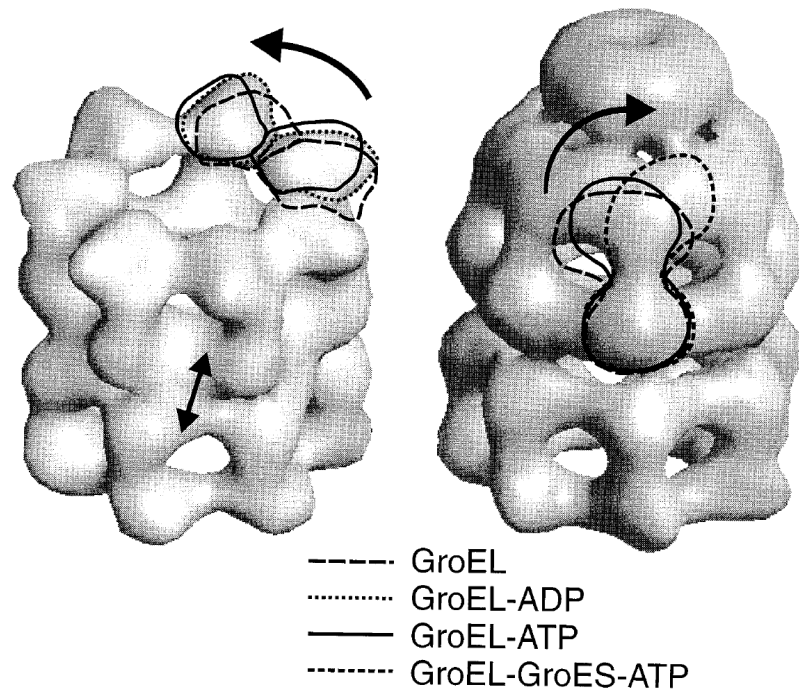


Figure 6: Cryoelectron microscopy images of GroEL (**left**) and the GroEL-GroES complex (**right**). The height of the GroEL molecule is about 15.1 nm; the height of the GroEL-ES complex is about 18.4 nm. Upon interaction with ADP or ATP, domain movements occur, as indicated. From [30] © 1996, Elsevier.

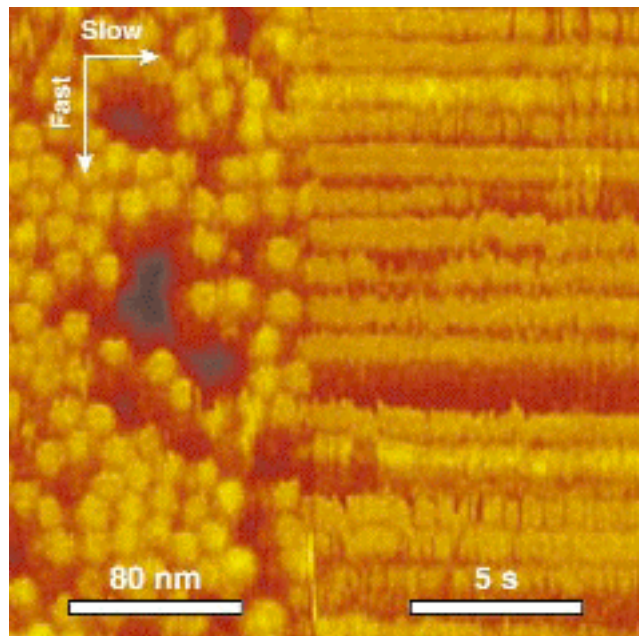


Figure 7: GroEL film deposited on mica scanned in two dimensions (**left**) and in one dimension (**right**). In this image of GroEL, the movement along the slow scan axis was disabled half way through the scan. From then on the AFM tip repeatedly scanned the same line of proteins. Each horizontal line therefore shows changes in time of an individual molecule. From [21], **Publication A2 in Appendix A**, © 2000, Nature Publishing Group.

A prototype small cantilever AFM [24] image of GroEL molecules deposited on mica repeatedly imaged without the aid of fixing agents is shown in **Figure 7**. GroEL adsorbs to mica in end-up orientation. The average diameter of the molecules in this image agrees with the X-ray and cryoelectron microscopy data. Upon the addition of GroES and ATP into the buffer solution, GroES molecules were observed as features that extend 3.6 ± 1 nm higher than the GroEL film (**Figure 8**).

The height of these features is also consistent with X-ray crystallography and cryoelectron microscopy data. The same sample region can be scanned repeatedly without excessively disturbing the GroEL-GroES complexes (for details, see [21], **Publication A2 in Appendix A**).

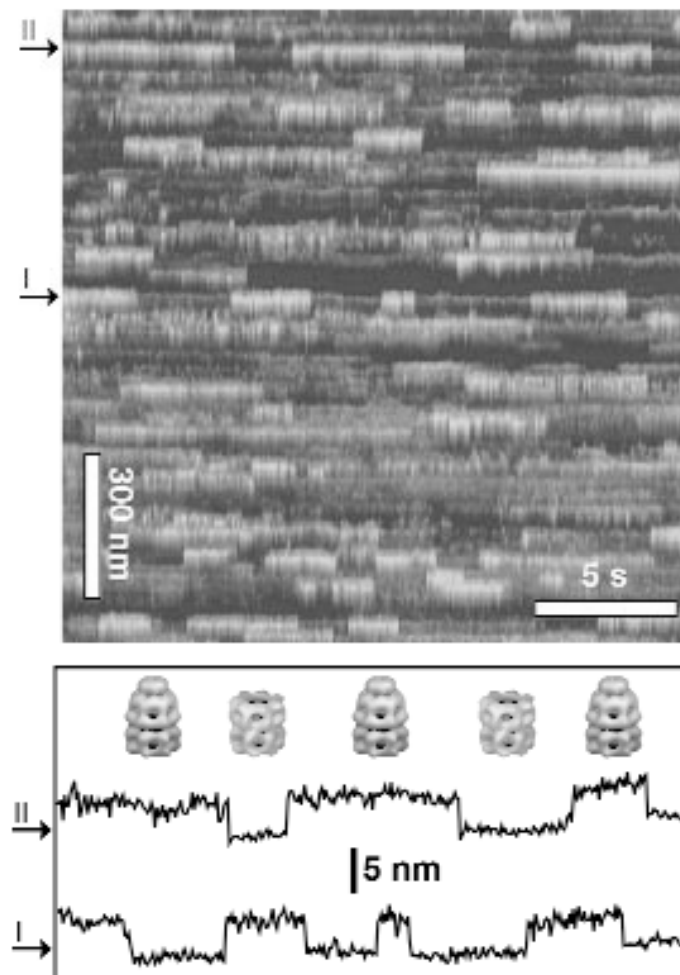


Figure 8: Tapping mode AFM in liquid. **Top:** After the addition of GroES and Mg-ATP into the buffer solution, variations in height along the lengths occur in the single protein lines, as exemplified by arrows I and II. **Bottom:** Time/height diagram of the protein lines indicated with the arrows in the top image. The height difference between two values is 3.6 ± 1 nm. This indicates the binding and unbinding of GroES. From [21], **Publication A2 in Appendix A**, © 2000, Nature Publishing Group.

Therefore, in order to obtain the temporal resolution required for observing the formation and dissociation of the GroEL-GroES complexes in the presence of Mg-ATP, the sample was scanned in one dimension rather than two (**Figure 8**). The time/height diagram of the protein lines displays repetitive well-defined step-like variations in height. The magnitude of these steps is 3.6 ± 1 nm. The observed height variations result from GroES molecules attaching to and then separating from the respective GroEL molecules. Without GroES and Mg-ATP no such steps can be observed.

A histogram of the complex lifetime for a single GroEL molecule that was investigated for about 120 seconds is shown in **Figure 9**. During this time, 18 times a complex with GroES is formed. The distribution of complex lifetime peaks near 5 seconds and the average lifetime is $\sim 7 \pm 1$ s ($n = 18$).

In future application of this kind of single molecule studies with the AFM, misfolded proteins could well be involved and e.g., the effect of various pharmaceuticals on folding efficiency could be tested.

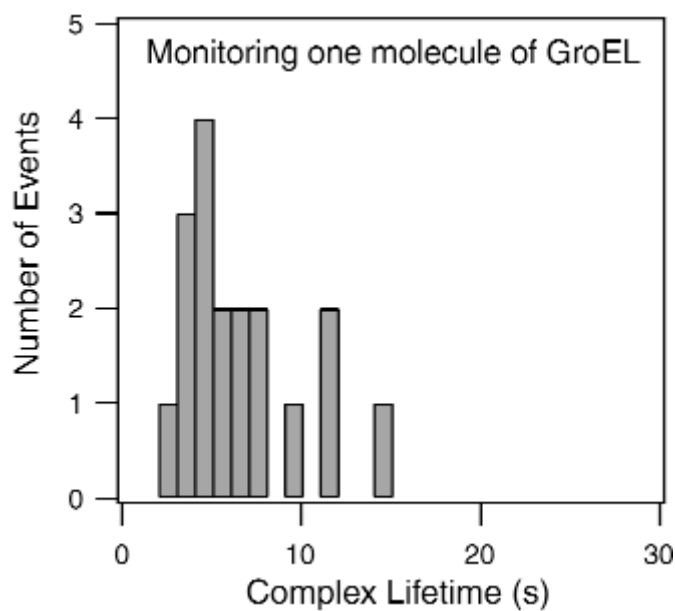


Figure 9: Histogram of measured GroEL-GroES complex lifetime in the presence of Mg-ATP. Individual GroES molecules attach to and then separate from the same GroEL molecule 18 times during an observation period of about 120 seconds. Note the absence of events with lifetimes < 2 seconds. This is interesting by itself, telling us about the GroEL-GroES complex lifetime on the single molecule level, and furthermore indicates gentle measuring, since strong disturbance of complex formation by the cantilever would also lead to subsecond complex lifetimes. From [21], **Publication A2 in Appendix A**, © 2000, Nature Publishing Group.

1.4 Nanodefects on atomically flat surfaces

Most of the small structures currently used in technology are in the micrometer range. One reason for this is silicon micromachining technology, which works fast and at low cost in this regime.

However, the needs for increased data-storage density and smaller devices call for nanometer-sized structures.

Nanofabrication techniques comprise techniques such as electron beam and nano-imprint fabrication, epitaxy and strain engineering, scanning probe techniques, as well as self-assembly and template manufacturing [31].

Nanotransfer printing is a more recent high-resolution printing technique that uses surface chemistries as interfacial “glues” and “release” layers to control the transfer of solid material layers from stamp relief features to a substrate [32].

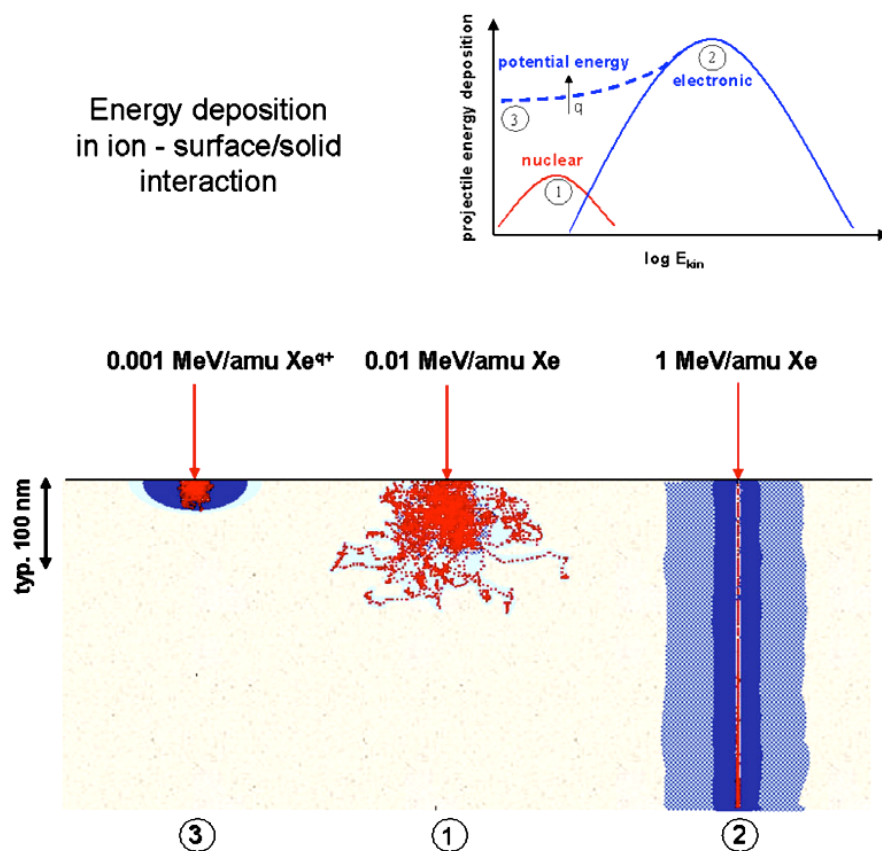


Figure 10: Energy deposition during interactions with a solid surface of slow highly charged ions or neutral atoms (1), swift ions or neutral atoms (2) and slow highly charged ions (3). Slow highly charged ions are a tool for gently nanostructuring the surface with minimal damage to the bulk material. From [33], **Publication A7 in Appendix A**, © 2006 Elsevier B.V.

One important way to produce nanostructures on surfaces involves kinetic sputtering by “fast” ions. However, fast ions unavoidably cause unwanted radiation damage. As opposed to this, potential sputtering (PS), i.e. desorption induced by the potential energy of slow multiply charged ions (MCI), holds great promise for more gentle nanostructuring of insulating surfaces [34][35] (Figure 10).

The potential (i.e. internal) energy E_p of highly charged ions (HCI) is equal to the total ionization energy required for producing the high charge state from its neutral ground state. E_p is known to have a strong influence on surface interaction processes such as electron-emission, sputtering and secondary ion emission [36].

Potential sputtering can cause high sputter yields even at such low ion impact energies where kinetic sputtering and defect creation in deeper layers is not possible. While the physical mechanisms of PS have been the subject of extensive investigation [37]-[41] technical applications of slow MCI have so far remained largely unexplored, despite the fact that they provide unique opportunities for etching, ultra-thin film growth and nanostructure fabrication.

The AFM is the microscope of choice for investigating ion induced nanodefects on flat crystals, because of its unprecedented resolution and because of the fact that it can also image insulating materials.

1.4.1 Ion bombardment of highly oriented pyrolytic graphite

Highly oriented pyrolytic graphite (HOPG) is used as a diffracting element in monochromators for x-ray and neutron scattering and as a calibration standard for STM and AFM. The graphite surface is easily prepared as a clean atomically flat surface by cleavage with an adhesive tape. HOPG is therefore used in many laboratories as the surface of choice for “seeing atoms”.

Surface defects in HOPG produced by the impact of individual (singly charged) ions have already been investigated via STM/AFM by a number of groups ([42]-[51] and further references therein).

However, only recently first results were reported for impact of slow multiply charged ions and the effect of the projectile charge state (or potential energy) on the size of the produced nanodefects [52]-[55].

Moreover, in most previous studies either STM in air was used or the irradiated samples were transported in air towards STM inspection after ion bombardment. If, e.g., chemical bonds at the surface are broken due to the ion impact, impurities could preferentially adsorb at these sites and thus change the topography of the surface (and the resulting STM image) during contact with air. Therefore, here MCI bombardment has been followed by STM/AFM investigations without breaking the ultra-high vacuum. In this way possible influences from target surface exposure to air can be ruled out.

Figure 11 shows STM and AFM scans of the HOPG surface before bombardment.

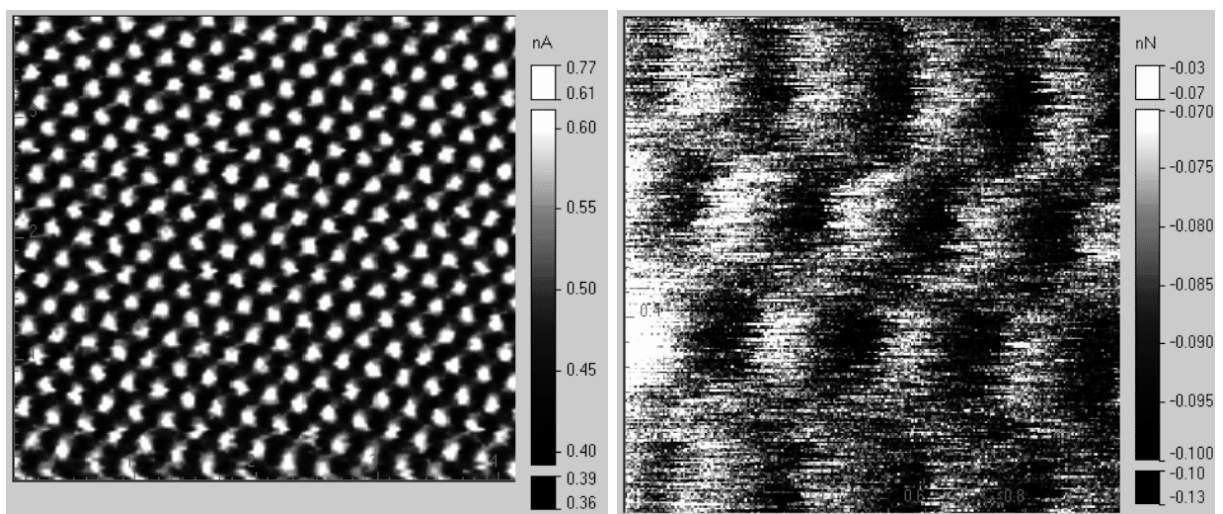


Figure 11: Highly oriented pyrolytic graphite imaged in ultrahigh vacuum with atomic resolution. **Left:** Scanning tunnelling microscopy image, image size $4 \times 4 \text{ nm}^2$. **Right:** Atomic force microscopy image; image size $1 \times 1 \text{ nm}^2$.

The STM image of HOPG bombarded with 800 eV Ar^+ ions reveals a large number of individual nanosized defects as result of ion bombardment (**Figure 12**). In AFM scans of the same surface, no significant topographic changes could be detected ([56], **Publication A6 in Appendix A**).

For very highly charged projectile ions, surface defects have recently also been observed in AFM studies [54][55].

Meguro and co-workers found that HCl impact and subsequent treatment either by electron injection from an STM tip or by He-Cd laser irradiation induce a localized transition from sp^2 to sp^3 hybridization in graphite, resulting in the formation of nanoscale diamond-like structures (nanodiamonds) at the impact region [57].

In an investigation of HOPG bombarded with 400 eV Ar^+ and Ar^{8+} ions involving Raman spectroscopy Hida and co-workers found that the charge state of the ions as well as their mass have an influence on the disordering of HOPG and that the defects introduced by Ar^{8+} are not simple vacancies but assumed to be vacancy clusters in contrast to their results for Ar^+ irradiation [58].

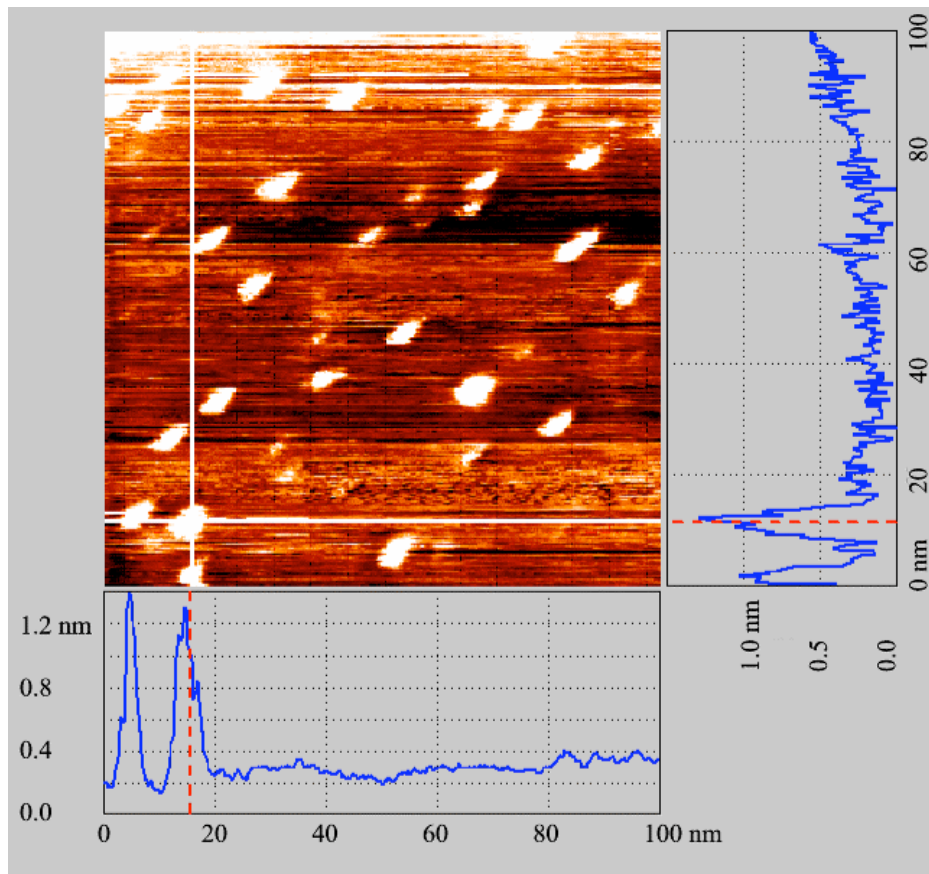


Figure 12: Highly oriented pyrolytic graphite bombarded with 800 eV Ar^+ ions imaged with STM in ultrahigh vacuum. Image size $100 \times 100 \text{ nm}^2$. The ion-induced nanodefects are clearly visible.

Several hundred defects from different sample positions have been statistically analyzed for each projectile type (Ar^+ , Ar^{8+} , Ar^{9+}).

Figure 13 (right image) shows the enlarged STM image of a typical defect on HOPG created by the impact of a single Ar^+ ion with a kinetic energy of 800 eV.

The only surface defects found in the STM images are protrusions (hillocks) with a mean lateral size of 0.8-1.25 nm and an average equivalent height of 0.22 nm. They are randomly dispersed on the originally flat surface. Their area density is in good agreement with the applied ion dose, implying that nearly every single ion impact has caused one protrusion. A $\sqrt{3} * \sqrt{3}R30^\circ$ surface, as characteristic for interstitial defects in HOPG [59]-[61], surrounded by undisturbed surface parts is observed in the vicinity of most defects (see **Figure 13**). Scanning with the AFM down to atomic resolution on the irradiated surface did not show any significant topographic changes due to ion bombardment. Therefore, we conclude that the nanodefects produced by slow ion impact are of electronic rather than of topographic nature.

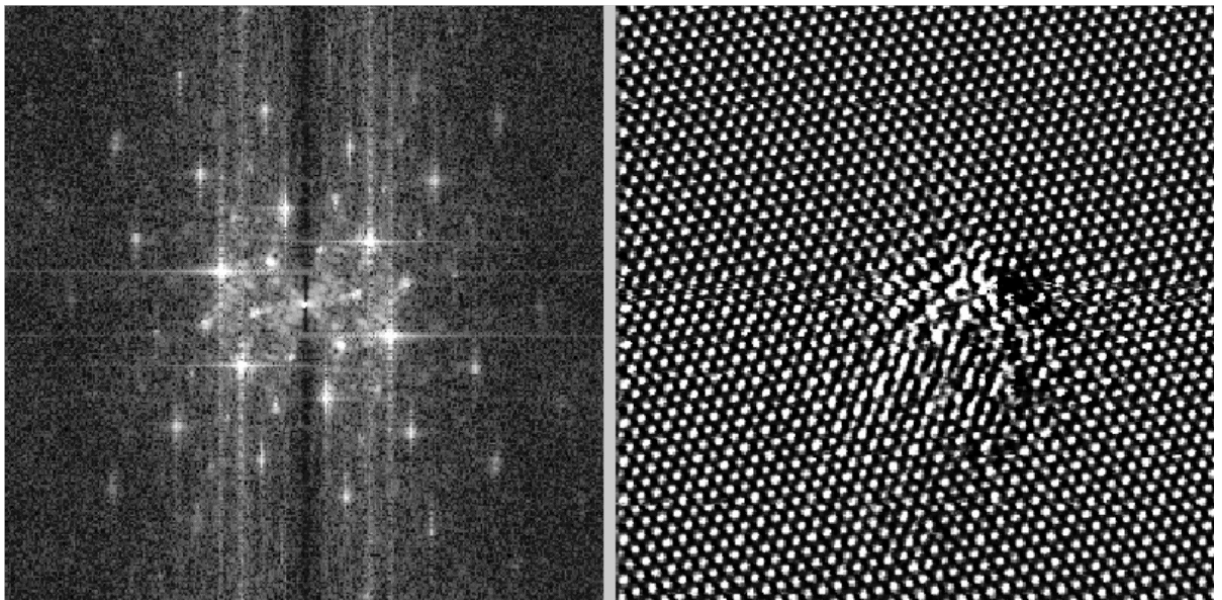


Figure 13: Highly oriented pyrolytic graphite bombarded with 800 eV Ar^+ ions imaged with STM in ultrahigh vacuum with atomic resolution (**right**). Image size $10 * 10 \text{ nm}^2$. The fast Fourier transform (**left**) of the Ar^+ ion-induced defect reveals a $\sqrt{3} * \sqrt{3}R30^\circ$ surface: the ion-induced features are larger than the features from the HOPG lattice and they are rotated with respect to them by 30 degrees.

For impact of singly charged ions, our findings are in good agreement with previous observations [46][60]. As a remarkable result, however, it was found that the measured mean diameter of the “hillocks” and to a somewhat lesser extent their “height” increase with projectile charge state ([56], **Publication A6 in Appendix A**). In a careful STM study, Hahn and Kang [60] showed that generally two kinds of defects in HOPG are created by low energy (100 eV) Ar^+ bombardment, namely carbon vacancy defects (VDs) and interstitial defects (IDs) formed by trapping the projectile beneath the first carbon plane.

Both types of defects are detected as protrusions in the STM topographic image. The dangling bonds at the VD site cause an enhancement of the local charge density-of-states (CDOS) near the Fermi energy, seen as a protrusion in the STM image [60].

The protrusion observed in the STM image at ID sites results from a small geometric deformation of the graphite basal plane due to the trapped projectile (not large enough to be visible in our AFM scans) and an apparently larger electronic defect due to an increased CDOS. Only for IDs but not for VDs a $\sqrt{3} * \sqrt{3}R30^\circ$ surface was reported [60]. From this $\sqrt{3} * \sqrt{3}R30^\circ$ superlattice structure also observed in our experiments (see Fig. 12), we therefore conclude that the majority of the “hillocks” observed are due to IDs, or VDs created along with IDs. The strong increase of the lateral protrusion size with increasing charge state of the projectile ion is interpreted as a “pre-equilibrium” effect of the stopping of slow multiply charged ions in HOPG, as has so far only been observed for higher charge states [47].

Although MCI are converted already into neutral hollow atoms (i.e., atoms whose inner shells remain essentially unoccupied) during their approach towards the surface, their captured electrons remain in highly excited states until surface impact, where they are gradually peeled off and replaced by conduction band electrons forming a partial screening cloud around the MCI [62].

Before final deexcitation of the hollow atom can take place within the solid, reduced screening should result in a strongly increased energy loss of the projectiles. According to SRIM-2000 (© IBM) calculations [63], the mean range of 150 eV Ar projectiles in HOPG is about two monolayers. An increased stopping and straggling of the higher charged Ar projectiles would lead to IDs located closer to the surface, as well as to more VDs due to a higher momentum transfer to the carbon atoms of the first plane. The pre-equilibrium effect in the stopping power is not masked by (equilibrium) bulk effects because of the extreme surface sensitivity of STM and is apparently observable with unprecedented clearness.

Extending pertinent work by other groups with singly charged ions only, our combined STM/AFM studies revealed nanodefects that comprise a disturbance of the electronic density-of-states of the surface rather than its topography.

Whereas the size of these defects increases with the ion charge (here up to $q = 9$), as expected for any conducting target surface they showed no evidence for potential sputtering.

For more information on these studies, see ([53][56], **Publication A6 in Appendix A**).

1.4.2 Bombardment of insulator single crystal surfaces with multicharged ions

Impact of slow ions on solid surfaces can give rise to inelastic processes which modify the geometric and electronic structure at and below the surface (**Figure 10**), cause emission of electrons and photons as well as neutral and ionized target particles (atoms, molecules, clusters), remove surface-adsorbed material and lead to projectile neutralization. The transfer of electrons between surface and projectile possibly acts as precursor for the above-mentioned processes and makes them to proceed irrespective of the kinetic projectile energy.

The importance of such “electronic” processes increases with multicharged projectile ions and their role is elucidated when slow ions of the same kinetic energy but with different charge states are applied as projectiles.

For certain insulator surfaces, the impact of slow multicharged ions (MCIs) Z^{q+} gives rise to considerably stronger ablation than the well-established kinetic sputtering by neutral or ionized projectiles. First experimental evidence for this PS was reported for alkali-halide surfaces and explained by “Coulomb explosion” [64], i.e., creation of small positively charged surface spots from the rapid electron capture by impinging MCI, and the subsequent ablation because of strong mutual target ion repulsion.

“Coulomb explosion” was also invoked in order to explain AFM observations of blister-like defects on mica samples produced by highly charged ions Z^{q+} (kinetic energy 1-3 keV/atomic mass unit) [65][39]. However, studies for impact of slow (≤ 1 keV) MCI on thin polycrystalline films of alkali-halides (LiF, NaCl) and Al_2O_3 deposited on quartz microbalance crystals [66] suggested a different explanation for PS, namely defect-stimulated desorption induced by very efficient electron capture [38].

It has been established that such desorption processes are induced by electrons (electron stimulated desorption, ESD) or photons (photon stimulated desorption, PSD) on such materials where self-trapping of specific crystal defects proceeds via electron-phonon coupling in the crystal lattice [67]. However, such defect trapping as the prerequisite for PS may also be caused or at least supported by the kinetic projectile energy (“kinetically assisted PS” [40]), which could also explain some PS-like effects reported for target species where no electron-phonon coupling can take place, i.e., for semiconductors like Si and GaAs [65]. In any case, for slow ion impact the self-trapping mechanism is most relevant for PS. Consequently, for metal and semiconductor surfaces no slow MCI-induced PS can be observed, so far [68].

A slow MCI captures electrons from a surface region that should be rather small (nm extensions). Therefore it is likely that the surface defects caused by PS are of similar size. In order to study such defect structures we applied AFM (in ultrahigh vacuum and in ambient conditions) on monocrystalline target surfaces of various insulator species such as Al_2O_3 , SiO_2 , diamond like carbon and $\text{LiF}(001)$ ([56],[69]-[72], **Publications A5-A8 in Appendix A**). For Al_2O_3 and SiO_2 , PS by slow MCI impact has already been demonstrated on polycrystalline thin films ([40],[66]-[68]). The long-term goal of the studies is to better understand the damage creation mechanisms; the short-term goal aims at obtaining information about the created surface features and their dependence on the ion-beam parameters and material properties.

1.4.3 Nanodefects generated on Al_2O_3 single crystal surfaces via bombardment with multicharged ions

Systematic AFM investigations on nanoscopic defect production at atomically clean insulator surfaces of Al_2O_3 after bombardment by slow (impact energy ≤ 1.2 keV) singly and multiply charged ions under strict ultrahigh vacuum (UHV) conditions is the topic of this section ([56],[69], **Publications A5 and A6 in Appendix A**).

It is demonstrated that on monocrystalline insulator surfaces, well-defined topographic features of typically nm extensions are produced (potential sputtering). For Al_2O_3 there exists a clear dependence of the defect size on the projectile ion charge. These results are discussed in view to possible new nanoscopic surface structuring and modification methods for which the kinetic projectile energy plays only a minor role.

Observations of slow ion-induced nanodefects on atomically clean target surfaces were performed under strict UHV conditions with a combined AFM/STM instrument (OMICRON Nanotechnology GmbH, Germany). Freshly prepared surfaces of sapphire c-plane $\text{Al}_2\text{O}_3(0001)$ after irradiation with low doses of slow singly and multiply charged ions were investigated for nanodefects. In order to avoid disturbing noise from an ion irradiation chamber directly attached to the AFM/STM instrument, a transportable UHV vault for target transfer that was alternately coupled via UHV locks to the target ion irradiation chamber and the AFM/STM was used. This procedure ensured that the target surfaces were kept under permanent UHV conditions after initial cleaning, thermal annealing, and during subsequent slow ion irradiation until completion of the AFM/STM inspection. Ion irradiation of the insulator surfaces was accompanied by low-energy (≤ 4 eV) electron flooding to compensate for surface charge-up which otherwise strongly inhibits AFM observation or makes it even impossible.

The electron gun was arranged at 2 cm distance to the sample. All AFM observations were made in the contact mode, with the base pressure in the AFM/STM chamber kept during measurements at about 10^{-10} mbar.

The singly and multiply charged ions for target irradiation have been extracted from a 5 GHz electron cyclotron resonance ion source [73], magnetically analyzed and guided via electrostatic lenses to the UHV irradiation chamber. The ions were decelerated in front of the target surface to their desired impact energy (≤ 1.2 keV). Uniform irradiation was assured by rapidly scanning the ion beam across the target surface by means of deflection plates.

Polished $\text{Al}_2\text{O}_3(0001)$ c-plane single crystals (TBL Kelpin, Neuhausen, Germany) were CO_2 snow cleaned (to remove micrometer and submicrometer particles and hydrocarbon-based contamination) and then annealed in UHV for three hours at 400 degrees C. This preparation technique yields very flat crystal surfaces.

AFM contact mode studies on 14 samples prepared by this standard preparation technique revealed a root mean square (rms) roughness of 0.093 ± 0.06 nm rms. Bombardment with Ar ions of different charge states and kinetic energies (500 eV Ar^+ and Ar^{7+} , 1.2 keV Ar^+ , Ar^{4+} and Ar^{7+}) results - as seen in AFM contact mode - in hillock-like nanodefects (see **Figure 14**).

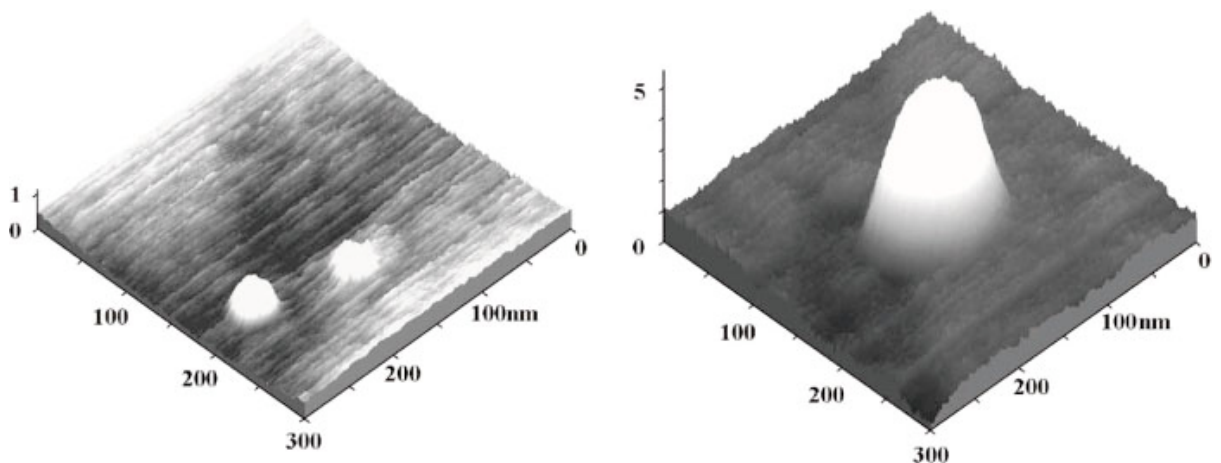


Figure 14: UHV AFM contact mode image of sapphire (Al_2O_3 , c-plane 0001) bombarded with 500 eV Ar^+ (left) and Ar^{7+} (right) ions. The nanodefects induced by Ar^{7+} ions (which have the same kinetic but higher potential energy than the Ar^+ ions) are considerably higher and wider than those caused by singly charged ions. The defects are real topographic features; the units on the three axes are nanometers. From [56], **Publication A6 in Appendix A**, © 2003, Elsevier Science B.V.

The ion-induced defects on the sapphire single crystal surface can be removed by annealing at 450 degrees C for 5 h. The density of nanodefects does not directly correspond 1:1 with the applied ion dose: an ion dose of $5 \cdot 10^{12}$ ions/cm², which is equivalent to five ions per 10 nm*10 nm, leads to a rather small, however reproducible, density of defects on the sapphire surface: about 10 nanodefects per 1000 nm*1000 nm can be observed after bombardment in the energy range reported here. This is equivalent to a dose to defect ratio of 5000. More detailed experiments with different ion doses are needed. Analysis of the statistics of random impacts will clarify how many individual ion impacts are needed to form a visible nanodefekt on the insulator surface.

A possibly similar migration and subsequent recombination of point defects at the surface has previously been reported for silicon bombarded by 5 keV He ions above 160 K [74].

In fact, the only cases where the number of defects corresponded fairly well to the applied ion dose were the conducting HOPG samples and the CaF₂(111) crystals (see 1.4.1 and 1.4.4).

The Al₂O₃ c-plane surface shows a clear dependence of the ion bombardment induced defects with the kinetic energy and charge states of the projectiles. 500 eV Ar⁺ ions produce defects which are about 1 nm high (**Figure 14**) and have lateral dimensions of some tens of nanometers (one should keep in mind that the height is more accurately measurable with the AFM than lateral dimensions), whereas the defects produced by 500 eV Ar⁷⁺ ions are several nanometers high (**Figure 14**) and show lateral dimensions of about 100 (!) nanometers. At higher kinetic energy the differences in the slow ion-induced nanodefects on the sapphire c-plane became even more distinct.

1.2 keV Ar⁺-induced defects are up to about 8 nm high and their width is some 10 nm. For a higher charge state as Ar⁴⁺, two different kinds of defects occurred on the sapphire surface. They have about the same height, but their lateral dimensions vary considerably: some are nearly 200 nm wide, whereas the smaller defects are only about 50 nm wide. The height of both kinds of defects is about 2 nm. For Ar⁷⁺, only one kind of defect was visible in the AFM images, with about 50 nm diameter and about 2 nm height (for a more detailed description of these results and for similar investigation on SiO₂ surfaces, see ([56][69], **Publications A5 and A6 in Appendix A**).

Therefore it can be concluded that Al₂O₃ is a good candidate for PS-induced nanostructuring. This material is relevant for applications in microelectronics and nanotechnology.

1.4.4 Bombardment of single crystal CaF_2 surfaces via with multicharged ^{129}Xe ions reveal a potential energy threshold for nanodefects generation

We present first results on the generation of surface nanostructures by slow HCI on cleaved $\text{CaF}_2(111)$ surfaces ([33][72], **Publications A7 and A8 in Appendix A**). CaF_2 is a non-amorphisable alkaline earth halide that is used as insulator in silicon microelectronic devices. Due to the small mismatch in lattice constants ($\sim 0.6\%$), CaF_2 can be epitaxially grown as insulator on silicon microelectronic devices [75]-[77].

The CaF_2 single crystals were irradiated at the distributed ITS LEIF infrastructure at MPI Heidelberg (Germany) with slow ($v < 1$ a.u.) multicharged Xe HCI from an electron beam ion trap (EBIT). One atomic unit of velocity (1 a.u.) corresponds to projectile energies below 25 keV per atomic mass unit. Like for other ionic fluoride single crystals, ion-induced surface structures in CaF_2 are known to be stable in atmospheric conditions at room temperature [78]. Therefore, ambient AFM is the method of choice to investigate any nanostructures on the crystal surface.

Ionic fluoride crystals that were irradiated with swift ions only show nanostructures on the surface when the electronic energy loss typically exceeds a threshold of 5 keV/nm [79][80]. Above this threshold both the diameter and height of the hillocks increase with the electronic stopping power [81]. At the surface of ionic crystals, swift ions induce nanometric hillocks [78][79] above a threshold value similar to that for swelling [82].

Experiments with slow HCI ($v < 1$ a.u.) that also induce hillock-like nanostructures on the surface of CaF_2 single crystals are the focus of this chapter.

Our experiments with slow Xe HCI were performed on $\text{CaF}_2(111)$ surfaces freshly cleaved in air. Cleavage is known to result in a fluorine-terminated surface. The CaF_2 crystals were transferred into the vacuum chamber that was evacuated to a base pressure in the 10^{-10} mbar range. Irradiation took place at room temperature with ^{129}Xe ions of various charge states and impact energies. Typical ion fluxes were between 10^3 and several 10^4 ions/s and irradiation times of several hours resulted in total ion fluences between $(0.5-5) * 10^9$ ions/cm².

After irradiation, the crystals were investigated under ambient conditions by an MFP-3D atomic force microscope (Asylum Research, Santa Barbara, USA). This system is equipped with closed-loop nanopositioning system sensors for the correction of piezo hysteresis and creep. Furthermore it allows for simultaneous AFM and optical measurements of transparent

and opaque samples due to top-view optics and an inverted microscope base.

The measurements have been performed in contact mode at constant loading force of less than 10 nN, using non-conductive Si₃N₄ sensors (Veeco Instruments, France) with cantilevers of force constants of about 0.1 N/m.

The initial study was performed with ¹²⁹Xe⁴⁴⁺ ions, a flux of 10⁴ ions/s, a fluence of 2*10⁹ ions/cm² and two distinct ion impact energies of 2.2 and 3.3 keV/amu ([69], **Publication A7 in Appendix A**). Contact-mode AFM in air on unbombarded CaF₂ crystal surfaces revealed large atomically flat surfaces with occasional cleavage steps separating individual terraces. Hillock-like nanostructures were observed on the bombarded surfaces (see Table 1), with the density of the nanodefects directly corresponding 1:1 with the applied ion dose: basically each observed hillock results from an individual ion impact.

	Slow Xe ⁴⁴⁺	Slow Xe ⁴⁴⁺	Swift Xe [82]
Kinetic energy (keV/amu)	2.2	3.3	6400
Mean hillocks diameter (nm)	28.1 ± 0.4	28.3 ± 0.5	23.5 ± 0.4
Mean hillocks height (nm)	0.9 ± 0.1	0.9 ± 0.1	3.8 ± 0.2

Table 1: Ion-beam parameters and measured hillock sizes. From [33], **Publication A7 in Appendix A**.

ion	Ar ¹¹⁺	Ar ¹²⁺	Ar ¹⁴⁺	Ar ¹⁶⁺	Ar ¹⁷⁺	Ar ¹⁸⁺
E _p [eV]	2017.85	2636.11	4077.97	5850.75	9971.67	14397.93

(“melting” potential energy threshold E_p ≈ 14.4 keV for Ar¹⁸⁺)

ion	Xe ²²⁺	Xe ²⁶⁺	Xe ²⁸⁺	Xe ³⁰⁺	Xe ³³⁺	Xe ³⁶⁺
E _p [eV]	5814	8922	11985	15379	21146	27766

(“melting” potential energy threshold E_p ≈ 12 keV for Xe²⁸⁺)

ion	Xe ⁴⁰⁺	Xe ⁴⁴⁺	Xe ⁴⁶⁺	Xe ⁴⁸⁺
E _p [eV]	38494	51111	66661	83187

Table 2: Potential energy of the highly charged ions used to bombard the CaF₂ crystals. The grey and dark grey marked energies are above the threshold, yielding nanohillocks.

No significant difference in hillock size was found for the two different Xe^{44+} impact energies of 2.2 and 3.3 keV/amu (**Figure 15**). This independence on impact energy together with the fact that our experiments were conducted for electronic stopping power values well below the kinetic threshold for hillock production leads us to the conclusion that the potential energy stored in Xe^{44+} ions (i.e. the sum of ionization potentials) of about 51 keV should be responsible for the hillock production.

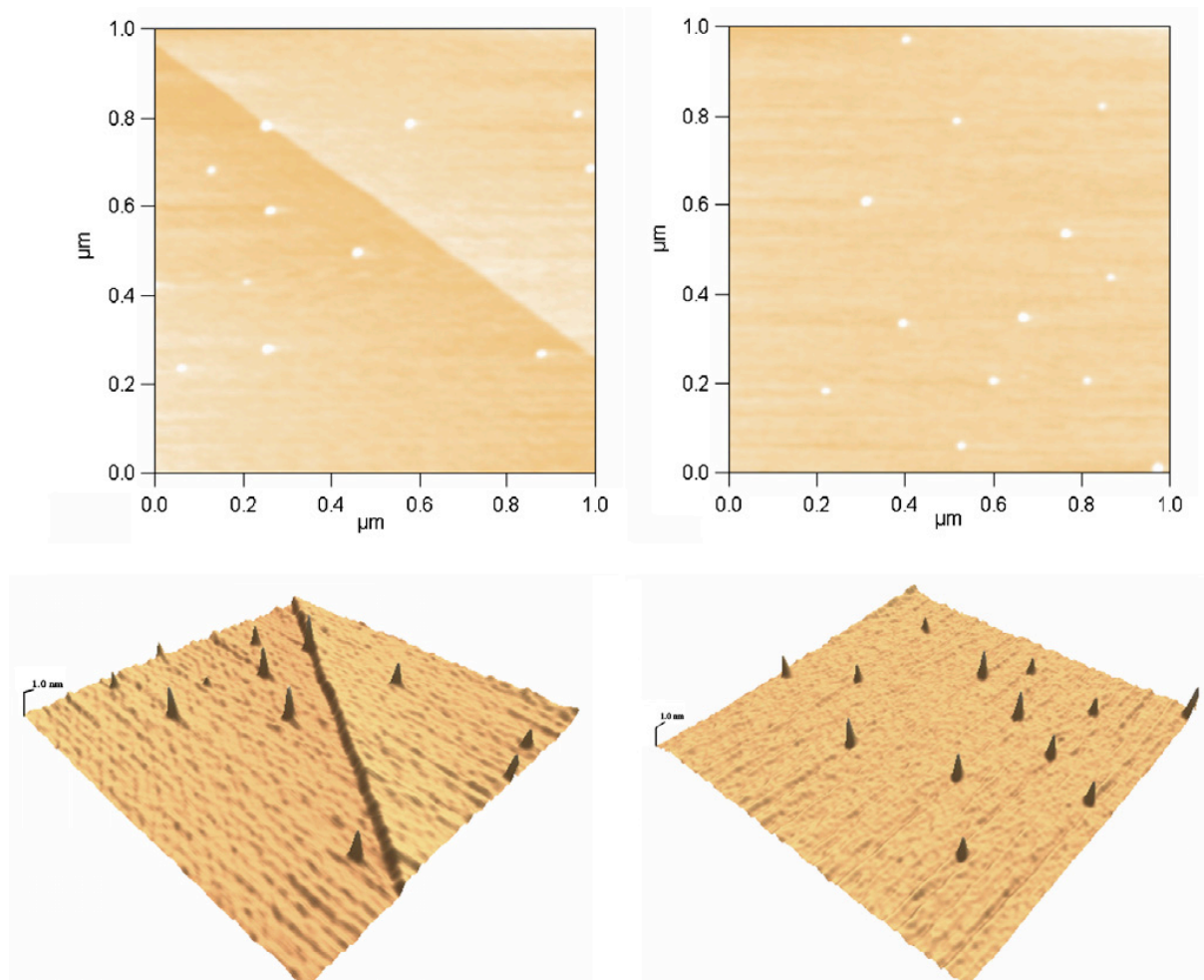


Figure 15: Topographic SFM images for CaF_2 single crystal irradiated with Xe^{44+} ($E_{kin} = 2.2$ keV/amu) (left) and Xe^{44+} ($E_{kin} = 3.3$ keV/amu) (right) ions. From [71], **Publication A7 in Appendix A**, © 2006 Elsevier B.V.

The results from measurements with 6.4 *q keV (2.2 keV/amu) Xe^{44+} differ by less than 5% from the data of 10 *q keV (i.e. 3.3 keV/amu) Xe^{44+} ions. It appears that the kinetic energy of the Xe^{44+} ions plays no decisive role for the size of the observed nanostructures.

Given this promising result, the CaF_2 crystals were bombarded with ions of various charge states (Table 2). Freshly cleaved CaF_2 crystals were irradiated normal to the (111) surface with HCl of kinetic energy below 5 keV per nucleon.

The irradiation was performed at the Heidelberg electron beam ion trap [81] using $^{40}\text{Ar}^{q+}$ ($q = 11, 12, 14, 16, 17$ and 18) as well as $^{129}\text{Xe}^{q+}$ ($q = 22, 26, 28, 30, 33, 36, 40, 44, 46$ and 48) projectiles during several runs. The extraction voltage was 10 kV (for Xe^{44+} also 6.4 kV) equivalent to a kinetic energy of 10 kV (6.4 kV) times charge q resulting in a projected range between 90 nm and 140 nm in CaF_2 , assuming that stopping power and range are unaffected by the high charge state (see below) [63].

The beam flux varied between 10^3 and several 10^4 ions/s and was measured via electron-emission statistics with close to 100% detection efficiency [76][77]. After exposure to fluences up to $(0.5\text{-}5) \times 10^9$ ions/cm², the surface of the crystals was inspected in ambient air by contact-mode AFM. As reported earlier for CaF_2 single crystals irradiated with swift heavy ions, the surface hillocks are stable in atmosphere at room temperature [78].

A strong dependence of the formation on the potential energy rather than on the stopping power is found. Most surprisingly, a well-defined threshold of potential energy is required for the onset of nano-hillock formation: Hillock-like nanostructures protruding from the surface are observed for highly charged Xe^{q+} ($q \geq 30$) and fully stripped Ar^{18+} ions whereas targets irradiated with Xe^{q+} ($q \leq 28$) and Ar^{q+} ($q \leq 17$) projectiles did not exhibit any hillocks.

The number of the hillocks per unit area was found to be in good agreement with the applied ion fluence, i.e. above the threshold, a large majority of projectiles ($> 70\%$) produces an individual hillock each. Their height ranges between 0.5 and 1 nm and their diameter between ~ 20 and 60 nm.

Furthermore, the size data were found to be strongly dependent on the potential energy the projectile carries into the HCI-surface collision (**Figure 16**).

Atomic force microscopy reveals a surprisingly sharp and well-defined threshold of potential energy carried into the collision of about 14 keV for hillock formation ([70]-[72], **Publication A8 in Appendix**). Estimates of the energy density deposited suggest that the threshold is linked to a solid-liquid phase transition (“melting”) on the nanoscale. With increasing potential energy, both the basal diameter and the height of the hillocks increase (**Figure 17**).

For both Xe and Ar ions a remarkably well-defined sharp threshold in potential energy (between $E_p \approx 12$ keV for Xe^{28+} and $E_p \approx 14.4$ keV for Ar^{18+}) for hillock formation emerges. Above this threshold, an increase of the potential energy leads to an increase of both the basal diameter and the height of the hillocks. Another steep increase of the mean hillock diameter potentially indicating a second threshold is found between Xe^{44+} and Xe^{46+} (**Figure 16**).

We are well aware of the possible occurrence of a systematic error of the order of few nanometers for the hillock diameter caused by the finite AFM tip curvature radius. In contrast to the diameter, the height should not be affected by the finite tip radius but mainly by the roughness of the sample.

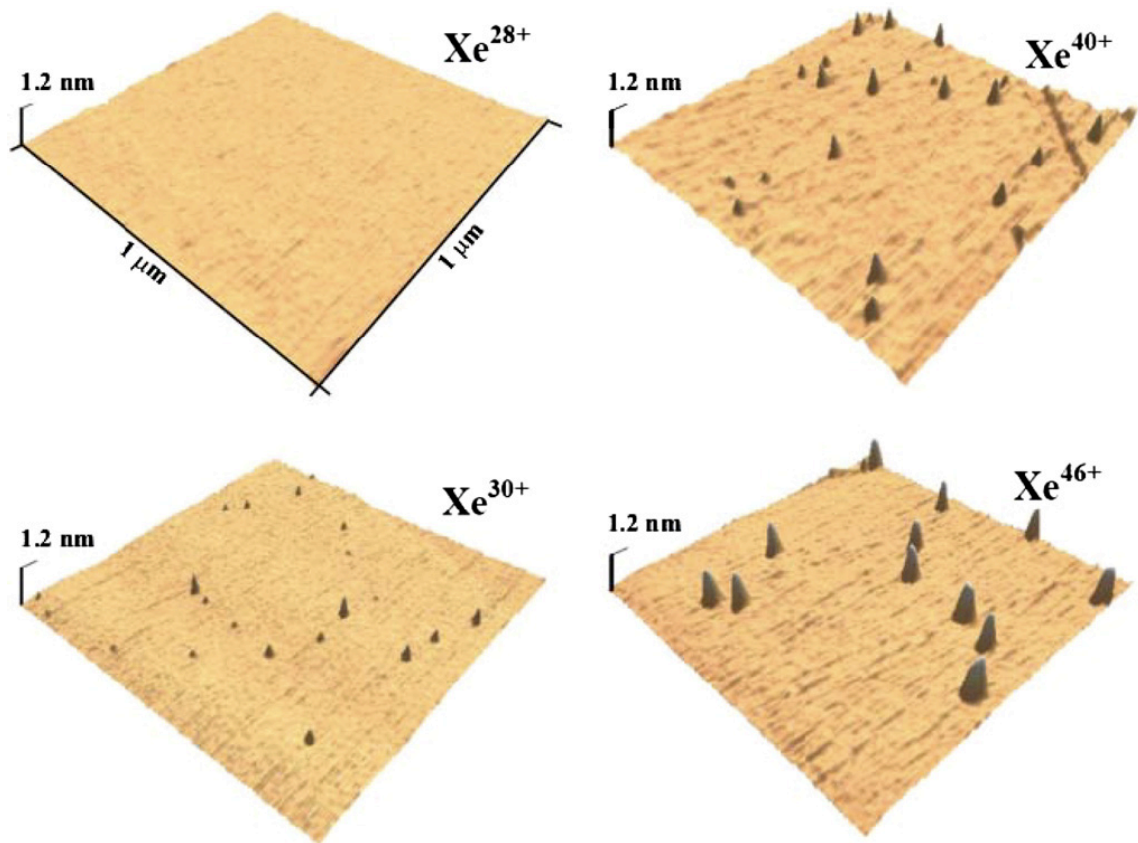


Figure 16: Topographic contact-mode AFM images of a $\text{CaF}_2(111)$ surface irradiated by $10q$ keV Xe^{q+} ions of charge state $q = 28, 30, 40, 46$. In each frame an area of $1 \mu\text{m} * 1 \mu\text{m}$ is displayed. Hill-ock-like nanostructures protruding from the surface are only observed for Xe projectiles with charge state $q \geq 30$. Above this threshold, the height and diameter of the hillocks increase with ion charge state. From [70], **Publication A8 in Appendix A**, © 2007 Elsevier B.V.

For an analysis and interpretation of our data, we adapt aspects of the inelastic thermal spike model developed for swift ions [83].

From calorimetric measurements it is known [84] that only part of the potential energy is transferred to the target. We suppose that this fraction is around 50% with an uncertainty of 20%. If the energy deposition per atom, E_D/N , within this locally heated volume exceeds the melting energy of $E_M = 0.55$ eV/atom [85] a solid–liquid phase transition is expected. Likewise, for $E_D/N > E_S = 1.55$ eV/atom [85], sublimation should set in. In order to have these energies available at the impact site, the HCI needs a potential energy above $E_M^{th} = 14$ keV (energy threshold for melting) and $E_S^{th} = 40$ V (energy threshold for sublimation) [70].

The estimates are remarkably, maybe even fortuitously, close to the observed threshold for hillock formation (E_M^{th}) and for the second drastic, almost step-like size increase E_S^{th} .

An alternative and additional heating mechanism could be the pre-equilibrium charge state dependent electronic and nuclear stopping in insulators strongly deviating from standard values for near-neutral projectiles in equilibrium [86].

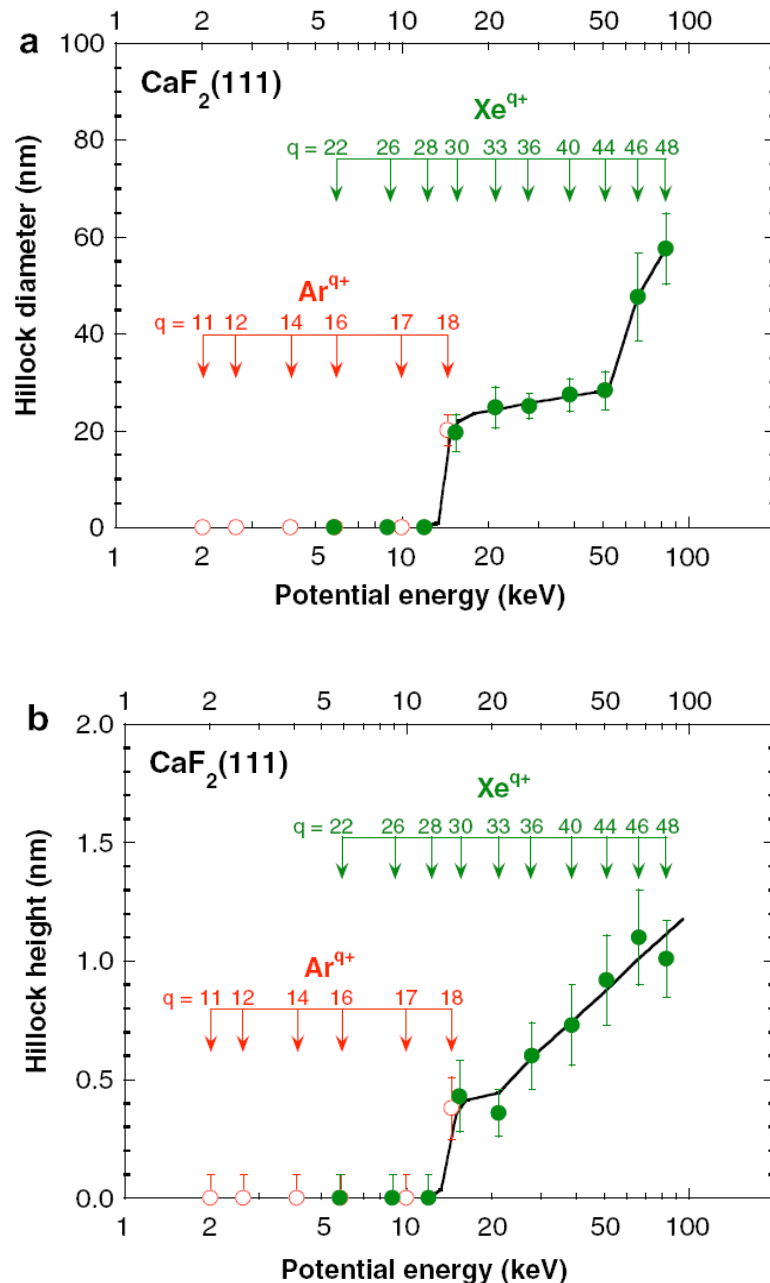


Figure 17: Mean diameter (a) and height (b) of hillock-like nanostructures as a function of the potential energy of Ar^{q+} (open symbol) and Xe^{q+} (full symbol) projectiles. Hillocks are found only above a potential energy threshold of about 14 keV. The error bars correspond to the standard deviation of the diameter and height distributions; the solid lines are drawn to guide the eye. From [70], **Publication A8 in Appendix A**, © 2007 Elsevier B.V.

Hillock formation is the result of local melting and swelling when the energy deposition by HCI near the surface exceeds the melting energy $E_M = 0.55$ eV/atom. If the energy deposition exceeds the critical value for sublimation $E_S = 1.55$ eV/atom, evaporation should lead to the formation of blisters of enhanced size.

In conclusion, the bombardment of a CaF_2 surface with moderately slow ($v_p = 0.3$ a.u., $v_p = 1$ a.u.) highly charged Ar and Xe ions produces hillock-like surface nanostructures. The formation of these protrusions requires a critical potential energy of 14 keV (Ar^{18+} and Xe^{30+}). A second threshold characterized by a steep increase of hillock diameter appears at 50 keV (Xe^{44+}). In analogy to hillock formation by swift heavy ions, we associate the two thresholds with phase transitions of melting and sublimation caused by the deposition of the potential energy within the electronic subsystem.

1.5 Conclusions and outlook

This chapter gave an impression on scanning probe microscopy across dimensions: from large samples such as single cells - via single biomolecules - to nanometer small ion-induced defects on crystal surfaces.

Scanning probe microscopy is becoming a standard laboratory method: subatomic features such as electronic orbitals [87] and single electron spins can be imaged (e.g. [88][89]), and with magnetic resonance force microscopy [90] SPM has even surpassed the two-dimensional surface regime. Perhaps in the not too distant future these powerful techniques will allow 3D imaging of (complex) molecules, at surfaces or in the bulk state, with atomic resolution. The 3-D magnetic resonance force microscope for example would then also deliver chemical element specific information due to the unique gyromagnetic ratio of each magnetic nucleus.

2 Diatom Tribology

In 1999 Gebeshuber and co-workers reported the first AFM images of living diatoms in ambient conditions [91]. AFM imaging and spectroscopic investigations of diatoms are reported above in chapter 1.2 ([7],[11], **Publications A3 and A4 from Appendix A**).

In 2004 Gebeshuber and Drack (a theoretical biologist from Vienna University) proposed the new field “diatom tribology” [92]. Tribology is the branch of engineering that deals with the interaction of surfaces in relative motion (as in bearings or gears): their design, friction, adhesion, lubrication and wear. Joints, hinges and interlocking devices are not very common in nature. Especially rare are biological systems with hinges and interlocking devices on the micro- and nanometer scale. Some diatoms have such parts in relative motion on this scale. This fact makes them interesting as inspiration for man-made devices on the small scale.

“Diatom tribology” was introduced in a number of scientific publications, and also at various international conferences, ranging from physics to tribology, from diatom science to nanotechnology, from nanoengineering to biomineralisation. In [92] and [93] first promising diatom species were introduced. An interlocking device of one of these species, *E. arenaria*, is shown in **Figure 18**.

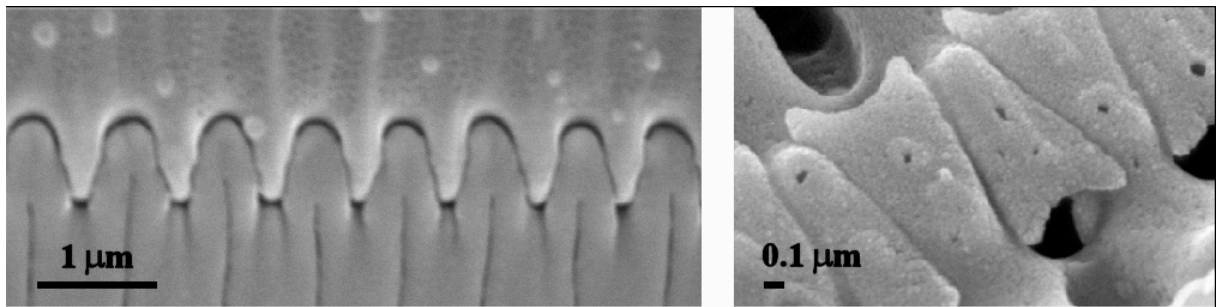


Figure 18: Structural details of rigid silica structures on the micro- and nanometer scale in *E. arenaria* (left) and another diatom species, possibly *Melosira* sp. (right, adapted from [93], **Publication A9 from Appendix A**, © 2005 American Scientific Publishers).

Especially for 3D-MEMS (micro-electro-mechanical devices) the intricate 3-dimensional structures of diatoms can serve as unique templates, both for the structure as well as for surface functionalization (**Figure 19**, [94]).

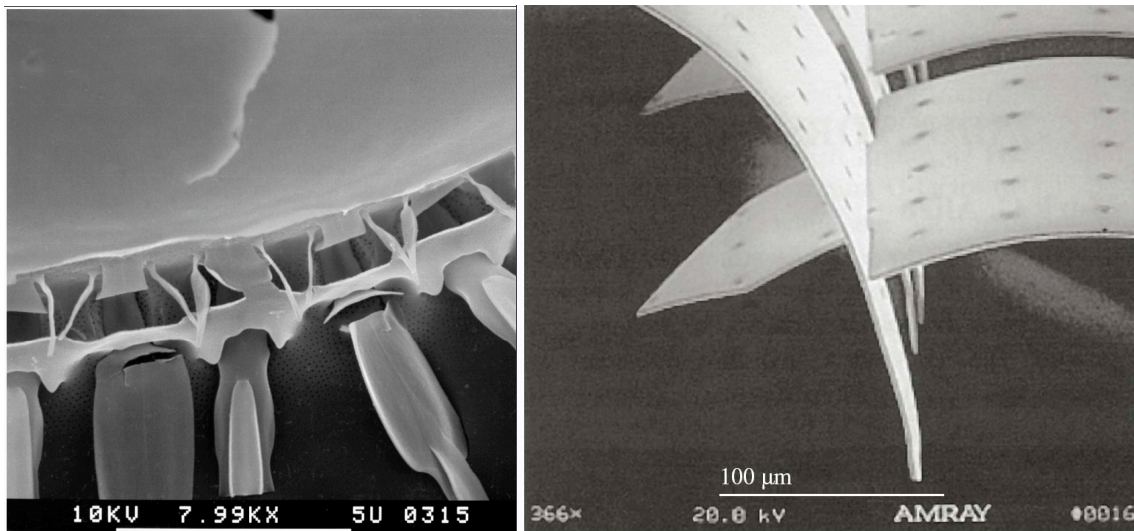


Figure 19: (a) Scanning electron micrograph of a surface detail in the diatom species *Corethron*. When new cells are mature after cell division, they expand and allow their spines to swing out to adopt their final position. In doing this they move past a click-stop that prevents them moving too far back from their required position. Scale bar 5 μm . From [94], © 2006 IEEE. (b) Detail of a self-assembled out of plane coil MEMS that has been fabricated using micromachining technology. The inductor winding traces interlock into each other to form coil windings. Scale bar 100 μm . From [95], © 2002, IEEE.

In 2006 Crawford and Gebeshuber report on micromechanics in hydrated silica ([96], **Publication A10 in appendix A**). Hinges and interlocking devices of several diatom species such as *Aulacoseira*, *Corethron*, and *Ellerbeckia* are presented in high-resolution SEM images and their structure and presumed functions are correlated.

Currently, the industry for micro- and nanoelectromechanical devices (MEMS and NEMS) puts great effort into investigating tribology on the micro- and nanometre scale. It is suggested that micro- and nanotribologists meet with diatomists to discuss future common research attempts regarding biomimetic ideas and approaches for novel and/or improved MEMS and NEMS with optimized tribological properties. This work on hinges and interlocking devices in diatoms was also featured in a popular science journal of the Russian Academy of Sciences ([97], for title page with an SEM image from the article see **Figure 20**).

The long-term goal of these studies is to reach a clear correlation between structure and function in diatoms. The short-term goal aims at collecting interesting diatom species with hinges and interlocking devices. The moving parts in relative motion provide first ideas about aspects of morphology as they relate to function. At this initial stage, the presentation is rather descriptive and efforts are undertaken to arise interest in a variety of fields (biology, electronic engineering, physics, biophysics, computer science, nanotechnology, mechanical engineering) for diatom tribology.

To further correlate structure with function in diatoms, fluid mechanics simulations on water flow along diatom colonies are currently performed. Furthermore, the application of surface analytical methods such as atomic force microscopy and spectroscopy shall yield first knowledge about surface functionalization of diatom hinges and interlocking devices.



Figure 20: Cover of *Science First Hand* from August 2006, featuring an SEM image of an interlocking device in *Aulacoseira* sp. [97], © 2006, Siberian Branch of Russian Academy of Sciences.

References

- [1] Dvorak JA (2003) *Methods* 29:86¹
- [2] Round FE, Crawford RM, Mann DG (1990) *Diatoms: Biology and morphology of the genera*. Cambridge University Press
- [3] Hecky RE, Mopper K, Kilham P, Degens ET (1973) *Marine Biol.* 19:323
- [4] Gordon R, Sterrenburg F, Sandhage K (guest eds) (2005) *Diatom Nanotechnology*, special issue *J. Nanosci. Nanotechnol.* 5:1
- [5] Werner D (1977) *The biology of diatoms*, University of California Press
- [6] Gordon R, Drum RW (1994) *Int. Rev. Cytol.* 150:243
- [7] Gebeshuber IC, Thompson JB, Del Amo Y, Stachelberger H, Kindt JH (2002) *Mat. Sci. Technol.* 18:763 [**Publication A4 in Appendix A**]
- [8] Linder A, Colchero J, Apell H-J, Marti O, Mlynek J (1992) *Ultramicrosc.* 42-44:329
- [9] Almqvist N, Delamo Y, Smith BL, Thomson NH, Bartholdson A, Lal R, Brzezinski M, Hansma PK (2001) *J Microsc.* 202:518
- [10] Higgins MJ, Crawford SA, Mulvaney P, Wetherbee R (2002) *Protist* 153:25
- [11] Gebeshuber IC, Kindt JH, Thompson JB, Del Amo Y, Stachelberger H, Brzezinski M, Stucky GD, Morse DE, Hansma PK (2003) *J. Microsc.* 212:292 [**Publication A3 in Appendix A**]
- [12] Higgins MJ, Sader JE, Mulvaney P, Wetherbee R (2003) *J. Phycol.* 39:722
- [13] Higgins MJ, Molino P, Mulvaney P, Wetherbee R (2003) *J. Phycol.* 39:1181
- [14] Lee Y, Ding Z, Bard AJ (2002) *Anal. Chem.* 74:3634
- [15] Hamm CE, Merkel R, Springer O, Jurkojc P, Maier C, Prechtel K, Smetacek V (2003) *Nature* 421:841
- [16] Arce FT, Avci R, Beech IB, Cooksey KE, Wigglesworth-Cooksey B. (2004) *Biophys J.* 87:4284
- [17] Solomon B, Taraboulos A, Katchalski-Katzir E (2002) *Conformational Diseases: A Compendium Based on the 1st International Workshop on Conformational Diseases*, S Karger Pub., Tunbridge Wells, UK.
- [18] Dobson CM (2002) *Nature* 418:729
- [19] Dobson CM (2003) *Nature* 426:884
- [20] Greulic KO (2004) *Curr. Pharmac. Biotech.* 5:243
- [21] Viani MB, Pietrasanta LI, Thompson JB, Chand A, Gebeshuber IC, Kindt JH, Richter M, Hansma HG, Hansma PK (2000) *Nature Struct. Biol.* 7:644 [**Publication A2 in Appendix A**]
- [22] Walters DA, Cleveland JP, Thomson NH, Hansma PK, Wendman MA, Gurley G, Ellings V (1996) *Rev. Sci. Instrum.* 67:3583

¹ Citation style according to the Springer Series NanoScience and Technology.

- [23] Viani MB, Schäffer TE, Chand A, Rief M, Gaub HE, Hansma PK (1999) *J. Appl. Phys.* 86:2258
- [24] Viani MB, Schäffer TE, Palocz GT, Pietrasanta LI, Smith BL, Thompson JB, Richter M, Rief M, Gaub HE, Plaxco KW, Cleland AN, Hansma HG, Hansma PK (1999) *Rev. Sci. Instrum.* 70:4300
- [25] Braig K, Otwinowski Z, Hegde R, Boisvert DC, Joachimiak A, Horwich AL, Sigler PB (1994) *Nature* 371:578
- [26] Hunt JF, Weaver AJ, Landry SJ, Gierasch L, Eisenhofer J (1996) *Nature* 379:37
- [27] Boisvert DC, Wang J, Otiwonowski Z, Horwich AL, Sigler PB (1996) *Nature Struct. Biol.* 3:170
- [28] Xu Z, Horwich AL, Sigler PB (1997) *Nature* 388:741
- [29] Chen S, Roseman AM, Hunter AS, Wood SP, Burston SG, Ranson NA, Clarke AR, Saibil HR (1994) *Nature* 371:261
- [30] Roseman AM., Chen S, White H, Braig K, Saibil HR (1996) *Cell* 87:241
- [31] Ziaie B, Baldi A, Atashbar MZ (2004) Introduction to Micro/Nanofabrication. In: Bhushan B (ed) *Springer Handbook of Nanotechnology*. Springer, Berlin, Heidelberg, New York, p 147
- [32] Rogers JA (2004) Stamping techniques for micro and nanofabrication: methods and applications. In: Bhushan B (ed) *Springer Handbook of Nanotechnology*. Springer, Berlin, Heidelberg, New York, p 185
- [33] El-Said AS, Meissl W, Simon MC, Crespo López-Urrutia JR, Gebeshuber IC, Lang M, Winter HP, Ullrich J, Aumayr F (2007) *Nucl. Instr. Meth. Phys. Res. B* 256:346, doi:10.1016/j.nimb.2006.12.140 [**Publication A7 in Appendix A**]
- [34] Arnau A, Aumayr F, Echenique PM, Grether M, Heiland W, Limburg J, Morgenstern R, Roncin P, Schippers S, Schuch R, Stolterfoht N, Varga P, Zouros TJM, Winter HP (1997) *Surf. Sci. Rep.* 27:113
- [35] Winter HP, Aumayr F (2002) *Europhys. News* 6:215
- [36] Arnau A, Aumayr F, Echenique PM, Grether M, Heiland W, Limburg J, Morgenstern R, Roncin P, Schippers S, Schuch R, Stolterfoht N, Varga P, Zouros TJM, Winter HP (1997) *Surf. Sci. Rep.* 27:113
- [37] Sporn M, Libiseller G, Neidhart T, Schmid M, Aumayr F, Winter HP, Varga P, Grether M, Niemann D, Stolterfoht N (1997) *Phys. Rev. Lett.* 79:945
- [38] Aumayr F, Burgdörfer J, Varga P, Winter HP (1999) *Comm. Atom. Molecul. Phys.* 34:201
- [39] Schenkel T, Hamza AV, Barnes AV, DH Schneider (1999) *Progr. Surf. Sci.* 61:23.
- [40] Hayderer G, Cernusca S, Schmid M, Varga P, Winter HP, Aumayr F, Niemann D, Hoffmann V, Stolterfoht N, Lemell C, Wirtz L, Burgdörfer J (2001) *Phys. Rev. Lett.* 86:3530
- [41] Hayderer G, Schmid M, Varga P, Winter HP, Aumayr F, Wirtz L, Lemell C, Burgdörfer J, Hägg L, Reinhold CO (1999) *Phys. Rev. Lett.* 83:3948
- [42] Porte L, de Villeneuve CH, Phaner M (1991) *J. Vac. Sci. Technol. B* 9:1064.
- [43] Coregater R, Claverie A, Chahboun A, Landry V, Ajustron F, Beauvillain J (1992) *Surf. Sci.* 262:208.

- [44] You HX, Brown NMD, Al-Assadi KF (1992) *Surf. Sci.* 279:189.
- [45] Mazukawa T, Suzuki S, Fukai T, Tanaka T, Ohdomari I (1996) *Appl. Surf. Sci.* 107:227
- [46] Mochiji K, Yamamoto S, Shimizu H, Ohtani S, Seguchi T, Kobayashi N (1997) *J. Appl. Phys.* 82:6037
- [47] Reimann KP, Bolse W, Geyer U, Lieb KP (1995) *Europhys. Lett.* 30:463
- [48] Habenicht S, Bolse W, Feldermann H, Geyer U, Hofsäss H, Lieb KP, Roccaforte F (2000) *Europhys. Lett.* 50:209
- [49] Neumann R (1999) *Nucl. Instrum. Meth. Phys. Res. B* 151:42
- [50] Hahn R, Kang K, Song S, Jeon IC (1996) *Phys. Rev. B* 53:1725.
- [51] Hahn R, Kang K (1999) *Phys. Rev. B* 60:600.
- [52] Minniti R, Ratliff LP, Gillaspay JD (2001) *Phys. Scr.* T92:22
- [53] Hayderer G, Cernusca S, Schmid M, Varga P, Winter HP, Aumayr F (2001) *Phys. Scr.* T92:156
- [54] Terada M, Nakamura N, Nakai Y, Kanai Y, Ohtani S, Komaki K, Yamazaki Y (2004) Observation of an HCl-induced nano-dot on an HOPG surface with STM and AFM. In: Rudzikas Z (ed) *Abstracts HCI-2004 12th International conference on the physics of highly charged ions.* European Physical Society, p 208
- [55] Nakamura N, Terada M, Nakai Y, Kanai Y, Ohtani S, Komaki K, Yamazaki Y (2005) *Nucl. Instrum. Meth. Phys. Res. B* 232:261
- [56] Gebeshuber IC, Cernusca S, Aumayr F, Winter HP (2003) *Int. J. Mass Spectrom.* 229:27 [**Publication A6 in Appendix A**]
- [57] Meguro T, Hida A, Koguchi Y, Miyamoto S, Yamamoto Y, Takai H, Maeda K, Aoyagi Y (2003) *Nucl. Instrum. Meth. Phys. Res. B* 209:170
- [58] Hida A, Meguro T, Maeda K, Aoyagi Y (2003) *Nucl. Instrum. Meth. Phys. Res. B* 205:736
- [59] Hahn R, Kang K, Song S, Jeon IC (1996) *Phys. Rev. B* 53:1725.
- [60] Hahn R, Kang K (1999) *Phys. Rev. B* 60:6007.
- [61] Krasheninnikov AV, Elsin F (2000) *Surf. Sci.* 519:454.
- [62] Winter HP, Aumayr F (1999) *J. Phys. B: At. Mol. Opt. Phys.* 32: R39
- [63] Ziegler JF, Biersack JP, Littmark U (1985) *The Stopping and Range of Ions in Matter 1*, Pergamon, New York.
- [64] Bitensky IS, Murakhmetov MN, Parilis ES (1979) *Sov. Phys. Tech. Phys.* 25:618
- [65] Schneider DH, Briere MA, McDonald J, Biersack J (1993) *Radiat. Eff. Def. Sol.* 127:113
- [66] Hayderer G, Schmid M, Varga P, Winter HP, Aumayr F (1999) *Rev. Sci. Instrum.* 70:3696
- [67] Townsend P (1983) Chapter 4. In: Behrisch R (ed) *Sputtering by particle bombardment II.* Springer, Berlin, p 147
- [68] Varga P, Neidhard T, Sporn M, Libiseller G, Schmid M, Aumayr F, Winter HP (1997) *Phys. Scr.* T73:307

- [69] Gebeshuber IC, Cernusca S, Aumayr F, Winter HP (2003) Nucl. Instr. Meth. Phys. Res. B 205:751 [**Publication A5 in Appendix A**]
- [70] El-Said AS, Meissl W, Simon MC, Crespo López-Urrutia JR, Lemell C, Burgdörfer J, Gebeshuber IC, Winter HP, Ullrich J, Trautmann C, Toulemonde M, Aumayr F (2007) Nucl. Instr. Meth. Phys. Res. B 258:167, doi:10.1016/j.nimb.2006.12.142 [**Publication A8 in Appendix A**]
- [71] El-Said AS, Meissl W, Simon MC, Crespo López-Urrutia JR, Gebeshuber IC, Laimer J, Winter HP, Ullrich J, Aumayr F (2007) Rad. Eff. Def. Sol. 162:467, doi: 10.1080/10420150701470803
- [72] Lemell C, El-Said AS, Meissl W, Gebeshuber IC, Trautmann C, Toulemonde M, Burgdörfer J, Aumayr F (2007) Sol.-St. Elect. 51:1398, doi:10.1016/j.sse.2007.06.016
- [73] Leitner M, Wutte D, Brandstätter J, Aumayr F, Winter HP (1994) Rev. Sci. Instrum. 65:1091
- [74] Bedrossian PJ, de la Rubia TD (1998) J. Vac. Sci. Technol. A 16:1043
- [75] Smith TP, Phillips JM, Augustyniak WM, Stils PJ. (1984) Appl. Phys. Lett. 45:907
- [76] Schowalter LJ, Fathauer RW. (1986) J. Vac. Sci. Technol. 4:1026
- [77] Lucas CA, Loretto D. (1992) Appl. Phys. Lett. 60:2071
- [78] Khalfaoui N, Rotaru CC, Bouffard S, Toulemonde M, Stoquert JP, Haas F, Trautmann C, Jensen J., Dunlop A (2005) Nucl. Instr. Meth. Phys. Res. B 240:819.
- [79] El-Said AS, Cranney M, Ishikawa N, Iwase A, Neumann R, Schwartz K, Toulemonde M, Trautmann C. (2004) Nucl. Instr. Meth. Phys. Res. B 218:492
- [80] Müller C, Cranney M, El-Said AS, Ishikawa N, Iwase A, Lang M, Neumann R (2002) Nucl. Instr. Meth. Phys. Res. B 191:246
- [81] Crespo López-Urrutia JR, Bapat B, Feuerstein B, Fischer D, Lörch H, Moshhammer R, Ullrich J (2003) Hyperfine Interact. 146/147:109
- [82] Müller C, Cranney M, El-Said AS, Ishikawa N, Iwase A, Lang M, Neumann R (2002) Nucl. Instr. Meth. Phys. Res. B 191:246
- [83] Toulemonde M, Dufour Ch, Meftah A, Paumier E (2000) Nucl. Instr. Meth. Phys. Res. B 166/167:903
- [84] Kentsch U, Tyrroff H, Zschornack G, Möller W (2001) Phys. Rev. Lett. 87:105504
- [85] Grochtmann G, Meyer RJ, Peters F, Gmelin L (1970) Gmelins Handbuch der anorganischen Chemie, Verlag Chemie, Berlin
- [86] Schenkel T et al. (1997) Phys. Rev. Lett. 79:2030
- [87] Hembacher S, Giessibl FJ, Mannhart J, Quate CF (2003) Proc Nat Acad Sci 100:12539
- [88] Manassen Y, Hamers RJ, Demuth JE, Castellano AJ jun (1989) Phys Rev Lett 62:2531
- [89] Rugar D, Budakian R, Mamin HJ, Chui BW (2004) Nature 430:329
- [90] Mozyrsky D, Martina I, Pelekhov D, PC Hammel (2003) Appl Phys Lett 82:1278
- [91] Gebeshuber IC, Kindt JH, Thompson JB, DeLamo Y, Brzezinski M, Stucky GD, Morse DE, Hansma PK (1999) Abstracts 15th North American Diatom Symposium, Spaulding S and Kingston J (eds), Pingree Park Campus, Colorado State University, September 1999, 8

- [92] Gebeshuber IC, Stachelberger H, Drack M (2004) In: Boblan I and Bannasch R (eds), First International Industrial Conference Bionik 2004, Fortschr.-Ber. VDI Reihe 15 Nr. 249, Düsseldorf: VDI Verlag. ISBN 3-18-324915-4, ISSN 0178-9589229-236, 229
- [93] Gebeshuber IC, Stachelberger H, Drack M (2005) J. Nanosci. Nanotechnol. 5:79
- [94] Gebeshuber IC, Pauschitz A, Franek F (2006) Proc. 2006 IEEE Conference on “Emerging Technologies - Nanoelectronics”, ISBN 0-7803-9357-0, 396
- [95] Chua CL, Fork DK, Schuylenbergh KV, Lu JP (2002) Hilton Head Solid-State Sens. Actuator Workshop, Tech. Digest 2002 IEEE “Electron Devices Meeting”, 372
- [96] Gebeshuber IC, Crawford RM (2006) J. Eng. Tribol. 220:787 [**Publication A10 in Appendix A**]
- [97] Crawford RM, Gebeshuber IC (2006) Science First Hand 5:30

List of Figures

- Figure 1:** The major types of microscopy cover at least eight orders of magnitude in sample size. Common examples for every scale are given. Note that scanning probe microscopy covers seven orders of magnitude in length.....6
- Figure 2:** Siliceous exoskeletons of three diatom species imaged with scanning electron microscopy. **Top:** *Tricaeratium favus*, whole cell (**left**), detail (**right**). **Bottom:** *Roperia tessellata* (**left**) and *Achnathes brevipes* (**right**). From [7], **Publication A4 in Appendix A**, © 2002 IoM Communications Ltd.....8
- Figure 3:** AFM image of parts of two living diatom cells of the species *Navicula seminulum* growing on a glass slide. Note that the flat area does not correspond to the surface of the glass slide, but is determined by the maximum possible extension of the z-piezo of the microscope. Image acquired using AFM contact-mode imaging in water, imaging parameter topography, scan size $8 \times 8 \mu\text{m}^2$, scanning frequency 1 Hz. From [11], **Publication A3 in Appendix A**, © 2003, The Royal Microscopical Society..... 10
- Figure 4:** **(a)** The adhesives in the contact region of two cells of *Eunotia sudetica* are apparent as small topographic features on the slightly undulated cell interface. The corrugation of the bead-like structures is between 10 and 20 nm, and their lateral dimension and spacing is about $1 \mu\text{m}$. **(b)** In the phase image these features are far more striking. The diatom adhesive causes a phase lag of about 10 degrees compared with the rest of the frustule surfaces, where on a single frustule it is within 1 degree. Note the 2-degree interfrustule phase step, which reveals slightly different viscoelastic properties of the two neighbouring valves. Tapping mode, topography and phase, scan size $10 \times 10 \mu\text{m}^2$, scan rate 5 Hz. Note that for better view (b) is rotated clockwise by 90 degrees as compared with (a). From [11], **Publication A3 in Appendix A**, © 2003, The Royal Microscopical Society. 12
- Figure 5:** Force-distance curves. **Left:** No adhesion can be recognized on the diatom surface. **Right:** Representative data for the diatom adhesive that attaches *Eunotia sudetica* to the substrate. Several debonding events occur. From [11], **Publication A3 in Appendix A**, © 2003, The Royal Microscopical Society. ... 13
- Figure 6:** Cryoelectron microscopy images of GroEL (**left**) and the GroEL-GroES complex (**right**). The height of the GroEL molecule is about 15.1 nm; the height of the GroEL-ES complex is about 18.4 nm. Upon interaction with ADP or ATP, domain movements occur, as indicated. From [30] © 1996, Elsevier..... 16
- Figure 7:** GroEL film deposited on mica scanned in two dimensions (**left**) and in one dimension (**right**). In this image of GroEL, the movement along the slow scan axis was disabled half way through the scan. From then on the AFM tip repeatedly scanned the same line of proteins. Each horizontal line therefore shows changes in time of an individual molecule. From [21], **Publication A2 in Appendix A**, © 2000, Nature Publishing Group. 16

- Figure 8:** Tapping mode AFM in liquid. **Top:** After the addition of GroES and Mg-ATP into the buffer solution, variations in height along the lengths occur in the single protein lines, as exemplified by arrows I and II. **Bottom:** Time/height diagram of the protein lines indicated with the arrows in the top image. The height difference between two values is 3.6 ± 1 nm. This indicates the binding and unbinding of GroES. From [21], **Publication A2 in Appendix A**, © 2000, Nature Publishing Group.....17
- Figure 9:** Histogram of measured GroEL-GroES complex lifetime in the presence of Mg-ATP. Individual GroES molecules attach to and then separate from the same GroEL molecule 18 times during an observation period of about 120 seconds. Note the absence of events with lifetimes < 2 seconds. This is interesting by itself, telling us about the GroEL-GroES complex lifetime on the single molecule level, and furthermore indicates gentle measuring, since strong disturbance of complex formation by the cantilever would also lead to subsecond complex lifetimes. From [21], **Publication A2 in Appendix A**, © 2000, Nature Publishing Group.....18
- Figure 10:** Energy deposition during interactions with a solid surface of slow highly charged ions or neutral atoms (1), swift ions or neutral atoms (2) and slow highly charged ions (3). Slow highly charged ions are a tool for gently nanostructuring the surface with minimal damage to the bulk material. From [33], **Publication A7 in Appendix A**, © 2006 Elsevier B.V.....19
- Figure 11:** Highly oriented pyrolytic graphite imaged in ultrahigh vacuum with atomic resolution. **Left:** Scanning tunnelling microscopy image, image size $4 * 4$ nm². **Right:** Atomic force microscopy image; image size $1 * 1$ nm².....21
- Figure 12:** Highly oriented pyrolytic graphite bombarded with 800 eV Ar⁺ ions imaged with STM in ultrahigh vacuum. Image size $100 * 100$ nm². The ion-induced nanodefects are clearly visible.....22
- Figure 13:** Highly oriented pyrolytic graphite bombarded with 800 eV Ar⁺ ions imaged with STM in ultrahigh vacuum with atomic resolution (**right**). Image size $10 * 10$ nm². The fast Fourier transform (**left**) of the Ar⁺ ion-induced defect reveals a $\sqrt{3} * \sqrt{3}R30^\circ$ surface: the ion-induced features are larger than the features from the HOPG lattice and they are rotated with respect to them by 30 degrees.23
- Figure 14:** UHV AFM contact mode image of sapphire (Al₂O₃, c-plane 0001) bombarded with 500 eV Ar⁺ (**left**) and Ar⁷⁺ (**right**) ions. The nanodefects induced by Ar⁷⁺ ions (which have the same kinetic but higher potential energy than the Ar⁺ ions) are considerably higher and wider than those caused by singly charged ions. The defects are real topographic features; the units on the three axes are nanometers. From [56], **Publication A6 in Appendix A**, © 2003, Elsevier Science B.V.....27
- Figure 15:** Topographic SFM images for CaF₂ single crystal irradiated with Xe⁴⁴⁺ ($E_{kin} = 2.2$ keV/amu) (**left**) and Xe⁴⁴⁺ ($E_{kin} = 3.3$ keV/amu) (**right**) ions. From [71], **Publication A7 in Appendix A**, © 2006 Elsevier B.V.31
- Figure 16:** Topographic contact-mode AFM images of a CaF₂(111) surface irradiated by 10q keV Xe^{q+} ions of charge state $q = 28, 30, 40, 46$. In each frame an area of $1 \mu\text{m} * 1 \mu\text{m}$ is displayed. Hillock-like nanostructures protruding from the surface are only observed for Xe projectiles with charge state $q \geq 30$. Above this threshold, the height and diameter of the hillocks increase with ion charge state. From [70], **Publication A8 in Appendix A**, © 2007 Elsevier B.V.....33

€

€

- Figure 17:** Mean diameter **(a)** and height **(b)** of hillock-like nanostructures as a function of the potential energy of $\text{Ar}^{\text{q}+}$ (open symbol) and $\text{Xe}^{\text{q}+}$ (full symbol) projectiles. Hillocks are found only above a potential energy threshold of about 14 keV. The error bars correspond to the standard deviation of the diameter and height distributions; the solid lines are drawn to guide the eye. From [70], **Publication A8 in Appendix A**, © 2007 Elsevier B.V.34
- Figure 18:** Structural details of rigid silica structures on the micro- and nanometer scale in *E. arenaria* **(left)** and another diatom species, possibly *Melosira* sp. **(right)**, adapted from [93], **Publication A9 from Appendix A**, © 2005 American Scientific Publishers.36
- Figure 19:** **(a)** Scanning electron micrograph of a surface detail in the diatom species *Corethron*. When new cells are mature after cell division, they expand and allow their spines to swing out to adopt their final position. In doing this they move past a click-stop that prevents them moving too far back from their required position. Scale bar 5 μm . From [94], © 2006 IEEE. **(b)** Detail of a self-assembled out of plane coil MEMS that has been fabricated using micromachining technology. The inductor winding traces interlock into each other to form coil windings. Scale bar 100 μm . From [95], © 2002, IEEE.37
- Figure 20:** Cover of Science First Hand from August 2006, featuring an SEM image of an interlocking device in *Aulacoseira* sp. [97], © 2006, Siberian Branch of Russian Academy of Sciences.38

Appendix A: Publications selected for review

A.1 Scanning Probe Microscopy: From living cells to the subatomic range

Gebeshuber I.C., Drack M., Aumayr F., Winter HP. and Franek F.

Applied Scanning Probe Methods III: Characterization, Springer Verlag, 27-53. (2006)

Abstract

In this chapter the reader will be introduced to scanning probe microscopy of samples varying by seven orders of magnitude in size. The largest samples presented are living cells, measuring some hundreds of micrometers. Small units of life, biomolecules with only some tens of nanometers, are the next sample. They are investigated while interacting with each other in real-time. One more step down in size, small ion-induced defects on atomically flat crystals represent structures in the nanometer regime. New data storage devices might result from such investigations. Finally, single electron spin detection (dozens of atomic layers beneath the surface) and the imaging of atom orbitals extend scanning probe microscopy to the subatomic regime. Gathering of 3D atomic-level information of (bio)molecules embedded in their natural environment or single defect imaging in bulk silicon might be possible with these new techniques in the near future. These versatile applications demand methods such as scanning tunneling microscopy at ultra-low temperatures (1.6 K) or atomic force microscopy in ultra-high vacuum (10^{-11} mbar). Furthermore, in many cases, specially engineered and/or functionalized scanning probe tips are needed.

13 Scanning Probe Microscopy: From Living Cells to the Subatomic Range

*Ille C. Gebeshuber · Manfred Drack · Friedrich Aumayr ·
Hannspeter Winter · Friedrich Franek*

Abbreviations

AFM	atomic force microscopy
ATP	adenosine triphosphate
BDPA	a, g-bisdiphenylene b-phenylallyl
CDOS	charge density-of-states
ESD	electron stimulated desorption
HOPG	highly oriented pyrolytic graphite
ID	interstitial defect
MCI	multiply charged ion
MEMS	microelectromechanical system
MR	magnetic resonance
MRFM	magnetic resonance force microscopy
MRI	magnetic resonance imaging
NEMS	nanoelectromechanical systems
PS	potential sputtering
PSD	photon stimulated desorption
rms	root mean square
SEM	scanning electron microscopy
SPM	scanning probe microscopy
UHV	ultra-high vacuum
VD	vacancy defect

13.1 Introduction

In this chapter the reader will be introduced to scanning probe microscopy of samples varying by seven orders of magnitude in size (Fig. 13.1). The largest samples presented are living cells, measuring some hundreds of micrometers. Small units of life, biomolecules with only some tens of nanometers, are the next sample. They are investigated while interacting with each other in real-time. One more step down in size, small ion-induced defects on atomically flat crystals represent structures in the nanometer regime. New data storage devices might result from such investigations. Finally, single electron spin detection (dozens of atomic layers beneath the surface) and the imaging of atom orbitals extend scanning probe microscopy to the subatomic regime. Gathering of 3D atomic-level information of (bio)molecules embedded in

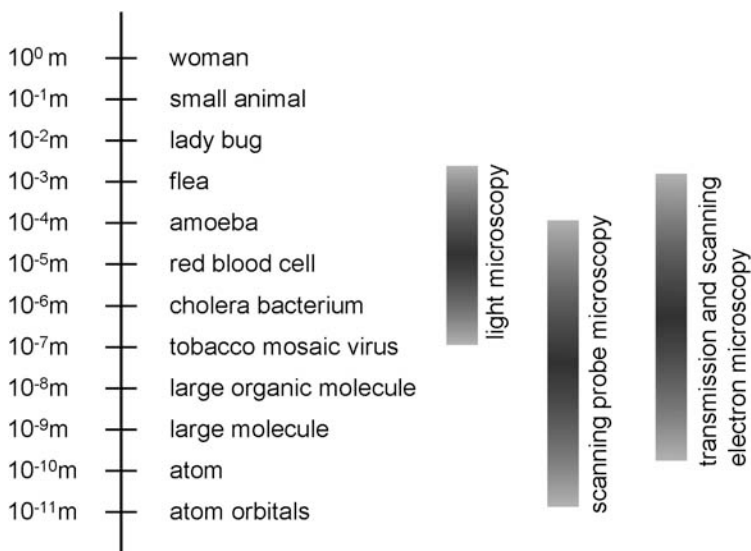


Fig. 13.1. The major types of microscopy cover at least eight orders of magnitude in size. Common examples for every scale are given. Note that scanning probe microscopy covers seven orders of magnitude

their natural environment or single defect imaging in bulk silicon might be possible with these new techniques in the near future.

These versatile applications demand methods such as scanning tunneling microscopy at ultra-low temperatures (1.6 K) or atomic force microscopy in ultra-high vacuum (10^{-11} mbar). Furthermore, in many cases, specially engineered and/or functionalized scanning probe tips are needed.

13.2 Cells *In Vivo* as Exemplified by Diatoms

13.2.1 Introduction to Diatoms

Diatoms [1] are unicellular microalgae with a cell wall consisting of a siliceous skeleton enveloped by an organic case essentially composed of polysaccharides and proteins [2].

Diatoms are small, mostly easy to cultivate, highly reproductive and, since many of them are transparent, they are accessible by different kinds of optical microscopy methods.

The cell walls form a pillbox-like shell (siliceous exoskeleton). This shell consists of two valves and a series of girdle bands. Diatoms vary greatly in shape, ranging from box-shaped to cylindrical; they can be symmetrical as well as asymmetrical and exhibit an amazing diversity of nanostructured frameworks (Fig. 13.2).

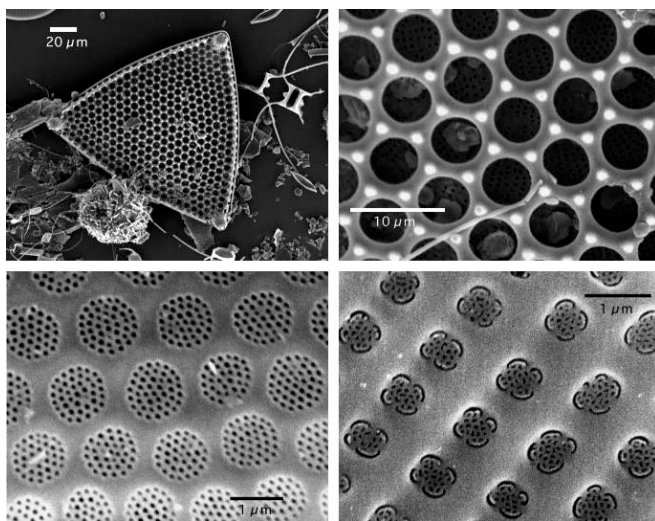


Fig. 13.2. Siliceous exoskeletons of three diatom species imaged with scanning electron microscopy. *Top: Tricaeratium favus*, whole cell (*left*), detail (*right*). *Bottom: Roperia tessellata* (*left*) and *Achnathes brevipes* (*right*). Reprinted with permission from Gebeshuber IC, Thompson JB, Del Amo Y, Stachelberger H, Kindt JH (2002) *Mat Sci Technol* 18:763 [4] © 2002 IoM Communications Ltd.

These naturally nanostructured surfaces gained the attention of nanoscientists, and diatom nanotechnology developed as a new interdisciplinary field of research [3].

Diatoms are found in freshwater, brackish and marine environments, as well as in moist soils, and on other regularly moist surfaces. They are either freely floating (planktonic forms) or attached to a substratum (benthic forms), and some species may form colonies in the form of chains of cells of varying length. Individual diatoms range from two micrometers up to several millimeters in size, although only few species are larger than 200 micrometers. Diatoms as a group are very diverse with 12,000 to 60,000 species reported [5, 6].

These unicellular organisms are interesting from the point of view of materials science and biomimetic studies, since they master challenges as diverse as building nanostructured glass-like shells with high load capacity (a problem interesting for lightweight structures architecture) and engineering strong and robust adhesives that are stable in wet environments (most man-made adhesives fail to bond in wet conditions, owing to chemical modification of the adhesive or its substrate). Furthermore, diatoms excel at preventing dissolution of their silica shells in water owing to a covering layer (up-to-date technology is currently facing the problem that man made glass fiber reinforced polymers show rapid deterioration when used in water).

Currently, human chemical synthesis cannot produce siliceous structures with the hierarchical structural detail of the diatom frustules nor can ordered siliceous structures be produced synthetically under the benign conditions of diatom biomine-

ralization. Biosilicification occurs at ambient temperatures and pressures, whereas artificial chemical synthesis of silica-based materials (e.g. resins, molecular sieves and catalysts) requires extreme conditions of temperature, pressure and pH.

13.2.2

SPM of Diatoms

The first AFM study of diatoms was presented in 1992 [7]. In this study, the surface structure of six different diatom species collected from a mud sample was imaged after the cells had been briefly rinsed with ethanol to kill, clean and immobilize them.

Topography and micromechanical properties like elasticity and hardness of dead diatom cells were reported by Almquist et al. in 2001 [8].

In contrast to these AFM images of dead cells, topography and micromechanical properties (such as viscoelastic properties, adhesion forces and hardness) of the surface of the living diatom cell has been investigated [e.g. 5, 10–13].

Lee and co-workers combined scanning electrochemical microscopy and scanning optical microscopy to obtain simultaneous electrochemical and optical images of living diatoms in a constant-current mode [13]. This kind of microscopy might prove useful in mapping the biochemical activity of a living cell.

The defense potential of the diatom shell was investigated by Hamm and co-workers by measuring its strength [14]. It was found that diatoms are remarkably strong by virtue of their architecture and the material properties of the diatom silica.

In 2004 Arce and co-workers used the AFM to compare the adhesion of diatoms to several surfaces. Tipless AFM cantilevers were functionalized with living diatom cells, and the surfaces investigated were tested with the same diatom bioprobe [15].

13.2.2.1

Diatom Topography as Investigated with AFM

Owing to the poor adhesion to the substrate, it is impossible to obtain stable images of most benthic diatom species with the AFM.

AFM-compatible diatom species can be selected from a large sample by following a simple and effective strategy: Freshwater aquarium plants covered with benthic diatoms are placed in a jar filled with water, as well as two left-handed European freshwater snail species, *Physa fontinalis* and *Planorbarius corneus*, and some glass slides. In the following weeks, the diatoms will colonize the jar and the glass slides. The snails will feed on the diatoms, predominantly leaving the species behind, which obviously strongly attach to the substrate.

By this strategy, Gebeshuber and co-workers [10] selected three different diatom species: *Eunotia sudetica*, *Navicula seminulum* and a yet unidentified species, and subsequently imaged them in contact mode AFM (Fig. 13.3).

The natural adhesives of these diatoms, which attach them to the substrate as well as to each other (all of them are colonial forms), prove to be sufficiently strong that stable AFM imaging conditions are achieved without further sample preparation.

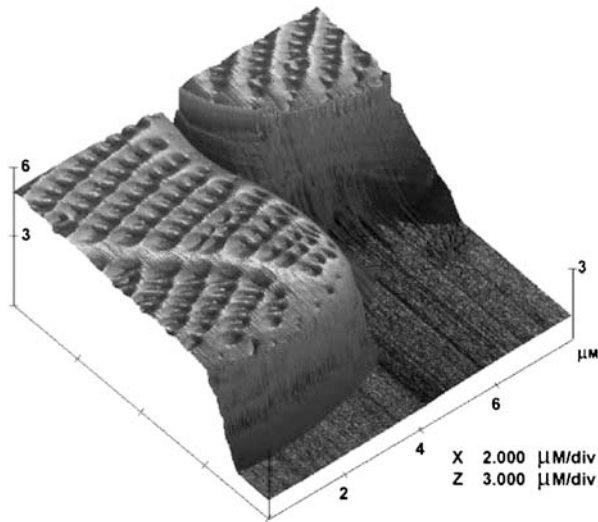


Fig. 13.3. AFM image of parts of two living diatom cells of the species *Navicula seminulum* growing on a glass slide. Note that the flat area does not correspond to the surface of the glass slide, but is determined by the maximum possible extension of the z-piezo of the microscope. Image acquired using AFM contact-mode imaging in water, imaging parameter topography, scan size $8 \times 8 \mu\text{m}^2$, scanning frequency 1 Hz. Reprinted with permission from Gebeshuber IC, Kindt JH, Thompson JB, Del Amo Y, Stachelberger H, Brzezinski M, Stucky, GD, Morse DE, Hansma PK (2003) *J Microsc* 212:292 [10] © 2003, The Royal Microscopical Society

The cells are imaged in their culture medium or in tap water while they are still growing on the glass slides. Tapping-mode as well as contact mode imaging is easy to achieve as long as engaging the cantilever takes place on the cell surface.

Navicula seminulum grows in stacks of cells pointing out from the glass slide. These chains of cells can be about 10 cells high, as investigated by SEM (data not shown). Figure 13.3 reveals detailed surface patterning of the top valve faces of two adjacent cells of *Navicula seminulum*.

The chains of *Eumotia sudetica* and of the yet unidentified species grow with the valve faces perpendicular to the surface of the glass slide, allowing for AFM investigation of the girdle bands.

The cells are alive and continue to divide after imaging.

13.2.2.2

Diatom Adhesives Investigated by SPM

Most man-made adhesives fail to bond in wet conditions, owing to chemical modification of the adhesive or its substrate. Engineering strong and robust underwater adhesives that are stable in wet environments is a challenge to current technology. Diatoms produce excellent adhesives that are stable and robust in wet environments.

Phase images depict the phase delay between the drive and response of the cantilever. These images contain information about the energy dissipated during

the interaction of the AFM tip with the sample, and can help us to understand the viscoelastic and adhesion properties of the surfaces investigated, specifically of the organic material responsible for diatom adhesion.

Because phase imaging highlights edges and is not affected by large-scale height differences, it provides clearer observation of fine features that can be hidden by rough topography (Fig. 13.4). To investigate the natural adhesives utilized to attach cells to each other and to the substratum, it was tried to probe the cleft between two connected diatom cells with the AFM. In the yet unidentified species, the cleft at the cell–cell interface proved too deep. In this region, even the use of electron-beam-deposited AFM tips with high aspect ratio merely results in tip imaging. Phase imaging reveals slight differences (2°) in viscoelastic and adhesion properties of the two adjacent valves. *Eunotia sudetica*, by contrast, is very convenient for *in situ* investigation of the diatom adhesive at the cell interface, because there is barely any cleft between adjacent cells and valve undulations are less pronounced than

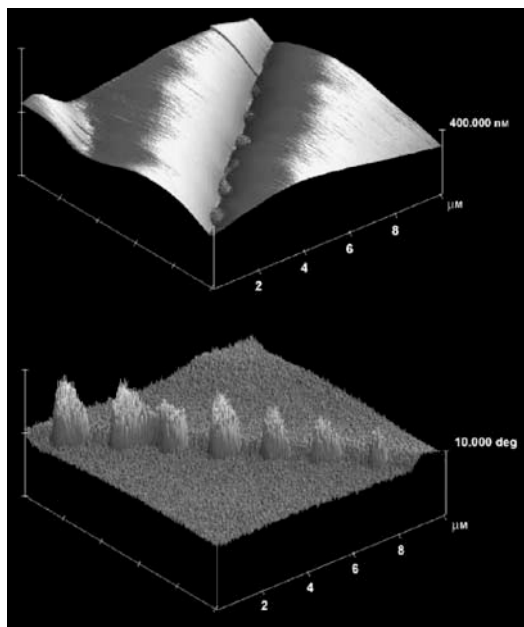


Fig. 13.4. (a) The adhesives in the contact region of two cells of *Eunotia sudetica* are apparent as small topographic features on the slightly undulated cell interface. The corrugation of the bead-like structures is between 10 and 20 nm, and their lateral dimension and spacing is about 1 μm. (b) In the phase image these features are far more striking. The diatom adhesive causes a phase lag of about 10° compared with the rest of the frustule surfaces, where on a single frustule it is within 1° . Note the 2° interfrustule phase step, which reveals slightly different viscoelastic properties of the two neighboring valves. Tapping mode, topography and phase, scan size $10 \times 10 \mu\text{m}^2$, scan rate 5 Hz. Note that for better view (b) is rotated clockwise by 90° as compared with (a). Reprinted with permission from Gebeshuber IC, Kindt JH, Thompson JB, Del Amo Y, Stachelberger H, Brzezinski M, Stucky, GD, Morse DE, Hansma PK (2003) *J Microsc* 212:292 [10] © 2003, The Royal Microscopical Society

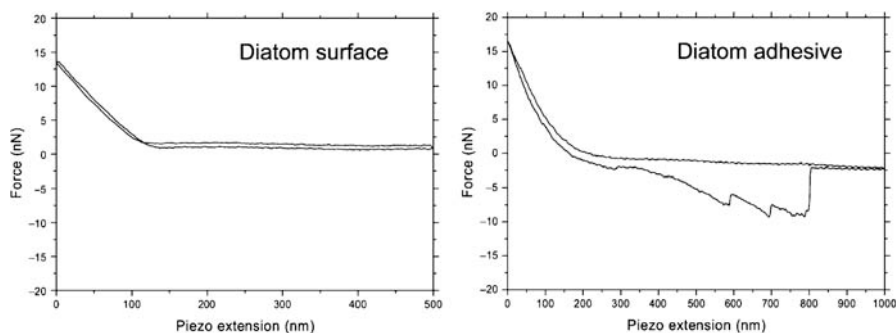


Fig. 13.5. Force–distance curves. *Left*: no adhesion can be recognized on the diatom surface. *Right*: representative data for the diatom adhesive that attaches *Eunotia sudetica* to the substrate. Several debonding events occur. Reprinted with permission from Gebeshuber IC, Kindt JH, Thompson JB, Del Amo Y, Stachelberger H, Brzezinski M, Stucky, GD, Morse DE, Hansma PK (2003) *J Microsc* 212:292 [10] © 2003, The Royal Microscopical Society

in the other species investigated (Fig. 13.4). The diatom adhesive is apparent as small topographic features at the cell interface. The bead-like structures are 10–20 nm high, have lateral dimensions of about 1 μm and are about 1 μm apart. The phase image clearly depicts the altered viscoelastic properties of these structures: the diatom adhesive causes a phase difference of up to 10° compared with the phase difference on the rest of each of the two frustules, where it is within 1° on each, apart from a 2° phase difference between the two adjacent valves, a feature which also appears in the other species, where the adhesives are not accessible because of deep clefts between the single organisms.

Force–distance curves on the surface and on the adhesive of *Eunotia sudetica* reveal basic differences in adhesion properties (Fig. 13.5). On the diatom surface, no adhesion force can be detected (Fig. 13.5 left). The diatom adhesive, by contrast, is strong and robust in the wet environment. To gain reproducible access to this natural adhesive, a chain of *Eunotia sudetica* that was embedded in a densely packed field of *Navicula seminulum* was scraped away from the glass slide with an STM-tip mounted on a three-dimensional micromanipulator. Over a period of several hours, force–distance curves were taken on the adhesive molecules that were used to attach the diatom cells to the glass slide (Fig. 13.5, right). No change in the basic shape of the force–distance curves can be detected within hours of repetitive pulling in the area where the colony was located. Typically, several debonding events occur until the natural adhesive molecules finally debond at a tip–surface separation of about 600 nm. For a detailed description of this study, see [4, 10].

13.3 Interaction of Large Organic Molecules

Conformational diseases such as Parkinson’s disease, Alzheimer’s disease, kuru, scrapie, BSE and vCJD (variant Creutzfeldt-Jakob Disease) result from misfolded proteins aggregating into detrimental structures like amyloid fibers [16–18].

The amount of protein involved ranges from scarcely detectable to kilograms.

Partial unfolding might expose significant regions of the polypeptide chain to the outside world, allowing the protein to aggregate and convert into amyloid fibrils. Once formed, the strong hydrogen bonding between molecules can make this process effectively irreversible.

As with crystallization, the formation of amyloid fibrils is “seeded” by preformed aggregates, a phenomenon that might also be responsible for the rapid progression of sporadic diseases such as Alzheimer’s once the symptoms become evident. BSE, for example, has almost undoubtedly resulted from the highly unnatural practice of feeding young cows on the remains of old ones, with the disease then being transmitted to humans as vCJD. Both kuru and BSE have virtually disappeared as a result of effective action taken once their origins were understood.

The proteins that have emerged under evolutionary pressure are normally robust enough to resist reversion to aggregated states. Evolutionary processes have selected sequences of amino acids with the remarkable ability to form monomeric structures in which the main chain is folded in a unique way within the mass of close-packed side chains, preventing it from interacting with other molecules.

Furthermore, “chaperone” proteins help to protect against such changes.

Chaperones are proteins whose function is to assist other proteins in achieving proper folding: They prevent protein aggregation by providing encapsulated hydrophobic environments that allow the protein to fold properly.

Many chaperones are heat or cold shock proteins, that is, proteins expressed in heat or cold shock conditions. The reason for this behavior is that protein folding is severely affected by extreme temperatures. Chaperones act to counteract the potential damage. Although most proteins can fold in the absence of chaperones, a minority strictly requires them.

A large number of chaperones need adenosine triphosphate (ATP) to function properly. Chaperones recognize unfolded proteins by the hydrophobic residues these expose to the solvent. Exposed hydrophobic residues are unusual for properly folded proteins. Since the environment of the cell is characterized by hydrophilic groups (mostly water), incompletely folded or misfolded proteins with exposed hydrophobic groups have a tendency to aggregate to larger structures, where again, the hydrophobic residues would be hidden from the surrounding.

Chaperonins are a subset of chaperone proteins found in prokaryotes, mitochondria and plastids.

The AFM has proven to be a useful tool for studying proteins at the single molecule level. For a review on single molecule techniques in biomedicine and pharmacology, see [19].

Many of the single molecule studies with the AFM have been restricted by noise and speed limitations.

The first protein–protein interactions on the single molecule level imaged in real time were presented in 2000 [20]. This study demonstrated the enormous contributions AFM can make to molecular biology. Bulk results are interesting, but there are many valuable properties that can only be investigated on the single molecule level.

This work was enabled by the development of small cantilevers [21–23]. Small cantilevers allow for faster imaging and faster force spectroscopy of single biopolymers, because they have higher resonant frequencies and lower coefficients of viscous damping.

A new generation of AFMs using small cantilevers will enable the study of biological processes with greater time resolution, possibly at video refresh rates. Furthermore, small cantilever AFMs allow to narrow the gap in time between results from force spectroscopy experiments and molecular dynamics calculations.

The small cantilevers are fabricated out of low stress silicon nitride. They are ten micrometers long, have widths of 3–5 μm , and their thickness is about 75 nm. These cantilevers can measure smaller forces than larger cantilevers with the same spring constant because they have lower coefficients of viscous damping.

The prototype small AFM detects the motion of small cantilevers by using high numerical aperture optics to focus a laser beam onto the cantilever and then measuring angular changes in the reflected light beam.

This microscopy was used to observe, in real time, the interactions between individual molecules of the *Escherichia coli* chaperonin protein GroES binding to and then dissociating from individual *E. coli* GroEL proteins, which were immobilized on a mica support.

Both X-ray crystallography and cryoelectron microscopy studies have been used to resolve the structures of GroEL and the GroEL–GroES complex in different stages of the folding cycle (Fig. 13.6, e.g. [24–29]).

A prototype small cantilever AFM [23] image of both GroEL deposited on mica and the GroEL–GroES complex repeatedly without the aid of fixing agents (Fig. 13.7).

GroEL adsorbs to mica in end-up orientation. The average diameter of the molecules in this image agrees with the X-ray and cryoelectron microscopy data.

Upon the addition of GroES and ATP into the buffer solution, GroES molecules were observed as features that extend 3.6 ± 1 nm higher than the GroEL film (Fig. 13.8).

The height of these features is also consistent with X-ray crystallography and cryoelectron microscopy data. The same sample region can be scanned repeatedly without excessively disturbing the GroEL–GroES complexes (for details, see [20]).

Fig. 13.6. Cryoelectron microscopy images of GroEL (*left*) and the GroEL–GroES complex. The height of the GroEL molecule is about 15.1 nm, the height of the GroEL–ES complex is about 18.4 nm. Upon interaction with ADP or ATP, domain movements occur, as indicated. Reprinted with permission from Roseman AM, Chen S, White H, Braig K, Saibil HR (1996) Cell 87:241 [29] © 1996, Elsevier

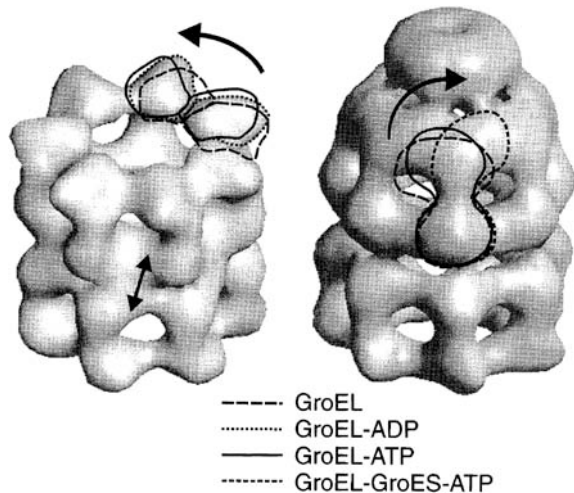
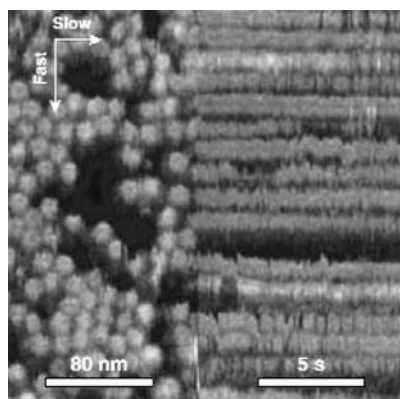


Fig. 13.7. GroEL film deposited on mica scanned in two dimensions (*left*) and in one dimension (*right*). In this image of GroEL, the movement along the slow scan axis was disabled half way through the scan. From then on the AFM tip repeatedly scanned the same line of proteins. Each *horizontal line*, therefore, shows changes in time of an individual molecule. Reprinted with permission from Viani MB, Pietrasanta LI, Thompson JB, Chand A, Gebeshuber IC, Kindt JH, Richter M, Hansma HG and Hansma PK (2000) Nature Struct Biol 7:644 [20] © 2000, Nature Publishing Group



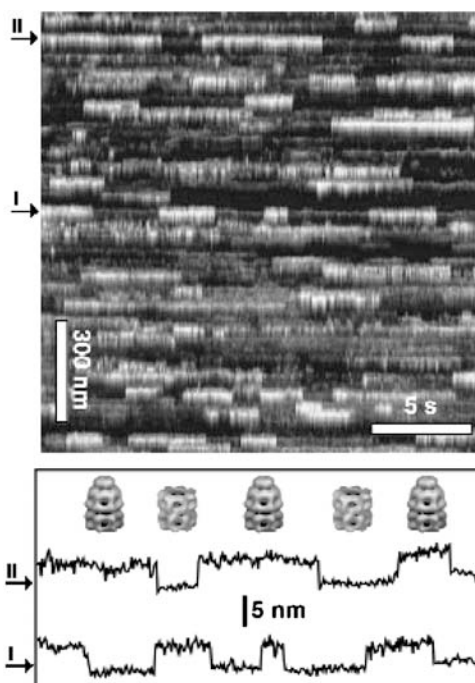
Therefore, in order to obtain the temporal resolution required for observing the formation and dissociation of the GroEL–GroES complexes in the presence of Mg-ATP, the sample was scanned in one dimension rather than two (Fig. 13.8).

The time/height diagram of the protein lines displays repetitive well-defined step-like variations in height (Fig. 13.8). The magnitude of these steps is 3.6 ± 1 nm. The observed height variations result from GroES molecules attaching to and then separating from the respective GroEL molecules.

Without GroES and Mg-ATP no such steps can be observed.

Fig. 13.8. Tapping mode AFM in liquid.

Top: after the addition of GroES and Mg-ATP into the buffer solution, variations in height along the lengths occur in the single protein lines, as exemplified by *arrows I and II*. *Bottom:* time/height diagram of the protein lines indicated with the *arrows* in the top image. The height changes between two values that differ by 3.6 ± 1 nm. This indicates the binding and unbinding of GroES. The cryoelectron microscopy images of GroEL and the GroEL–GroES complex are from Roseman et al., 1996 (reprinted with permission, © 1996, Elsevier). Adapted with permission from Viani MB, Pietrasanta LI, Thompson JB, Chand A, Gebeshuber IC, Kindt JH, Richter M, Hansma HG, Hansma PK [20] (2000) Nature Struct Biol 7:644 [20] © 2000, Nature Publishing Group



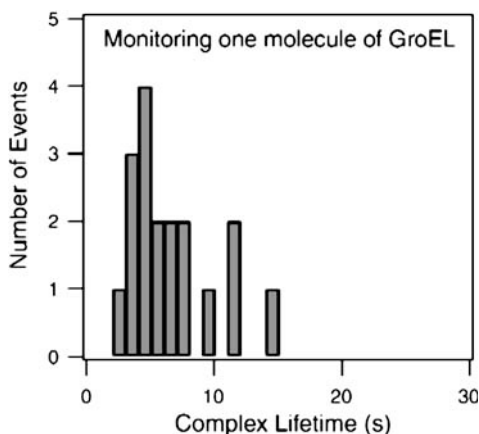


Fig. 13.9. Histogram of measured GroEL–GroES complex lifetime in the presence of Mg-ATP. Individual GroES molecules attach to and then separate from the same GroEL molecule 18 times during an observation period of about 120 seconds. Note the absence of events with lifetimes < 2 seconds. This is interesting in itself, telling us about the GroEL–GroES complex lifetime on the single molecule level, and furthermore indicates gentle measuring, since strong disturbance of complex formation by the cantilever would also lead to subsecond complex lifetimes. Reprinted with permission from Viani MB, Pietrasanta LI, Thompson JB, Chand A, Gebeshuber IC, Kindt JH, Richter M, Hansma HG, Hansma PK [20] (2000) *Nature Struct Biol* 7:644 © 2000, Nature Publishing Group

A histogram of the complex lifetime for a single GroEL molecule that was investigated for about 120 seconds is shown in Fig. 13.9. During this time interval, 18 times a complex with GroES has formed. The distribution of complex lifetime peaks near five seconds and the average lifetime is $\sim (7 \pm 1)$ s ($n = 18$).

In future application of this kind of single molecule studies with the AFM, misfolded proteins could well be involved and, e.g. the effect of various pharmaceuticals on folding efficiency could be tested.

13.4

Nanodefects on Atomically Flat Surfaces

Most of the small structures currently used in technology are in the micrometer range. One reason for this is silicon micromachining technology, which works fast and at low cost in this regime.

However, needs for increased data-storage density and smaller devices call for nanometer-sized structures.

Nanofabrication techniques comprise techniques such as electron beam and nano-imprint fabrication, epitaxy and strain engineering, scanning probe techniques, as well as self-assembly and template manufacturing [30].

Nanotransfer printing is a more recent high-resolution printing technique, which uses surface chemistries as interfacial “glues” and “release” layers to control the transfer of solid material layers from stamp relief features to a substrate [31].

One important way to produce nanostructures on surfaces involves kinetic sputtering by “fast” ions. However, fast ions unavoidably cause unwanted radiation damage. As opposed to this, potential sputtering (PS), i.e. desorption induced by the potential energy of slow multiply charged ions (MCI), holds great promise for more gentle nanostructuring of insulating surfaces [32, 33].

It can cause high sputter yields even at such low ion impact energies where kinetic sputtering and defect creation in deeper layers is not possible. While the physical mechanisms of PS have been the subject of extensive investigation [34–38], technical applications of slow MCI have so far remained largely unexplored, despite the fact that they provide unique opportunities for etching, ultra-thin film growth and nanostructure fabrication.

The AFM is the microscope of choice for investigating ion induced nanodefects on flat crystals, because of its unprecedented resolution and of the fact that it can also image insulating materials.

13.4.1

Ion Bombardment of Highly Oriented Pyrolytic Graphite (HOPG)

HOPG is used as a diffracting element in monochromators for X-ray and neutron scattering and as a calibration standard for STM and AFM. The graphite surface is easily prepared as a clean atomically flat surface by cleavage with an adhesive tape. HOPG is, therefore, used in many laboratories as the surface of choice for “seeing atoms”.

Surface defects in HOPG produced by the impact of individual (singly charged) ions have already been investigated via STM/AFM by a number of groups [40–49, and further references therein].

However, first results were reported only recently for impact of slow multiply charged ions and the effect of the projectile charge state (or potential energy) on the size of the produced nanodefects [49–52].

Moreover, in most previous studies, either STM in air was used or the irradiated samples were transported in air towards STM inspection after ion bombardment. If, e.g., chemical bonds at the surface are broken due to the ion impact, impurities could preferentially adsorb at these sites and thus change the topography of the surface (and the resulting STM image) during contact with air. Therefore, here MCI bombardment has been followed by STM/AFM investigations without breaking the ultra-high vacuum. In this way, possible influences from target surface exposure to air can be ruled out.

Figure 13.10 shows STM and AFM scans of the HOPG surface before bombardment.

The STM image of HOPG bombarded with 800 eV Ar⁺ ions reveals a large number of individual nanosized defects as a result of ion bombardment (Fig. 13.11). In AFM scans of the same surface, no significant topographic changes could be detected [53].

For very highly charged projectile ions, surface defects have recently also been observed in AFM studies [51, 52].

Meguro and co-workers found that HCl impact and subsequent treatment either by electron injection from an STM tip or by He-Cd laser irradiation induce a localized

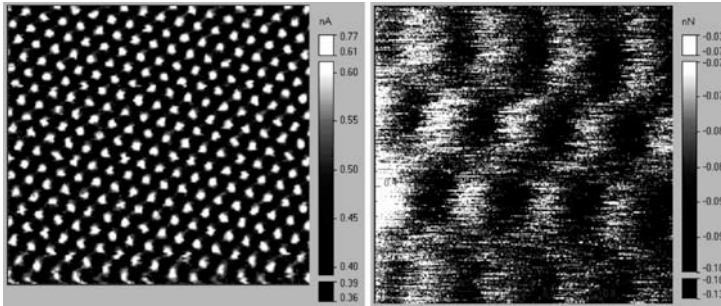


Fig. 13.10. Highly oriented pyrolytic graphite imaged in ultrahigh vacuum with atomic resolution. *Left:* scanning tunneling microscopy image, image size $4 \times 4 \text{ nm}^2$. *Right:* atomic force microscopy image, image size $1 \times 1 \text{ nm}^2$

transition from sp^2 to sp^3 hybridization in graphite, resulting in the formation of nanoscale diamond-like structures (nanodiamonds) at the impact region [54].

In an investigation of HOPG bombarded with 400 eV Ar^+ and Ar^{8+} ions involving Raman spectroscopy, Hida and co-workers found that the charge state of the ions as well as their mass have an influence on the disordering of HOPG and that the defects introduced by Ar^{8+} are not simple vacancies, but assumed to be vacancy clusters in contrast to their results for Ar^+ irradiation [55].

Several hundred defects from different sample positions have been statistically analyzed for each projectile type (Ar^+ , Ar^{8+} , Ar^{9+}).

Fig. 13.11. Highly oriented pyrolytic graphite bombarded with 800 eV Ar^+ ions imaged with STM in ultrahigh vacuum. Image size $100 \times 100 \text{ nm}^2$. The ion induced nanodefects are clearly visible

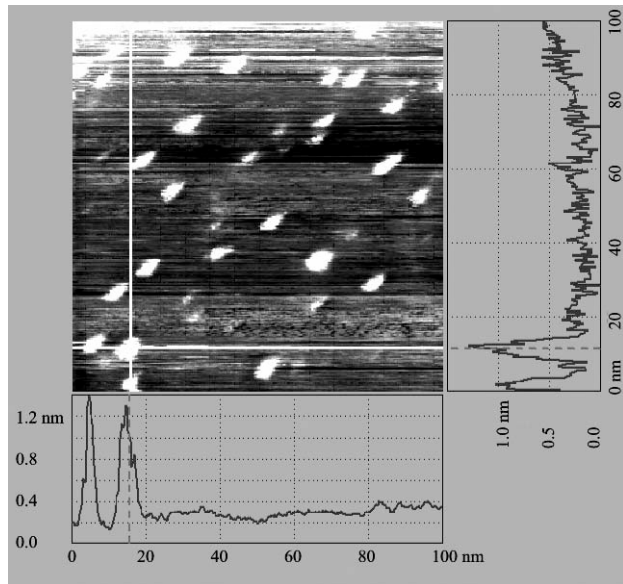


Figure 13.12 (right trace) shows the enlarged STM image of a typical defect on HOPG created by the impact of a single Ar^+ ion of 800 eV kinetic energy

The only surface defects found in the STM images are “protrusions” (hillocks) with a mean lateral size of 0.8–1.25 nm and an average equivalent height of 0.22 nm. They are randomly dispersed on the originally flat surface. Their area density is in good agreement with the applied ion dose, implying that nearly every single ion impact has caused one protrusion. A $\sqrt{3} \times \sqrt{3}\text{R}30^\circ$ surface, as characteristic for interstitial defects in HOPG [56–58], surrounded by undisturbed surface parts is observed in the vicinity of most defects (see Fig. 13.12). Scanning with the AFM down to atomic resolution on the irradiated surface did not show any significant topological changes due to ion bombardment. Therefore, we conclude that the nanodefects produced by slow ion impact are of electronic rather than of topographic nature.

For impact of singly charged ions, our findings are in good agreement with previous observations [43, 57].

As a remarkable result, however, it was found that the measured mean diameter of the “hillocks”, and to a somewhat lesser extent their “height”, increase with the projectile charge state [53]. In a careful STM study, Hahn and Kang [57] showed that generally two kinds of defects in HOPG are created by low energy (100 eV) Ar^+ bombardment, namely carbon vacancy defects (VDs) and interstitial defects (IDs) formed by trapping the projectile beneath the first carbon plane.

Both types of defects are detected as protrusions in the STM topographic image. The dangling bonds at the VD site cause an enhancement of the local charge density-of-states (CDOS) near the Fermi energy, seen as a protrusion in the STM image [57].

The protrusion observed in the STM image at ID sites results from a small geometric deformation of the graphite basal plane due to the trapped projectile (not large enough to be visible in our AFM scans) and an apparently larger electronic defect due to an increased CDOS. A $\sqrt{3} \times \sqrt{3}\text{R}30^\circ$ surface was reported [57] only for IDs but not for VD. From this $\sqrt{3} \times \sqrt{3}\text{R}30^\circ$ superlattice structure also

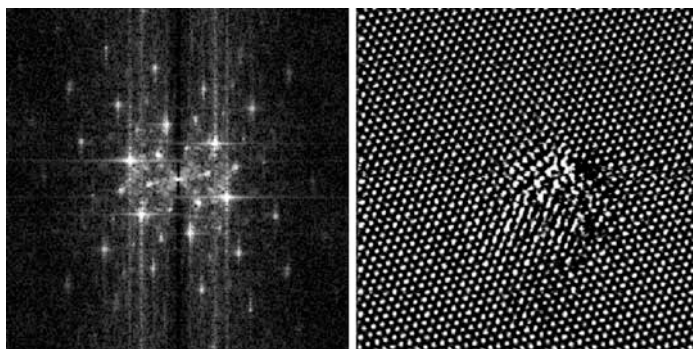


Fig. 13.12. Highly oriented pyrolytic graphite bombarded with 800 eV Ar^+ ions imaged with STM in ultrahigh vacuum with atomic resolution (*right*). Image size $10 \times 10 \text{ nm}^2$. The fast Fourier transform (*left*) of the Ar^+ ion-induced defect reveals a $\sqrt{3} \times \sqrt{3}\text{R}30^\circ$ surface: the ion induced features are larger than the features from the HOPG lattice and they are rotated with respect to them by 30 degrees

observed in our experiments (see Fig. 13.12), we therefore conclude that the majority of the “hillocks” observed are due to IDs, or VDs created along with IDs. The strong increase of the lateral protrusion size with increasing charge state of the projectile ion is interpreted as a “pre-equilibrium” effect of the stopping of slow multiply charged ions in HOPG, as has so far only been observed for higher charge states [44].

Although MCI are converted already into neutral hollow atoms (i.e., an atom whose inner shells remain essentially unoccupied) during their approach towards the surface, their captured electrons remain in highly excited states until surface impact, where they are gradually peeled off and replaced by conduction band electrons forming a partial screening cloud around the MCI [59].

Before final deexcitation of the hollow atom can take place within the solid, reduced screening should result in a strongly increased energy loss of the projectiles. According to SRIM-2000 (© IBM) calculations [60], the mean range of 150 eV Ar projectiles in HOPG is about two monolayers. An increased stopping and straggling of the higher charged Ar projectiles would lead to IDs located closer to the surface, as well as to more VDs due to a higher momentum transfer to the carbon atoms of the first plane. Because of the extreme surface sensitivity of STM, this pre-equilibrium effect in the stopping power is not masked by (equilibrium) bulk effects and is apparently observable with unprecedented clearness.

Extending pertinent work by other groups with singly charged ions only, our combined STM/AFM studies revealed nanodefects that comprise a disturbance of the electronic density-of-states of the surface rather than its topography.

Whereas the size of these defects increases with the ion charge (here up to $q = 9$), as expected for any conducting target surface they showed no evidence for potential sputtering.

For more detailed information on these studies, see [50, 53].

13.4.1.1

Revealing the Hidden Atom in Graphite by Low-Temperature AFM

Despite the proverbial ease of imaging graphite by STM with atomic resolution, every second atom in the hexagonal surface unit cell remains hidden, and STM images show only a single atom in the unit cell.

The reason for this is that the tunneling current is not a function of the surface topography, but of the local electronic structure. On the graphite surface, there are two different types of carbon atoms in the basal plane, as distinguished by the presence (α) or absence (β) of a carbon atom in the plane immediately below the surface. The α atoms are located directly above another α atom, in the layer directly underneath, the β atoms are located above a hollow site. These local electronic structure variations imply that the STM can only detect every other atom on the graphite surface. Consequently, an alternative imaging method is required to detect the “hidden” α atoms on the graphite surface [61].

Also in contact-mode AFM images of graphite the quasi-atomic resolution images show only one protrusion per unit cell [62].

Recent progress in dynamic AFM allows researchers to routinely achieve true atomic resolution on conductors and insulators [63, 64], but once again only one

maximum within a hexagonal unit cell of the graphite surface was obtained in the attractive noncontact mode [65].

In 2003, Hembacher and co-workers presented measurements with a low-temperature atomic force microscope with pico-Newton force sensitivity that reveal the hidden surface atom [66].

The instrument used in this investigation is a combined ultrahigh vacuum (UHV) STM/AFM to simultaneously probe the charge density at the Fermi level and the total charge density of graphite by recording tunneling currents and forces, respectively. The instrument is immersed in a liquid He bath cryostat, yielding a sample temperature of 4.89 K and exceptionally low thermal drifts of about 0.02 nm/h (at room temperature, even with drift correction, currently 2–10 nm/h are achieved). To protect the microscopy from external vibrations, the setup is built on a foundation with a mass of 30,000 kg.

In their dynamic AFM images of graphite, recorded at small oscillation amplitudes and with weak repulsive forces, both the α atoms and the β atoms are detected. The reason for this is that the repulsive forces utilized in AFM involve different electrons in the tungsten tip than in the STM mode.

Revealing the hidden atoms in graphite by means of room-temperature AFM might become possible with miniaturized AFMs based on nano- or microelectromechanical systems (NEMS/MEMS) technology (since they show small drift). In such an instrument, the operating frequency could be commensurately increased and there would be no need for a 30,000 kg fundament [61].

13.4.2

Bombardment of Single Crystal Insulators with Multicharged Ions

Systematic STM/AFM investigations on nanoscopic defect production at atomically clean insulator surfaces of Al_2O_3 after bombardment by slow (impact energy ≤ 1.2 keV) singly and multiply charged ions under strict UHV conditions is the topic of this section.

It will be demonstrated that on monocrystalline insulator surfaces, well-defined topographic features of typically nm extensions are produced (“potential sputtering”). For Al_2O_3 , there exists a clear dependence of the defect size on the projectile ion charge. These results are discussed in view of possible new nanoscopic surface structuring and modification methods for which the kinetic projectile energy plays only a minor role.

Impact of slow ions on solid surfaces can give rise to inelastic processes that modify the geometric and electronic structure at and below the surface, cause emission of electrons and photons as well as neutral and ionized target particles (atoms, molecules, clusters), remove surface-adsorbed material and lead to projectile neutralization. The transfer of electrons between surface and projectile possibly acts as precursor for the above-mentioned processes and makes them proceed irrespective of the kinetic projectile energy.

The importance of such “electronic” processes increases with multicharged projectile ions and their role is elucidated when slow ions of the same kinetic energy, but with different charge states are applied as projectiles.

For certain insulator surfaces, the impact of slow multicharged ions (MCIs) Z^{q+} gives rise to considerably stronger ablation than the well-established kinetic sputtering by neutral or ionized projectiles. First experimental evidence for this PS was reported for alkali-halide surfaces and explained by “Coulomb explosion” [67], i.e. the creation of small positively charged surface spots from the rapid electron capture by impinging MCI, and the subsequent ablation because of strong mutual target ion repulsion.

“Coulomb explosion” was also invoked in order to explain AFM observations of blister-like defects on mica samples produced by highly charged ions Z^{q+} (kinetic energy 1–3 keV/atomic mass unit) [36, 68].

However, studies for impact of slow (≤ 1 keV) MCI on thin polycrystalline films of alkali-halides (LiF, NaCl) and Al_2O_3 deposited on quartz microbalance crystals [69] suggested a different explanation for PS, namely defect-stimulated desorption induced by very efficient electron capture [35].

It has been established that such desorption processes are induced by electrons (electron stimulated desorption, ESD) or photons (photon stimulated desorption, PSD) on such materials where self-trapping of specific crystal defects proceeds via electron–phonon coupling in the crystal lattice [70].

However, such defect trapping as the prerequisite for PS may also be caused or at least supported by the kinetic projectile energy (“kinetically assisted PS” [37]), which could also explain some PS-like effects reported for target species where no electron–phonon coupling can take place, i.e. for semiconductors like Si and GaAs [68]. In any case, for slow ion impact, the self-trapping mechanism is most relevant for PS. Consequently, for metal and semiconductor surfaces no slow MCI-induced PS can be observed, so far [71].

As the surface region from which a slow MCI does capture electrons should be rather small (nm extensions), it is probable that the surface defects caused by PS are of similar size. In order to study such defect structures, we applied AFM in UHV on monocrystalline target surfaces of insulator species for which PS by slow MCI impact has already been demonstrated on polycrystalline thin films [37, 69, 71].

The results for Al_2O_3 presented below are of possible interest for nanostructuring these surfaces.

Observations of slow ion-induced nanodefects on different atomically clean target surfaces were performed under strict UHV conditions with a combined AFM/STM instrument (UHV-AFM/STM, OMICRON Nanotechnology GmbH, Germany). Nanodefects were looked for on freshly prepared surfaces of sapphire *c*-plane $\text{Al}_2\text{O}_3(0001)$ after irradiation with low doses of slow singly and multiply charged ions. In order to avoid disturbing noise from an ion irradiation chamber directly attached to the AFM/STM instrument, a transportable UHV vault for target transfer, which was alternatingly coupled via UHV locks to the target ion irradiation chamber and the AFM/STM was used. This procedure kept the target surfaces under permanent UHV conditions after initial cleaning, thermal annealing, and during subsequent slow ion irradiation until completion of the AFM/STM inspection. Ion irradiation of the insulator surfaces was accompanied by low-energy (≤ 4 eV) electron flooding to compensate for surface charge-up, which otherwise strongly inhibits AFM observation or makes it even impossible. The electron gun was arranged at 2 cm distance

to the sample. All AFM observations were made in the contact mode, with the base pressure in the AFM/STM chamber kept at about 10^{-10} mbar during measurements.

The singly and multiply charged ions for target irradiation have been extracted from a 5 GHz electron cyclotron resonance ion source [72], magnetically analyzed and guided via electrostatic lenses to the UHV irradiation chamber. The ions were decelerated in front of the target surface to their desired impact energy (≤ 1.2 keV). Uniform irradiation was assured by rapidly scanning the ion beam across the target surface by means of deflection plates.

13.4.2.1

Production of Slow Ion-Induced Surface Defects on Al_2O_3 Insulator Targets

Polished $\text{Al}_2\text{O}_3(0001)$ *c*-plane single crystals (TBL Kelpin, Neuhausen, Germany) were CO_2 snow cleaned (to remove micrometer and submicrometer particles and hydrocarbon-based contamination) and then annealed in UHV for 3 h at 400°C . This preparation technique yields very flat crystal surfaces.

AFM contact mode studies on 14 samples prepared by the standard preparation technique revealed a root mean square (rms) roughness of 0.093 ± 0.06 nm rms. Bombardment with Ar ions of different charge states and kinetic energies (500 eV Ar^+ and Ar^{7+} , 1.2 keV Ar^+ , Ar^{4+} and Ar^{7+}) results – as seen in AFM contact mode – in hillock-like nanodefects (see Fig. 13.13).

The ion-induced defects on the sapphire single crystal surface can be removed by annealing at 450°C for 5 h. The density of nanodefects does not directly correspond with the applied ion dose: an ion dose of 5×10^{12} ions/ cm^2 , which is equivalent to five ions per $10\text{ nm} \times 10\text{ nm}$, leads to a rather small, however reproducible, density of defects on the sapphire surface: about 10 nanodefects per $1000\text{ nm} \times 1000\text{ nm}$ can be observed after bombardment in the energy range reported here. This is equivalent

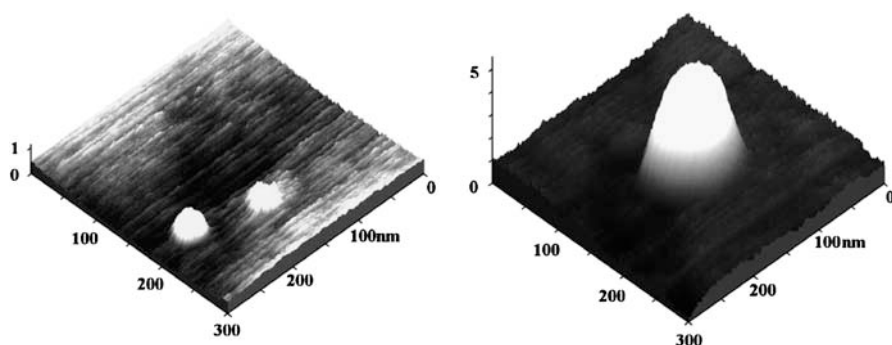


Fig. 13.13. UHV AFM contact mode image of sapphire (Al_2O_3 , *c*-plane 0001) bombarded with 500 eV Ar^+ (*left image*) and Ar^{7+} (*right image*) ions. The nanodefects induced by Ar^{7+} ions (which have the same kinetic but higher potential energy than the Ar^+ ions) are considerably higher and wider than those caused by singly charged ions. The defects are real topographic features; the units on the three axes are nanometers. Reprinted with permission from Gebeshuber IC, Cernusca S, Aumayr F, Winter HP (2003) *Int J Mass Spectrom* 229:27 [53] © 2003, Elsevier Science B.V.

to a dose to defect ratio of 5000. More detailed experiments with different ion doses are needed. Analysis of the statistics of random impacts will clarify how many individual ion impacts are needed to form a visible nanodefekt on the insulator surface.

A possibly similar migration and subsequent recombination of point defects at the surface has previously been reported for silicon bombarded by 5 keV He ions above 160 K [73].

In fact, the only case where the number of defects corresponded fairly well to the applied ion dose was for the conducting HOPG samples (see Sect. 13.4.1).

The Al_2O_3 *c*-plane proved to be the insulator surface showing most clearly a dependence of the ion bombardment induced defects with the kinetic energy and charge states of the projectiles. 500 eV Ar^+ ions produce defects that are about 1 nm high (Fig. 13.13) and have lateral dimensions of some tens of nanometers (one should keep in mind that the height is more accurately measurable with the AFM than lateral dimensions), whereas the defects produced by 500 eV Ar^{7+} ions are several nanometers high (Fig. 13.13) and show lateral dimensions of about 100 (!) nanometers. At higher kinetic energy the differences in the slow ion-induced nanodefekts on the sapphire *c*-plane became even more distinct.

1.2 keV Ar^+ -induced defects are up to about 8 nm high and their width is some 10 nm. For a higher charge state such as Ar^{4+} , two different kinds of defects occurred on the sapphire surface.

They have about the same height, but their lateral dimensions vary considerably: some are nearly 200 nm wide, whereas the smaller defects are only about 50 nm wide.

The height of both kinds of defects is about 2 nm. For Ar^{7+} , only one kind of defect was visible in the AFM images, with about 50 nm diameter and about 2 nm height (for a more detailed description of these results and for similar investigation on SiO_2 surfaces, see [53]).

Al_2O_3 is, therefore, a good candidate for PS-induced nanostructuring. This material is relevant for applications in microelectronics and nanotechnology.

13.5 Subatomic Features

In this section, the detection of atomic orbitals and single electron spins by means of SPM is described. In many cases, sophisticated signal acquisition techniques have to be applied, and the instruments have to be operated at very low temperature, since extremely small drift is required.

13.5.1 Atom Orbitals

Silicon and tungsten are the two chemical elements that already have been investigated with SPM regarding their atomic orbitals.

13.5.1.1

Silicon (111)-(7 × 7) Surface

Publications concerning the imaging of subatomic features with the AFM started in the year 2000, when Giessibl and co-workers published their paper on imaging of subatomic features on the reconstructed silicon (111)-(7 × 7) surface [74]. For a review on semiconductor surface reconstruction, see [75].

A scientific discussion, in which Hug and co-workers questioned this result by proposing that the subatomic features are caused by a feedback artifact, followed this publication [76].

In the course of this argument, Giessibl and co-workers presented refined calculations, showing striking similarities to the experimental images (see Fig. 13.14).

In 2003, Huang and co-workers presented a theoretical work demonstrating the feasibility of seeing atomic orbitals on the Si(111)-(7 × 7) surface with AFM [77].

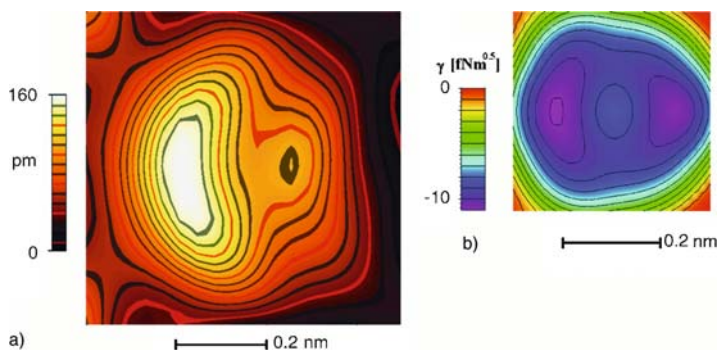


Fig. 13.14. Refined calculations of the normalized frequency shift of a single adatom on the reconstructed silicon (111)-(7 × 7) surface (*right*) performed by the Giessibl group, showing striking similarities with the experimental images (*left*). Reprinted with permission from Hug HJ, Lantz MA, Abdurixit A, van Schendel PJA, Hoffmann R, Kappenberger P, Baratoff A, Giessibl FJ, Hembacher S, Bielefeldt H, Mannhart J (2001) *Science* 291:2509 [76] © 2001, AAAS

13.5.1.2

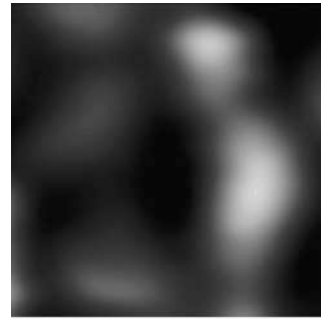
Tungsten

In 2004, Giessibl and co-workers finally ended this discussion by presenting images of an individual tungsten atom by AFM at a resolution of 77 pm [78]. The diameter of a tungsten atom is 274 pm. Four distinct peaks that are attributed to highly localized electron clouds can be identified (Fig. 13.15).

The experiment was performed in UHV at a temperature of about five Kelvin. The microscope was isolated from vibrations by a 30 t foundation and from sound and electromagnetic stray fields by a metal chamber.

In contrast to STM (which only probes the most loosely bound electrons with energies at the Fermi level) AFM can resolve the charge density variations within a single atom, because the forces between the AFM tip and the sample are of electrostatic nature.

Fig. 13.15. UHV low temperature (5 K) AFM constant-height mode image reveals four-fold symmetry in the amplitudes of the higher harmonics signal (centered close to the maximum of the tunneling current, data not shown). Reprinted with permission from Hembacher S, Giessibl FJ and Mannhart J (2004) *Science* 305:380 [78] © 2004, AAAS



— 50 pm

The electron structure originates from the quantum-mechanical nature of tungsten bonding: tungsten develops a body centered cubic crystal structure such that every tungsten atom is surrounded by eight nearest neighbor atoms, causing “arms” of increased charge density which point to the next neighbors. Four of these precisely localized electron clouds are visible on surface atoms.

The role of tip and sample was switched in the experiment: the front atom in a sharp tungsten tip was imaged by a light carbon atom of a graphite surface. The reason a light atom was used for probing was to minimize image blurring, since the mapping of one atom with another atom always involves a convolution of the electronic states. The tunneling current is confined to the top atom because of the sharp increase of tunneling probability with decreasing distance.

Instead of measuring static deflections or frequency changes, higher harmonics triggered by forces between the tip and the sample are recorded in this technique. These higher harmonics are much more sensitive to short-range interactions than static deflections or frequency changes.

13.5.2

Single Electron Spin Detection with AFM and STM

Single-spin detection is a vital goal for read-out in quantum computing, and single nuclear spin detection could solve the problem of how to distinguish between materials at the atomic level.

Several research groups have reported various single spin-detection methods [79–86].

In 1989, Manassen and co-workers presented the first direct observation of the precession of individual paramagnetic spins on partially oxidized silicon (111) surfaces [79].

They used an STM to detect the modulation in the tunneling current at the Larmor frequency. The Larmor frequency is the frequency at which magnetic resonance can be excited. It is given by the Larmor equation, which states that the resonant frequency is proportional to the overall (macroscopic and microscopic) magnetic field. Balatsky and Martin presented the theoretical explanation of this result [87] in 2001.

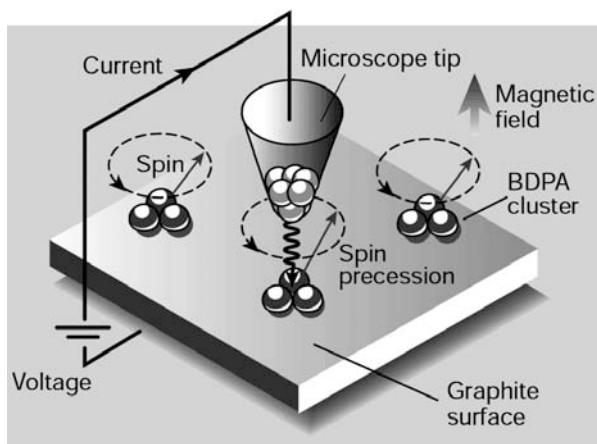


Fig. 13.16. Spin detection through the union of high-resolution microscopy and resonance techniques. The sample is a HOPG surface coated with clusters of organic BDPA molecules. In the applied magnetic field, the electron-spin vectors associated with free radicals in the molecules precess at a certain frequency. The STM tunneling current is modulated at the precession frequency. Detecting the modulation effectively measures electronic spin in the molecule. Reprinted with permission from Manoharan HC (2002) *Nature* 416:24 [88] © 2002, Nature Publishing Group

In 2002, Durkan and Welland published an article that essentially reproduced this experimental result with a different sample: BDPA (a, g-bisdiphenylene b-phenylallyl) on HOPG [80].

The idea of combining magnetic resonance (MR) with force microscopy in magnetic resonance force microscopy (MRFM) was published as a concept in 1991 [89].

Sidles settled on force microscopy because the performance of induction coils, the detectors in conventional MR, scales unfavorably with size. Shrinking the coil to detect a single spin reduces the signal irretrievably below noise. A force microscope, on the other hand, becomes more sensitive the smaller it gets.

In 1992, Rugar and co-workers demonstrated that the force exerted by 10^{12} electron spins could be detected at room temperature with a conventional cantilever for AFM [90].

Since then they have improved their spin detection limit by 12 orders of magnitude:

MRFM was proposed as a means to improve detection sensitivity to the single-spin level, and thus enable 3D imaging of (bio)molecules with atomic resolution [91, 92].

MRFM is essentially a combination of 3D magnetic resonance imaging (MRI) with the unprecedented resolution of AFM.

For an overview on MRFM, see Hammel and co-workers, 2003 [93] and for the theory of spin relaxation in MRFM, see Mozyrsky et al. 2003 [94].

In the year 2004, the force exerted by a single electron spin was measured by MRFM ([86], Fig. 13.17).

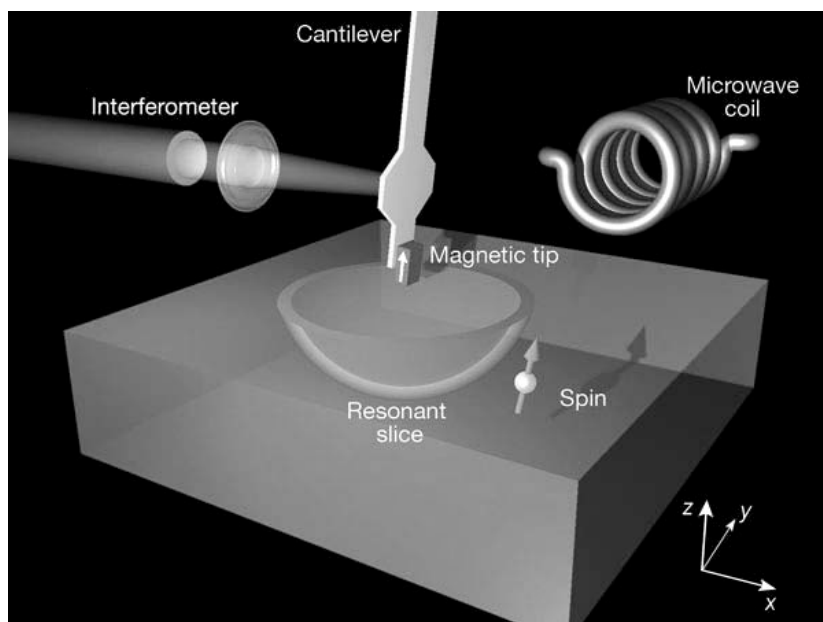


Fig. 13.17. A wiggling cantilever with a tiny CoSm magnet is the key element of a magnetic resonance force microscope. Elaborated signal acquisition makes it possible to detect a single electron spin dozens of atomic layers beneath the surface. In this way, scanning probe microscopy left the surface regime. Perhaps even atomic resolution images of molecules beneath the surface might be possible in the near future. Reprinted with permission from Rugar D, Budakian R, Mamin HJ, Chui BW (2004) *Nature* 430:329 [86] © 2004, Nature Publishing Group

The force detected in the Rugar 2004 experiment is a million times smaller than the forces usually encountered in AFM (van der Waals forces, electrostatic forces). The single electron spin was buried 250 nm below the surface of an irradiated vitreous silicon sample and exerted a force of 2 aN (2×10^{-18} N).

The sample had been prepared by irradiation with a 2 Gy dose of ^{60}Co gamma rays, producing a low concentration of Si dangling bonds containing unpaired electron spins known as E' centers. Unpaired electrons and many atomic nuclei behave like tiny bar magnets. Estimated spin concentration was between 10^{13} and 10^{14} cm^{-3} . The experiment was performed at 1.6 K in a small vacuum chamber that fits within the bore of a superconducting magnet. The low operating temperature minimizes thermal noise and reduces the relaxation rate of the spins.

The force exerted by a single electron spin is the smallest ever detected. Currently, the smallest volume elements in an image must contain at least 10^{12} nuclear spins for MRI-based microscopy [95], or 10^7 electron spins for electron spin resonance microscopy [96].

The cantilever used in the experiment is only 100 nm thick and had to be aligned vertically to the surface. In the conventional AFM configuration with the cantilever parallel to the surface, van der Waals forces and electrostatic forces would make it stick on the surface. Directly on the cantilever a strong 150 nm wide CoSm magnet

is attached. It generates a field gradient of 200,000 T/m. The cantilever is slowly scanned over the surface. A laser interferometer records the cantilever deflections and sophisticated measurement signal acquisition techniques are needed for successful single spin detection. The strong magnetic field gradient allows for distinguishing magnetic resonance signals arising from different spatial locations, enabling accurate spin localization. By scanning the tip over the sample, a local magnetic resonance force is detected, which corresponds with a spatial resolution of about 25 nm. This spatial isolation of the signal is also the main argument that a single spin is being detected. Currently this method is very slow. As Stokstad mentions in his “Science News of the Week” article on the Rugar experiment, scanning a 170 nm stretch of the irradiated silicon sample took several weeks [97].

MRFM could serve as an invaluable tool for the implementation of a spin-based solid state quantum computer. It provides an attractive means for addressing the characterization and control of the fabrication process of the device during its construction and the readout of the computational result [98, 99].

If developed further, the MRFM technique could prove useful for investigating the atomic structure inside materials used in the electronics industry and to image biomolecules – such as proteins – at atomic resolution. However, to reach this goal, nuclear spins have to be detected. Nuclear spins are harder to detect than electron spins, because a proton’s magnetic moment is 658 times smaller than that of an electron.

13.6

Conclusions and Outlook

In this review, we have presented scanning probe microscopy across dimensions from large samples like single cells, via single biomolecules and nanometer small ion induced defects on crystal surfaces to subatomic features like electronic orbitals and single electron spins.

Scanning probe microscopy is on its way to a standard laboratory method: subatomic features can be imaged, and with magnetic resonance force microscopy it has even left the two-dimensional surface regime. Perhaps in the not too distant future 3D-imaging of (complex) molecules, at surfaces or in the bulk state, with atomic resolution might become possible with these powerful techniques. The 3-D MRFM would also deliver chemical specific information because each magnetic nucleus has a unique gyromagnetic ratio.

Acknowledgements. Part of this work was supported by the Austrian Science Fund (FWF) and was carried out at Vienna University of Technology.

Part of this work was funded by the “Austrian Kplus-Program” and was done at the “Austrian Center of Competence for Tribology”, AC²T research GmbH.

References

1. Round FE, Crawford RM, Mann DG (1990) *Diatoms: biology and morphology of the genera*, Cambridge University Press
2. Hecky RE, Mopper K, Kilham P, Degens ET (1973) *Marine Biol* 19:323
3. Gordon R, Sterrenburg F, Sandhage K (guest eds) (2005) *Diatom nanotechnology*, special issue *J Nanosci Nanotechnol* 5:1
4. Gebeshuber IC, Thompson JB, Del Amo Y, Stachelberger H, Kindt JH (2002) *Mat Sci Technol* 18:763
5. Werner D (1977) *The biology of diatoms*, University of California Press
6. Gordon R, Drum RW (1994) *Int Rev Cytol* 150:243
7. Linder A, Colchero J, Apell H-J, Marti O, Mlynek J (1992) *Ultramicrosc* 42-44:329
8. Almqvist N, Delamo Y, Smith BL, Thomson NH, Bartholdson A, Lal R, Brzezinski M, Hansma PK (2001) *J Microsc* 202:518
9. Higgins MJ, Crawford SA, Mulvaney P, Wetherbee R (2002) *Protist* 153:25
10. Gebeshuber IC, Kindt JH, Thompson JB, Del Amo Y, Stachelberger H, Brzezinski M, Stucky GD, Morse DE, Hansma PK (2003a) *J Microsc* 212:292
11. Higgins MJ, Sader JE, Mulvaney P, Wetherbee R (2003a) *J Phycol* 39:722
12. Higgins MJ, Molino P, Mulvaney P, Wetherbee R (2003b) *J Phycol* 39:1181
13. Lee Y, Ding Z, Bard AJ (2002) *Anal Chem* 74:3634
14. Hamm CE, Merkel R, Springer O, Jurkojc P, Maier C, Prechtel K, Smetacek V (2003) *Nature* 421:841
15. Arce FT, Avci R, Beech IB, Cooksey KE, Wigglesworth-Cooksey B (2004) *Biophys J* 87(6):4284
16. Solomon B, Taraboulos A, Katchalski-Katzir E (2002) *Conformational diseases: a compendium based on the 1st international workshop on conformational diseases*, S Karger Pub, Tunbridge Wells, UK
17. Dobson CM (2002) *Nature* 418:729
18. Dobson CM (2003) *Nature* 426:884
19. Greulic KO (2004) *Curr Pharmac Biotech* 5:243
20. Viani MB, Pietrasanta LI, Thompson JB, Chand A, Gebeshuber IC, Kindt JH, Richter M, Hansma HG, Hansma PK (2000) *Nature Struct Biol* 7:644
21. Walters DA, Cleveland JP, Thomson NH, Hansma PK, Wendman MA, Gurley G, Elings V (1996) *Rev Sci Instrum* 67:3583
22. Viani MB, Schäffer TE, Chand A, Rief M, Gaub HE, Hansma PK (1999a) *J Appl Phys* 86:2258
23. Viani MB, Schäffer TE, Palocz GT, Pietrasanta LI, Smith BL, Thompson JB, Richter M, Rief M, Gaub HE, Plaxco KW, Cleland AN, Hansma HG, Hansma PK (1999b) *Rev Sci Instrum* 70:4300
24. Braig K, Otwinowski Z, Hegde R, Boisvert DC, Joachimiak A, Horwich AL, Sigler PB (1994) *Nature* 371:578
25. Hunt JF, Weaver AJ, Landry SJ, Gierasch L, Eisenhofer J (1996) *Nature* 379:37
26. Boisvert DC, Wang J, Otiwonowski Z, Horwich AL, Sigler PB (1996) *Nature Struct Biol* 3:170
27. Xu Z, Horwich AL, Sigler PB (1997) *Nature* 388:741
28. Chen S, Roseman AM, Hunter AS, Wood SP, Burston SG, Ranson NA, Clarke AR, Saibil HR (1994) *Nature* 371:261
29. Roseman AM, Chen S, White H, Braig K, Saibil HR (1996) *Cell* 87:241
30. Ziaie B, Baldi A, Atashbar MZ (2004) *Introduction to micro/nanofabrication* In: Bhushan B (ed) *Springer handbook of nanotechnology*. Springer, Berlin Heidelberg New York, p 147

31. Rogers JA (2004) Stamping techniques for micro and nanofabrication: methods and applications. In: Bhushan B (ed) Springer handbook of nanotechnology. Springer, Berlin Heidelberg New York, p 185
32. Arnau A, Aumayr F, Echenique PM, Grether M, Heiland W, Limburg J, Morgenstern R, Roncin P, Schippers S, Schuch R, Stolterfoht N, Varga P, Zouros TJM, Winter HP (1997) Surf Sci Rep 27:113
33. Winter HP, Aumayr F (2002) Europhys News 6:215
34. Sporn M, Libiseller G, Neidhart T, Schmid M, Aumayr F, Winter HP, Varga P, Grether M, Niemann D, Stolterfoht N (1997) Phys Rev Lett 79:945
35. Aumayr F, Burgdörfer J, Varga P, Winter HP (1999) Comm Atom Molecul Phys 34:201
36. Schenkel T, Hamza AV, Barnes AV, DH Schneider (1999) Progr Surf Sci 61:23
37. Hayderer G, Cernusca S, Schmid M, Varga P, Winter HP, Aumayr F, Niemann D, Hoffmann V, Stolterfoht N, Lemell C, Wirtz L, Burgdörfer J (2001) Phys Rev Lett 86:3530
38. Hayderer G, Schmid M, Varga P, Winter HP, Aumayr F, Wirtz L, Lemell C, Burgdörfer J, Hägg L, Reinhold CO (1999) Phys Rev Lett 83:3948
39. Porte L, de Villeneuve CH, Phaner M (1991) J Vac Sci Technol B 9, 1064
40. Coregater R, Claverie A, Chahboun A, Landry V, Ajustron F, Beauvillain J (1992) Surf Sci 262:208
41. You HX, Brown NMD, Al-Assadi KF (1992) Surf Sci 279:189
42. Mazukawa T, Suzuki S, Fukai T, Tanaka T and Ohdomari I (1996) Appl Surf Sci 107:227
43. Mochiji K, Yamamoto S, Shimizu H, Ohtani S, Seguchi T, Kobayashi N (1997) J Appl Phys 82:6037
44. Reimann KP, Bolse W, Geyer U, Lieb KP (1995) Europhys Lett 30:463
45. Habenicht S, Bolse W, Feldermann H, Geyer U, Hofsäss H, Lieb KP, Roccaforte F (2000) Europhys Lett 50:209
46. Neumann R (1999) Nucl Instrum Meth B 151:42
47. Hahn R, Kang K, Song S, J Jeon (1996) Phys Rev B 53:1725
48. Hahn R, Kang K (1999) Phys Rev B 60:600
49. Minniti R, Ratliff LP, Gillaspay JD (2001) Phys Scr T92:22
50. Hayderer G, Cernusca S, Schmid M, Varga P, Winter HP, Aumayr F (2001) Phys Scr T92:156
51. Terada M, Nakamura N, Nakai Y, Kanai Y, Ohtani S, Komaki K, Yamazaki Y (2004) Observation of an HCl-induced nano-dot on an HOPG surface with STM and AFM In: Rudzikas Z (ed) Abstracts HCI-2004 12th international conference on the physics of highly charged ions, European Physical Society, p 208
52. Terada M, Nakamura N, Nakai Y, Kanai Y, Ohtani S, Komaki K, Yamazaki Y (2005) Nucl Instrum Meth Phys Res B 235:452
53. Gebeshuber IC, Cernusca S, Aumayr F and Winter HP (2003) Int J Mass Spectrom 229:27
54. Meguro T, Hida A, Koguchi Y, Miyamoto S, Yamamoto Y, Takai H, Maeda K, Aoyagi Y (2003) Nuc Instrum Meth B 209:170
55. Hida A, Meguro T, Maeda K, Aoyagi Y (2003) Nuc Instrum Meth B 205:736
56. Hahn R, Kang K, Song S, Jeon J (1996) Phys Rev B 53:1725
57. Hahn R, Kang K (1999) Phys Rev B 60:6007
58. Krashennnikov AV, Elsin F (2000) Surf Sci 519:454
59. Winter HP, Aumayr F (1999) J Phys B: At Mol Opt Phys 32: R39
60. Ziegler JF, Biersack JP, Littmark U (1985) The stopping and range of ions in matter 1. Pergamon, New York
61. Hersam MC and Chung Y-W (2003) Proc Natl Acad Sci 100:12531
62. Albrecht TR and Quate CF (1988) J Vac Sci Technol A 6:271
63. Morita S, Wiesendanger R, Meyer E (2002) (eds) Noncontact atomic force microscopy. Springer, New York

64. Giessibl FJ (2003) *Rev Mod Phys* 75:949
65. Hölscher H, Allers W, Schwarz UD, Schwarz A, Wiesendanger R (2000) *Phys Rev B* 62:6967
66. Hembacher S, Giessibl FJ, Mannhart J, Quate CF (2003) *Proc Nat Acad Sci* 100:12539
67. Bitensky IS, Murakhmetov MN, Parilis ES (1979) *Sov Phys Tech Phys* 25:618
68. Schneider DH, Briere MA, McDonald J, Biersack J (1993) *Radiat Eff Def Sol* 127:113
69. Hayderer G, Schmid M, Varga P, Winter HP, Aumayr F (1999) *Rev Sci Instrum* 70:3696
70. Townsend P (1983) In: Behrisch R (ed) *Sputtering by particle bombardment II*. Berlin, Heidelberg, New York, p 147
71. Varga P, Neidhard T, Sporn M, Libiseller G, Schmid M, Aumayr F, Winter HP (1997) *Phys Scr T73*:307
72. Leitner M, Wutte D, Brandstötter J, Aumayr F, Winter HP (1994) *Rev Sci Instrum* 65:1091
73. Bedrossian PJ, de la Rubia TD (1998) *J Vac Sci Technol A* 16:1043
74. Giessibl FJ, Hembacher S, Bielefeldt H, Mannhart J (2000) *Science* 289:422
75. Duke CB (1996) *Chem Rev* 96:1237
76. Hug HJ, Lantz MA, Abdurixit A, van Schendel PJA, Hoffmann R, Kappenberger P, Baratoff A, Giessibl FJ, Hembacher S, Bielefeldt H, Mannhart J (2001) *Science* 291:2509
77. Huang M, Cuma M, Liu F (2003) *Phys Rev Lett* 90:256101
78. Hembacher S, Giessibl FJ, Mannhart J (2004) *Science* 305:380
79. Manassen Y, Hamers RJ, Demuth JE, Castellano AJ jun (1989) *Phys Rev Lett* 62:2531
80. Durkan C, Welland ME (2002) *Appl Phys Lett* 80:458
81. Wrachtrup J, von Borczyskowski C, Bernard J, Orritt M, Brown R (1993) *Nature* 363:244
82. Köhler J, Disselhorst JAJM, Donckers MCJM, Groenen EJJ, Schmidt J, Moerner WE (1993) *Nature* 363:242
83. Jelezko F, Popa I, Gruber A, Tietz C, Wrachtrup J, Nizovtsev A, Kilin S (2002) *Appl Phys Lett* 81:2160
84. Elzerman JM, Hanson R, Willems van Beveren LH, Witkamp B, Vandersypen LMK, Kouwenhoven LP (2004) *Nature* 430:431
85. Xiao M, Martin I, Yablonovitch E, Jiang HW (2004) *Nature* 430:435
86. Rugar D, Budakian R, Mamin HJ, Chui BW (2004) *Nature* 430:329
87. Balatsky AV, Martin I (2002) *Quant Inf Proc* 1:355
88. Manoharan HC (2002) *Nature* 416:24
89. Sidles JA (1991) *Appl Phys Lett* 58:2854
90. Rugar D, Yannoni CS, Sidles JA (1992) *Nature* 360:563
91. Sidles JA (1992) *Phys Rev Lett* 68:1124
92. Sidles JA, Garbini JL, Bruland KJ, Rugar D, Züger O, Hoen S, Yannoni CS (1995) *Rev Mod Phys* 67:249
93. Hammel PC, Pelekhov DV, Wigen PE, Gosnell TR, Midzor MM, Roukes ML (2003) *Proc IEEE* 91:789
94. Mozyrsky D, Martina I, Pelekhov D, PC Hammel (2003) *Appl Phys Lett* 82:1278
95. Ciobanu L, Seeber DA, Pennington CH (2002) *J Magn Reson* 158:178
96. Blank A, Dunnam CR, Borbat PP, Freed JH (2003) *J Magn Reson* 165:11
97. Stokstad E (2004) *Science* 305:322
98. Berman GP, Doolen GD, Hammel PC, Tsifrinovich VI (2000) *Phys Rev B* 61:14694
99. Pelekhov DV, Martin I, Suter A, Reagor, DW, Hammel PC (2002) *Proc SPIE* 4656:1

A.2 Probing protein-protein interactions in real time

Viani M.B., Pietrasanta L.I., Thompson J.B., Chand A., **Gebeshuber I.C.**, Kindt J.H., Richter M., Hansma H.G. and Hansma P.K.

Nature Structural Biology 7, 644-647 (2000)

Abstract

We have used a prototype small cantilever atomic force microscope to observe, in real time, the interactions between individual protein molecules. In particular, we have observed individual molecules of the chaperonin protein GroES binding to and then dissociating from individual GroEL proteins, which were immobilized on a mica support. This work suggests that the small cantilever atomic force microscope is a useful tool for studying protein dynamics at the single molecule level.

Probing protein–protein interactions in real time

Mario B. Viani, Lia I. Pietrasanta, James B. Thompson, Ami Chand, Ilse C. Gebeshuber, Johannes H. Kindt, Michael Richter, Helen G. Hansma and Paul K. Hansma

Department of Physics, University of California at Santa Barbara, Santa Barbara, California 93106, USA.

We have used a prototype small cantilever atomic force microscope to observe, in real time, the interactions between individual protein molecules. In particular, we have observed individual molecules of the chaperonin protein GroES binding to and then dissociating from individual GroEL proteins, which were immobilized on a mica support. This work suggests that the small cantilever atomic force microscope is a useful tool for studying protein dynamics at the single molecule level.

The atomic force microscope (AFM) has proven to be a useful tool for studying proteins at the single molecule level. In particular, the AFM has been used to measure both structural^{1–3} and mechanical properties^{4–6} of individual proteins in physiologically relevant buffers. The AFM has also been used, to a lesser extent, to observe the activity of individual proteins by detecting protein motion^{7,8}. These studies have been restricted, in part, by both the noise and speed limitations of the AFM. Recently, however, it has been shown that small cantilever AFMs can be used for making faster and quieter measurements⁹. In this work, we used a small cantilever AFM¹⁰ to observe individual protein interactions. We have observed, in real time, individual *Escherichia coli* GroES proteins binding to and then subsequently dissociating from individual *E. coli* GroEL proteins. This work suggests that the small cantilever AFM is a useful tool for studying protein dynamics at the single molecule level.

The *E. coli* chaperonin GroEL and its co-chaperonin GroES play important roles in helping proteins reach their native states. GroEL and GroES work together in a series of ATP-mediated steps to capture misfolded proteins, free them from local energy minima, and finally provide them with an environment conducive to folding to their native states^{11–14}. Both X-ray crystallography^{15–18} and cryoelectron microscopy^{19,20} studies have been used to resolve the structures of GroEL and the GroEL–GroES complex in different stages of the folding cycle. The time dependence of the folding cycle has been probed in bulk samples by experiments that employ hydrogen exchange²¹, fluorescence techniques^{22–25}, and surface plasmon resonance²⁶.

The surface plasmon resonance studies²⁶ demonstrate that GroEL proteins adsorbed onto a support still retain their ability to bind and release GroES. This observation led us to believe that it would be possible to observe the interaction between GroEL and GroES with an AFM. Previous AFM studies of the chaperonin system by Mou *et al.*^{1,2} used contact mode (in which the tip scans

the sample at constant force) to obtain high resolution static images of both GroEL and GroES adsorbed to mica in solution. In these studies, the authors state that it was often difficult to image the proteins more than once, unless they had been treated with a fixative such as glutaraldehyde. This is consistent with our experiences with commercial AFMs. In our study reported here, we used a prototype AFM¹⁰ designed to work with small cantilevers (Fig. 1a), which can image both GroEL and the GroEL–GroES complex in solution repeatedly without the aid of fixing agents. This led us to try to observe the association and dissociation of individual GroEL–GroES complexes.

Imaging GroEL and GroEL–GroES

A small cantilever AFM image of a monolayer of GroEL molecules in buffer solution is shown in Fig. 1b. The central channel of the protein ring can be resolved on many of the molecules, which is consistent with previous AFM observations that GroEL adsorbs to mica in an end-up orientation¹. The average diameter of the molecules in this image is 14.6 ± 2.2 nm, which agrees well with both X-ray¹⁵ and cryoelectron microscopy¹⁹ data. Upon the addition of GroES and ADP into the buffer solution, GroES molecules were observed as features that extend ~3 nm higher than the GroEL film (Fig. 2). The height of these features is also consistent with X-ray crystallography^{15–18} and cryoelectron microscopy¹⁹ data. We were able to repeatedly scan the same sample region without excessively disturbing the GroEL–GroES complexes. This is demonstrated in Fig. 2, which shows the first and last of seven consecutive scans of the same sample region. Most of the GroES proteins remain attached to the GroEL film at the same location throughout the scanning. To verify that the interactions between GroES and GroEL were specific, we also tried adding GroES to the buffer without ADP. In this case, we did not observe any GroES molecules binding to the GroEL film, which is consistent with solution experiments that have shown that GroEL and GroES do not interact in the absence of nucleotides.

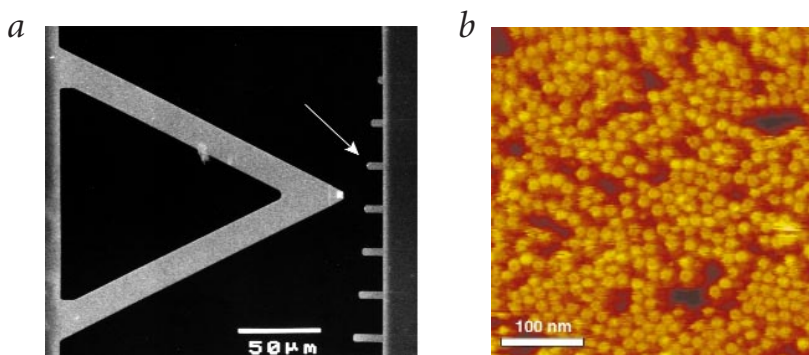


Fig. 1 Small cantilevers and image of GroEL taken with the small cantilever AFM. **a**, This scanning electron micrograph shows an array of prototype small cantilevers (on the right) next to a commercially available cantilever. Compared to commercially available cantilevers, for a given spring constant, small cantilevers yield higher resonant frequencies, thereby allowing faster measurements. They also are able to detect smaller forces than larger cantilevers⁹. The results reported here were obtained using cantilevers similar to the one indicated by the arrow. This cantilever has approximately the same spring constant as the commercial cantilever and a resonant frequency 30 times greater. Our prototype microscope¹⁰ can use small cantilevers because it focuses the laser beam onto the cantilever with a spot diameter of ~3 μ m (compared to ~20 μ m in commercial microscopes). **b**, This height image of GroEL adsorbed on mica in buffer solution (full height scale, from black to yellow, is 15 nm) was taken by running our small cantilever AFM in tapping mode. The central channels of the GroEL molecules are visible as a dark region at the center of a bright ring. These fields of densely packed molecules could be imaged repeatedly with small cantilevers. The image (256 \times 256 pixels) was taken with a scan rate of 10.2 Hz.

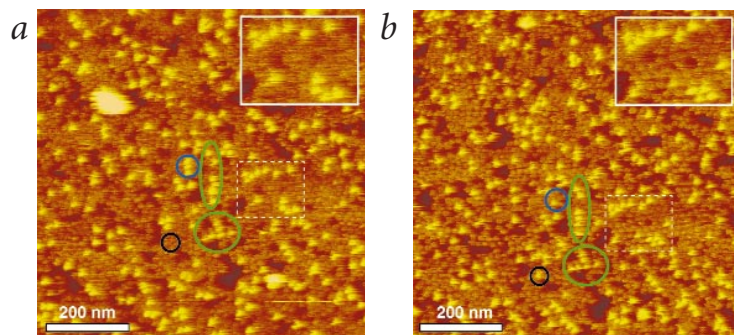


Fig. 2 GroEL and isolated GroEL–GroES complexes in buffer solution on a mica support. **a,b** The first and last images, respectively, of seven consecutive images of a film of GroEL with isolated GroEL–GroES complexes. The GroES can be seen as the bright (that is, tall) features that extend above the level of the GroEL film. The GroEL–GroES complexes are ~3 nm taller than the surrounding film. Note that most of the GroES proteins remained attached to the film in the same location. For example, the green ellipses identify two groups of molecules that are present in both images. The black circle identifies a molecule that has attached at some time after the original image was captured. The blue circle highlights three molecules in which two become unbound before the final image. The insets (upper right corner of each image) provide enlarged views of the sample region inside the (dashed) box. The final concentrations of GroES and ADP in the buffer solution were 100 nM and 0.2 mM.

Although small cantilever AFMs are able to scan biological samples such as DNA much faster than conventional AFMs¹⁰, we found that we were unable to scan the GroEL–GroES complex (which is much more fragile than DNA) with tip speeds much faster than $20 \mu\text{m s}^{-1}$ due to the limited bandwidth of the feedback electronics. Therefore, in order to obtain the temporal resolution required for observing the formation and dissociation of the GroEL–GroES complexes in the presence of Mg-ATP, we scanned the sample in one dimension rather than two. By repeatedly scanning a single line across the sample we were able to monitor the height of a series of protein molecules at rates as high as 20 Hz. This method⁸ is illustrated in Fig. 3, which shows an image of GroEL molecules in buffer in which the slow scan axis was disabled half way through the scan. From this image it is clear that each ‘tube’ is associated with a single protein molecule. The height variations along the length of the tubes reflect the time dependent changes in the protein structure.

GroEL–GroES complex formation and dissociation

The images of the tubes shown in Figs 3 and 4a were taken in a buffer solution that did not contain Mg-ATP or GroES. Under these conditions we typically observed root mean square height variations of ~0.5 nm (Fig. 4b). However, upon the addition of both GroES and Mg-ATP, we observed that many of the tubes displayed repetitive well-defined step-like variations in height (Fig. 4c). The cross section of the two featured tubes clearly shows the step-like variations in height (Fig. 4d). The magnitude of these steps is 3.6 ± 1 nm. This is consistent with the height difference measured between structures of GroEL and the GroEL–GroES complex obtained by X-ray crystallography^{15–18} and cryoelectron microscopy¹⁹ studies. We therefore conclude that the observed height variations are caused by a GroES molecule attaching to and then separating from the GroEL molecule associated with the tube. It is important to emphasize that we observed these step-like variations in height only when the buffer solution contained both GroES and Mg-ATP. This implies that the height fluctuations we observed in

the presence of Mg-ATP and GroES are caused by complex formation and not by nonspecific interactions between GroEL and GroES, or by Mg-ATP activated motion of the GroEL.

In repeated experiments, we identified multiple tubes in which we saw two or more cycles of complex formation and dissociation. In one case, we recorded an active molecule for ~2 min and saw the complex form and dissociate 18 times. A histogram of the complex lifetime for this molecule is shown in Fig. 5. The distribution of complex lifetime is peaked near 5 s and the average lifetime is $\sim 7 \pm 1$ s ($n = 18$). This distribution is representative of all active molecules that we observed.

Control experiment

To quantify the effect that tip–sample interactions were having on the measured complex lifetimes, we performed the following control experiment. First GroE complex lifetimes were measured in the presence of ADP alone (0.2 mM). After acquiring data for ~30 min, Mg-ATP was added to the buffer (making the concentrations of Mg-ATP and ADP 2.5 mM and 0.14 mM, respectively) and the complex lifetimes were re-measured. After adding the Mg-ATP to the buffer, the lifetime of the complex had a distribution similar to what is shown in Fig. 5. However, in the presence of ADP alone, the complex lifetime was much longer. In fact, a majority of the ADP complexes did not dissociate at all within the time of observation. (Our current observation time was limited by thermal drift of the microscope and was usually on the order of one minute.) From bulk measurements, the half-life of the complex in the presence of ADP has been shown to be ~4 h²⁶. We observed, however, that a small percentage (< 10%) of complexes had lifetimes < 30 s. We hypothesize that this small percentage of events may reflect the effects of tip–sample interactions. We cannot, however, rule out the possibility of short complex lifetimes, in the presence of ADP, for some of the molecules based on our data alone.

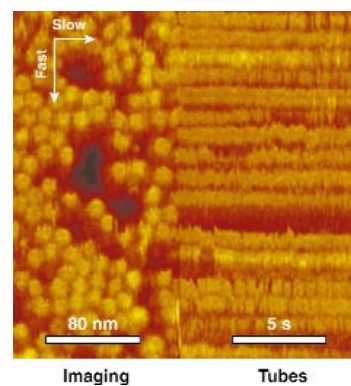
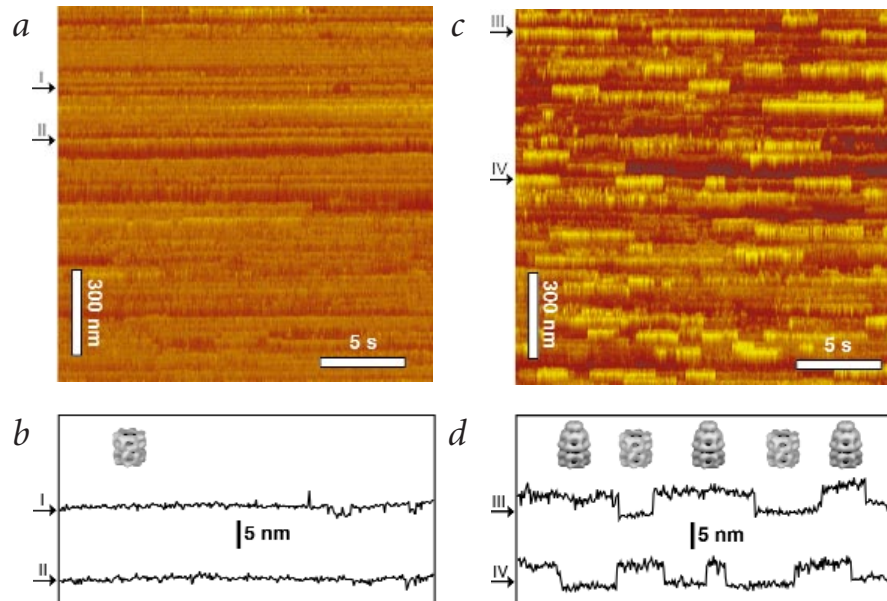


Fig. 3 GroEL scanned in two dimensions (left) and in one dimension (right). In this image of GroEL, the slow scan axis was disabled half way through the scan. After the slow scan axis was disabled, the tip repeatedly scanned the same line of proteins, thereby generating protein ‘tubes’. Each tube corresponds to an individual protein molecule. The advantage of recording tubes is that it is possible to monitor the heights of molecules at much higher temporal resolution (100 ms here) than allowable with conventional imaging in two dimensions (25 s here) because the rest of the field does not need to be imaged before returning to the molecules of interest. The long and short arrows indicate the directions of the fast and slow scan axes respectively.

Fig. 4 Association and dissociation of the GroEL–GroES complex. **a**, These tubes of GroEL were scanned at 15.3 Hz in buffer solution that did not contain GroES. **b**, The cross sections of two selected tubes show typical height fluctuations. The first cross section shows some structure towards the right end of the trace that is probably caused by the protein being pushed around by the tip. **c**, After the addition of GroES (144 nM) and Mg-ATP (2.5 mM) into the buffer solution, we observed large repeated variations in height along the lengths of many tubes. **d**, The cross sections of these tubes show the height stepping between two values that differed by 3.6 ± 1 nm. This height variation is consistent with the height differences seen between GroEL and the GroEL–GroES complex in cryoelectron microscopy and X-ray crystallographic data. Therefore, we conclude that we are observing the association and dissociation of the complex at the single molecule level. This is depicted with the aid of cryoelectron microscopy images of GroEL and the GroEL–GroES complex reported by Roseman *et al.*²⁰.



Immobilized GroEL is a model system

The GroE system studied here is a model system that differs from solution experiments because the GroEL is adsorbed onto a support, thereby making one of the GroEL rings inaccessible to GroES. However, pioneering work on this type of model system has established its relevance. Burston *et al.*²⁷ showed that a modified mixed-ring GroEL protein, in which one of the rings was unable to bind GroES or substrate polypeptides, showed kinetics for the refolding of rhodanese that were identical to those of the wild type GroEL. It is not essential, therefore, for both rings of GroEL to be accessible to GroES in order for the protein to retain its normal activity. This conclusion is also supported by Hayer-Hartl *et al.*²⁶, who showed through surface plasma resonance experiments that the immobilization of the GroEL proteins on a support did not destroy their functional properties.

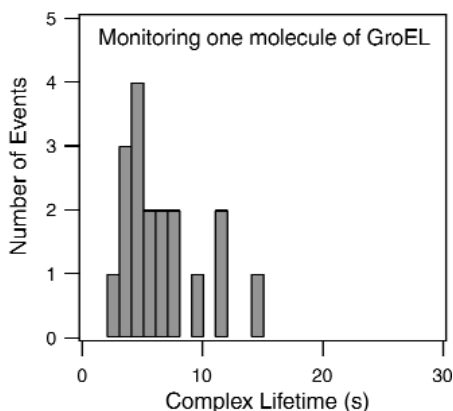


Fig. 5 Measured complex lifetime of an individual GroEL molecule in the presence of Mg-ATP and GroES. We observed individual GroES molecules attach to and then separate from the same GroEL molecule 18 times over an observation time of ~2 min. This histogram shows the distribution of complex lifetimes that we measured during the observation time. Note the absence of events with lifetimes < 2 s. As pointed out by Lu *et al.*³⁴, a non-exponential distribution can be expected when there are one or more intermediate steps in a process, even when all individual steps are exponential.

Comparison to bulk experiments

The distribution of the lifetimes of the complex is peaked near 5 s, which is significantly shorter than lifetimes determined from bulk measurements (15–30 s; refs 25,26,28). The difference in measured lifetimes may be caused by differences in the experimental conditions, such as the immobilization of GroEL. However, we also note that comparing results of the bulk experiments to results of these single molecule experiments is problematic. For example, many of the bulk experiments measured lifetimes for an ensemble of proteins with an unknown distribution of initial states, whereas these experiments measured lifetimes of single molecules with a well-defined initial state. Another problem is that bulk experiments and single molecule experiments do not measure the same functional form for the distribution of complex lifetimes: the bulk experiments measure an exponential distribution while these single molecule experiments measure a non-exponential distribution.

Finally, we note that the distribution of complex lifetimes we measured agrees well with the distribution measured in the only other single molecule study of the GroE system of which we are currently aware. Taguchi *et al.*²⁹ reported a non-exponential distribution for the complex lifetimes peaked at 5 s, which they measured using a single molecule fluorescence technique. This is significant because the distribution that Taguchi *et al.* measured is similar to the distribution that we measured (Fig. 5), despite completely different experimental techniques (optical fluorescence *versus* AFM) and different orientations of the GroEL molecules (sideways *versus* end-up) on different supports (glass *versus* mica).

Our experiments demonstrate the possibility of using the small cantilever AFM as a tool for studying the dynamics of single proteins. This technique will augment other single molecule methods that use optical techniques, by allowing real time measurements of length changes associated with protein activity.

Methods

Imaging. All imaging was performed in a prototype AFM designed to be used with small cantilevers^{9,10,30–32}. The prototype AFM detects the motion of small cantilevers by using high numerical aperture

optics to focus a laser beam onto the cantilever and then measuring angular changes in the reflected light beam. The cantilevers (Fig. 1) were fabricated out of low stress silicon nitride using standard micro-machining techniques⁹. The cantilevers used were typically 10 μm long, 5 μm wide, and 75 nm thick. Each cantilever had an electron beam deposited tip that was 1–2 μm long. The spring constants were approximately 60–120 pN nm⁻¹ and the resonant frequencies in water were 130–200 kHz. All imaging was done in tapping mode³³ to minimize sample damage. The tapping frequency was usually chosen to be 130 kHz and the free amplitude of oscillation was set to 10–20 nm. All imaging was performed at ambient temperature.

Sample preparation. GroEL was purified from overexpression in *E. coli* (SIGMA) and reconstituted to 1 mg ml⁻¹ (50 mM Tris, 150 mM KCl, 10 mM MgCl₂, 1 mM dithiothreitol (DTT) and 2.5% (w/v) trehalose, pH 7.5). The samples were prepared for imaging by applying a 10 μL drop of GroEL solution to freshly cleaved mica. After incubation at room temperature for ~30 min, the sample was rinsed with buffer (50 mM HEPES (pH 7.5), 50 mM KCl and 10 mM MgCl₂) to remove loosely bound GroEL proteins, and then imaged in this same buffer. The GroES was purified from overexpression in *E. coli* (SIGMA) and reconstituted to 0.25 mg ml⁻¹ (25 mM Tris, 75 mM KCl, 0.5 mM DTT and 1.25% (w/v) trehalose, pH 7.5) and diluted in buffer (50 mM HEPES (pH 7.5), 50 mM KCl and 10 mM MgCl₂).

Acknowledgments

We thank G. Lorimer for his encouragement and many useful suggestions. We thank H. Saibil for her generous permission to use the cryo-electron microscopy images of GroEL and the GroEL–GroES complex. The Materials Research Division and the Molecular Biophysics Division of the National Science Foundation supported this work.

Correspondence and requests for materials should be addressed to M.B.V. *email:* viani@physics.ucsb.edu

Received 24 May, 2000; accepted 23 June, 2000.

- Mou, J., Sheng, S. J., Ho, R. & Shao, Z. *Biophys. J.* **71**, 2213–2221 (1996).
- Mou, J., Czajkowski, D.M., Sheng, S.J., Ho, R. & Shao, Z. *FEBS Lett.* **381**, 161–164 (1996).
- Muller, D.J. & Engel, A.J. *Mol. Biol.* **285**, 1347–1351 (1999).
- Rief, M., Gautel, M., Oesterhelt, F., Fernandez, J.M. & Gaub, H.E. *Science* **276**, 1109–1112 (1997).
- Oberhauser, A.F., Marszalek, P.E., Carrion-Vazquez, M. & Fernandez, J.M. *Nature Struct. Biol.* **6**, 1025–1028 (1999).
- Oesterhelt, F. *et al. Science* **288**, 143–146 (2000).
- Radmacher, M., Fritz, M., Hansma, H.G. & Hansma, P.K. *Science* **265**, 1577–1579 (1994).
- Thomson, N.H. *et al. Biophys. J.* **70**, 2421–2431 (1996).
- Viani, M.B. *et al. J. Appl. Phys.* **86**, 2258–2262 (1999).
- Viani, M.B. *et al. Rev. Sci. Instrum.* **70**, 4300–4303 (1999).
- Hartl, F.-U. *Nature* **381**, 571–580 (1996).
- Ranson, N.A., White, H.E. & Saibil, H.R. *Biochem. J.* **333**, 233–242 (1998).
- Sigler, P.B. *et al. Annu. Rev. Biochem.* **67**, 581–608 (1998).
- Fink, A.L. *Physiol. Rev.* **79**, 425–449 (1999).
- Braig, K. *et al. Nature* **371**, 578–586 (1994).
- Hunt, J.F., Weaver, A.J., Landry, S.J., Gierasch, L. & Eisenhofer, J. *Nature* **379**, 37–45 (1996).
- Boisvert, D.C., Wang, J., Otiwonowski, Z., Horwich, A.L. & Sigler, P.B. *Nature Struct. Biol.* **3**, 170–177 (1996).
- Xu, Z., Horwich, A.L. & Sigler, P.B. *Nature* **388**, 741–750 (1997).
- Chen, A. *et al. Nature* **371**, 261–264 (1994).
- Roseman, A.M., Chen, S., White, H., Braig, K. & Saibil, H.R. *Cell* **87**, 241–251 (1996).
- Shtilerman, M., Lorimer, G.H. & Englander, S.W. *Science* **284**, 822–825 (1999).
- Weissman, J.S. *et al. Cell* **83**, 577–587 (1995).
- Sparrer, H., Lilie, H. & Buchner, J. *J. Mol. Biol.* **258**, 74–87 (1996).
- Rye, H.S. *et al. Nature* **388**, 792–798 (1997).
- Rye, H.S. *et al. Cell* **97**, 325–338 (1999).
- Hayer-Hartl, M.K., Martin, J. & Hartl, F.-U. *Science* **269**, 836–841 (1995).
- Burston, S.G., Weissman, J.S., Farr, G.W., Fenton, W.A. & Horwich, A.L. *Nature* **383**, 96–99 (1996).
- Burston, S.G., Ranson, N.A. & Clarke, A.R. *J. Mol. Biol.* **249**, 138–152 (1995).
- Taguchi, H., Tadakuma, H., Ueno, T., Yoshida, M. & Funatsu, T. *Biophys. J.* **78**, 36A (2000).
- Walters, D.A. *et al. Rev. Sci. Instrum.* **67**, 3583–3590 (1996).
- Schaffer, T.E. *et al. Proc. SPIE* **3009**, 48–52 (1997).
- Walters, D.A. *et al. Proc. SPIE* **3009**, 43–47 (1997).
- Hansma, P.K. *et al. Appl. Phys. Lett.* **64**, 1738–1740 (1994).
- Lu, H. P., Xun, L. & Xie, X. S. *Science* **282**, 1877–1881 (1998).

A.3 Atomic force microscopy study of living diatoms in ambient conditions

Gebeshuber I.C., Kindt J.H., Thompson J.B., Del Amo Y., Stachelberger H., Brzezinski M., Stucky G.D., Morse D.E. and Hansma P.K.

J. Microsc. 212, 292-299 (2003) (incl. title page)

Abstract

We present the first in vivo study of diatoms using atomic force microscopy (AFM). Three chain-forming, benthic freshwater species - *Eunotia sudetica*, *Navicula seminulum* and a yet unidentified species - are directly imaged while growing on glass slides. Using the AFM, we imaged the topography of the diatom frustules at the nanometre range scale and we determined the thickness of the organic case enveloping the siliceous skeleton of the cell (10 nm). Imaging proved to be stable for several hours, thereby offering the possibility to study long-term dynamic changes, such as biomineralization or cell movement, as they occur. We also focused on the natural adhesives produced by these unicellular organisms to adhere to other cells or the substratum. Most man-made adhesives fail in wet conditions, owing to chemical modification of the adhesive or its substrate. Diatoms produce adhesives that are extremely strong and robust both in fresh- and in seawater environments. Our phase-imaging and force-pulling experiments reveal the characteristics of these natural adhesives that might be of use in designing man-made analogues that function in wet environments. Engineering stable underwater adhesives currently poses a major technical challenge.

Journal of

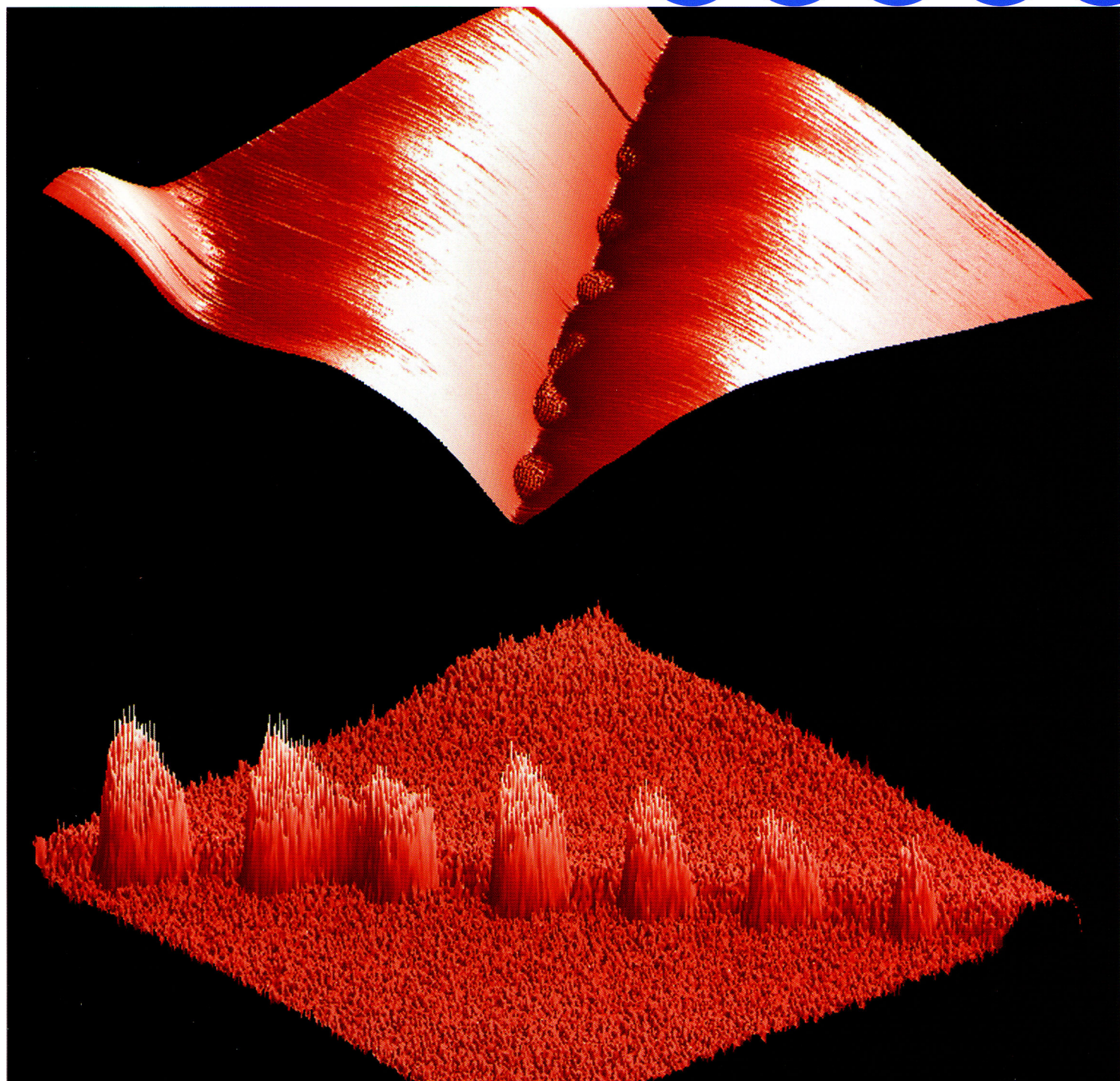
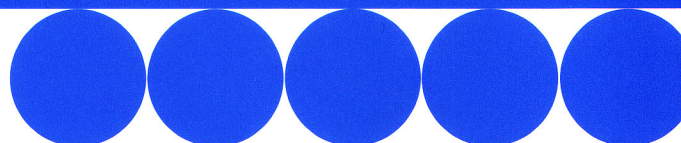
ISSN 0022-2720

81

Microscopy

Blackwell Publishing

Volume 212, Part 3, December 2003



Atomic force microscopy study of living diatoms in ambient conditions

I. C. GEBESHUBER*, J. H. KINDT†, J. B. THOMPSON†,
Y. DEL AMO‡, H. STACHELBERGER§, M. A. BRZEZINSKI¶,
G. D. STUCKY**, D. E. MORSE†† & P. K. HANSMA†

*Austrian Center of Competence for Tribology AC 2T Research GmbH, Viktor-Kaplan-Strasse 2, A-2700 Wiener Neustadt, Austria and Institut für Allgemeine Physik, Technische Universität Wien, Wiedner Hauptstr. 8–10, A-1040 Vienna, Austria

†Department of Physics, ¶Department of Ecology, Evolution and Marine Biology & Marine Science Institute, **Department of Chemistry and Materials, and ††Department of Molecular, Cellular, and Developmental Biology & Marine Science Institute, University of California at Santa Barbara, CA 93106, U.S.A.

‡Laboratoire Océanographique Biologique, Station Marine d'Arachon, 2 rue du Professeur Jolyet, Université Bordeaux, 33120 Arachon, France

§Institute of Chemical Engineering, Technische Universität Wien, Getreidemarkt 9/1667, A-1060 Vienna, Austria

Key words. AFM, atomic force microscopy, biogenic glass, biomimetics, diatoms, natural adhesives, natural lubricants, naturally nanostructured biomaterials.

Summary

We present the first *in vivo* study of diatoms using atomic force microscopy (AFM). Three chain-forming, benthic freshwater species – *Eunotia sudetica*, *Navicula seminulum* and a yet unidentified species – are directly imaged while growing on glass slides. Using the AFM, we imaged the topography of the diatom frustules at the nanometre range scale and we determined the thickness of the organic case enveloping the siliceous skeleton of the cell (10 nm). Imaging proved to be stable for several hours, thereby offering the possibility to study long-term dynamic changes, such as biomineralization or cell movement, as they occur. We also focused on the natural adhesives produced by these unicellular organisms to adhere to other cells or the substratum. Most man-made adhesives fail in wet conditions, owing to chemical modification of the adhesive or its substrate. Diatoms produce adhesives that are extremely strong and robust both in fresh- and in seawater environments. Our phase-imaging and force-pulling experiments reveal the characteristics of these natural adhesives that might be of use in designing man-made analogues that function in wet environments. Engineering stable underwater adhesives currently poses a major technical challenge.

Introduction

Diatoms are unicellular microalgae with a cell wall consisting of a siliceous skeleton enveloped by an organic case essentially composed of polysaccharides and proteins (Hecky *et al.*, 1973). The cell walls form a pillbox-like shell (called the frustule) consisting of two valves that fit within each other with the help of a set of girdle bands. Frustules vary greatly in shape, ranging from box-shaped to cylindrical; they can be symmetrical as well as asymmetrical and exhibit an amazing diversity of nanostructured frameworks (Fig. 1).

Diatoms are found in both freshwater and marine environments, as well as in moist soils, and on moist surfaces. They are either freely floating (planktonic forms) or attached to a substrate (benthic forms), and some species may form chains of cells of varying length. Individual diatoms range from 2 µm up to several millimetres in size, although only few species are larger than 200 µm. Diatoms as a group are very diverse with 12 000–60 000 species reported (Werner, 1977; Gordon & Drum, 1994).

Currently, human chemical synthesis cannot produce siliceous structures with the hierarchical structural detail of the diatom frustules nor can ordered siliceous structures be produced synthetically under the benign conditions of diatom biomineralization. Biosilicification occurs at ambient temperatures and pressures, whereas artificial chemical synthesis of silica-based materials (e.g. resins, molecular sieves and catalysts) requires extreme conditions of temperature, pressure and pH.

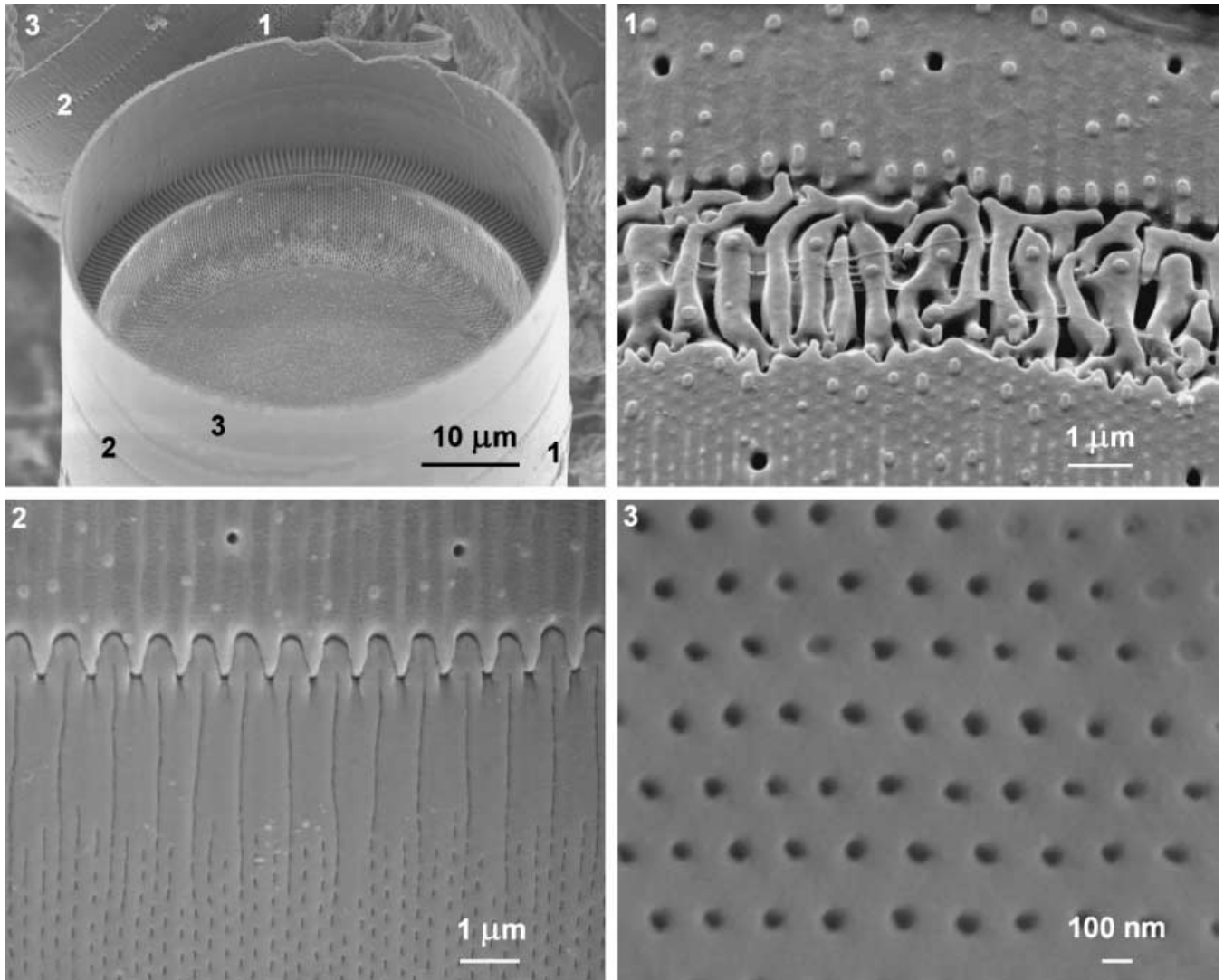


Fig. 1. Diatoms are unicellular organisms whose surface comprises nanostructured amorphous glass. Scanning electron micrographs of frustules of *Ellerbeckia arenaria*, a freshwater diatom, reveal amazingly beautiful and diverse details on a single cell (diatoms collected in Salzburg and kindly supplied by A. M. Schmid). The 'tower of life' (top left), the 'holy syllable OM written in glass' (top right), 'microman' complete with eyes, teeth and beard (bottom left) and nearly perfect hexagonal patterns (bottom right). The images on the top right and bottom are magnified regions denoted by the respective numbers in the top left image.

Linder *et al.* (1992) presented the first atomic force microscopy (AFM) study of diatoms. The surface structure of six different diatom species collected from a mud sample was imaged after the cells had been briefly rinsed with ethanol to kill, clean and immobilize them. In contrast to these still images, the present study demonstrates for the first time the ability to image living diatoms using the AFM. In contrast to conventional scanning electron microscopy (SEM), the samples do not have to be covered with an electrically conductive layer. Furthermore, the AFM allows for investigations of micromechanical properties of the cell surface, for example viscoelastic properties, adhesion forces and hardness measurements. Further advantages of AFM are effortless sample

preparation and unprecedented resolution on insulating materials.

The results from this AFM study provide important basic information to researchers working in biomimetics. Biomimetics is a new interdisciplinary research field seeking to understand the relationships between structures and functions of biological composite systems in order to design and synthesize new materials, possibly without the toxic residues characteristic of non-biological modes of industrial mass production (Mann, 1993; Sarikaya, 1994). Understanding the processes involved in biomineralization may eventually allow us to mimic these structures and produce optimized materials with minimal environmental impact.

Materials and methods

Imaging with the AFM requires a means of firmly attaching the sample to a 'holder' to permit stable scanning. Linder *et al.* (1992) and Almqvist *et al.* (2001) fixed dead diatoms to their respective sample holders. We used a different approach. By following a simple and effective strategy, we 'naturally selected' AFM-compatible diatom species from a number of species living in a freshwater aquarium. For that purpose, freshwater aquarium plants covered with benthic diatoms were placed in a jar filled with water, as well as two left-handed European freshwater snail species, *Physa fontinalis* and *Planorbarius corneus*, and some glass slides. In the following 3 weeks, the diatoms colonized the jar and the glass slides. The snails were feeding on the diatoms, predominantly leaving three species behind, which obviously strongly attached to the substrate: *Eunotia sudetica* (a diatom species that is abundant in acidic ponds but absent in alkaline environments; Beakes *et al.*, 1988), *Navicula seminulum* and a yet unidentified species. The glass slides were then transferred to an Si-enriched diatom growth solution (Diatom Medium, Culture Collection of Algae and Protozoa, Cumbria, U.K.; Beakes *et al.*, 1988) in order selectively to favour diatom growth, until they densely populated each slide. New samples can be prepared by adding clean glass slides and allowing the cells to colonize the new surface for about 2 weeks. Before imaging, the glass slides are rinsed with tap water to remove any green algae and debris.

Sample holders are vacuum mounted on a Zeiss Axiovert inverted microscope. Imaging is performed in tap water or diatom medium with a Digital Instruments BioScope with

Nanoscope Controller Phase Extension Box (Digital Instruments, Santa Barbara, CA, U.S.A.) and a home-made tapping-mode fluid cell. Engaging the cantilever (Si_3N_4 , spring constant $k = 0.06 \text{ N m}^{-1}$ and 0.12 N m^{-1} , Digital Instruments) takes place under optical control (the largest cells are about $50 \mu\text{m}$ in length and therefore easily visible in the inverted microscope).

Results and discussion

The AFM-compatible benthic freshwater diatom species selected by our 'natural selection' strategy are *Navicula seminulum* and *Eunotia sudetica* and a yet unidentified species. The natural adhesives of these cells, which attach them to the substrate as well as to each other (all of them are colonial forms), prove to be sufficiently strong that stable AFM imaging conditions are achieved without further sample preparation. The cells are imaged in their culture medium or in tap water while they are still growing on the glass slides. Tapping-mode as well as contact-mode imaging is easy to achieve as long as engaging the cantilever takes place on the cell surface. Engaging the cantilever on the glass slide might lead to problems with the z-range of the piezo, because the height of the cells can be several tens of micrometres, which might exceed maximum piezo extension.

Cell wall topography of living diatoms

Navicula seminulum grows in stacks of cells pointing out from the glass slide. These chains of cells can be about 10 cells high, as investigated by SEM (data not shown). Figure 2 reveals

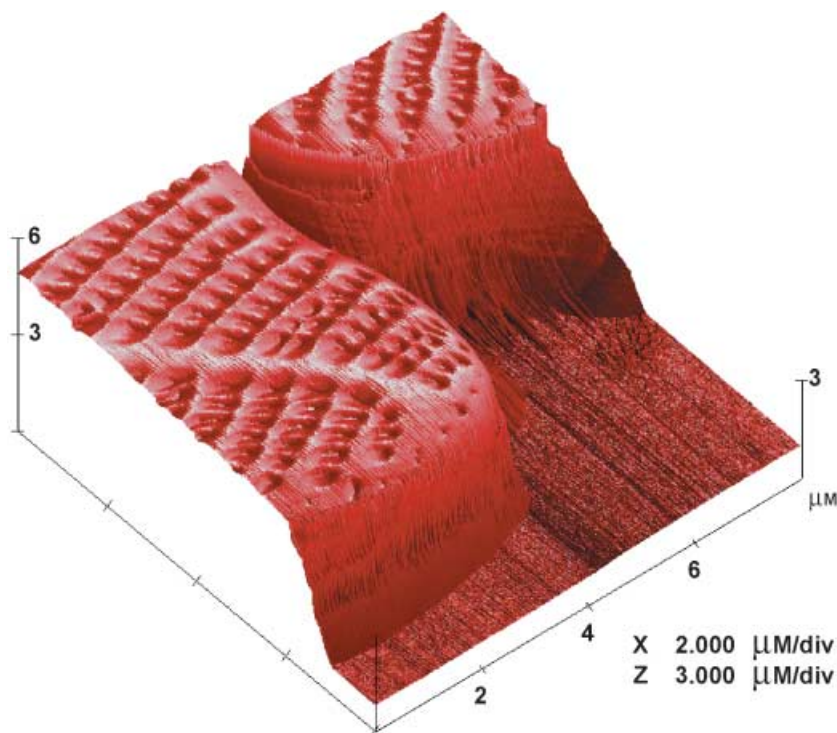


Fig. 2. Atomic force microscopy image of living *Navicula seminulum* cells. These benthic freshwater diatoms grow in tower-like colonies by adhesion of valve faces. The AFM image shows the top valve faces of adjacent cells of two different chains, growing on a glass slide. After imaging, the slides were put back into growth solution, and the diatoms continued to divide. Note that the flat area does not correspond to the surface of the glass slide, but is determined by the maximum possible extension of the z-piezo. Image acquired using AFM contact-mode imaging in water, imaging parameter topography, scan size $8 \times 8 \mu\text{m}^2$, scan frequency 1 Hz.

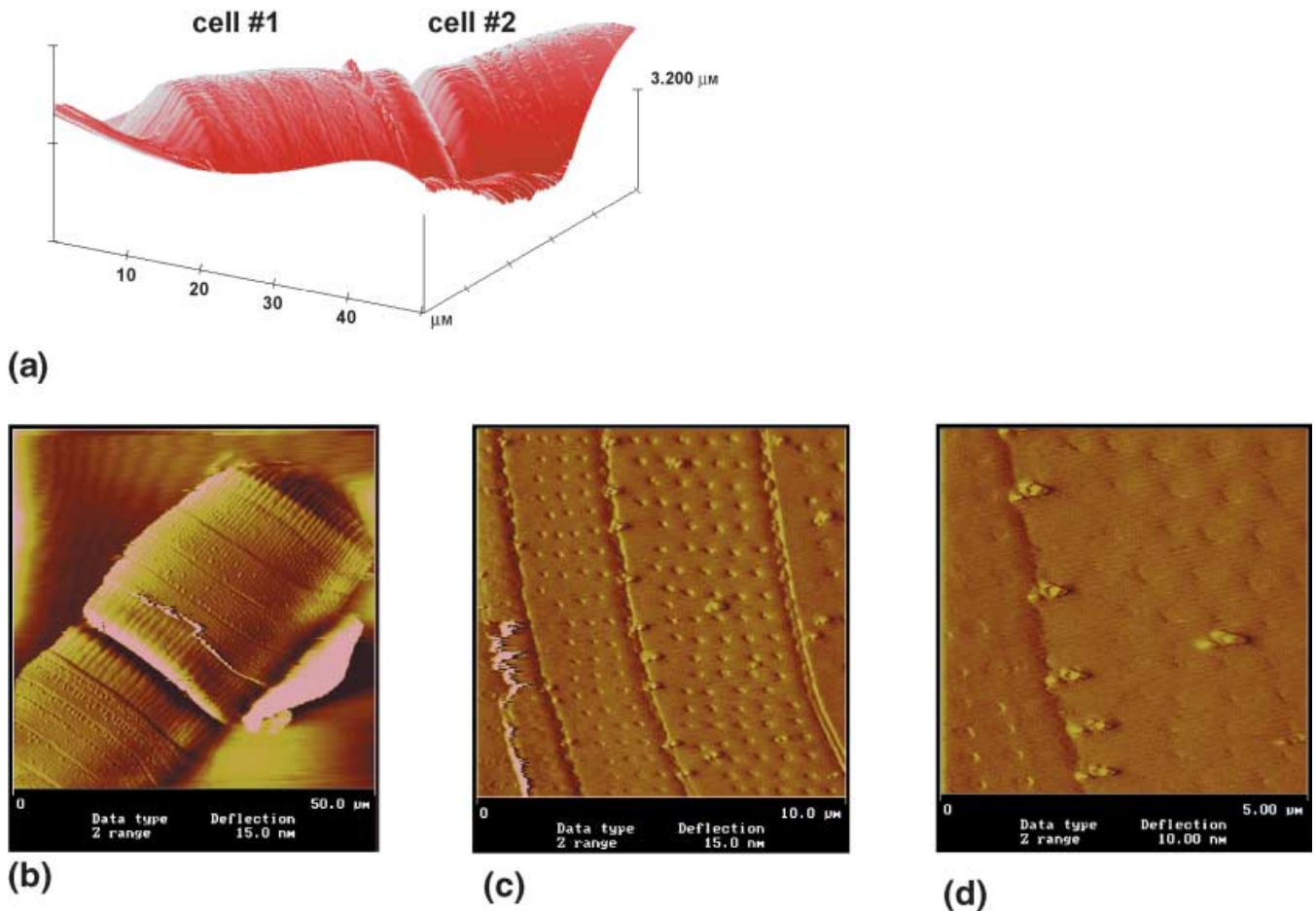


Fig. 3. (a) Topography three-dimensional representation and (b–d) deflection images of two cells of a stack of three of a yet unidentified diatom species. Contact made in growth medium, topography and deflection, scan sizes $50 \times 50 \mu\text{m}^2$, $10 \times 10 \mu\text{m}^2$ and $5 \times 5 \mu\text{m}^2$, scan frequency between 0.3 Hz and 1 Hz.

detailed surface patterning of the top valve faces of two adjacent cells of *Navicula seminulum*. Note that the flat area in the figure does not correspond to the surface of the glass slide, but is an artefact originating from the maximum piezo extension of our AFM.

The chains of *Eunotia sudetica* and of the yet unidentified species (see Fig. 3) grow with the valve faces perpendicular to the surface of the glass slide, allowing for AFM investigation of the girdle bands. Figure 3(a) shows the topography of two adjacent cells at the beginning of a chain of three cells (as seen in the light microscope) of the yet unidentified diatom species. The sides of both valves as well as the girdle bands from cell #1, the connecting region between the two cells and the side of one valve, and some of the girdle bands from cell #2 can be discriminated. The cells are alive and even continued to divide after imaging.

Girdle bands can telescope as cells elongate and grow. This might be visible in Fig. 3. The bead-like features on the edges of the girdle bands (Fig. 3b–d) are yet to be identified. This is the first time that such features have been seen. One possibility is that they are organic material that lubricates the connection between girdle bands. When a diatom cell divides it inherits

both a valve and a set of girdle bands from the mother cell. Deposition of a new valve occurs prior to daughter cell separation, and then girdle bands are deposited sequentially beginning at the edge of the new valve. In Fig. 3, the new girdle bands would be those adjacent to the connection between daughter cells. We cannot tell whether any of these are new, but they all appear to overlap in the same direction. This suggests that they are all from the mother cell; this could be clarified if we knew how many girdle bands this species has. Note that the girdle bands on the opposite end of the cell are fully extended (i.e. they appear wider). The newest ones are more closely packed and are probably extending. This suggests to us that the beads are a lubricant because they only occur on the new bands. Identification of the diatom species will help to clarify this matter.

Determination of the thickness of the organic coating enveloping the siliceous skeleton

The siliceous skeleton of the diatom is enveloped by an organic coating consisting essentially of polysaccharides and proteins

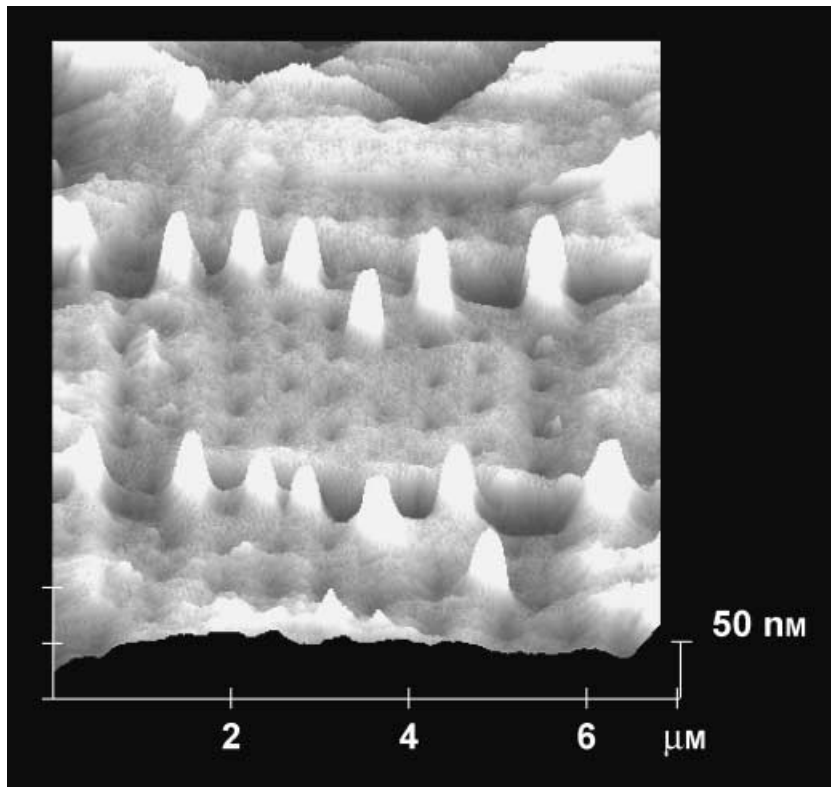


Fig. 4. Using the AFM cantilever as a tool. A $5 \times 5\text{-}\mu\text{m}^2$ area is repetitively scanned in AFM contact mode at high feedback force (about 100 nN). After 2 days, a slightly larger area comprising the area where the organic layer had died off meanwhile is imaged, revealing a height of the organic layer of about 10 nm. Contact mode, topography, scan size $7 \times 7\text{ }\mu\text{m}^2$, scan frequency 2 Hz.

and some lipids (Hecky *et al.*, 1973). A rough determination of the thickness of this layer is performed by following this protocol: a $5 \times 5\text{-}\mu\text{m}^2$ area is repetitively scanned with increased force set point (contact mode, about 100 nN) to mechanically remove and/or alter the organic material on this area, exposing the silica. After this, the cells are put back into their growth solution. Two days later, a larger area comprising the altered $5 \times 5\text{-}\mu\text{m}^2$ diatom surface is imaged with a force set point of about 1 nN. As can be seen in Fig. 4, the altered area, where the organic layer has been mechanically destroyed, is about 10 nm 'lower' than the unaltered surface. Experimental evidence reported by Volcani (1981) and TEM investigations by Leppard (1999) on extracellular polymeric substances corroborate this result.

Diatom adhesion and viscoelastic properties of the diatom frustule

Diatoms produce adhesives that are stable and robust in wet environments. All three diatom species investigated form chains by adhesion of their valve faces and are strongly attached to the glass slides, either with their valve face (*Navicula seminulum*) or with part of their girdle bands and valve sides (*Eunotia sudetica* and the yet unidentified diatom species).

Phase images depict the phase delay between the drive and response of the cantilever. These images contain information about the energy dissipated during the interaction of the AFM tip with the sample, and can help us to understand the viscoelastic and adhesion properties of the surfaces investigated,

specifically of the organic material responsible for diatom adhesion. For a review article on extracellular proteoglycans and extracellular polymeric substances see Lind *et al.* (1997).

Because phase imaging highlights edges and is not affected by large-scale height differences, it provides clearer observation of fine features that can be hidden by rough topography (compare Fig. 3a with Fig. 3b–d). To investigate the natural adhesives utilized to attach cells to each other and to the substratum, we tried to probe the cleft between two connected diatom cells with the AFM. In the yet unidentified species, the cleft at the cell–cell interface proved too deep. In this region, even the use of electron-beam-deposited AFM tips with high aspect ratio merely results in tip imaging (data not shown). Phase imaging reveals slight differences (2°) in viscoelastic and adhesion properties of the two adjacent valves.

Eunotia sudetica, by contrast, is very convenient for *in situ* investigation of the diatom adhesive at the cell interface, because there is barely any cleft between adjacent cells and valve undulations are less pronounced than in the other species investigated (Fig. 5a). The diatom adhesive is apparent as small topographic features at the cell interface. The bead-like structures are 10–20 nm high, have lateral dimensions of about $1\text{ }\mu\text{m}$ and are about $1\text{ }\mu\text{m}$ apart. The phase image clearly depicts the altered viscoelastic properties of these structures: the diatom adhesive causes a phase difference of up to 10° compared with the phase difference on the rest of each of the two frustules, where it is within 1° on each, apart from a 2° phase difference between the two adjacent valves (Fig. 5b), a

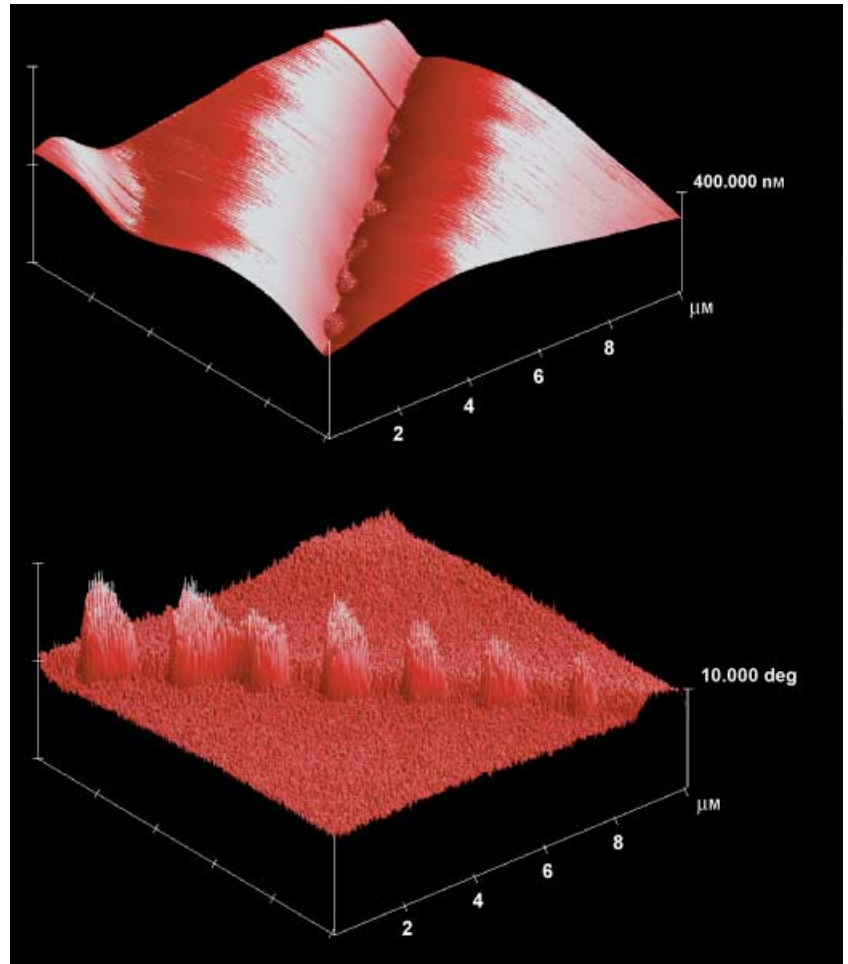


Fig. 5. (a) The adhesives in the contact region of two cells of *Eunotia sudetica* are apparent as small topographic features on the slightly undulated cell interface. The corrugation of the bead-like structures is between 10 and 20 nm, and their lateral dimension and spacing is about 1 μm . (b) In the phase image these features are far more striking. The diatom adhesive causes a phase lag of about 10° compared with the rest of the frustule surfaces, where on a single frustule it is within 1° . Note the 2° interfrustule phase step, which reveals slightly different viscoelastic properties of the two neighbouring valves. Tapping mode, topography and phase, scan size $10 \times 10 \mu\text{m}^2$, scan rate 5 Hz. Note that for better view (b) is rotated clockwise by 90° as compared with (a).

feature which also appears in the other species, where the adhesives are not accessible because of deep clefts between the single organisms.

Force–distance curves on a natural and a man-made adhesive

Force–distance curves on double-sided sticky tape, on the surface and on the adhesive of *Eunotia sudetica* reveal basic differences in adhesion properties (see Fig. 6 for representative data). On double-sided sticky tape, the maximum adhesion force is about 15 nN; the molecules debond from the tip at a tip–surface separation of about 200 nm (Fig. 6a). The double-sided sticky adhesive quickly deteriorates in water, with the adhesion force decreasing within a few minutes (data not shown). On the diatom surface, no adhesion force can be detected (Fig. 6b). The diatom adhesive, by contrast, is strong and robust in the wet environment. To gain reproducible access to this natural adhesive, a chain of *Eunotia sudetica* that was embedded in a densely packed field of *Navicula seminulum* was scraped away from the glass slide with an STM-tip mounted on a three-dimensional micromanipulator. Over a period of

several hours, force–distance curves were taken on the adhesive molecules that were used to attach the diatom cells to the glass slide. No change in the basic shape of the force–distance curves can be detected within hours of repetitive pulling in the area where the colony was located (see Fig. 6c,d for representative data). Typically, several debonding events occur until the natural adhesive molecules finally debond at a tip–surface separation of about 600 nm. For a detailed description of this study, see Gebeshuber *et al.* (2002).

Conclusions and outlook

Here, we present the first *in vivo* study of diatoms with AFM. Previous attempts to image living diatoms with AFM were not successful, because the cells did not attach strongly enough to the sample holders. Using natural selection involving freshwater snails feeding on algae we obtained – from a sample of numerous benthic freshwater diatom species growing on glass slides – three species that obviously produce outstanding natural adhesives: *Eunotia sudetica*, *Navicula seminulum* and a yet unidentified species. Such adhesives are strong enough to

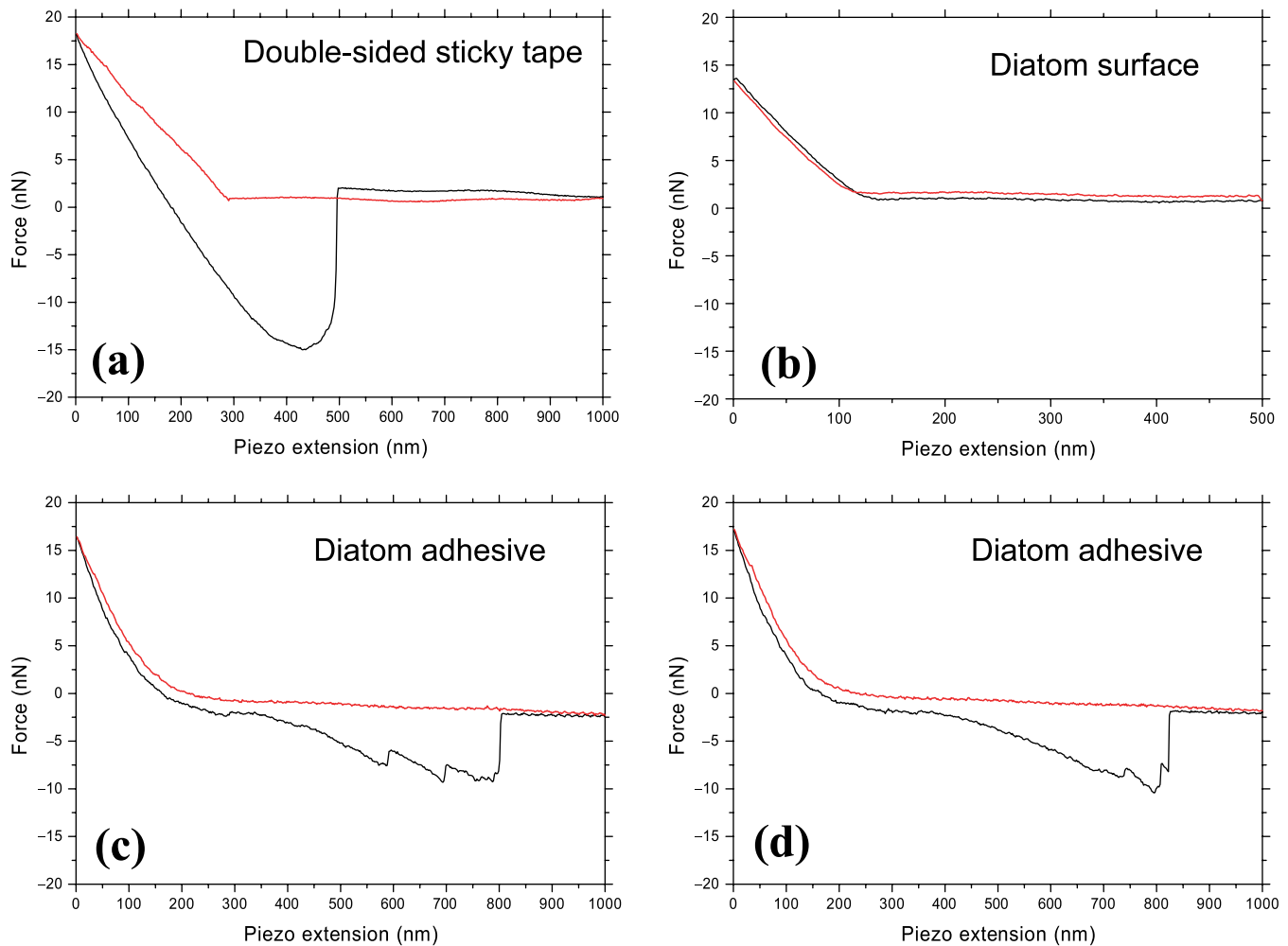


Fig. 6. Force–distance curves. (a) On double-sided sticky tape, the maximum adhesion force is 15 nN; debonding from the tip occurs at a tip–sample separation of about 200 nm. (b) No adhesion can be recognized on the diatom surface. (c,d) Representative data for the diatom adhesive that attaches *Eumotia sudetica* to the substrate. Note that several debonding events occur and that the pulling force must be applied over much larger extensions than in the double-sided sticky tape adhesive.

withstand the coarse snail grazing. The nanostructured siliceous shell of diatoms (e.g. Fig. 1) has been a favourite subject for assessing various aspects of the optical performance of microscopes (Dippel, 1882). In addition, diatom biogenic silica still poses a challenge for chemical synthesis or engineering. Our study includes the imaging of the cell wall of living cells (Figs 2–5) and using the cantilever as a tool to determine the thickness of the organic layer covering the siliceous skeleton (10 nm, Fig. 4). Furthermore, viscoelastic and adhesive properties of the frustule and diatom adhesion molecules as well as a man-made adhesive have been investigated (Figs 5 and 6). Phase imaging demonstrates rather uniform viscoelastic properties on the frustule, apart from the cell interface. Force pulling experiments reveal a strong and tough natural adhesive that is stable and robust in wet environments. Because imaging has proven to be stable over several hours, further *in vivo* AFM studies on diatoms will investigate dynamic biomin-

eralization processes like the production of new frustules at the nanometre scale. These studies will provide important data regarding biomineralization. They might contribute to understanding the diatoms' solutions to challenges such as building – with environmental friendly conditions – nanostructured glass shells with high load capacity (Helmcke, 1985), engineering strong and robust adhesives that are stable in wet environments (Birchall, 1989), and the prevention of their silica shell dissolving in water owing to an organic layer. Modern technology is, for example, currently facing the problem that man-made glass-fibre-reinforced polymers show rapid quality deterioration when used in water (e.g. Connor *et al.*, 1997).

Furthermore, force pulling experiments will provide further data on the natural diatom adhesive at the molecular scale, perhaps resulting in new, more powerful adhesives, and also satisfy Sir Isaac Newton's comment in *Opticks* (1704):

'There are agents in Nature able to make the particles of joints stick together by very strong attraction, and it is the business of experimental philosophy to find them out.'

Acknowledgements

This research was supported by: NASA University Research, Engineering and Technology Institute on Bio Inspired Materials under award NCC-1-02037, NIH under award GM65354, NSF under award DMR-9988640, a research agreement with Veeco, and the UCSB Materials Research Laboratory under an NSF award DMR00-80034. We thank P. Roger Sweets, University of Indianapolis, for identifying the diatom species, A. M. Schmid for providing samples of *Ellerbeckia arenaria*, D. G. Mann for fruitful discussions and J. C. Weaver from the Marine Biotechnology Center for Materials Research Laboratory at UCSB for help in using the SEM to obtain the images presented in Fig. 1. We also thank Tony Wenzelhuemer for carefully reading a previous version of this manuscript.

References

- Almqvist, N., Del Amo, Y., Smith, B.L., Thomson, N.H., Bartholdsson, Å., Lal, R., Brzezinski, M. & Hansma, P.K. (2001) Micromechanical and structural properties of a pennate diatom investigated by atomic force microscopy. *J. Microsc.* **202**, 518–532.
- Beakes, G., Canter, H.M. & Jaworski, G.H.M. (1988) Zoospores ultrastructure of *Zygorhizidium affluens* Canter and *Z. planktonicum* Canter, two chytrids parasitizing the diatom *Asterionella formosa* Hasall. *Can. J. Bot.* **66**, 1054–1067.
- Birchall, J.D. (1989) The importance of the study of biomaterials to materials technology. *Biomaterialization – Chemical and Biochemical Perspectives* (ed. by S. Mann, J. Webb and R. J. P. Williams), pp. 491–507. VCH, Weinheim.
- Connor, M., Bidaux, J.E. & Manson, J.A.E. (1997) A criterion for optimum adhesion applied to fibre reinforced composites. *J. Mater. Sci.* **32**, 5059–5067.
- Dippel, L. (1882) *Das Mikroskop und seine Anwendung*. Braunschweig.
- Gebeshuber, I.C., Thompson, J.B., Del Amo, Y., Stachelberger, H. & Kindt, J.H. (2002) *In vivo* nanoscale atomic force microscopy investigation of diatom adhesion properties. *Mat. Sci. Technol.* **18**, 763–766.
- Gordon, R. & Drum, R.W. (1994) The chemical basis for diatom morphogenesis. *Int. Rev. Cytol.* **150**, 243–372.
- Hecky, R.E., Mopper, K., Kilham, P. & Degens, E.T. (1973) The amino acid and sugar composition of diatom cell walls. *Mar. Biol.* **19**, 323–331.
- Helmcke, J.G. (1985) *Diatomeen I – Schalen in Natur und Technik, Diatoms I – Shells in Nature and Technics*. Krämer Verlag, Stuttgart; Cramer Verlag, Braunschweig.
- Leppard, G.G. (1999) Structure/Function/Activity relationships in marine snow. Current understanding and suggested research thrusts. *Ann. Ist. Super. Sanità*, **35**, 389–396.
- Lind, J.L., Heimann, K., Miller, E.A., van Vliet, C., Hoogenraad, N.J. & Wetherbee, R. (1997) Substratum adhesion and gliding in a diatom are mediated by extracellular proteoglycans. *Planta*, **203**, 213–221.
- Linder, A., Colchero, J., Apell, H.-J., Marti, O. & Mlynek, J. (1992) Scanning force microscopy of diatom shells. *Ultramicroscopy*, **42–44**, 329–332.
- Mann, S. (1993) Molecular tectonics in biomineralisation and biomimetic materials chemistry. *Nature*, **365**, 499–505.
- Newton, I. (1704) *Optiks*. London.
- Sarikaya, M. (1994) An introduction to biomimetics: A structural viewpoint. *Microsc. Res. Techn.* **27**, 360–375.
- Volcani, B.E. (1981) Cell wall formation in diatoms: morphogenesis and biochemistry. *Silicon and Siliceous Structures in Biological Systems* (ed. by T. L. Sinsom and B. E. Volcani), pp. 157–200. Springer Verlag, Berlin.
- Werner, D. (1977) *The Biology of Diatoms*. University of California Press.

A.4 In vivo nanoscale atomic force microscopy investigation of diatom adhesion properties

Gebeshuber I.C., Thompson J.B., Del Amo Y., Stachelberger H. and Kindt J.H.

Mat. Sci. Technol. 18, 763-766 (2002)

Abstract

Most state of the art adhesives fail to bond under wet conditions. Therefore, knowledge of the intrinsic properties of natural adhesives might give valuable information for future engineering approaches. This work investigates the adhesive that *Eunotia sudetica*, a species of benthic freshwater diatoms, produces to attach itself to a substrate. Atomic force spectroscopy under aqueous solution reveals the modular, self-healing properties of this natural adhesive.

In vivo nanoscale atomic force microscopy investigation of diatom adhesion properties

91

I. C. Gebeshuber, J. B. Thompson, Y. Del Amo, H. Stachelberger, and J. H. Kindt

Most state of the art adhesives fail to bond under wet conditions. Therefore, knowledge of the intrinsic properties of natural adhesives might give valuable information for future engineering approaches. This work investigates the adhesive that *Eunotia sudetica*, a species of benthic freshwater diatoms, produces to attach itself to a substrate. Atomic force spectroscopy under aqueous solution reveals the modular, self-healing properties of this natural adhesive. MST/5209

Dr Gebeshuber (gebeshuber@tuwien.ac.at) is in the Institut für Allgemeine Physik and Professor Stachelberger is in the Institut für Verfahrenstechnik, Umwelttechnik und Technische Biowissenschaften, Technische Universität Wien, Wiedner Hauptstrasse 8–10, A–1040 Vienna, Austria, Dr Thompson and Mr Kindt are in the Department of Physics, University of California at Santa Barbara, California 93106, USA, and Dr Del Amo is in the Laboratoire d’Océanographie Biologique, Station Marine d’Arcachon, 2 rue du Professeur Jolyet, Université Bordeaux, 33120 Arcachon, France. Based on a presentation at the 3rd Euroconference on Nanoscience for Nanotechnology, held in Oxford, UK on 16–19 September 2000.

© 2002 IoM Communications Ltd.

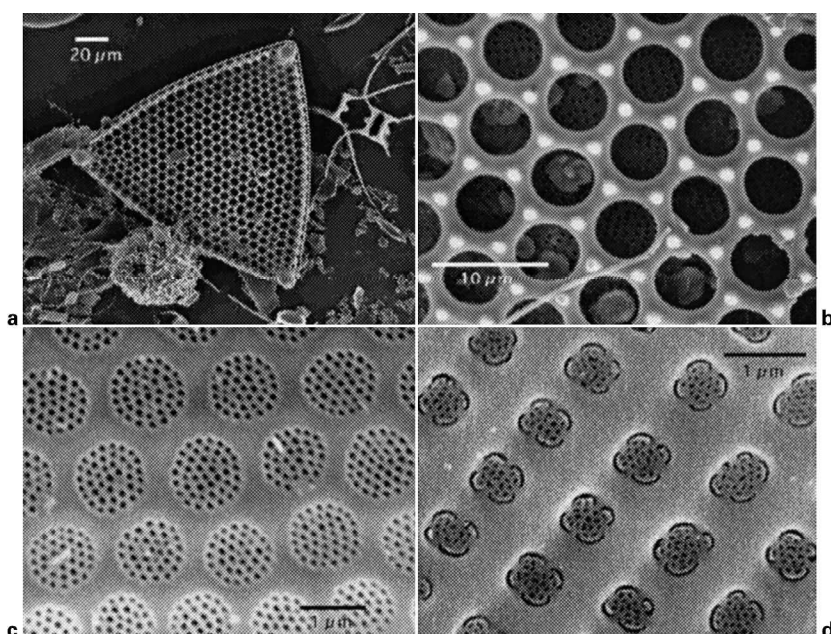
Introduction

Biomimetics is a new interdisciplinary field seeking to understand relationships between structures and functions of biological composites in order to design and synthesise new materials, possibly without the toxic residues characteristic of non-biological modes of industrial mass production.^{1,2} Understanding the processes involved in biomineralisation may eventually allow to mimic these structures to produce optimised materials with minimal environmental impact. This research may lead to the synthesis of novel magnetic, electronic, magnetopharmaceutical or adhesive materials on a nanometre scale.

Diatoms are unicellular microalgae with cell walls consisting of a siliceous skeleton enveloped by an organic case. The skeletons exhibit an amazing diversity of nanostructured frameworks (Fig. 1, SEMs courtesy of M. A. Tiffany, San

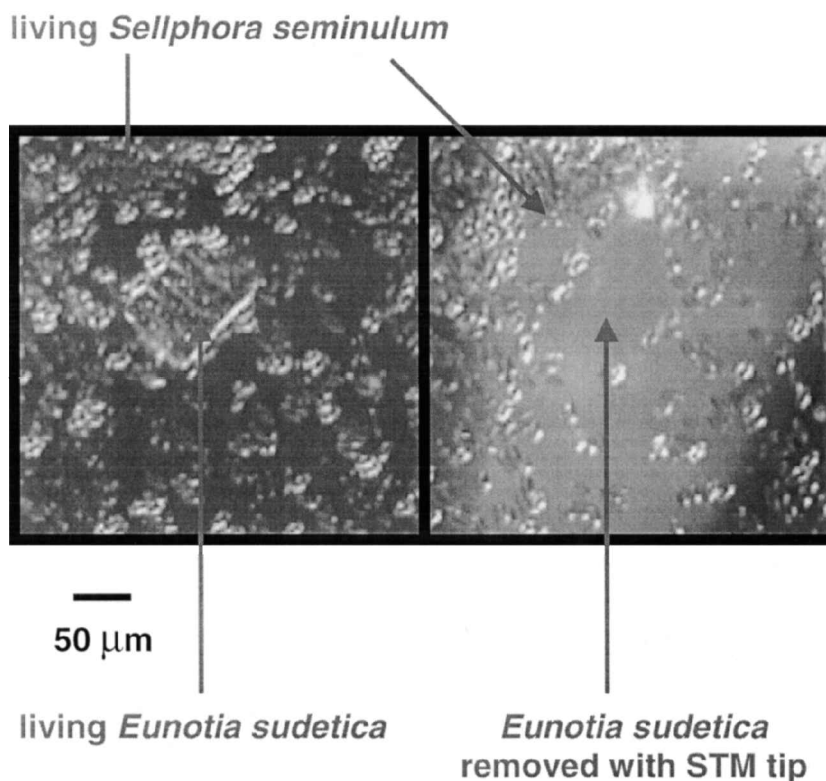
Diego State University, CA, USA). Diatoms live in various wet environments, like salt water or freshwater and on wet surfaces. They can either be freely floating (planctonic forms), or be attached to substrates like rocks or plants (benthic forms).

These unicellular organisms are interesting from the point of materials science and biomimetic studies, since they master challenges as diverse as building nanostructured glass shells with high load capacity (a problem interesting for lightweight structures architecture)³ and engineering strong and robust adhesives that are stable in wet environments (most man made adhesives fail to bond in wet conditions, owing to chemical modification of the adhesive or its substrate).⁴ Furthermore, diatoms excel at preventing dissolution of their silica shells in water owing to an organic layer (up to date technology is currently facing the problem that man made glass fibre reinforced polymers show rapid quality deterioration when used in water).⁵ Currently, human chemical synthesis can not produce siliceous structures with



a and b *Triceratium favus*; c *Roperia tessellata*; d *Achnanthes brevipes*

1 Micrographs showing siliceous skeletons of three different marine diatom species (SEM)



2 Living diatoms covering glass slide: chain of *Eunotia sudetica* that is embedded in field of *Sellphora seminulum* is removed with help of scanning tunnelling microscope (STM) tip to expose natural adhesive to atomic force microscope (AFM) tip for acquisition of force *v.* distance curves and AFM imaging

the hierarchical structural detail of the diatom skeletons nor can ordered siliceous structures be produced synthetically under the benign conditions of diatom biomineralisation.

Atomic force microscopy (AFM) has opened the possibility of studying these interesting organisms *in vivo* with high spatial resolution.⁶ The mechanical behaviour of the diatom adhesive under extension on a molecular level is investigated in this paper.

Materials and methods

Three different species of benthic freshwater diatoms (*Eunotia sudetica*, *Sellphora seminulum*, and a yet unidentified species) were selected for their strong adhesives by exposure of a greater plethora of species to highly selective environmental conditions.⁶ *Eunotia sudetica* was then selected for this study, because its greater size (several tens of micrometres) simplifies the following micromanipulation and engage step (Fig. 2).

The diatoms were grown and studied in fluid culture medium⁷ (Diatom medium, Culture Collection of Algae and Protozoa, UK), where they attach themselves onto glass slides immersed in this medium.

To access the adhesive *Eunotia sudetica* produces for its attachment, an *Eunotia sudetica* cell was mechanically removed using an scanning tunnelling microscope tip,⁸ i.e. a sharpened wire, on a micromanipulator stage. Its former location is clearly marked by the gap in the surrounding *Sellphora seminulum* (Fig. 2).

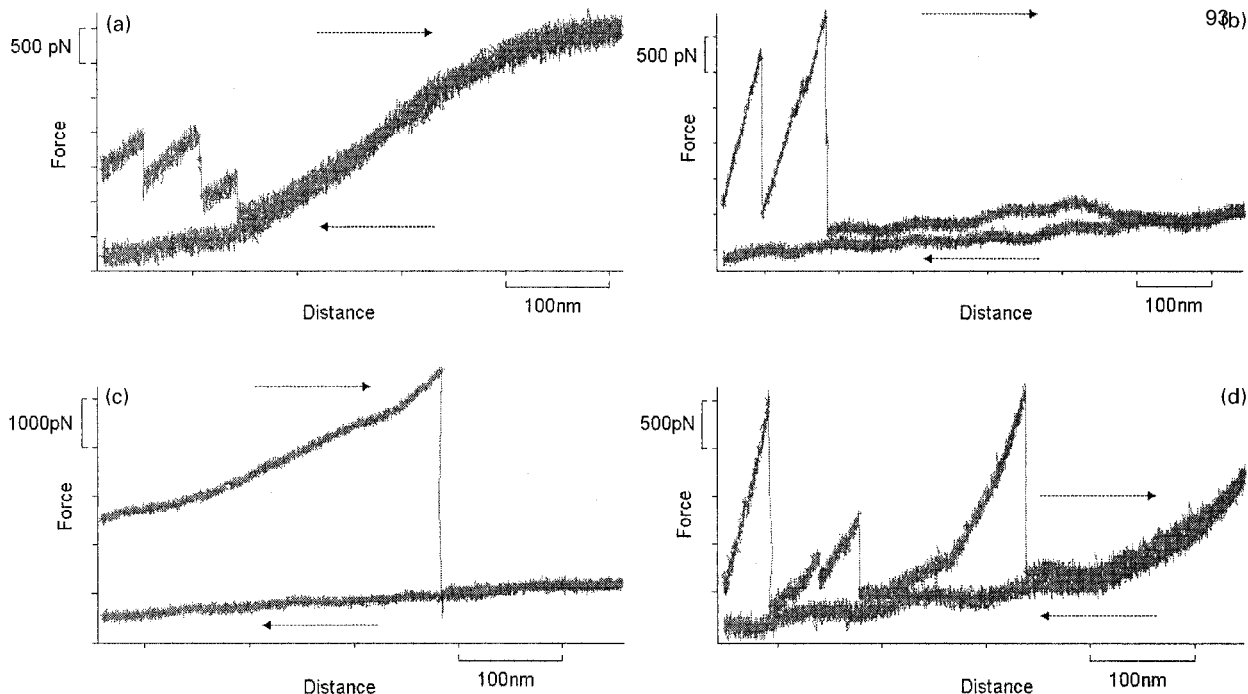
An AFM (BioScope, Digital Instruments, Santa Barbara, CA, USA) was now engaged at this location under optical control (Zeiss Axiovert). The AFM⁹ consists of a micro-machined springy cantilever¹⁰ (Si_3N_4 , $k=0.06 \text{ N m}^{-1}$, Digital Instruments, Santa Barbara, CA) with a sharp tip perpendicular to the cantilever. When a force is applied to the tip, the

cantilever is deflected proportionally. A low spring constant of a cantilever is desirable so that large deflections are obtained with small forces of interaction. This deflection is detected by a laser beam that reflects off the cantilever.¹¹ The AFM is suitable for studies in water and aqueous solutions.¹² Besides imaging applications, the AFM can also be used for stress-strain experiments of small specimens, down to the size of single molecules. In these experiments, the cantilever tip is approached to the material under study. When retracting the cantilever from the specimen, it can occur that a small strand of the specimen stays attached to the AFM tip. Under further extension, the deflection of the cantilever represents the force exerted on the attached strand, and can be plotted as a function of extension.¹³

Force *v.* distance curves of the adhesive residue on the glass slide were now acquired for several hours (Figs. 3 and 4). Control experiments of the adjacent glass slide were acquired for comparison. All experiments were performed in fluid diatom growth medium.⁷

Results and discussion

Owing to the poor adhesion to the substrate, it is impossible to obtain stable images of most benthic diatom species with the AFM. The foundation of the authors' interest in the natural adhesives of the three diatom species is that they turned out to be AFM compatible. *Eunotia sudetica* and the yet unidentified species form chains which grow in parallel to the surface of the glass slide, whereas *Sellphora seminulum* grows in stacks pointing out from the surface of the glass, like little skyscrapers, tens of micrometres high. Phase imaging data on the adhesive produced by the yet unidentified species to build stable chains is presented elsewhere.⁶ This work concentrates on force *v.* distance curves on the adhesive *Eunotia sudetica* produces to attach to the substrate.



a adhesive forces are still acting upon cantilever at maximum retraction of piezo; *b* complete unbinding takes place; *c* complete unbinding takes place; *d* adhesive forces are still acting upon cantilever at maximum retraction of piezo

- 3 Force *v.* distance curves performed on natural adhesive *Eunotia sudetica* produces to attach to substrate: sawtooth pattern structure of unbinding events is clearly visible in *a*, *b*, and *d*; wavy structures in *b* and *d* origin from interference of laser on glass slide; time between pulls several minutes; cantilever spring constant $k=0.06 \text{ N m}^{-1}$; pulling velocity $1 \mu\text{m s}^{-1}$

The elongation of the adhesive under stress takes place in a sawtooth pattern (Figs. 3 and 4); the force rises with extension, some unbinding takes place, yet the adhesive force is still acting and again increasing with extension, once more some unbinding takes place, but there is still some adhesive force, and the cycle starts again. The hysteresis observed after a complete pulling cycle demonstrates that work has been done. This work is irreversibly dissipated as heat, and the area between the retracting and the approaching parts of the curve quantifies this heat (Figs. 3 and 4). Dissipation mechanisms that contribute to this area are energy dissipation inside the pulled adhesive matrix, and energy dissipated either inside the cantilever itself or by fluid dynamic effects. Control experiments, i.e. force *v.* distance curves on areas of the glass slide which are not covered with the adhesive, exhibit negligible energy dissipation;⁶ the area between the retracting and the approaching parts of a pulling curve in the control experiment is only a small fraction compared with the energy dissipation in the adhesive pulling experiments.

The sawtooth pattern elongation behaviour of the adhesive under stress may reflect the successive unbinding of intrachain loops or the successive release of interchain bonds holding a cross-linked multichain adhesive matrix together. Experimental data on the molecular mechanistic origin of the toughness of natural adhesives, fibres, and composites show that this strategy is even applied on the single molecule level.¹⁴

Consecutive acquisition of force *v.* distance curves on a small amount of the adhesive with the tip of the cantilever staying away from the bulk adhesive on the glass slide reveals 'self-healing' properties of the adhesive matrix, when the time between curve acquisition is longer than 30 s. First, the tip of the cantilever 'dips' into the natural adhesive remaining on the glass slide after removing the chain of *Eunotia sudetica*. The cantilever is then carefully brought to a position at a given distance away from the substrate, with some adhesive molecules attached to it (like in Fig. 3, top

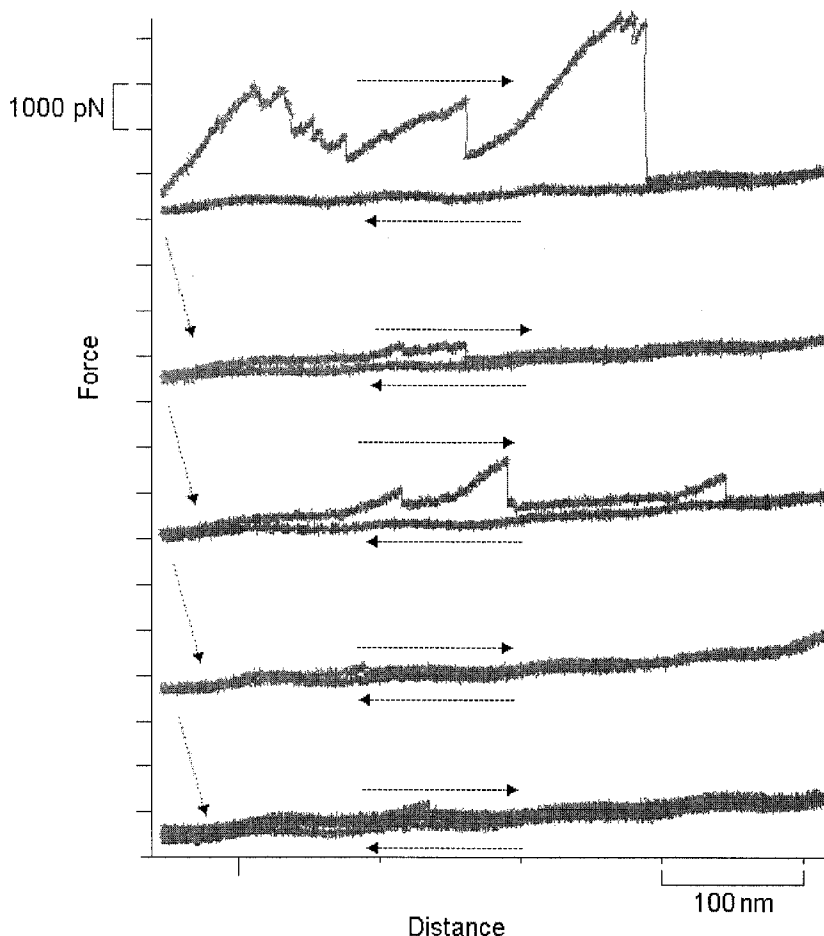
left and bottom right traces). From this new cantilever 'resting position', five consecutive force *v.* distance curves (Fig. 4) are acquired, pulling the adhesives even further up, away from the glass slide. In the control experiment, i.e. when the time between the acquisition of two consecutive force *v.* distance curves is less than 30 s, no more sawtooth pattern detaching events can be detected in consecutive pulls. This result seems to indicate that the natural adhesive *Eunotia sudetica* produces to attach to the substrate is 'self-healing' and that rebonding needs several seconds to occur.

Conclusions and outlook

Atomic force microscopy (AFM) has proven to be a valid method for *in vivo* studies of diatoms.^{6,15} Force *v.* distance curves on the diatom adhesive reveal a sawtooth pattern structure which considerably differs from data obtained from current man made adhesives⁶ and reveal self-healing properties. Further investigations on this adhesive with AFM single molecule pulling experiments and other methods might provide the scientific basis for the production of adhesives that are stable and robust in wet environments, properties that still pose considerable challenges to current man made adhesives.

Acknowledgements

This work was supported by a grant from the US Army Research Office Multidisciplinary University Research Initiative program (DAAH04-96-1-0443). The authors thank M. A. Brzezinski, G. D. Stucky, D. E. Morse, and P. K. Hansma from UCSB for providing ample time for discussions and generous support in any possible way. Furthermore, the authors thank A. M. Schmid and D. G.



4 Five consecutive force *v.* distance curves performed away from surface on natural adhesive *eunotia sudetica* produces to attach to substrate: time between pulls 30 s; sawtooth pattern structure of adhesive unbinding characteristics clearly visible; if time between pulls is less than 30 s, no multiple unbinding events occur anymore

Mann for fruitful discussions and T. Wenzelhuemer for carefully reading the manuscript.

References

1. M. SARIKAYA: *Microsc. Res. Technol.*, 1994, **27**, 360–375.
2. S. MANN: *Nature*, 1993, **365**, 499–505.
3. K. BACH (ed.), 'IL28 diatoms I – shells in nature and technics (Mitteilungen des Instituts für leichte Flächentragwerke, Universität Stuttgart)'; 1984, Stuttgart, Krämer.
4. J. D. BIRCHALL: 'Biom mineralisation – chemical and biochemical perspectives', (ed. S. Mann *et al.*), 491–507; 1989, Weinheim, VCH.
5. M. CONNOR, J. E. BIDAUX, and J. AE. MANSON: *J. Mater. Sci.*, 1997, **32**, 5059–5067.
6. I. C. GEBESHUBER, J. H. KINDT, J. B. THOMPSON, Y. DELAMO, H. STACHELBERGER, M. BRZEZINSKI, G. D. STUCKY, D. E. MORSE, and P. K. HANSMA: to be published.
7. G. BEAKES, H. M. CANTER, and G. H. M. JAWORSKI: *Can. J. Bot.*, 1988, **66**, 1054–1067.
8. G. BINNIG, H. ROHRER, C. GERBER, and E. WEIBEL: *Phys. Rev. Lett.*, 1982, **49**, 57–61.
9. G. BINNIG, C. F. QUATE, and C. GERBER: *Phys. Rev. Lett.*, 1986, **56**, 930–933.
10. T. R. ALBRECHT, S. AKAMINE, T. E. CARVER, and C. F. QUATE: *J. Vac. Sci. Technol. A*, 1990, **8A**, 3386–3396.
11. D. SARID: 'Scanning force microscopy'; 1991. New York, NY, Oxford University Press.
12. A. L. WEISENHORN, P. K. HANSMA, T. R. ALBRECHT, and C. F. QUATE: *Appl. Phys. Lett.*, 1989, **54**, 2651–2653.
13. E.-L. FLORIN, V. T. MOY, and H. E. GAUB: *Science*, 1994, **264**, 415–417.
14. B. L. SMITH, T. E. SCHÄFFER, M. VIANI, J. B. THOMPSON, N. A. FREDERICK, J. KINDT, A. BELCHER, G. D. STUCKY, D. E. MORSE, and P. K. HANSMA: *Nature*, 1999, **399**, 761–763.
15. I. C. GEBESHUBER, J. H. KINDT, J. B. THOMPSON, Y. DELAMO, M. BRZEZINSKI, G. D. STUCKY, D. E. MORSE, and P. K. HANSMA: Proc. 15th North American Diatom Symp., Fort Collins, CO, USA, September 1999, 8.

A.5 AFM search for slow MCI-produced nanodefects on atomically clean monocrystalline insulator surfaces

Gebeshuber I.C., Cernusca S., Aumayr F. and Winter HP.

Nucl. Instr. Meth. Phys. Res. B 205, 751-757 (2003)

Abstract

We have investigated by means of atomic force microscopy (AFM) single impacts of slow singly and multiply charged Ar ions on atomically clean insulator surfaces for LiF(100), SiO₂(0001) α -quartz, muscovite mica and sapphire c-plane Al₂O₃(0001) crystals. The target samples have been continuously kept under UHV conditions by transferring them in a transportable UHV vault from the vacuum chamber for ion bombardment to the AFM instrument. Slow ion bombardment was accompanied by low-energy electron flooding to compensate for possible target surface charge-up. For Al₂O₃ clear ion-charge dependent surface defects in lateral and vertical directions give evidence for potential sputtering, which until now has only been demonstrated with thin polycrystalline insulator films.



ELSEVIER

Available online at www.sciencedirect.com

SCIENCE @ DIRECT®

Nuclear Instruments and Methods in Physics Research B 205 (2003) 751–757

NIM B
 Beam Interactions
 with Materials & Atoms

www.elsevier.com/locate/nimb

AFM search for slow MCI-produced nanodefects on atomically clean monocrystalline insulator surfaces

I.C. Gebeshuber *, S. Cernusca, F. Aumayr, HP. Winter

Institut für Allgemeine Physik, TU Wien, Wiedner Hauptstrasse 8-10, A-1040 Wien, Austria

Abstract

We have investigated by means of atomic force microscopy (AFM) single impacts of slow singly and multiply charged Ar ions on atomically clean insulator surfaces for LiF(100), SiO₂(0001) α -quartz, muscovite mica and sapphire *c*-plane Al₂O₃(0001) crystals. The target samples have been continuously kept under UHV conditions by transferring them in a transportable UHV vault from the vacuum chamber for ion bombardment to the AFM instrument. Slow ion bombardment was accompanied by low-energy electron flooding to compensate for possible target surface charge-up. For Al₂O₃ clear ion-charge dependent surface defects in lateral and vertical directions give evidence for potential sputtering, which until now has only been demonstrated with thin polycrystalline insulator films.

© 2003 Elsevier Science B.V. All rights reserved.

PACS: 79.20.Rf; 68.37.Ps; 68.35.Dv

Keywords: Nanodefects; Insulators; HCI; In situ AFM; Monocrystalline insulator surfaces; Potential sputtering

1. Introduction

Impact of slow multicharged ions (MCI) Z^{q+} on certain insulator materials can give rise to considerably stronger ablation than the common kinetic sputtering by neutral or singly charged projectiles. First experimental evidence for such “potential sputtering” (PS) was reported by Radzhabov et al. [1] and Morozov et al. [2], who for some alkali halide surfaces observed strongly *q*-dependent secondary ion yields. Their results have been explained by “Coulomb explosion” [3], i.e. the creation of small positively charged surface

spots from rapid electron capture by the impinging MCI, with subsequent ablation because of the strong mutual target ion repulsion. As further evidence for PS, much larger etching patterns have been found on KCl crystal surfaces irradiated with 500 eV Kr⁴⁺ than with equally fast Kr⁺ ions [4]. “Coulomb explosion” was also invoked for explaining atomic force microscopy (AFM) observations of blister-like defects on mica samples which had been bombarded with highly charged ions as Xe⁴⁴⁺ and U⁷⁰⁺ of several 100 keV impact energy [5]. On the other hand, studies involving the impact of slow (≤ 1 keV) MCI on thin polycrystalline films of alkali halides (LiF, NaCl) and Al₂O₃ deposited on microbalance quartz crystals [6] did suggest another explanation for PS, namely defect-stimulated desorption induced by the rapid electron capture [7]. Such desorption processes have

* Corresponding author. Tel.: +43-1-58801-13484; fax: +43-1-58801-13499.

E-mail address: ille@iap.tuwien.ac.at (I.C. Gebeshuber).

earlier been studied for impact of electrons (ESD) or photons (PSD) on materials in which a self-trapping of specific crystal defects can take place [8], which proceeds by electron–phonon coupling. However, for impact of faster ions the defect trapping necessary for PS can also be forced or at least supported by kinetic projectile energy (“kinetically assisted PS” [9]), which fact may explain PS-like effects reported for target species where no electron–phonon coupling can take place [5].

We have carried out a systematic search for PS with atomically clean monocrystalline insulator targets which have been bombarded by low-energy ions on the single impact level, by searching for resulting surface defects by means of AFM. The targets remained under UHV conditions during ion irradiation and subsequent AFM inspection. An important motivation for this study are interesting applications of PS for, e.g., nanostructuring of insulator surfaces. There are also suspicions that earlier PS studies involving polycrystalline insulator films might have been influenced by some defects in these target samples.

2. Experimental methods

We have looked for nanodefects on freshly prepared surfaces of LiF(100), SiO₂(0001) α -quartz, muscovite mica and sapphire *c*-plane Al₂O₃(0001) after their irradiation with low doses of slow singly and multiply charged ions. The ion bombardment was accompanied by low-energy electron flooding to compensate for surface charge-up which otherwise would have strongly inhibited the AFM observation. The applied electron gun produced very slow electrons (4 eV energy, 200 nA current, 2 cm distance to the sample).

In a first stage of this study we had used a NIER-type electron impact ion source with its turbomolecular pump directly attached to our UHV-AFM instrument [10]. However, in this arrangement inconveniently high AFM system noise was produced. We then changed to a transportable UHV vault for target transfer which is alternately coupled by UHV locks to the target irradiation chamber and the AFM. This procedure kept target surfaces under permanent UHV conditions

after their initial cleaning, thermal annealing and subsequent irradiation until completion of their AFM inspection, and also drastically reduced the disturbing AFM system noise. Singly and multiply charged ions for target irradiation have been extracted from a 5 GHz ECR ion source [11], magnetically analyzed and guided via electrostatic lenses to the UHV irradiation chamber. The ions were decelerated in front of the target surface to their desired impact energy.

3. Description of the AFM observations

In the following we describe so far gained experience from AFM observations of different insulator target surfaces. In all measurements the AFM contact mode has been employed, and sometimes also other AFM modes (non-contact, lateral force) have been used. Where possible, our results are compared with similar work from other groups.

3.1. LiF(100)

Nanoscale modifications of different alkali-halide surfaces (NaCl, KCl, KBr) induced by electronic transitions (ESD, PSD) have been studied with AFM down to atomic resolution [12]. In our case we have used LiF(100) single crystals (TBL Kelpin, Neuhausen, Germany) which were cleaved in air, CO₂ snow cleaned (Applied Surface Technologies, New Providence, NJ, USA), transferred into the UHV irradiation chamber and annealed at 400 °C for 3 h. CO₂ snow cleaning is an efficient way to remove micro- and nanometer sized debris from single-crystal surfaces. With this crystal preparation techniques we could routinely image monoatomic terraces with atomic resolution in the AFM contact mode. However, the complex structure of the LiF(100) surface resulting after slow ion bombardment made a correlation of possible ion induced nanodefects to ion doses and charge states rather difficult. So far, we could not find significant changes in surface topography between the unbombarded LiF(100) surfaces and their bombardment with 100 eV Ar²⁺, 400 eV Ar²⁺, 250 eV Ar³⁺ and even 3 keV Ar⁷⁺. For

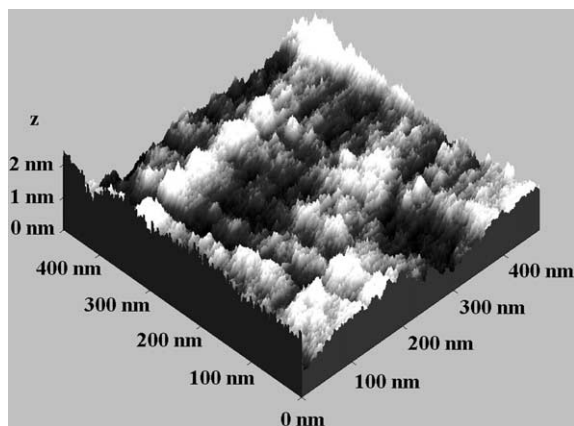


Fig. 1. LiF(100) single-crystal surfaces after standard preparation (see text) and bombardment with 250 eV Ar^{3+} ions ($480 \times 480 \text{ nm}^2$, imaging parameter height z).

demonstration, Fig. 1 shows a LiF(100) surface after preparation and bombardment with Ar^{3+} ions with a dose of 5×10^{12} ions/ cm^2 (i.e. about five ions per $10 \times 10 \text{ nm}^2$ only). Bombardment with 100 eV Ar^{2+} ions with larger doses up to 5×10^{15} ions/ cm^2 did not produce distinctive changes in surface topography. The investigations are continued by preparing flatter LiF(100) surfaces on which the ion induced defects can probably be diagnosed, which will be important for comparison with our earlier studies on PS involving polycrystalline LiF films [7].

3.2. $\text{SiO}_2(0001)$

Quartz is the only monocrystalline target surface for which the microbalance technique has been applied in order to demonstrate PS [13]. For the present work, polished $\text{SiO}_2(0001)$ α -quartz single crystals (TBL Kelpin, Neuhausen, Germany) were CO_2 snow cleaned and annealed in UHV at 400°C for 3 h. This procedure resulted in very flat crystal surfaces for which our AFM contact mode measurements on fourteen samples revealed a root-mean-squares (rms) roughness of $0.16 \pm 0.01 \text{ nm}$, as a hopefully excellent start for our PS investigations. These quartz crystals were then bombarded with 1 keV Ar^+ ions. AFM imaging of resulting surface topography indeed clearly revealed ion induced nanostructures as

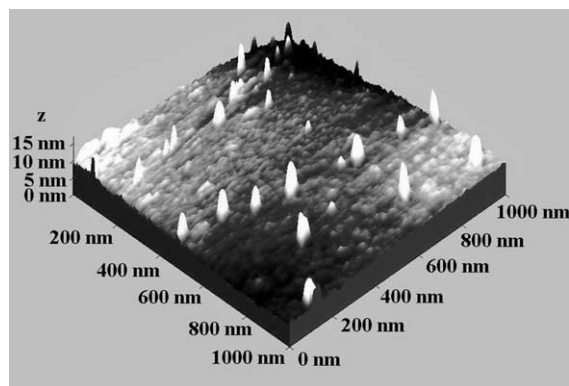


Fig. 2. Polished $\text{SiO}_2(0001)$ α -quartz single crystal after CO_2 cleaning, annealing and bombardment with 1 keV Ar^+ ions (UHV AFM contact mode). Ion bombardment results in hillocks with a height of several nanometers.

shown in Fig. 2. The surface is covered with hillocks a few nanometers high. However, the density of these hillocks did not directly correspond to the applied ion doses: for a dosis of about one incident 1 keV Ar^+ ion per $10 \times 10 \text{ nm}^2$, we observe only about 30 nanostructures on an area of $1000 \times 1000 \text{ nm}^2$, which indicates that not every single ion has caused one nanod defect on the quartz surface. Probably several ion impacts are necessary to induce a detectable surface modification: the ion dosis in all cases reported in this paper was 5×10^{12} ions/ cm^2 , equivalent to five incident ions per $10 \times 10 \text{ nm}^2$. Probably individual ion tracks do not need to overlap to induce multiple ion induced nanostructures, but may cause defects on the insulator surface which increase the chance that impact of another ion in the near vicinity gives rise to an observable surface structure. The fact that surface modifications found after ion bombardment are observed as hillocks instead of craters is also not yet understood, but several possible explanations can be conceivable: in AFM as for other scanning probe microscopy methods it is more straightforward to image elevated structures than craters. Even worse, narrow but highly elevated surface features in the vicinity of craters would completely mask the latter because of their convolution with the tip shape.

So far, very few studies have been performed in this field, in particular for insulating surfaces.

Several groups having applied AFM did report hillocks as surface modifications after bombardment with heavy ions, in some cases even for GeV impact energies. Audouard et al. [14] studied by AFM the surface of amorphous metals irradiated with swift heavy ions. The ion impacts apparently caused formation of hillocks for irradiation at 300 K if the ions provided sufficiently large electronic stopping (>55 keV/nm). On the other hand, irradiation at 80 K did not induce noticeable modifications of the metal surface. These results indicate that formation of hillocks which are flattened by the sample growth, is essentially caused by the damage from electronic excitation in individual ion tracks. In another experiment the same group [15] studied with AFM modifications of the surface topography of amorphous metallic alloys. Irradiation with swift Pb or U ions led to formation of hillocks surrounded by craters, whereas no visible surface modifications were observed after irradiation with Kr ions which caused less electronic stopping. In the view of these authors formation of hillocks can be ascribed to damage created in individual ion tracks, while craters would be linked to the occurrence of anisotropic growth. Both processes are induced by severe electronic excitation in the wake of incident ions.

3.3. $KAl_2[AlSi_3]O_{10}(OH)_2$ (muscovite mica)

Muscovite mica is an aluminosilicate growing in sheets. Our mica samples which have been provided by Omicron Nanotechnology can be easily prepared to atomical flatness by cleavage in air with adhesive tape. The samples were then transferred to UHV and annealed for 3 h at 400 °C. We could routinely obtain atomic resolution on these mica surfaces both in the AFM height mode and the lateral force mode. Mica features large atomically flat terraces with small steps between them. In searching for nanod defect formation by singly and multiply charged ions we bombarded these mica surfaces with 400 eV Ar^+ , 500 eV Ar^+ , Ar^{2+} and Ar^{7+} , 800 eV Ar^+ and Ar^{4+} , 1 keV Ar^+ and 1.2 keV Ar^+ . After bombardment with the slowest ions (400 eV Ar^+ , 500 eV Ar^+ and Ar^{2+}) no surface modifications were found in AFM contact as well as non-contact modes. For bombardment by 800

eV Ar^+ and Ar^{4+} only very few nanod defects could be seen on the irradiated surfaces. We observed hillocks with a few nanometers high and about 50 nm in diameter. They appeared in very low densities on the surface and might not necessarily have been caused by the ion bombardment. Surface modifications could only be attributed unambiguously to ion bombardment for ≥ 1 keV Ar^+ ions. Fig. 3 shows a mica surface after 1.2 keV Ar^+ ion bombardment where the density of observable surface nanod defects was already considerably larger than for 1 keV Ar^+ impacts administered with similar doses (1 keV Ar^+ ions induced about 10 nanod defects per 1000×1000 nm², whereas for 1.2 keV Ar^+ ions the density of ion induced nanod defects was about 200 per 1000×1000 nm²). However, also for mica no clear dependence on the ion-charge state could be found, so far. Several groups have performed AFM investigations of mica surfaces irradiated with highly charged ions. All these investigations were made on ambient air conditions.

We believe that only under UHV conditions imposed throughout the procedures of irradiation and AFM for investigating ion induced nanod defects an indisputable assignment of the latter to MCI bombardment is possible. Anyhow, as a general result from these studies MCI impact on mica left bumps with about 1 nm height and 15 nm

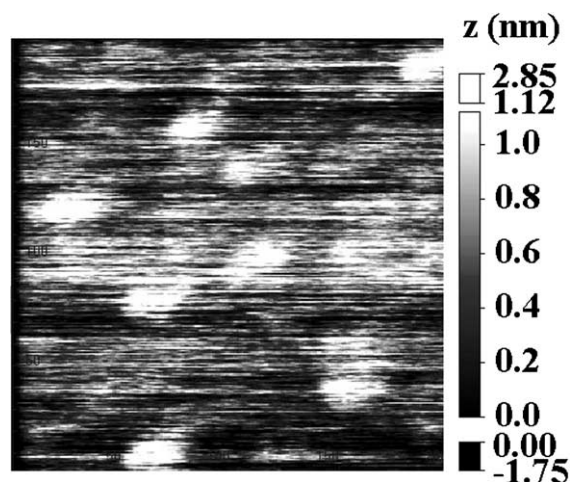


Fig. 3. AFM scan of muscovite mica bombarded with 1.2 keV Ar^+ ions. Observed features are ion induced topographic defects.

diameter. Parks et al. [16] showed that the size of these bumps was not strongly correlated to the kinetic ion energy. This work was later extended in order to demonstrate that the size of observed nanodefects was strongly correlated with the potential ion energy [17]. With 100 keV Xe^{q+} ions ($25 \leq q \leq 50$) impinging on mica, damage caused by single ion impacts was observed with AFM at ambient conditions, with the impact sites typically appearing as circular hillocks. In the view of these authors this hillock- rather than crater-like feature

is caused by the highly anisotropically layered structure of mica.

3.4. $\text{Al}_2\text{O}_3(0001)$

Polished $\text{Al}_2\text{O}_3(0001)$ *c*-plane single crystals (TBL Kelpin, Neuhausen, Germany) have been CO_2 snow cleaned and annealed for 3 h at 400 °C in UHV. This yielded as for SiO_2 very flat crystal surfaces. AFM contact mode studies on numerous samples prepared by this technique revealed a rms

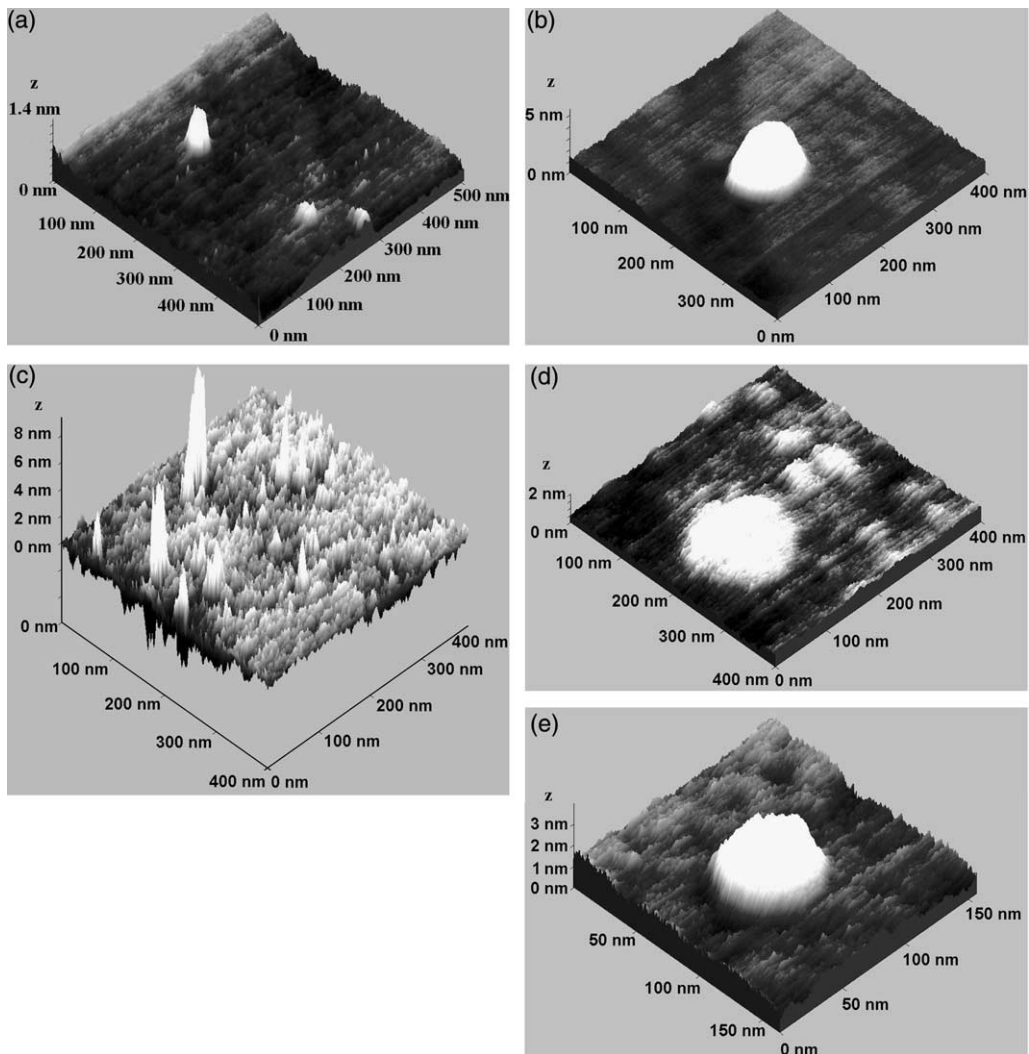


Fig. 4. $\text{Al}_2\text{O}_3(0001)$ single-crystal surface after annealing and bombardment with 500 eV Ar^+ ions (a), 500 eV Ar^{7+} ions (b), 1.2 keV Ar^{1+} ions (c), 1.2 keV Ar^{4+} ions (d) and 1.2 keV Ar^{7+} ions (e).

roughness of 0.09 ± 0.06 nm. Bombardment with Ar ions with different charge states and kinetic energies (500 eV Ar⁺, Ar⁷⁺, 1.2 keV Ar⁺, Ar⁴⁺ and Ar⁷⁺) resulted in hillock-like nanodefects seen in AFM contact mode (cf. Fig. 4(a)–(e)). The density of ion induced nanodefects did not directly correspond to the applied ion dose but was rather small, however reproducible: about 10 nanodefects per 1000×1000 nm² can be observed after bombardment in the energy range reported in this paper. Such a direct correspondence has only been found in STM investigations of HOPG [18]. However, on the Al₂O₃ *c*-plane crystals we could show a clear correlation of slow ion induced defects with both kinetic energy and charge state of the projectile ions. We also found that the defects caused by slow ion impact could completely be removed by annealing the Al₂O₃ crystals at 450 °C for about 5 h. 500 eV Ar⁺ ion impact produced defects with about one nanometer height and some tens of nanometers width (Fig. 4(a)). One should keep in mind that with AFM the height of surface features can more accurately be measured than their lateral dimension. Defects produced by 500 eV Ar⁷⁺ ions were several nanometers high (see Fig. 4(b)) and had lateral dimensions of about 100 (!) nanometers. At higher kinetic ion energy differences of ion induced nanodefects became even more distinct. 1.2 keV Ar⁺ induced defects were up to 8 nm high and some ten nanometers wide (Fig. 4(c)). For impact of higher charged Ar⁴⁺ two different kinds of defects appeared on the surface (Fig. 4(d)) with similar heights of about 2 nm, but considerably different lateral extensions.

Some were nearly 200 nm wide, but smaller defects (only about 50 nm wide) were found as well. Finally, for impact of Ar⁷⁺ only one kind of defects was visible in the AFM images, measuring about 50 nm across and 2 nm in height (see Fig. 4(e)).

4. Summary and conclusions

The present study describes systematic efforts to find evidence for PS by means of AFM inspection of atomically clean monocrystalline insulator surfaces which have been bombarded by slow (typically ≤ 1 keV) singly and multiply charged Ar^{*q+*}

ions (up to $q = 7$). The study may be seen as an extension of earlier work by other groups who looked for similar effects. In contrast to the present work, however, they have shot much faster multiply charged ions on various gas-covered surfaces and inspected them by AFM in air [5,16,17], or made STM investigations of atomically clean HOPG surfaces bombarded by slow (150 eV) Ar^{*q+*} ions (up to $q = 9$ [18]) or much faster (several 100 keV) Xe^{*q+*} ions (up to $q = 44$ [19]). AFM in UHV is probably indispensable for finding clear-cut evidence of PS related nanodefects induced by slow MCI with a size clearly depending on the ion-charge state. In this work Al₂O₃ has been identified as a good candidate for such PS induced nanostructuring, and for SiO₂ further research might lead to a similar conclusion. Both materials are of great relevance for applications in a rapidly emerging field combining microelectronics and nanotechnology.

Our studies on atomically clean insulator surfaces indicate that the PS effect – which has been found to be rather strong for thin films of the materials investigated here – might be more dependent on defect-mediation than so far assumed. For sure, we see potential energy dependent nanodefects generated on the single-crystal surfaces, but their density is too low to prove that the PS effects in thin films and single crystals are of equal importance.

Our expectations concerning the use of PS on monocrystalline surfaces for, e.g., nanostructuring applications, which originated from our previous experience with thin films, have not been met so far. Further studies along these lines are thus highly desirable.

Acknowledgements

This work has been supported by Austrian FWF under project no. 13543-PHY. The authors thank Dr. R. Wörgötter-Plunger for her cooperation in the early phase of these investigations.

References

- [1] S.S. Radzhabov, R.R. Rakhimov, P. Abdusalamov, *Izv. Akad. Nauk SSSR Ser. Fiz.* 40 (1976) 2543.

- [2] S.N. Morozov, D.D. Gurich, T.U. Arifov, *Izv. Akad. Nauk SSSR Ser. Fiz.* 43 (1979) 137.
- [3] I.S. Bitensky, M.N. Murakhmetov, E.S. Parilis, *Sov. Phys. Tech. Phys.* 24 (1979) 618.
- [4] S.S. Radzhabov, R.R. Rakhimov, *Izv. Akad. Nauk SSSR Ser. Fiz.* 49 (1985) 1812.
- [5] D.H. Schneider, M.A. Briere, J. McDonald, J. Biersack, *Radiat. Eff. Def. Solids* 127 (1993) 113.
- [6] G. Hayderer, M. Schmid, P. Varga, HP. Winter, F. Aumayr, *Rev. Sci. Instr.* 70 (1999) 3696.
- [7] F. Aumayr, J. Burgdörfer, P. Varga, HP. Winter, *Comments At. Mol. Phys.* 34 (1999) 201.
- [8] P. Townsend, in: R. Behrisch (Ed.), *Sputtering by Particle Bombardment II*, Springer, Berlin, 1983, p. 147 (Chapter 4).
- [9] G. Hayderer, S. Cernusca, M. Schmid, P. Varga, HP. Winter, F. Aumayr, D. Niemann, V. Hoffmann, N. Stolterfoht, C. Lemell, et al., *Phys. Rev. Lett.* 86 (2001) 3530.
- [10] UHV-AFM/STM, OMICRON Nanotechnology GmbH, Germany.
- [11] M. Leitner, D. Wutte, J. Brandstötter, F. Aumayr, HP. Winter, *Rev. Sci. Instr.* 65 (1994) 1091.
- [12] M. Szymonski, J. Kolodziej, B. Such, P. Piatkowski, P. Struski, P. Czuba, F. Krok, *Prog. Surf. Sci.* 67 (2001) 123.
- [13] M. Sporn, G. Libiseller, T. Neidhart, M. Schmid, F. Aumayr, HP. Winter, P. Varga, M. Grether, D. Niemann, N. Stolterfoht, *Phys. Rev. Lett.* 79 (1997) 945.
- [14] A. Audouard, R. Mamy, M. Toulemonde, G. Szenes, L. Thomé, *Nucl. Instr. and Meth. B* 146 (1998) 217.
- [15] A. Audouard, R. Mamy, M. Toulemonde, G. Szenes, L. Thomé, *Europhys. Lett.* 40 (1997) 527.
- [16] D.C. Parks, R. Bastasz, R.W. Schmieder, M. Stoeckli, *J. Vac. Sci. Technol. B* 13 (1995) 941.
- [17] D.C. Parks, F.G. Serpa, J.D. Gillaspay, M.P. Stoeckli, L.P. Ratliff, E.W. Bell, R.W. Schmieder, *Nucl. Instr. and Meth. B* 134 (1998) 46.
- [18] G. Hayderer, S. Cernusca, M. Schmid, P. Varga, HP. Winter, F. Aumayr, *Phys. Scr. T* 92 (2001) 156.
- [19] R. Minniti, L.P. Ratliff, J.D. Gillaspay, *Phys. Scr. T* 92 (2001) 22.

A.6 Nanoscopic surface modification by slow ion bombardment

Gebeshuber I.C., Cernusca S., Aumayr F. and Winter HP.

Int. J. Mass Spectrom. 229, 27-34 (2003)

Abstract

We present systematic scanning tunneling microscopy (STM)/atomic-force microscopic (AFM) investigations on nanoscopic defect production at atomically clean surfaces of SiO₂, Al₂O₃ and highly oriented pyrolytic graphite (HOPG) after bombardment by slow (impact energy ≤ 1.2 keV) singly and multiply charged ions under strict ultra-high vacuum (UHV) conditions. Combined STM and AFM studies show that on HOPG only “electronic” but no visible topographic defects are created by such ion bombardment. On the monocrystalline insulator surfaces, well-defined topographic features of typically nm extensions are produced (“potential sputtering”). For Al₂O₃ and HOPG, a clear dependence of the defect size on the projectile ion charge is demonstrated. These results are discussed in view to possible new nanoscopic surface structuring and modification methods for which the kinetic projectile energy plays a minor role only.

Nanoscopic surface modification by slow ion bombardment

I.C. Gebeshuber, S. Cernusca, F. Aumayr, H.P. Winter*

Institut für Allgemeine Physik, Technische Universität Wien, Wiedner Hauptstraße 8-10, A-1040 Vienna, Austria

Received 9 January 2003; accepted 24 January 2003

Abstract

We present systematic scanning tunneling microscopy (STM)/atomic-force microscopic (AFM) investigations on nanoscopic defect production at atomically clean surfaces of SiO_2 , Al_2O_3 and highly oriented pyrolytic graphite (HOPG) after bombardment by slow (impact energy ≤ 1.2 keV) singly and multiply charged ions under strict ultra-high vacuum (UHV) conditions. Combined STM and AFM studies show that on HOPG only “electronic” but no visible topographic defects are created by such ion bombardment. On the monocrystalline insulator surfaces, well-defined topographic features of typically nm extensions are produced (“potential sputtering”). For Al_2O_3 and HOPG, a clear dependence of the defect size on the projectile ion charge is demonstrated. These results are discussed in view to possible new nanoscopic surface structuring and modification methods for which the kinetic projectile energy plays a minor role only.

© 2003 Elsevier Science B.V. All rights reserved.

Keywords: Ion–surface interaction; Potential sputtering; Surface defects; Multicharged ions

1. Introduction

Impact of slow ions on solid surfaces can give rise to inelastic processes which modify the geometric and electronic structure at and below the surface, cause emission of electrons and photons as well as neutral and ionized target particles (atoms, molecules, clusters), remove surface-adsorbed material and lead to projectile neutralization. The transfer of electrons between surface and projectile possibly acts as precursor for the above-mentioned processes and makes them to proceed irrespective of the kinetic projectile energy. The importance of such “electronic” processes increases with multicharged projectile ions and their role is elucidated when slow ions of same kinetic energy but with different charge states are applied as projectiles.

For certain insulator surfaces, the impact of slow multicharged ions (MCIs) Z^{q+} gives rise to considerably stronger ablation than the well-established kinetic sputtering by neutral or ionized projectiles. First experimental evidence for “potential sputtering” (PS) was reported for alkali-halide surfaces and explained by “Coulomb explosion” [1], i.e., creation of small positively charged surface spots from the

rapid electron capture by impinging MCI, and the subsequent ablation because of strong mutual target ion repulsion. “Coulomb explosion” was also invoked in order to explain atomic-force microscopic (AFM) observations of blister-like defects on mica samples produced by highly charged ions Z^{q+} (kinetic energy 1–3 keV/amu) [2]. However, studies for impact of slow (≤ 1 keV) MCI on thin polycrystalline films of alkali-halides (LiF, NaCl) and Al_2O_3 deposited on quartz microbalance crystals [3] suggested a different explanation for PS, namely defect-stimulated desorption induced by very efficient electron capture [4]. It has been established that such desorption processes are induced by electrons (ESD) or photons (PSD) on such materials where self-trapping of specific crystal defects proceeds via electron–phonon coupling in the crystal lattice [5]. However, such defect trapping as the prerequisite for PS may also be caused or at least supported by the kinetic projectile energy (“kinetically assisted PS” [6]), which could also explain some PS-like effects reported for target species where no electron–phonon coupling can take place, i.e., for semiconductors like Si and GaAs [2]. In any case, for slow ion impact the self-trapping mechanism is most relevant for PS. Consequently, for metal and semiconductor surfaces no slow MCI-induced PS can be observed, so far [7].

As the surface region from which a slow MCI does capture electrons should be rather small (nm extensions), it is

* Corresponding author. Tel.: +43-1-58801-13401;

fax: +43-1-58801-13499.

E-mail address: winter@iap.tuwien.ac.at (H.P. Winter).

probable that the surface defects caused by PS are of similar size. In order to study such defect structures we have applied AFM in ultra-high vacuum (UHV) on monocrystalline target surfaces of insulator species for which PS by slow MCI impact has already been demonstrated on polycrystalline thin films [3,6,7].

We have carried out AFM studies for, e.g., SiO₂ and Al₂O₃ (cf. Section 3) and obtained results which are of possible interest for nanostructuring these surfaces.

For comparison, similar studies have also been performed with a highly oriented pyrolytic graphite (HOPG) surface. As graphite is a good electrical conductor, no PS is expected to take place there. On the other hand, numerous studies have shown that for HOPG characteristic surface modifications can be produced by ion irradiation. In contrast to an insulator surface, for HOPG defects can be conveniently studied down to the atomic scale by means of scanning tunneling microscopy (STM), which has been applied with a combined AFM/STM setup (see Section 2). We could show (cf. Section 4) that impact of slow singly and multiply charged ions on a HOPG surface results in local modifications of the electronic structure but no topographical changes due to potential sputtering effects.

2. Experimental methods

Observations of slow ion-induced nanodefects on different atomically clean target surfaces have been made under strict UHV conditions with a combined AFM/STM instrument (UHV-AFM/STM, OMICRON Nanotechnology GmbH, Germany). We have looked for nanodefects on freshly prepared surfaces of SiO₂(0001) and sapphire *c*-plane Al₂O₃(0001) after irradiation with low doses of slow singly and multiply charged ions. In order to avoid disturbing noise from an ion irradiation chamber directly attached to the AFM/STM instrument, we have used a transportable UHV vault for target transfer which was alternately coupled via UHV locks to the target ion irradiation chamber and the AFM/STM. This procedure kept the target surfaces under permanent UHV conditions after initial cleaning, thermal annealing, and during subsequent slow ion irradiation until completion of the AFM/STM inspection. Ion irradiation of the insulator surfaces was accompanied by low-energy (≤ 4 eV) electron flooding to compensate for surface charge-up which otherwise strongly inhibits AFM observation or makes it even impossible. The electron gun was arranged at 2 cm distance to the sample. All AFM observations were made in the contact mode, with the base pressure in the AFM/STM chamber kept at about 10^{-10} mbar during measurements.

HOPG is rather easy to prepare with surface terraces which extend over several hundreds of nm. The HOPG samples were cleaved in air with adhesive tape and immediately put into the ultra-high vacuum chamber (base pressure below 10^{-9} mbar). Before ion irradiation a sample was heated

up to 300 °C, but during the irradiation experiment kept at room temperature. STM images were taken at constant current mode with negative sample bias voltage in the range of some mV to V and tunneling currents of 1–10 nA.

Electrochemically etched tungsten tips were used which provided excellent atomic resolution. Again, AFM data were taken in the contact mode.

The singly and multiply charged ions for target irradiation have been extracted from a 5 GHz ECR ion source [8], magnetically analyzed and guided via electrostatic lenses to the UHV irradiation chamber. The ions were decelerated in front of the target surface to their desired impact energy (≤ 1.2 keV). Uniform irradiation was assured by rapidly scanning the ion beam across the target surface by means of deflection plates.

3. Production of slow ion-induced surface defects on insulator targets (Al₂O₃, SiO₂)

3.1. Al₂O₃

Polished Al₂O₃(0001) *c*-plane single crystals (TBL Kelpin, Neuhausen, Germany) have been CO₂ snow cleaned and then annealed in UHV for 3 h at 400 °C. This preparation technique yields very flat crystal surfaces (see Fig. 1). AFM contact mode studies on 14 samples prepared by the standard preparation technique revealed a root mean square (rms) roughness of 0.093 ± 0.06 nm rms. Bombardment with Ar ions of different charge states and kinetic energies (500 eV Ar⁺ and Ar⁷⁺, 1.2 keV Ar⁺, Ar⁴⁺ and Ar⁷⁺) results—as seen in AFM contact mode—in hillock-like nanodefects (see Figs. 2 and 3).

We found that the ion-induced defects on the sapphire single crystal surface could be removed by annealing at 450 °C for 5 h. The density of nanodefects does not directly correspond with the applied ion dose: an ion dose of $5 \times$

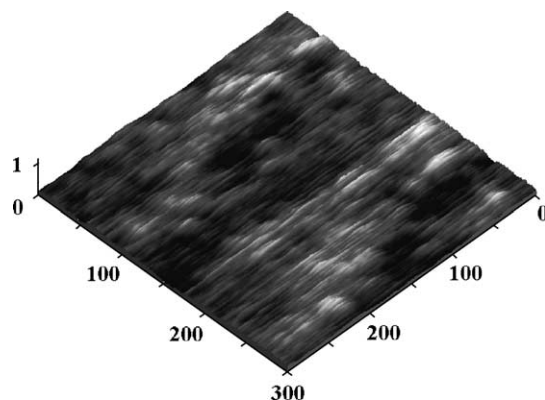


Fig. 1. UHV AFM contact mode image of a sapphire crystal prepared with standard single crystal preparation technique reveals very flat surfaces (rms *z* noise below 0.1 nm). Flat surfaces are a prerequisite for unambiguous assignment of the surface nanostructures produced by slow single ion impacts. All dimensions in nanometers.

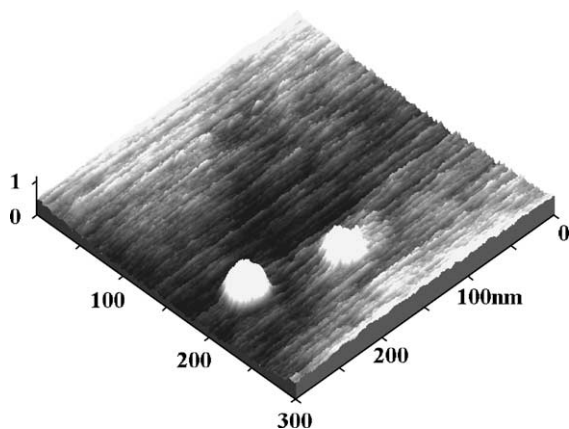


Fig. 2. UHV AFM contact mode image of sapphire (Al_2O_3 , c -plane 0001) bombarded with 500 eV Ar^+ ions. The defects are real topographic features; all dimensions in nanometers.

10^{12} ions/ cm^2 , which is equivalent to five ions per $10\text{ nm} \times 10\text{ nm}$, leads to a rather small, however reproducible, density of defects on the sapphire surface: about 10 nanodisks per $1000\text{ nm} \times 1000\text{ nm}$ can be observed after bombardment in the energy range reported in this paper. This is equivalent to a dose to defect ratio of 5000. A possibly similar migration and subsequent recombination of point defects at the surface has previously been reported for silicon bombarded by 5 keV He ions above 160 K [9]. In fact, the only case where the number of defects corresponded fairly well to the applied ion dose was for the conducting HOPG samples (see Section 4).

The Al_2O_3 c -plane proved to be the insulator surface showing most clearly a dependence of the ion bombardment-induced defects with the kinetic energy and charge states of the projectiles. 500 eV Ar^+ ions produce defects which are about 1 nm high (Fig. 2) and have lateral dimensions of some tens of nanometers (one should keep in mind that the

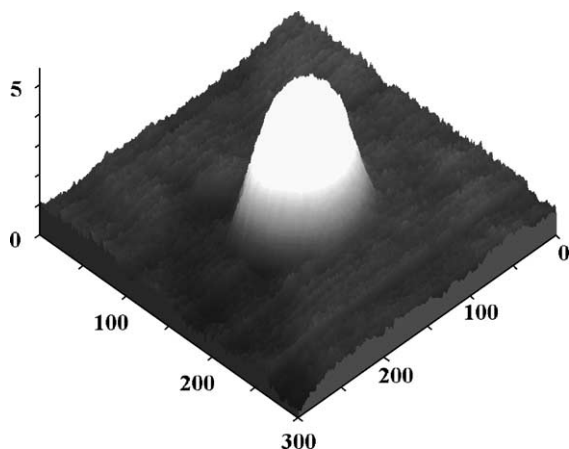


Fig. 3. UHV AFM contact mode image of sapphire (Al_2O_3 , c -plane 0001) bombarded with 500 eV Ar^{7+} ions. Nanodisks induced by these ions with same kinetic but higher potential energy as compared to Ar^+ ions (see Fig. 2) are considerably higher and wider than the ones caused by singly charged ions. All dimensions in nanometers.

height is more accurately measurable with the AFM than lateral dimensions), whereas the defects produced by 500 eV Ar^{7+} ions are several nanometers high (Fig. 3) and show lateral dimensions of about 100 (!) nanometers. At higher kinetic energy the differences in the slow ion-induced nanodisks on the sapphire c -plane became even more distinct. 1.2 keV Ar^+ -induced defects are up to about 8 nm high and their width is some 10 nm. For a higher charge state as Ar^{4+} , two different kinds of defects occurred on the sapphire surface. They have about the same height, but their lateral dimensions vary considerably: some are nearly 200 nm wide, whereas the smaller defects are only about 50 nm wide.

The height of both kinds of defects is about 2 nm. For Ar^{7+} , only one kind of defect was visible in the AFM images, with about 50 nm diameter and about 2 nm height (for a more detailed description of these results, see Gebeshuber et al., 2003).

3.2. SiO_2

Polished $\text{SiO}_2(0001)$ α -quartz single crystals (TBL Kelpin, Neuhausen, Germany) were CO_2 snow cleaned and then annealed in UHV at 400°C for 3 h. This preparation technique yielded very flat crystal surfaces. AFM contact mode studies on 14 such prepared crystals revealed a rms roughness of $0.16 \pm 0.01\text{ nm rms}$. The quartz crystals were then bombarded with 1 keV Ar^+ ions. UHV AFM imaging of the surface topography revealed ion-induced nanostructures, i.e., the surface was covered with hillocks a few nanometers high (see Fig. 4). The density of these hillocks did not directly correspond to the applied ion dose: for a dose of five incident 1 keV Ar^+ ions per $10\text{ nm} \times 10\text{ nm}$ (5×10^{12} ions/ cm^2), we observe about 30 nanostructures on an area of $1000\text{ nm} \times 1000\text{ nm}$, which indicates that not every single ion has caused one nanodisk on the quartz surface. The dose to defect ratio on the quartz substrate is about 1700. Probably several ion impacts are needed to induce one AFM-detectable surface modification. We could not yet establish an ion-charge state dependence of observed defects.

The fact that apparently hillocks are observed instead of craters is not yet understood. Several possible explanations can be given. In AFM as for other scanning probe microscopy (SPM) methods it is more straightforward to image elevated structures than craters. Narrow tall surface features in the vicinity of craters would completely mask the latter because of their convolution with the tip shape. Several other groups have used AFM as investigative method and reported hillock-like surface modifications after bombardment with heavy ions for up to GeV energies. By means of AFM, Audouard et al. [10] have studied the surface of amorphous metallic ribbons irradiated with swift heavy ions. Ion impacts resulted in the formation of hillocks at 300 K for ions with high stopping power of $\geq 55\text{ keV/nm}$. However, irradiation at 80 K did not induce noticeable modifications of the surface of the ribbons. These results

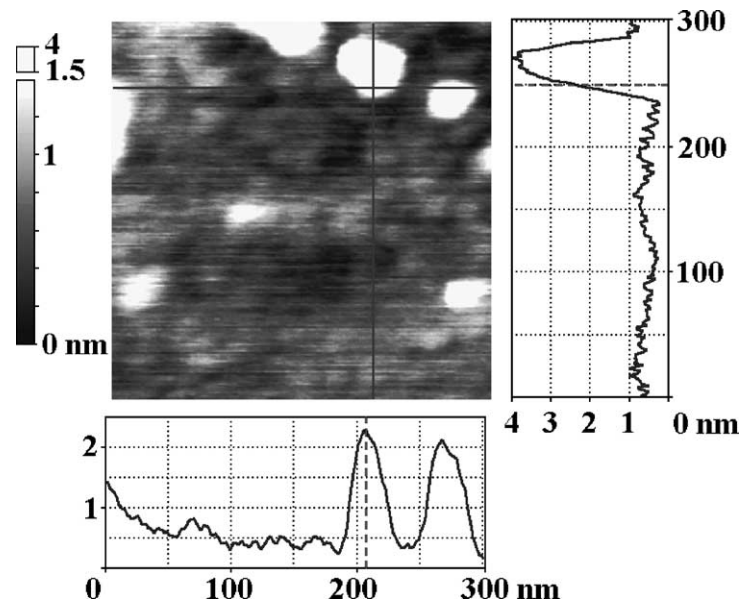


Fig. 4. Line profiles of $\text{SiO}_2(0001)$ single crystal surface after bombardment with 1 keV Ar^+ ions (UHV AFM contact mode).

indicate that formation of hillocks, which are flattened by the sample growth, is essentially caused by the damage created by electronic excitation in individual ion tracks. In another experiment, Audouard et al. [11] studied with AFM modifications of surface topography of amorphous metallic alloys irradiated with swift heavy ions. Irradiation with Pb or U ions with rather high stopping power $(dE/dx)_e$ led to the formation of hillocks surrounded by craters, whereas no visible modifications of the specimen surface was observed after irradiation with Kr ions with lower $(dE/dx)_e$. These authors ascribed formation of hillocks to the damage created in individual ion tracks, while craters were linked to anisotropic growth phenomena. Both processes are thus induced by severe electronic excitation in the wake of incident ions.

4. Slow ion-induced surface defects on HOPG

Surface defects in HOPG produced by the impact of individual (singly charged) ions have already been investigated via STM/AFM by a number of groups (see [12–21] and further references therein). However, only recently first results have been reported for impact of slow multiply charged ions and the effect of the projectile charge state (or potential energy) on the size of the produced nanodefects [22,23]. Moreover, in most previous studies either STM in air was used or the irradiated samples were transported in air towards STM inspection after ion bombardment. If, e.g., chemical bonds at the surface are broken due to the ion impact, impurities could preferentially adsorb at these

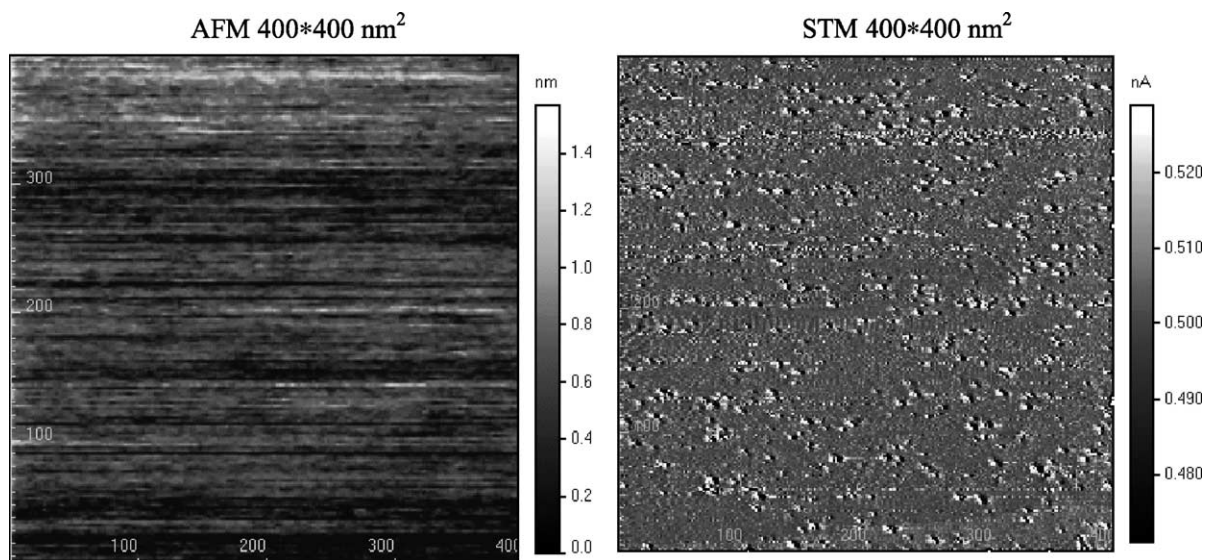


Fig. 5. AFM and STM scans of HOPG bombarded with 1200 eV Ar^+ ions. In the AFM scan no topographic changes can be detected. Only the STM reveals the defects in the electronic structure.

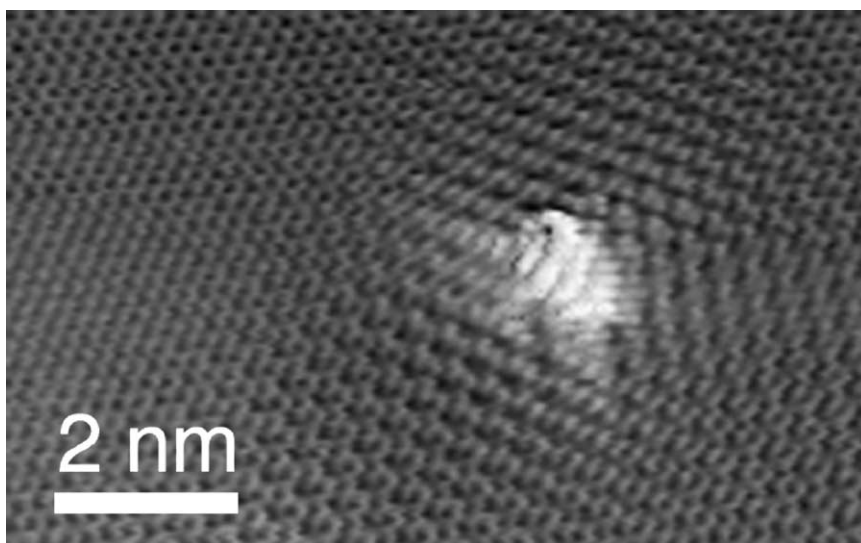


Fig. 6. STM image of defect produced by the impact of a single (150 eV) Ar^{9+} ion on HOPG.

sites and thus change the topography of the surface (and the resulting STM image) during contact with air. Therefore, in our studies MCI bombardment has been followed by STM/AFM investigations without breaking the ultra-high vacuum (see Section 2). In this way possible influences from target surface exposure to air could be ruled out.

Fig. 5 shows typical AFM and STM scans of HOPG samples bombarded with 1200 eV Ar^+ ions. In the AFM scan, no significant topographic changes can be detected. On the contrary, the STM image reveals a large number of individual nanosized defects as the result of the ion bombardment. Several hundred defects from different sample positions have been statistically analyzed for each projectile type (Ar^+ , Ar^{8+} , Ar^{9+}). Fig. 6 shows the enlarged STM image of a typical defect on HOPG created by the impact of a single Ar^{9+} ion of 150 eV kinetic energy.

Figs. 7 and 8 show examples of STM 3D-images of a highly oriented pyrolytic graphite surface bombarded with 150 eV Ar^+ and Ar^{9+} ions, respectively. The images were

taken from a 16-bit black and white graphics and processed by the SXM image program using a calculated shadow by illuminating the images from the right.

The only surface defects found in the STM images (cf. examples in Figs. 6–8) are “protrusions” (hillocks) with a mean lateral size of 0.8–1.25 nm and an average equivalent height of 0.22 nm. They are randomly dispersed on the originally flat surface. Their area density is in good agreement with the applied ion dose, implying that nearly every single ion impact has caused one protrusion. A $\sqrt{3} \times \sqrt{3} R30^\circ$ surface reconstruction, as characteristic for interstitial defects in HOPG [20,21,24], surrounded by undisturbed surface parts is observed in the vicinity of most defects (see Figs. 6–8).

Scanning with our AFM down to atomic resolution on the irradiated surface did not show any significant topological changes due to ion bombardment. Therefore, we conclude that the defects observed are mainly due to changes in the electronic density of states of the surface.

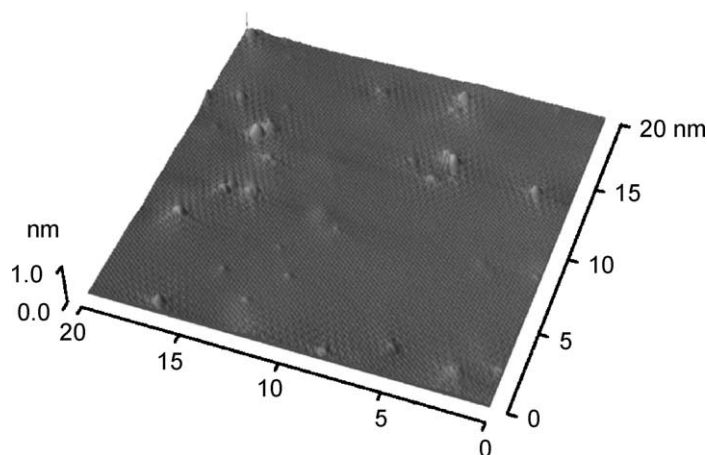


Fig. 7. STM image of HOPG surface bombarded by singly charged Ar ions of 150 eV kinetic energy (tunneling current: 0.58 nA, bias voltage: 0.5 V).

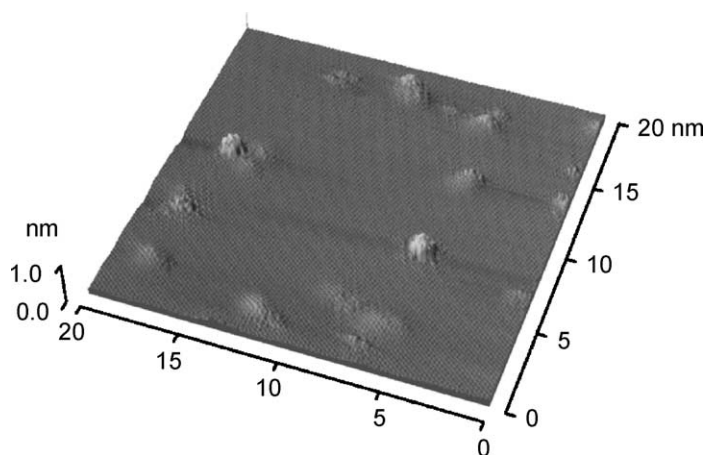


Fig. 8. STM image of HOPG surface bombarded by Ar^{9+} ions of 150 eV kinetic energy (tunneling current: 0.55 nA, bias voltage: 0.4 V).

For impact of singly charged ions, our findings are in good agreement with previous observations [16,21]. As a remarkable result, however, we find that the measured mean diameter of the “hillocks” and to a somewhat lesser extent their “height” increase with projectile charge state (see Fig. 9). The corresponding statistical distribution of the evaluated damage height and the full width at half maximum (FWHM) due to Ar^+ and Ar^{9+} ion bombardment of the HOPG surface are shown in Fig. 10.

In a careful STM study, Hahn and Kang [21] have shown that generally two kinds of defects in HOPG are created under low energy (100 eV) Ar^+ bombardment, namely carbon vacancy defects (VDs) and interstitial defects (IDs) formed by trapping the projectile beneath the first carbon plane.

Both types of defects are detected as protrusions in the STM topographic image. The dangling bonds at the VD site cause an enhancement of the local charge density-of-states (CDOS) near the Fermi energy, seen as a protrusion in the STM image [21]. The protrusion observed in the STM image at ID sites results from a small geometric deformation of the graphite basal plane due to the trapped projectile (not large enough to be visible in our AFM scans) and an apparently larger electronic defect due to an increased CDOS. Only for IDs but not for VDs a $\sqrt{3} \times \sqrt{3} R30^\circ$ surface reconstruction was reported [21]. From this $\sqrt{3} \times \sqrt{3} R30^\circ$ superlattice structure also observed in our experiments (see Fig. 11), we, therefore, conclude that the majority of the “hillocks” observed are due to IDs, or VDs created along with IDs.

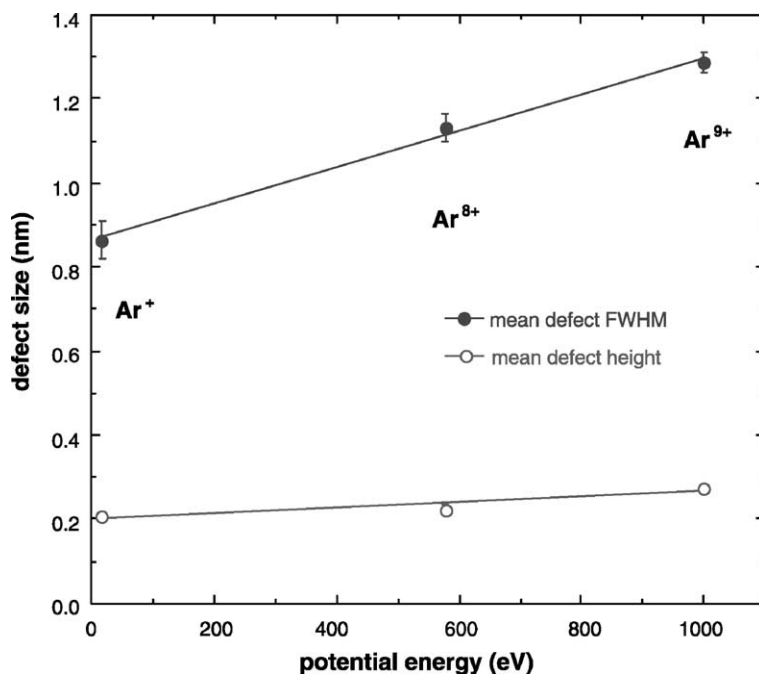


Fig. 9. Mean height and width (FWHM) of defect structures produced by impact of 150 eV Ar^{q+} ($q = 1, 8, 9$) ions on HOPG. For each projectile species data were obtained from different STM images by evaluating all visible defects.

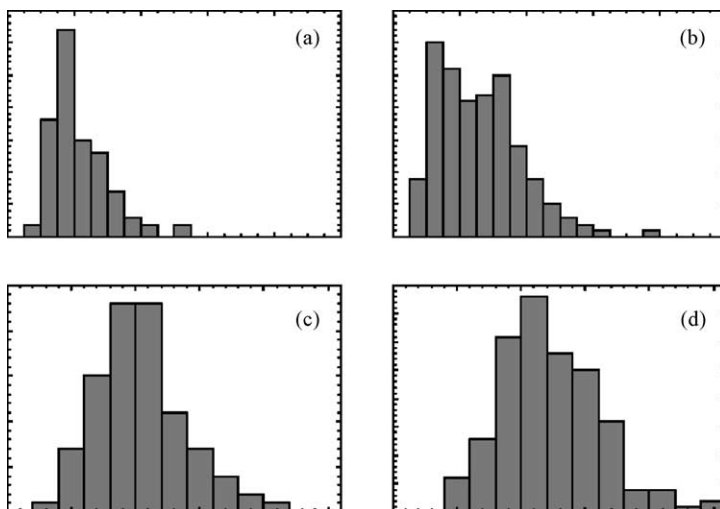


Fig. 10. Statistical distribution of damage height (a, b) and full width at half maximum (FWHM) (c, d) due to singly charged Ar ion impact (a, c) and Ar^{9+} ion impact (b, d) on HOPG.

The strong increase of the lateral protrusion size with increasing charge state of the projectile ion is interpreted as a “pre-equilibrium” effect of the stopping of slow multiply charged ions in HOPG, as has so far only been observed

for higher charge states [17]. Although MCI are converted already into neutral hollow atoms during their approach towards the surface, their captured electrons remain in highly excited states until surface impact, where they are gradually

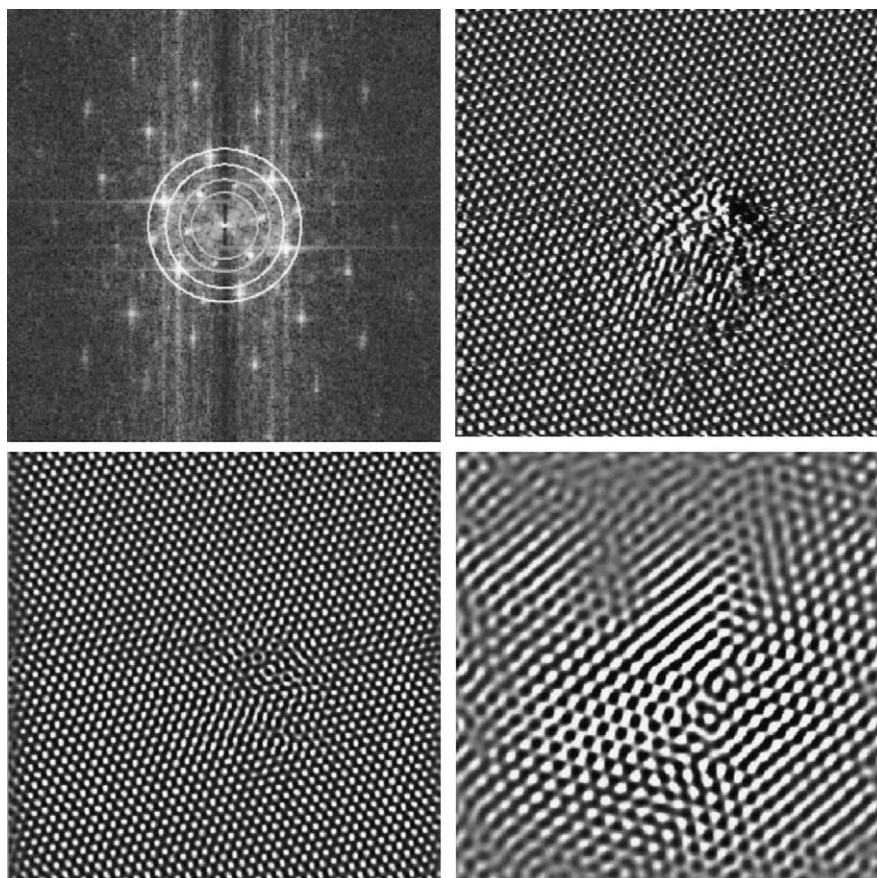


Fig. 11. Fourier transform (top left) of a tunneling current image of a Ar^+ ion-induced defect on HOPG (top right). Filtering and inverse fast Fourier transformation allow for separation of the contributions from the undisturbed crystal lattice (bottom left, reconstructed from frequencies within the white circles) and ion-induced superstructure (bottom right, reconstructed from frequencies within the green circles), respectively. Top left and bottom tunneling current images $10 \text{ nm} \times 10 \text{ nm}$.

peeled off and replaced by conduction band electrons forming a partial screening cloud around the MCI [25]. Before final deexcitation of the hollow atom can take place within the solid, reduced screening should result in a strongly increased energy loss of the projectiles. According to SRIM 2000 calculations [26], the mean range of 150 eV Ar projectiles in HOPG is about two monolayers. An increased stopping and straggling of the higher charged Ar projectiles would lead to IDs located closer to the surface, as well as to more VDs due to a higher momentum transfer to the carbon atoms of the first plane. Because of the extreme surface sensitivity of STM this pre-equilibrium effect in the stopping power is not masked by (equilibrium) bulk effects and apparently observable with unprecedented clearness. From this AFM data we conclude that the nanodefects produced by slow ion impact are of electronic rather than of topographic nature.

5. Summary and conclusions

In this paper, we have described first evidence for potential sputtering (PS) effects on some atomically clean monocrystalline insulator surfaces, which was obtained by means of UHV AFM. Target samples were bombarded with slow (typically <1 keV) singly and multiply charged Ar^{q+} ions (up to $q = 7$). Keeping these target surfaces permanently under UHV conditions during initial annealing, ion irradiation and AFM inspection was found indispensable for obtaining unambiguous evidence for PS, i.e., nanodefects with a size clearly depending on the slow ion charge state. The fact that the observed number of defects does not correspond one-to-one to the ion dose will be investigated in more detailed experiments with different ion doses. Analysis of the statistics of random impacts will clarify how many individual ion impacts are needed to form a visible nanodefect on the insulator surface. In particular, Al_2O_3 was identified as a good candidate for PS-induced nanostructuring, and further studies for SiO_2 might probably lead to similar results. Both target materials are relevant for applications in microelectronics and nanotechnology.

In addition, we have searched for slow ion-induced nanodefects on atomically clean HOPG. Extending pertinent work by other groups with singly charged ions only, our combined STM/AFM studies revealed nanodefects which comprise a disturbance of the electronic density-of-states of the surface rather than its topography. Whereas the size of these defects increases with the ion charge (here up to $q = 9$), as expected for any conducting target surface they showed no evidence for potential sputtering.

Acknowledgements

This work has been supported by Austrian FWF under project no. 13543-PHY. The authors thank Dr. R. Wörgötter-Plunger for her cooperation in the early studies of insulator surfaces. Initial work with HOPG has greatly benefited from support by Drs. M. Schmid and P. Varga.

References

- [1] I.S. Bitensky, M.N. Murakhmetov, E.S. Parilis, *Sov. Phys. Tech. Phys.* 25 (1979) 618.
- [2] D.H. Schneider, M.A. Briere, J. McDonald, J. Biersack, *Radiat. Eff. Defects Solids* 127 (1993) 113; T. Schenkel, A.V. Hamza, A.V. Barnes, D.H. Schneider, *Progr. Surf. Sci.* 61 (1999) 23.
- [3] G. Hayderer, M. Schmid, P. Varga, H.P. Winter, F. Aumayr, *Rev. Sci. Instrum.* 70 (1999) 3696.
- [4] F. Aumayr, J. Burgdörfer, P. Varga, H.P. Winter, *Comments At. Mol. Phys.* 34 (1999) 201.
- [5] P. Townsend, in: R. Behrisch (Ed.), *Sputtering by Particle Bombardment II*, Springer, Berlin, 1983, Chapter 4, p. 147.
- [6] G. Hayderer, S. Cernusca, M. Schmid, P. Varga, H.P. Winter, F. Aumayr, D. Niemann, V. Hoffmann, N. Stolterfoht, C. Lemell, et al., *Phys. Rev. Lett.* 86 (2001) 3530.
- [7] P. Varga, T. Neidhard, M. Sporn, G. Libiseller, M. Schmid, F. Aumayr, H.P. Winter, *Phys. Scr.* T73 (1997) 307.
- [8] M. Leitner, D. Wutte, J. Brandstötter, F. Aumayr, H.P. Winter, *Rev. Sci. Instrum.* 65 (1994) 1091.
- [9] P.J. Bredrossian, T.D. de la Rubia, *J. Vac. Sci. Technol. A* 16 (1998) 1043.
- [10] A. Audouard, R. Mamy, M. Toulemonde, G. Szenes, L. Thome, *Nucl. Inst. Meth. Phys. Res. B* 146 (1998) 217.
- [11] A. Audouard, R. Mamy, M. Toulemonde, G. Szenes, L. Thome, *Europhys. Lett.* 40 (1997) 527.
- [12] L. Porte, C.H. de Villeneuve, M. Phaner, *J. Vac. Sci. Technol. B* 9 (1991) 1064.
- [13] R. Coregater, A. Claverie, A. Chahboun, V. Landry, F. Ajustron, J. Beauvillain, *Surf. Sci.* 262 (1992) 208.
- [14] H.X. You, N.M.D. Brown, K.F. Al-Assadi, *Surf. Sci.* 279 (1992) 189.
- [15] T. Mazukawa, et al., *Appl. Surf. Sci.* 107 (1996) 227.
- [16] K. Mochiji, S. Yamamoto, H. Shimizu, S. Ohtani, T. Seguchi, N. Kobayashi, *J. Appl. Phys.* 82 (1997) 6037.
- [17] K.P. Reimann, W. Bolse, U. Geyer, K.P. Lieb, *Europhys. Lett.* 30 (1995) 463.
- [18] S. Habenicht, W. Bolse, H. Feldermann, U. Geyer, H. Hofsäss, K.P. Lieb, F. Roccaforte, *Europhys. Lett.* 50 (2000) 209.
- [19] R. Neumann, et al., *Nucl. Instrum. Meth. B* 151 (1999) 42.
- [20] R. Hahn, K. Kang, S. Song, J. Jeon, *Phys. Rev. B* 53 (1996) 1725.
- [21] R. Hahn, K. Kang, *Phys. Rev. B* 60 (1999) 6007.
- [22] R. Minniti, L.P. Ratliff, J.D. Gillaspay, *Phys. Scr.* T92 (2001) 22.
- [23] G. Hayderer, S. Cernusca, M. Schmid, P. Varga, H.P. Winter, F. Aumayr, *Phys. Scr.* T92 (2001) 156.
- [24] A.V. Krashennnikov, F. Elsin, *Surf. Sci.* 454–456 (2000) 519.
- [25] H.P. Winter, F. Aumayr, *J. Phys. B: At. Mol. Opt. Phys.* 32 (1999) R39; A. Arnau, *Surf. Sci. Rep.* 229 (1997) 1.
- [26] J.F. Ziegler, J.P. Biersack, U. Littmark, *The Stopping and Range of Ions in Matter*, vol. 1, Pergamon, New York, 1985.

A.7 Surface nanostructures induced by slow highly charged ions on CaF₂ single crystals

El-Said A.S., Meissl W., Simon M.C., Crespo López-Urrutia J.R.,

Gebeshuber I.C., Lang M., Winter HP., Ullrich J. and Aumayr F.

Nucl. Instr. Meth. Phys. Res. B 256, 346-349 (2007)

Abstract

We present first results on the generation of surface nanostructures by slow HCI on cleaved CaF₂(111) surfaces. The CaF₂ single crystals were irradiated with slow ($v \leq 1$ a.u.) Xe⁴⁴⁺ HCI from the Heidelberg-EBIT. Like for other ionic fluoride single crystals, ion-induced surface structures in CaF₂ are known to be stable in atmospheric conditions at room temperature. After irradiation the crystals were investigated by scanning force microscopy. Topographic images reveal the generation of nanometric hillocks protruding from the surface. The number of hillocks per unit area is in agreement with the applied ion fluence. A discussion of the role of the potential energy as well as a comparison with observations for swift heavy ion irradiations of CaF₂ single crystals are presented.

Surface nanostructures induced by slow highly charged ions on CaF₂ single crystals

A.S. El-Said^a, W. Meissl^a, M.C. Simon^a, J.R. Crespo López-Urrutia^b, I.C. Gebeshuber^a, M. Lang^c, HP. Winter^a, J. Ullrich^b, F. Aumayr^{a,*}

^a *Institut für Allgemeine Physik, Technische Universität Wien, A-1040 Wien, Austria*

^b *Max-Planck Institut für Kernphysik, D-69029 Heidelberg, Germany*

^c *Gesellschaft für Schwerionenforschung, D-64291 Darmstadt, Germany*

Available online 5 January 2007

Abstract

We present first results on the generation of surface nanostructures by slow HCI on cleaved CaF₂ (111) surfaces. The CaF₂ single crystals were irradiated with slow ($v \ll 1$ a.u.) Xe⁴⁴⁺ HCI from the Heidelberg-EBIT. Like for other ionic fluoride single crystals, ion-induced surface structures in CaF₂ are known to be stable in atmospheric conditions at room temperature. After irradiation the crystals were investigated by scanning force microscopy. Topographic images reveal the generation of nanometric hillocks protruding from the surface. The number of hillocks per unit area is in agreement with the applied ion fluence. A discussion of the role of the potential energy as well as a comparison with observations for swift heavy ion irradiations of CaF₂ single crystals are presented.

© 2006 Elsevier B.V. All rights reserved.

PACS: 79.20.Rf; 68.37.Ps; 68.35.Dv

1. Introduction

Damage creation in ion-surface collisions is strongly correlated to ion-energy deposition in the solid and therefore depends on both the kinetic and the potential energies carried by the ions [1]. The kinetic energy loss of a projectile (stopping power) is usually subdivided into an “electronic” (inelastic) and a “nuclear” (elastic) part (see insert in Fig. 1).

For slow singly charged or neutral atoms, nuclear stopping dominates the energy loss (case ① in Fig. 1). This energy transfer to target cores leads to atomic displacements and lattice vibrations in the target (phonons) and can become sufficiently large to initiate a collision cascade where also the recoiling target atoms contribute to electronic excitation and displacement in the solid [2]. The low kinetic energy of the incident projectile limits its total

path length and therefore the region where energy is deposited to a few monolayers close to the surface [3].

For swift ions or atoms (case ② in Fig. 1) scattering from the target nuclei becomes negligible, but in this case dominant electronic energy loss leads to a high ionization density around the (practically straight) ion tracks (see e.g. [4,5] and references therein). In addition, inner shell ionization processes produce fast δ electrons which can considerably enlarge the region where electronic excitation/ionization of the target takes place.

For slow highly charged ions (HCI, case ③ in Fig. 1) the potential energy (e.g. 51 keV in the case of Xe⁴⁴⁺) can be similar to or even exceed the ions kinetic energies. Via series of Auger processes, e.g. Auger neutralization, resonant capture followed by Auger de-excitation or multiple resonant capture followed by auto-ionization, the HCI potential energy is then transferred to the electronic subsystem of the solid within a shallow region close to the HCI impact zone (formation of “hollow atoms” see e.g. [6–9]), leading to a strong electronic excitation of a nanometer size surface area [2].

* Corresponding author. Tel.: +43 1 58801 13430; fax: +43 1 58801 13499.

E-mail address: aumayr@iap.tuwien.ac.at (F. Aumayr).

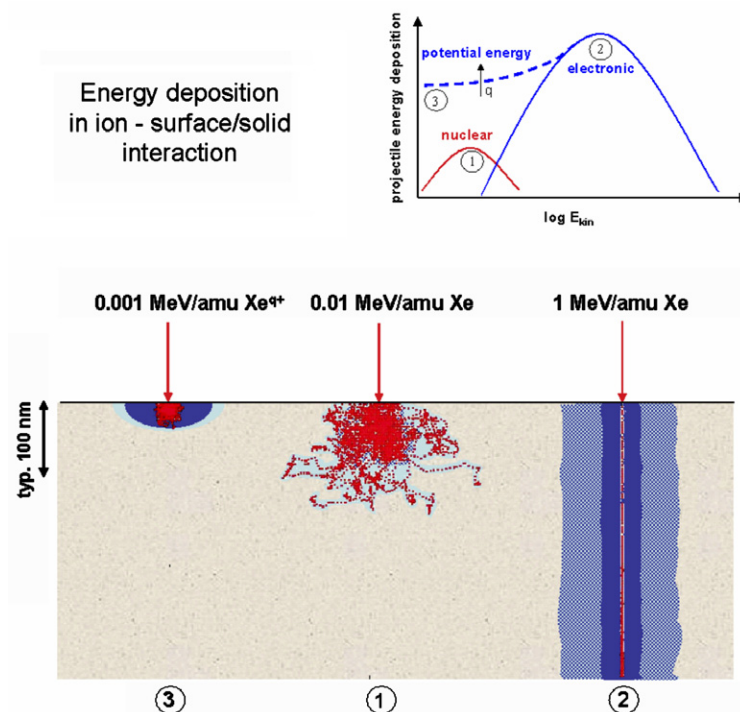


Fig. 1. Energy deposition during interaction with a solid surface (schematic, c.f. text) of ① slow single charged ions or neutral atoms, ② swift ions or neutral atoms, ③ slow highly charged ions.

In recent years, great efforts have been made to investigate the surface damage induced by high energy ions (MeV to GeV impact energy region) in several ionic fluoride single crystals e.g. LiF, CaF₂, BaF₂, MgF₂ and LaF₃ [10–14]. While the long term goal of these studies has been to reach a clearer understanding of the damage creation mechanisms, the short term goal aimed at obtaining information about the created surface features and their dependence on the ion-beam parameters and material properties. Scanning force microscopy (SFM) has been used as the primary tool to observe surface structures on insulating surfaces on a nanometer scale [15]. The SFM micrographs of the swift ion-irradiated single ionic fluoride crystals showed nanoscopic hillocks protruding from the surface. However, such hillocks are only found for projectile ions where the electronic energy loss (S_e) typically exceeds a threshold of 5 keV/nm [11,13]. Above this threshold both the diameter and height of the hillocks increase with the electronic stopping power S_e [13].

The nanostructures created by swift heavy ions are usually accompanied by damage created deep inside the bulk. This sets limits for using high-energy ions in nanotechnological applications. Continuous development of ion source technology in the recent years made it possible to produce beams of slow ($v < v_{\text{Bohr}} = 2.19 \times 10^6$ m/s) highly charged ions (HCI) and use them for ion-surface interaction studies [9,16–22].

In this report we present first results from SFM investigations of surface nanostructures induced by HCI in an ionic crystal interesting for various applications, namely calcium fluoride (CaF₂).

2. Experiments

The experiments were performed on CaF₂(1 1 1) surfaces freshly cleaved in air. Cleavage is known to result in a fluorine-terminated surface. Contact mode ambient SFM on this surface has been performed and revealed large atomically flat terraces with occasional cleavage steps, separating individual terraces. Several freshly cleaved samples were mounted on a special target holder and transferred into the vacuum chamber which was evacuated to a base pressure in the 10^{-10} mbar range. The CaF₂(1 1 1) single crystal targets were then irradiated at room temperature with ¹²⁹Xe⁴⁴⁺ ions from the Heidelberg-EBIT (electron beam ion trap) [23] using two different ion impact energies (2.2 and 3.3 keV/amu). Typical ion fluxes of 10^4 ions/s (measured via electron emission statistics detection [24,25]) and an irradiation time of several hours resulted in a total ion fluence of 2×10^9 ions/cm².

After irradiation, the crystals were investigated by an MFP-3D scanning force microscope (Asylum Research, Santa Barbara, US) under ambient conditions. This system is equipped with closed-loop nanopositioning system sensors for the correction of piezo hysteresis and creep. Furthermore it allows for simultaneous SFM and optical measurements of transparent and opaque samples due to top-view optics and an inverted microscope base. The measurements have been performed in contact mode at constant loading force of less than 10 nN, using non-conductive Si₃N₄ sensors (Veeco Instruments, France) with cantilevers of force constants of about 0.1 N/m.

3. Results and discussion

Fig. 2 shows examples of typical SFM topographic images of $\text{CaF}_2(111)$ after irradiation with Xe^{44+} ions of 2.2 and 3.3 keV/amu impact energy per unit mass, respectively. Surprisingly, hillock-like nanostructures protruding from the surface are observed despite the fact that the electronic energy loss of the projectile ions in CaF_2 is well below the kinetic threshold for hillock production of 5 keV/nm (see Table 1). The SFM images were evaluated with respect to hillock height and width distributions (see Fig. 3) as well as hillock number. The number of hillocks per unit area was found to be in good agreement with the applied ion fluence. This means that (similar to the case of slow HCI impact on HOPG; see e.g. [19,26]) basically each observed hillock results from an individual ion impact. The shape of the hillocks is almost circular. Due to the low surface roughness of the non-irradiated samples, the dimensional analysis was easy to perform. The diameter of the hillocks is defined by two opposite points marking the intersections of a vertical line profile through the hillock maximum with the undisturbed CaF_2 surface [13]. A slight change of the set point (loading force) did not lead to an observable change of the measured features. We are well aware of the possible occurrence of a systematic error of the order of few nanometers for the hillock diameter caused by the finite tip curvature radius. In contrast to the diameter, the height should not be affected by the finite SFM tip radius but mainly by the roughness of the sample. The mean hillocks diameter and

Table 1

Ion-beam parameters and measured hillock sizes

	Slow Xe^{44+}	Slow Xe^{44+}	Swift Xe [11]
Kinetic energy (keV/amu)	2.2	3.3	6400
Ion range (nm) [3]	84	117	46000
Electronic energy loss (keV/nm) [3]	1.09	1.31	19.5
Nuclear energy loss (keV/nm) [3]	2.85	2.56	0.02
Mean hillocks diameter (nm)	28.1 ± 0.4	28.3 ± 0.5	23.5 ± 0.4
Mean hillocks height (nm)	0.9 ± 0.1	0.9 ± 0.1	3.8 ± 0.2

height were determined by fitting a Gaussian function to the hillock frequency-versus-diameter/-height histograms (Fig. 3). In Table 1 the ion-irradiation parameters (some of them estimated by using TRIM [3]) as well as the measured mean hillock diameters and height values are given. No significant difference in hillock size was found for the two different Xe^{44+} impact energies of 2.2 and 3.3 keV/amu. This independence on impact energy together with the fact that our experiments were conducted for S_e values well below the kinetic threshold for hillock production leads us to the conclusion that the potential energy stored in Xe^{44+} ions (i.e. the sum of ionization potentials) of about 51 keV should be responsible for the hillock production.

Table 1 also compares the results of our measurements to the hillock dimensions observed for swift Xe ion impact from [11]. Surprisingly, the mean diameter of the hillocks in case of low energy Xe^{44+} bombardment is comparable to (even slightly larger than) the diameters observed after irra-

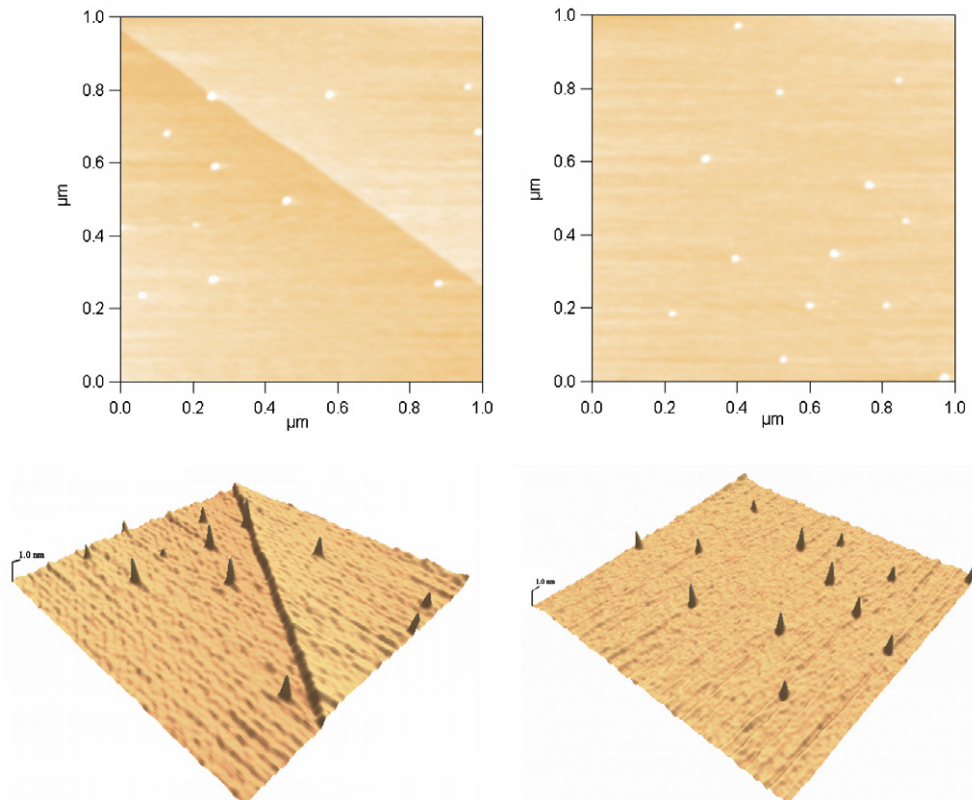


Fig. 2. Topographic SFM images for CaF_2 single crystal irradiated with Xe^{44+} ($E_k = 2.2$ keV/amu) [left] and Xe^{44+} ($E_k = 3.3$ keV/amu) [right] ions.

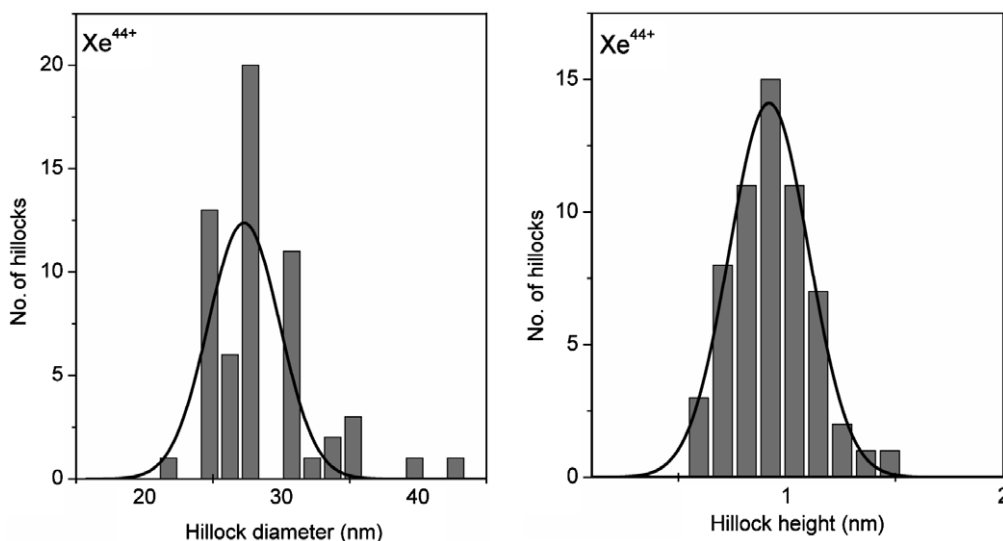


Fig. 3. Frequency distribution of hillock diameter (left) and hillock height (right) for CaF_2 single crystal irradiated with Xe^{44+} ($E_k = 3.3$ keV/amu) ions. The mean values are obtained by fitting a Gaussian curve to the data.

diation with Xe ions of more than 800 MeV kinetic energy, while the hillock height is about a factor of 4 smaller. The similarity between the two cases is probably a result of the fact that both swift heavy ions and slow HCI initially transfer their energy to the electronic system of the target, leading to a region of strong electronic excitation (see Fig. 1 and discussion in Section 1).

Our results therefore not only show for the first time that nano-sized hillocks on a CaF_2 (111) surface can be produced by impact of slow HCI, but also demonstrate the relevance of the potential energy of the projectiles for creation of these nanostructures. By performing SFM investigations of the hillock size as a function of the potential of the projectile HCI (by varying the projectile charge state and species) we hope to achieve a clearer understanding of the hillock formation mechanism. Such investigations are currently in progress.

Acknowledgement

This work has been supported by Austrian Science Foundation FWF (Projects Nos. M894-N02 and P17449). The experiments were performed at the distributed ITS-LEIF-Infrastructure at MPI Heidelberg Germany, supported by Transnational Access granted by the European Project RII3 026015.

References

- [1] H. Gnaser, *Low-Energy Ion Irradiation of Solid Surfaces*, Springer, Berlin, 1999.
- [2] P. Sigmund (Ed.), *Fundamental Processes in Sputtering of Atoms and Molecules (SPUT 92)*, Mat.Fys.Medd., Copenhagen, 1993.
- [3] J.F. Ziegler, J.P. Biersack, U. Littmark, *The Stopping and Range of Ions in Matter*, Pergamon, New York, 1985.
- [4] G. Schiewietz, E. Luderer, G. Xiao, P.L. Grande, *Nucl. Instr. and Meth. B* 175 (2001) 1.
- [5] W.M. Arnoldbik, N. Tomozeiu, F.H.P.M. Habraken, *Nucl. Instr. and Meth. B* 203 (2003) 151.
- [6] A. Arnau et al., *Surf. Sci. Rep.* 27 (1997) 113.
- [7] HP. Winter, F. Aumayr, *J. Phys. B: At. Mol. Opt. Phys.* 32 (1999) R39.
- [8] HP. Winter, F. Aumayr, *Eur. Phys. News* 33 (2002) 215.
- [9] F. Aumayr, HP. Winter, *Phil. Trans. Roy. Soc. (London)* 362 (2004) 77.
- [10] C. Müller, A. Benyagoub, M. Lang, R. Neumann, K. Schwartz, M. Toulemonde, C. Trautmann, *Nucl. Instr. and Meth. B* 209 (2003) 175.
- [11] C. Müller, M. Cranney, A.S. El-Said, N. Ishikawa, A. Iwase, M. Lang, R. Neumann, *Nucl. Instr. and Meth. B* 191 (2002) 246.
- [12] N. Khalfaoui, C.C. Rotaru, S. Bouffard, M. Toulemonde, J.P. Stoquert, F. Haas, C. Trautmann, J. Jensen, A. Dunlop, *Nucl. Instr. and Meth. B* 240 (2005) 819.
- [13] A.S. El-Said, M. Cranney, N. Ishikawa, A. Iwase, R. Neumann, K. Schwartz, M. Toulemonde, C. Trautmann, *Nucl. Instr. and Meth. B* 218 (2004) 492.
- [14] A.S. El-Said, R. Neumann, K. Schwartz, C. Trautmann, *Rad. Eff. Def. Sol.* 157 (2002) 649.
- [15] G. Binning, C.F. Quate, C. Gerber, *Phys. Rev. Lett.* 56 (1986) 930.
- [16] D. Schneider et al., *Phys. Rev. A* 42 (1990) 3889.
- [17] T. Schenkel, A.V. Hamza, A.V. Barnes, D.H. Schneider, *Progr. Surf. Sci.* 61 (1999) 23.
- [18] L.P. Ratliff, E.W. Bell, D.C. Parks, A.I. Pikin, J.D. Gillaspay, *Appl. Phys. Lett.* 75 (1999) 590.
- [19] G. Hayderer, S. Cernusca, M. Schmid, P. Varga, HP. Winter, F. Aumayr, *Physica Scripta T92* (2000) 156.
- [20] F. Aumayr, HP. Winter, *e-J. Surf. Sci. Nanotech.* 1 (2003) 171.
- [21] N. Nakamura, M. Terada, Y. Nakai, Y. Kanai, S. Ohtani, K. Komaki, Y. Yamazaki, *Nucl. Instr. and Meth. B* 232 (2005) 261.
- [22] M. Terada, N. Nakamura, Y. Nakai, Y. Kanai, S. Ohtani, K. Komaki, Y. Yamazaki, *Nucl. Instr. and Meth. B* 235 (2005) 452.
- [23] J.R. Crespo López-Urrutia, B. Bapat, B. Feuerstein, D. Fischer, H. Lörch, R. Moshhammer, J. Ullrich, *Hyperfine Interact.* 146/147 (2003) 109.
- [24] F. Aumayr, G. Lakits, HP. Winter, *Appl. Surf. Sci.* 47 (1991) 139.
- [25] W. Meissl, M.C. Simon, J.R. Crespo Lopez-Urrutia, H. Tawara, J. Ullrich, HP. Winter, F. Aumayr, *Rev. Sci. Instrum.* 77 (2006) 093303.
- [26] S. Takahashi, M. Tona, K. Nagata, N. Yoshiyasu, N. Nakamura, M. Sakurai, C. Yamada, S. Ohtani, *Nucl. Instr. and Meth. B* 235 (2005) 456; N. Yoshiyasu et al., *Jpn. J. Appl. Phys* 45 (2006) 995.

A.8 Potential energy threshold for nanohillock formation by impact of slow highly charged ions on a CaF₂(111) surface

El-Said A.S., Meissl W., Simon M.C., Crespo López-Urrutia J.R., Lemell C., Burgdörfer J., **Gebeshuber I.C.**, Winter HP., Ullrich J., Trautmann C., Toulemonde M. and Aumayr F.

Nucl. Instr. Meth. Phys. Res. B 258, 167-171 (2007)

Abstract

We investigate the formation of nano-sized hillocks on the (111) surface of CaF₂ single crystals by impact of slow highly charged ions. Atomic force microscopy reveals a surprisingly sharp and well-defined threshold of potential energy carried into the collision of about 14 keV for hillock formation. Estimates of the energy density deposited suggest that the threshold is linked to a solid-liquid phase transition (“melting”) on the nanoscale. With increasing potential energy, both the basal diameter and the height of the hillocks increase. The present results reveal a remarkable similarity between the present predominantly potential energy driven process and track formation by the thermal spike of swift (~ GeV) heavy ions.

Potential energy threshold for nano-hillock formation by impact of slow highly charged ions on a $\text{CaF}_2(111)$ surface

A.S. El-Said^a, W. Meissl^a, M.C. Simon^a, J.R. Crespo López-Urrutia^c, C. Lemell^b,
J. Burgdörfer^b, I.C. Gebeshuber^a, HP. Winter^a, J. Ullrich^c, C. Trautmann^d,
M. Toulemonde^c, F. Aumayr^{a,*}

^a Institut für Allgemeine Physik, Vienna University of Technology, 1040 Vienna, Austria

^b Institute for Theoretical Physics, Vienna University of Technology, 1040 Vienna, Austria

^c Max-Planck Institute for Nuclear Physics, 69029 Heidelberg, Germany

^d Gesellschaft für Schwerionenforschung (GSI), 64291 Darmstadt, Germany

^e Centre Interdisciplinaire de Recherches Ions Laser (CIRIL), Laboratoire Commun CEA, CNRS, UCBN, ENSICAEN, BP5133, 14070 Caen Cedex 5, France

Available online 8 January 2007

Abstract

We investigate the formation of nano-sized hillocks on the (111) surface of CaF_2 single crystals by impact of slow highly charged ions. Atomic force microscopy reveals a surprisingly sharp and well-defined threshold of potential energy carried into the collision of about 14 keV for hillock formation. Estimates of the energy density deposited suggest that the threshold is linked to a solid–liquid phase transition (“melting”) on the nanoscale. With increasing potential energy, both the basal diameter and the height of the hillocks increase. The present results reveal a remarkable similarity between the present predominantly potential energy driven process and track formation by the thermal spike of swift ($\sim\text{GeV}$) heavy ions.

© 2007 Elsevier B.V. All rights reserved.

PACS: 34.50.Dy; 79.20.Rf; 61.80.Jh

1. Introduction

The surface topography of many solids experiences drastic modifications when exposed to energetic ions. The changes induced depend on the target material as well as on various beam parameters such as charge, energy, mass and fluence of the incoming projectiles and can result in well-ordered patterns, such as ripples or self ordered dots [1–3]. Impact of single ions has been demonstrated to induce nano-sized hillocks on metals, semiconductors and dielectric targets. Remarkably enough, the hillocks observed have a similar height (a few nm) and diameter

(20–40 nm) although the beam energies used span several orders of magnitude reaching up to GeV.

Impact of swift heavy ions is known to induce physical, chemical and structural modifications not only on the surface but also in the bulk (see e.g. [4–6] and references therein). Individual projectiles form cylindrical tracks around their trajectory of a few nanometers in diameter. Track formation sets in above a critical value of the energy loss dE/dx of the projectiles and occurs particularly in insulators (e.g. polymers, oxides, ionic crystals). Depending on the solid, tracks consist of amorphised or defect-rich material. In non-amorphisable alkali and alkaline earth halides (e.g. LiF and CaF_2) the damage process is governed by exciton-mediated defects such as color centers and defect clusters [7,8]. Above a critical value of dE/dx , damage produced in the core of the track leads to a macroscopic

* Corresponding author. Tel.: +43 1 58801 13430; fax: +43 1 58801 13499.

E-mail address: aumayr@iap.tuwien.ac.at (F. Aumayr).

volume increase (swelling, [9,10]), track etchability [7], and stress [11]. At the surface of ionic crystals, swift ions induce nanometric hillocks [12,13] above a threshold value similar to that for swelling [10]. Although numerous experimental data are available for hillock formation due to swift heavy ion impact, the principle of the mechanism is still not yet fully understood.

In this paper we present experiments with *slow* ($v_p \approx 0.3$ a.u.) highly charged ions (HCI) which also induce hillock-like nanostructures on the surface of CaF_2 single crystals. These nanostructures closely resemble those created by fast ions. Moreover, we find a strong dependence of the formation on the potential energy rather than on the stopping power. Most surprisingly, we find a well-defined threshold of potential energy required for the onset of nano-hillock formation. Since CaF_2 is used as an insulator in silicon microelectronic devices [14,15] epitaxially grown on semiconductor surfaces [16], our findings might be of importance for high resolution patterning of thin CaF_2 films on Si and for the creation of nanostructured templates for adlayer growth during fabrication of CaF_2/Si -based epitaxial insulator-semiconductor structures.

2. Experimental setup

Our experiments were performed on air-cleaved $\text{CaF}_2(111)$ surfaces. Cleavage is known to result in a fluorine-terminated surface. Contact-mode atomic force

microscopy (AFM) in air revealed large atomically flat surfaces with occasional cleavage steps separating individual terraces. Several freshly cleaved CaF_2 samples were mounted in a vacuum chamber of pressure in the 10^{-10} mbar range and irradiated normal to the (111) surface with HCI of kinetic energy below 5 keV per nucleon. The irradiation was performed at the Heidelberg electron beam ion trap [17] using $^{40}\text{Ar}^{q+}$ ($q = 11, 12, 14, 16, 17$ and 18) as well as $^{129}\text{Xe}^{q+}$ ($q = 22, 26, 28, 30, 33, 36, 40, 44, 46$ and 48) projectiles during several runs. The extraction voltage was 10 kV (for Xe^{44+} also 6.4 kV) equivalent to a kinetic energy of 10 kV (6.4 kV) times charge q resulting in a projected range between 90 and 140 nm in CaF_2 , assuming that stopping power and range are unaffected by the high charge state (see below) [18]. The beam flux varied between 10^3 and several 10^4 ions/s and was measured via electron-emission statistics with close to 100% detection efficiency [19,20]. After exposure to fluences up to $(0.5 - 5) \times 10^9$ ions/cm², the surface of the crystals was inspected in ambient air by contact-mode AFM. As reported earlier for CaF_2 single crystals irradiated with swift heavy ions, the surface hillocks are stable in atmosphere at room temperature [12].

3. Results and discussion

Fig. 1 shows examples of AFM topographic images of $\text{CaF}_2(111)$ after irradiation with Xe^{28+} (2.2 keV/amu),

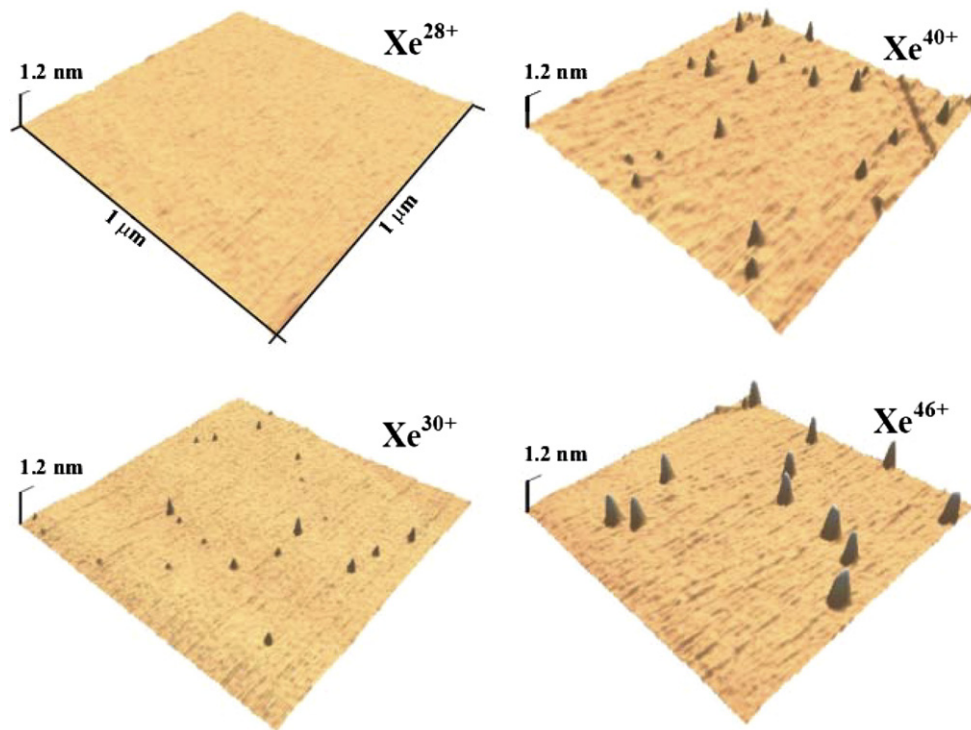


Fig. 1. Topographic contact-mode AFM images of a $\text{CaF}_2(111)$ surface irradiated by $10q$ keV Xe^{q+} ions of charge state $q = 28, 30, 40, 46$. In each frame an area of $1 \mu\text{m} \times 1 \mu\text{m}$ is displayed. Hillock-like nanostructures protruding from the surface are only observed for Xe projectiles with charge state $q \geq 30$. Above this threshold, the height and diameter of the hillocks increase with ion charge state.

Xe^{30+} (2.3 keV/amu), Xe^{40+} (3.1 keV/amu) and Xe^{46+} (3.6 keV/amu) ions. Hillock-like nanostructures protruding from the surface are observed for highly charged Xe^{q+} ($q \geq 30$) and fully stripped Ar^{18+} ions whereas targets irradiated with Xe^{q+} ($q \leq 28$) and Ar^{q+} ($q \leq 17$) projectiles did not exhibit any hillocks. The sharp transition, e.g. between $q = 17$ and 18 of argon cannot be associated with irradiation parameters in an obvious way. Moreover, results from measurements with $6.4 \cdot q$ keV (2.2 keV/amu) Xe^{44+} differ by less than 5% from the data of $10 \cdot q$ keV (i.e. 3.4 keV/amu) Xe^{44+} ions. It appears that the kinetic energy plays no decisive role for the size of the observed nanostructures.

The AFM images were evaluated with respect to number density, height and width distributions of the hillocks. The number of the hillocks per unit area was found to be in good agreement with the applied ion fluence, i.e. above the threshold, a large majority of projectiles (>70%) produces an individual hillock each. Their height ranges between 0.5 and 1 nm and their diameter between ~ 20 and 60 nm. Due to the finite curvature radius of the AFM tip (nominally 4–5 nm), the diameter (but not the height) of the hillocks is subject to a systematic error. The protrusions are rather flat with a diameter to height ratio between 40 and 60. In contrast to hillocks induced by swift heavy ions [12], we observe only a weak correlation between the diameter and height value of a given hillock. Furthermore, the size data were found to be strongly dependent on the potential energy the projectile carries into the HCI-surface collision (Fig. 2).

The potential (i.e. internal) energy E_p of HCI is equal to the total ionization energy required for producing the high charge state from its neutral ground state. E_p is known to have a strong influence on surface interaction processes such as electron-emission, sputtering and secondary ion emission [20]. For both Xe and Ar ions a remarkably well-defined sharp threshold in potential energy (between $E_p \approx 12$ keV for Xe^{28+} and $E_p \approx 14.4$ keV for Ar^{18+}) for hillock formation emerges. Above this threshold, an increase of the potential energy leads to an increase of both the basal diameter and the height of the hillocks. Another steep increase of the mean hillock diameter potentially indicating a second threshold is found between Xe^{44+} and Xe^{46+} (top of Fig. 2).

A convenient starting point for an analysis of the observed hillock formation is the interaction of the HCI above the surface involving a series of complex processes on different time and energy scales. When the ion approaches the surface, neutralization starts by electron transfer from the target into highly excited states of the projectile [21–23]. Deexcitation of the projectile proceeds via Auger-type processes producing primarily low energy electrons. Only for very highly charged heavy ions with open K and L shells electron energies up to several keV can be expected. For these states, however, radiative decay becomes important as a competing deexcitation mechanism with fluorescence yields of typically $\sim 12\%$ [24]. An increasing amount of potential energy is therefore dissipated by

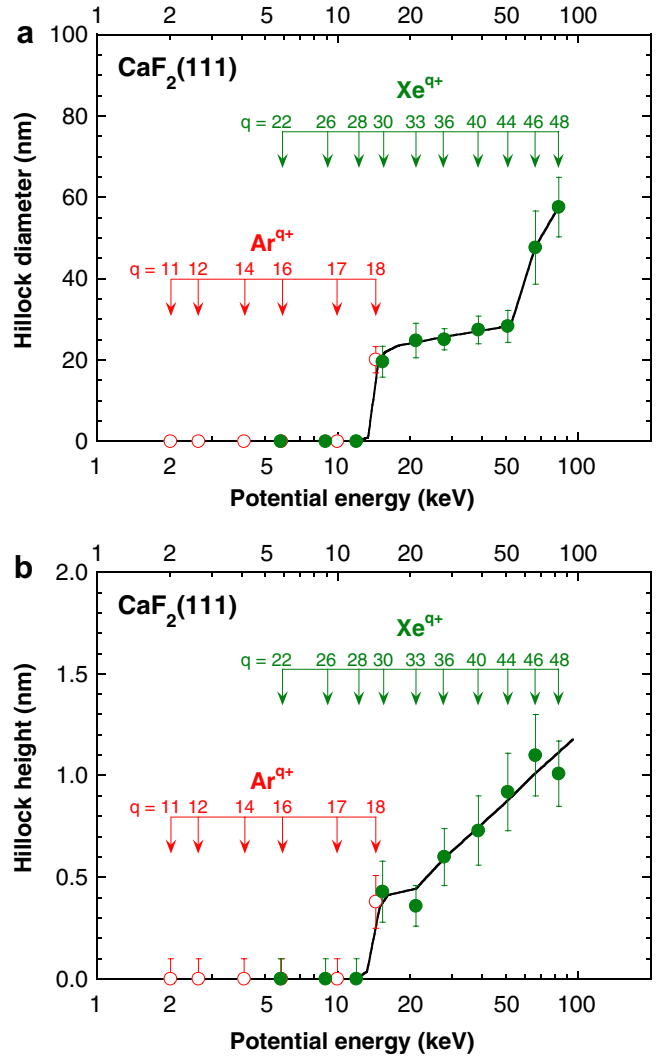


Fig. 2. Mean diameter (top) and height (bottom) of hillock-like nanostructures as a function of the potential energy of Ar^{q+} (open symbol) and Xe^{q+} (full symbol) projectiles. Hillocks are found only above a potential energy threshold of about 14 keV. The error bars correspond to the standard deviation of the diameter and height distributions; the solid lines are drawn to guide the eye.

X-ray emission. The critical distance R_c from the surface for electron transfer to the HCI can be estimated as [25]

$$R_c \approx \frac{\sqrt{2q\varepsilon(8i + \varepsilon - 1)}}{(\varepsilon + 1)W}, \quad (1)$$

where i is the amount of charge left behind (for the first electron capture $i = 1$) and W and ε are the work function and the dielectric constant of the material, respectively. For CaF_2 we find $R_c \approx 0.16\sqrt{q}$ nm, which sets an upper limit for the time available for the above-surface neutralization sequence. As an example, for an ion of $q = 40$, R_c is about 1 nm and the neutralization time is of the order of 1 fs. As the projectile velocity is also proportional to \sqrt{q} in our experiment, the above-surface interaction time is the same for all projectiles with equal acceleration voltage. The transfer of electrons to the projectile leaves unbalanced holes in

the surface which store part of the potential energy of the HCI. It is known from electron-emission yield measurements that $\sim 3q$ electrons are emitted per projectile [20]. For the impact of a $q = 40$ ion we therefore estimate a number of about 150 unbalanced holes (emitted electrons + electrons required for neutralization) created. They diffuse only slowly into the material (hole velocity in the valence band derived from tight-binding calculations is smaller than 0.33 nm/fs [26]). Furthermore, two holes (F^0 atoms) in adjacent sites recombine to volatile fluorine gas molecules leaving behind a Ca-enriched metallic surface. Upon impact of the projectile the target is structurally weakened and features fluorine depleted, defect-enriched areas.

For an analysis and interpretation of our data, we adapt aspects of the inelastic thermal spike model developed for swift ions [27]. The underlying assumption is that the initial deposition of projectile energy involves the electronic subsystem of the target and proceeds on a (sub-) femtosecond scale while the energy transfer to the lattice and the concomitant lattice deformation and defect production occurs on a (sub-) picosecond scale. The present case of slow HCI differs, however, substantially in two aspects. The primary energy distribution of “hot” electrons results from a relaxation process of a hollow-atom rather than from a Bethe-Born type ionization spectrum. A significant fraction of the potential energy is emitted by energetic (\sim keV) inner-shell Auger electrons. Moreover, slow HCI deposit their potential energy in a shallow surface region, whereas swift ions deposit kinetic energy along the full length of their trajectory within a cylindrical volume.

In the following we estimate the amount of energy and the target volume in which HCI deposit their potential energy. From calorimetric measurements it is known [28] that only part of the potential energy is transferred to the target. We suppose that this fraction is around 50% with an uncertainty of 20%. The excited target electrons spread their energy within ~ 100 fs by diffusion into a hemispherical volume around the impact site with a radius large compared to the source volume determined by the hollow-atom relaxation ($R_c \approx 1$ nm). In turn, the diffusing hot electron distribution transfers energy to the lattice by inelastic electron-phonon scattering with a characteristic time constant τ_e —ph of a few hundred fs. Phonon-mediated energy transport leads to further spread and thermalization.

Assuming, for simplicity, the same overall thermal diffusion length $\lambda_D \approx 4$ nm as observed for swift ions in CaF_2 [27], the fraction of internal energy E_D is deposited in a hemisphere of radius λ_D comprising about $N \approx 8.5 \times 10^3$ atoms. If the energy deposition per atom, E_D/N , within this locally heated volume exceeds the melting energy of $E_M = 0.55$ eV/atom [29] a solid–liquid phase transition is expected. Likewise, for $E_D/N > E_S = 1.55$ eV/atom [29], sublimation should set in. In order to have these energies available at the impact site, the HCI needs a potential energy above $E_M^{\text{th}} = 14$ keV and $E_S^{\text{th}} = 40$ V, respectively. Such a crude estimate carries a large error bar of about $\pm 50\%$ due to the uncertainty in the effective λ_D and the

fraction of deposited energy. The estimates are remarkably, maybe even fortuitously, close to the observed threshold for hillock formation (E_M^{th}) and for the second drastic, almost steplike size increase (E_S^{th}).

It should be noted, that the conceptual difficulty in applying the model of the thermalization of the internal energy within λ_D to slow HCI lies in the fact that the difference in internal energy between subthreshold (Ar^{17+}) and above threshold (Ar^{18+}) is emitted in one additional K-Auger electron with an energy of $E_K \approx 4.5$ keV and its large inelastic mean free path $\lambda_K \gg \lambda_D$. The deposition of this energy difference is thus not confined to the critical volume of melting or evaporation. Moreover, a large fraction of K-Auger electrons emitted near the surface is directly ejected into vacuum and a fraction of K-holes is dissipated by X-rays and thus unavailable for thermalization.

An alternative and additional heating mechanism could be the pre-equilibrium charge state dependent electronic and nuclear stopping in insulators strongly deviating from standard values for near-neutral projectiles in equilibrium [30]. Such deviations have been found for low but not negligible projectile velocity of $v_p \approx 0.3v_{\text{Bohr}}$. In a shallow region at and below the surface, a strong enhancement with charge state q of the kinetic energy deposition and, correspondingly, reduction of range is expected for highly charged ions. This could increase the energy deposition dE/dx near the surface to above the critical value for phase transition observed for swift heavy ions [27]. Future experiments at lower v_p should shed light on the role of this energy deposition process.

4. Conclusion

Irrespective of the not yet fully understood details of the heating mechanism, the following scenario emerges: hillock formation is the result of local melting and swelling when the energy deposition by HCI near the surface exceeds the melting energy $E_M = 0.55$ eV/atom. If the energy deposition exceeds the critical value for sublimation $E_S = 1.55$ eV/atom, evaporation should lead to the formation of blisters of enhanced size. Moreover, one should expect the transition from blister to crater formation when the evaporation is further enhanced. This scenario, however, suggests that crater formation should be more likely for even higher q and at near-grazing impact angles when the energy deposition concentrates near the topmost atomic layer, and direct evaporation into vacuum becomes possible.

In conclusion, the bombardment of a CaF_2 surface with moderately slow ($v_p = 0.3$ a.u.) highly charged Ar and Xe ions produces hillock-like surface nanostructures. The formation of these protrusions requires a critical potential energy of 14 keV (Ar^{18+} and Xe^{30+}). A second threshold characterized by a steep increase of hillock diameter appears at 50 keV (Xe^{44+}). In analogy to hillock formation by swift heavy ions, we associate the two thresholds with phase transitions of melting and sublimation caused by the deposition of the potential energy within the electronic

subsystem. The presently discussed scenario suggests future investigations of HCI induced nanostructures at smaller v_p , larger q and grazing incidence.

Acknowledgement

This work has been supported by Austrian Science Foundation FWF (Projects No. 17449 and M894-N02). The irradiation experiments were performed at the distributed ITS-LEIF-Infrastructure at MPI Heidelberg Germany, supported by Transnational Access granted by the European Project RII3#026015.

References

- [1] S. Facsko et al., *Science* 285 (1999) 1551.
- [2] M. Castro, R. Cuerno, L. Vázquez, R. Gago, *Phys. Rev. Lett.* 94 (2005) 016102.
- [3] B. Ziberi, F. Frost, Th. Höche, B. Rauschenbach, *Phys. Rev. B* 72 (2005) 235310.
- [4] R.L. Fleischer, P.B. Price, R.M. Walker, *J. Appl. Phys.* 36 (1965) 3645.
- [5] H. Dammak et al., *Phys. Rev. Lett.* 74 (1995) 1135.
- [6] L.T. Chadderton, *Radiat. Meas.* 36 (2003) 13.
- [7] C. Trautmann, K. Schwartz, O. Geiss, *J. Appl. Phys. A* 66 (1998) 3560.
- [8] K. Schwartz et al., *Phys. Rev. B* 70 (2004) 184104; C. Trautmann, M. Toulemonde, K. Schwartz, J.M. Costantini, A. Müller, *Nucl. Instr. and Meth. B* 164–165 (2000) 365.
- [9] M. Boccanfuso, A. Benyagoub, K. Schwartz, C. Trautmann, M. Toulemonde, *Nucl. Instr. and Meth. B* 191 (2002) 301.
- [10] C. Trautmann, M. Toulemonde, J.M. Costantini, J.J. Grob, K. Schwartz, *Phys. Rev. B* 62 (2000) 13; M. Boccanfuso, A. Benyagoub, K. Schwartz, M. Toulemonde, C. Trautmann, *Prog. Nucl. Energ.* 38 (2001) 271.
- [11] I. Manika, J. Maniks, K. Schwartz, M. Toulemonde, C. Trautmann, *Nucl. Instr. and Meth. B* 209 (2003) 93.
- [12] N. Khalfaoui et al., *Nucl. Instr. and Meth. B* 240 (2005) 819.
- [13] A.S. El-Said et al., *Nucl. Instr. and Meth. B* 218 (2004) 492; C. Müller et al., *Nucl. Instr. and Meth. B* 209 (2003) 175.
- [14] T.P. Smith, J.M. Phillips, W.M. Augustyniak, P.J. Stils, *Appl. Phys. Lett.* 45 (1984) 907.
- [15] L.J. Schowalter, R.W. Fathauer, *J. Vac. Sci. Technol.* 4 (1986) 1026.
- [16] C.A. Lucas, D. Loretto, *Appl. Phys. Lett.* 60 (1992) 2071.
- [17] J.R. Crespo López-Urrutia et al., *Hyperfine Interactions* 146–147 (2003) 109.
- [18] J.F. Ziegler, J.P. Biersack, U. Littmark, *The Stopping and Range of Ions in Solids*, Pergamon Press, New York, 1984.
- [19] W. Meissl et al., *Rev. Sci. Instrum.* 77 (2006) 093303.
- [20] A. Arnau et al., *Surf. Sci. Rep.* 27 (1997) 113.
- [21] J. Burgdörfer, P. Lerner, F.W. Meyer, *Phys. Rev. A* 44 (1991) 5674.
- [22] L. Hägg, C.O. Reinhold, J. Burgdörfer, *Phys. Rev. A* 55 (1997) 2097.
- [23] L. Wirtz, C.O. Reinhold, C. Lemell, J. Burgdörfer, *Phys. Rev. A* 67 (2003) 12903.
- [24] C.P. Bhalla, *Phys. Rev. A* 8 (1973) 2877.
- [25] A. Barany, C.J. Setterlind, *Heavy Ion Phys.* 1 (1995) 115.
- [26] J.P. Albert, C. Jouanin, C. Gout, *Phys. Rev. B* 16 (1977) 925.
- [27] M. Toulemonde, Ch. Dufour, A. Meftah, E. Paumier, *Nucl. Instr. and Meth. B* 166–167 (2000) 903; A. Meftah et al., *Nucl. Instr. and Meth. B* 237 (2005) 563.
- [28] U. Kentsch, H. Tyrroff, G. Zschornack, W. Möller, *Phys. Rev. Lett.* 87 (2001) 105504.
- [29] G. Grochtmann, R.J. Meyer, F. Peters, L. Gmelin, *Gmelins Handbuch der anorganischen Chemie*, Verlag Chemie, Berlin, 1970.
- [30] T. Schenkel et al., *Phys. Rev. Lett.* 79 (1997) 2030.

A.9 Diatom bionanotribology - Biological surfaces in relative motion: their design, friction, adhesion, lubrication and wear

Gebeshuber I.C., Stachelberger H. and Drack M.

J. Nanosci. Nanotechnol. 5(1), 79-87 (2005) (incl. title page)

Abstract

Tribology is the branch of engineering that deals with the interaction of surfaces in relative motion (as in bearings or gears): their design, friction, adhesion, lubrication and wear. Continuous miniaturization of technological devices like hard disc drives and biosensors increase the necessity for the fundamental understanding of tribological phenomena at the micro- and nanoscale.

Biological systems show optimized performance also at this scale. Examples for biological friction systems at different length scales include bacterial flagella, joints, articular cartilage and muscle connective tissues.

Scanning probe microscopy opened the nanocosmos to engineers: not only is microscopy now possible on the atomic scale, but even manipulation of single atoms and molecules can be performed with unprecedented precision. As opposed to this top-down approach, biological systems excel in bottom-up nanotechnology.

Our model system for bionanotribological investigations are diatoms, for they are small, highly reproductive, and since they are transparent, they are accessible with different kinds of optical microscopy methods. Furthermore, certain diatoms have proved to be rewarding samples for mechanical and topological in vivo investigations on the nanoscale.

There are several diatom species that actively move (e.g. *Bacillaria paxillifer* forms colonies in which the single cells slide against each other) or which can, as cell colonies, be elongated by as much as a major fraction of their original length (e.g. *Ellerbeckia arenaria* colonies can be reversibly elongated by one third of their original length). Therefore, we assume that some sort of lubrication of interactive surfaces is present in these species.

Current studies in diatom bionanotribology comprise techniques like atomic force microscopy, histochemical analysis, infrared spectrometry, molecular spectroscopy and confocal infrared microscopy.

January 2005

Volume 5 Number 1

Journal of
**NANOSCIENCE and
 NANOTECHNOLOGY**



Editor-in-Chief: Hari Singh Nalwa, USA

www.aspbs.com/jnn

A Special Issue on

Diatom Nanotechnology

GUEST EDITORS

Richard Gordon, Frithjof Sterrenburg, and Kenneth Sandhage



**AMERICAN
 SCIENTIFIC
 PUBLISHERS**



Diatom Bionanotribology—Biological Surfaces in Relative Motion: Their Design, Friction, Adhesion, Lubrication and Wear

Ille C. Gebeshuber,^{1,*} Herbert Stachelberger,² and Manfred Drack³

¹ Austrian Center of Competence for Tribology AC²T research GmbH, Viktor Kaplan-Strasse 2, A-2700 Wiener Neustadt, Austria and Institut für Allgemeine Physik, Technische Universität Wien, Wiedner Hauptstr. 8-10/E134, A-1040 Vienna, Austria

² Institute of Chemical Engineering, Technische Universität Wien, Getreidemarkt 9/E1667, A-1060 Vienna, Austria

³ Center for Appropriate Technology, Technische Universität Wien, Wiedner Hauptstr. 8-10/E0965, A-1040 Vienna, Austria

Tribology is the branch of engineering that deals with the interaction of surfaces in relative motion (as in bearings or gears): their design, friction, adhesion, lubrication and wear. Continuous miniaturization of technological devices like hard disc drives and biosensors increases the necessity for the fundamental understanding of tribological phenomena at the micro- and nanoscale.

Biological systems show optimized performance also at this scale. Examples for biological friction systems at different length scales include bacterial flagella, joints, articular cartilage and muscle connective tissues.¹

Scanning probe microscopy opened the nanocosmos to engineers: not only is microscopy now possible on the atomic scale, but even manipulation of single atoms and molecules can be performed with unprecedented precision. As opposed to this top-down approach, biological systems excel in bottom-up nanotechnology.

Our model system for bionanotribological investigations are diatoms, for they are small, highly reproductive, and since they are transparent, they are accessible with different kinds of optical microscopy methods. Furthermore, certain diatoms have proved to be rewarding samples for mechanical and topological *in vivo* investigations on the nanoscale.²

There are several diatom species that actively move (e.g. *Bacillaria paxillifer* forms colonies in which the single cells slide against each other) or which can, as cell colonies, be elongated by as much as a major fraction of their original length (e.g. *Ellerbeckia arenaria* colonies can be reversibly elongated by one third of their original length). Therefore, we assume that some sort of lubrication of interactive surfaces is present in these species.

Current studies in diatom bionanotribology comprise techniques like atomic force microscopy, histochemical analysis, infrared spectrometry, molecular spectroscopy and confocal infrared microscopy.

Keywords: Tribology, Lubrication, Friction, Wear, Biomimetics, Diatoms, Nanotribology, Bionanotribology, Natural Lubricants, Natural Adhesives, Environmentally Friendly Materials, Renewable Resources.

*Author to whom correspondence should be addressed.

1. INTRODUCTION

Diatoms are excellent. Their beauty is breathtaking and as organisms they are adapted to the many different aquatic environments in which they live. They offer invaluable hints about Nature's response to challenges. After all, Nature is an "engineering office" which has been "in business" for millions of years. We can learn a lot from these little gems. You are a tribologist and would like to understand lubrication in microsystems? Look at diatoms! You are an architect who wants to build lightweight, beautiful yet robust structures? Look at diatoms! You are a nanotechnologist who is looking for fast bottom-up rather than slow top-down approaches?^a Look at diatoms!

Nanotechnology is the creation of functional materials, devices, and systems through control of matter on the nanometer (1 to 100+ nm) scale and the exploitation of novel properties and phenomena developed at that scale. Nanotechnology has just begun, whereas many natural systems have evolved complex nanostructures during millions of years (see e.g. Fig. 1). Even the most complex molecular machines of a biological cell are no bigger than 25–50 nm. For a captivating description of miniature machinery in nature and technology see the book "Travels to the nanoworld."³

On December 29th 1959, the Nobel prize laureate Feynman gave his classic after-dinner speech "There's plenty of room at the bottom—an invitation to enter a new field of physics" at the annual meeting of the American Physical Society at the California Institute of Technology⁴ (for online version see <http://www.zyvex.com/nanotech/feynman.html>). In his speech, Feynman encouraged the scientific community to "think small" and predicted that many developments would accrue from our acquiring the ability to manipulate matter on very fine, even atomic, scales. He predicted the development of ultra-fast integrated circuits, electron beam lithography and even the ability to make objects by picking-and-placing single atoms. As a consequence, many consider him justifiably to be the father of the subject.

From Feynman's speculative beginnings, the field of nanotechnology has grown to the point of general public recognition of its philosophies and ideals. The total societal impact of nanotechnology is expected to be greater than the combined influences that the silicon integrated circuit, medical imaging, computer-aided engineering, and man-made polymers have had in the 20th century.

In 1999, Parkinson and Gordon pointed out the potential role of diatoms in nanotechnology via designing and producing specific frustule morphologies.⁵ In the same year, at the 15th North American Diatom Symposium, Gebeshuber and co-authors introduced atomic force

^a Top-down refers to the increasingly precise machining and finishing of materials from the macroscopic down to nanoscopic scales, bottom-up to synthesis from individual molecules or atoms.

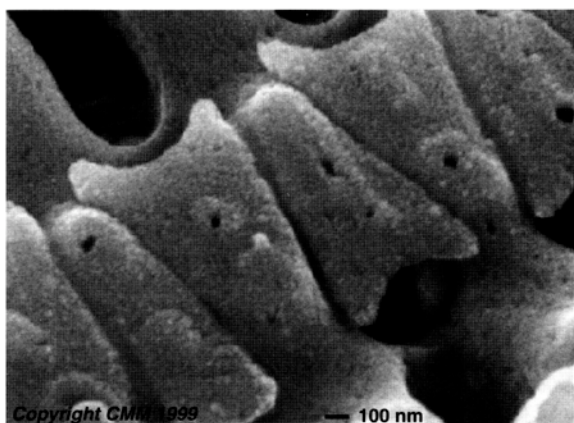


Fig. 1. Zipper-like structural detail on a diatom frustule (sample obtained from swimming pool filter material, probably *Aulacoseira granulata*). © Centre for Microscopy and Microanalysis, University of Queensland, Australia. Scalebar 100 nm.

microscopy and spectroscopy to the diatom community as new techniques for *in vivo* investigations of diatoms.⁶ These scanning probe techniques allow not only for the imaging of diatom topology, but also for the determination of physical properties like stiffness and adhesion.^{2, 7–11}

2. SCANNING PROBE MICROSCOPY METHODS

In scanning probe microscopy (SPM), surface properties can be studied at or near the atomic level. A scanning probe microscope raster scans a sharp probe over a surface. The mechanical, electrical, magnetic, optical and chemical interaction between the sharp probe and the surface provides a 3D representation of surface parameters. The samples can be in air, vacuum, or immersed in some liquid.

The most versatile and prominent type of SPM for uses in physics, chemistry and biology is the atomic force microscope (AFM). There are many good overviews on AFM available, e.g. Refs [12, 13]. The AFM senses forces that occur between a probe tip and a substratum. The probe used in AFM is a flexible cantilever, i.e. a horizontal structural element supported at one end, with a sharp tip at its free end. AFM cantilevers are very soft, i.e. have small spring constants, which allow for measurement of very small forces.

The development of scanning probe microscopy (SPM) with its ability not only to image but also to systematically organize and manipulate matter on the nanometer scale down to single atoms and molecules largely contributed to the birth of nanotechnology.

A classic experiment in SPM-related nanotechnology took place in 1990 when researchers from IBM Almaden positioned 35 Xenon atoms on a Nickel surface to spell the letters "IBM".¹⁴ In 1993, Eigler and co-workers positioned 48 iron atoms into a circular ring in order to

“corral” some surface state electrons and force them into quantum states of the circular structure. The ripples in the ring of atoms reveal the density distribution of a particular set of quantum states of the “corral”.¹⁵

As beautiful and interesting as these top-down nanotechnological experiments are, it takes many hours to manipulate and place the individual atoms and the experiments must be carried out at very low temperatures close to absolute zero. Another problem of top-down nanotechnology is that it faces problems building complex three dimensional structures.

Bottom-up nanotechnology, on the other hand, attempts to build up complex entities by using the self-assembling properties of molecular systems. This is more like a chemical or biological approach and it has some potential for making three dimensional structures cheaply, and in large quantities.

3. APPROPRIATE TECHNOLOGY IN TRIBOLOGY

The aim of biotribology is to gather information about friction, adhesion, lubrication and wear of biological systems and to apply this knowledge to innovate technology as well as to develop environmentally sound products. More specifically, the development of monolayer lubricants, of new adhesives and the construction of advanced artificial joints can result from such studies.¹ Especially in sensitive environments, the use of non toxic biodegradable lubricants is of paramount interest.¹⁶

The total amount of chain oils discharged into forest nature has been calculated at about two million litres per annum. The biodegradation of tall oil and rape seed oil (green oils) is clearly faster than that of mineral oils both in the laboratory and on the field.¹⁷

The release of lubricants into the water stream after passage through hydraulic turbines is also an environmental issue of concern. It was found that the use of self-lubricating bearing materials is the predominant technology available to satisfy environmental concerns for hydraulic equipment.¹⁸ As an alternative to the currently widely used metallic and polymer materials, hydraulic equipment can be lubricated with an environmentally sound lubricant. However, further research is necessary to optimize these lubricants concerning biodegradability and non-toxicity.

4. DIATOMS AS TRIBOLOGICAL MODEL SYSTEMS

We propose a new field in diatom nanotechnology: diatom bionanotribology.

Biological systems which endure friction have optimized their lubrication during evolution as far as necessary. The better the lubrication of a system which experiences friction is, the less is the wear. However, total

elimination of wear is impossible in any system with moving parts.

Algae can serve as interesting model organisms for nanotribological investigations. For an overview on algae see van den Hoek and co-authors.¹⁹ The class within the algae, which we favour for tribological studies, are diatoms (Fig. 2). For an overview on diatoms see Round et al.²⁰

Ellerbeckia arenaria is a diatom which lives in waterfalls (Fig. 3). *E. arenaria* cells form string like colonies which can be several millimeters long. A. M. Schmid told us in 2001 about their interesting mechanical properties: not only can these colonies be elongated by about one third of their original length, when released, they even swing back like a spring. Therefore, we performed the following experiment: *E. arenaria* cell colonies in water were visualized with a Zeiss Axiovert inverted microscope. One end of the colony, which was several millimeters long, was tightly held in place with forceps mounted on a 3D micromanipulator. The other end of the colony was approached with a very sharp scanning

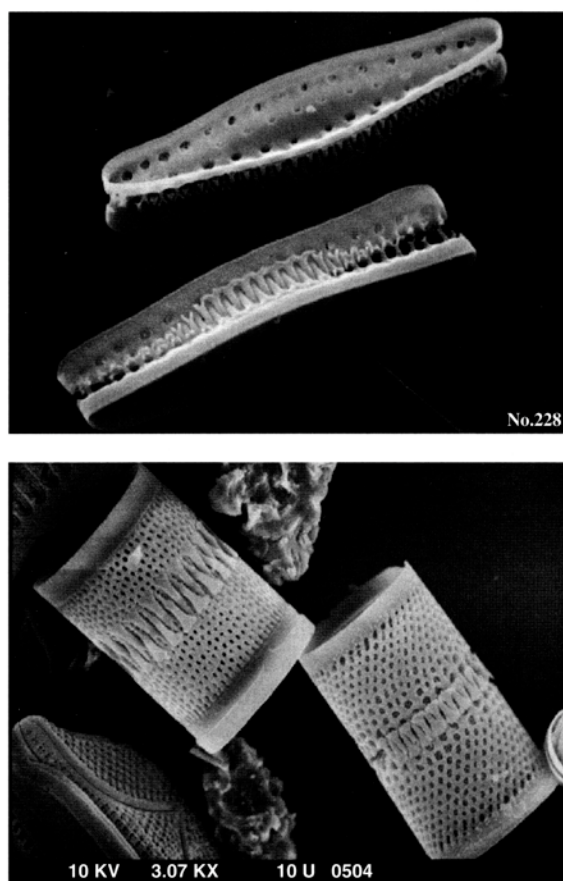


Fig. 2. The images show structural details of various diatom species which have interlocking fingerlike protuberances. These mechanical interlocks experience stress and strain, and therefore these species might be rewarding samples for bionanotribological investigations. Top: *Cymatoseira belgica* Grunow, bottom: *Aulacoseira italica* (Ehrenberg) Simonsen (left) and *Aulacoseira valida* (Grunow) Krammer (right). © RM Crawford, AWI Bremerhaven, Germany.

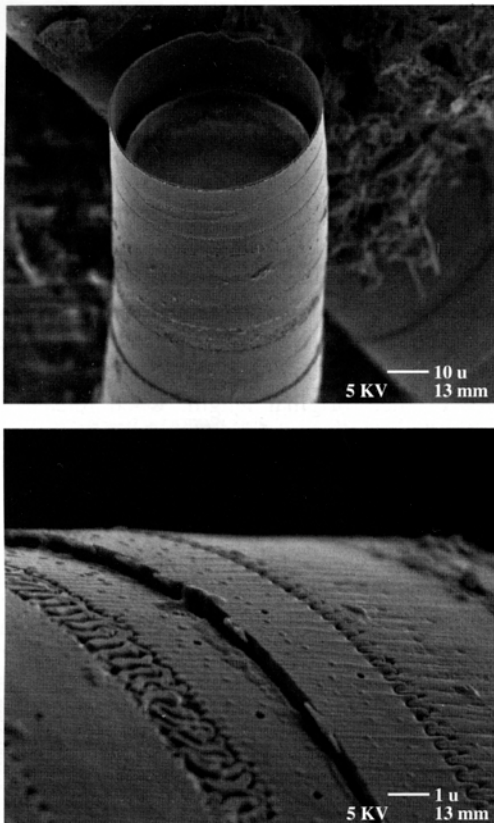


Fig. 3. *Ellerbeckia arenaria* is a colonial diatom which lives in waterfalls. The cell colonies can be reversibly elongated by about one third of their original length. These “biological rubber bands” might have solved any lubrication problems with techniques yet unknown to engineers.

tunneling microscope tip mounted on a second 3D micro-manipulator. Under visual control, the tip was stuck into one diatom close to the end of the colony. Now, the STM tip was horizontally moved until the elongation of the attached diatom colony was about one third of its original length. The STM tip was then released from the cell colony (via vertical movement), resulting in a “swing back” of the colony. From inserting the tip until release, the experiment took about five seconds.

This elongation and “swing back” indicate that there are parts in relative motion in *E. arenaria* colonies. It is yet to be determined whether these moving parts face friction and wear because of shear forces in the interface or whether expansion and contraction of organic material which links the parts takes place.

There might also be tribologically interesting processes in growing diatoms: Diatoms seem to show highly efficient self lubrication while girdle bands telescope, as the cells grow (for detailed discussion, see Ref. [2]). When we investigated an unknown benthic freshwater diatom species *in vivo* on the nanoscale with an atomic force microscope, we found bead-like features on the edges of certain girdle bands which might well act as lubricant, either by means of ball bearings or as solid lubricant—or

following a lubrication strategy which still is completely unknown to engineers (Fig. 4).

Although diatoms are photosynthesising microalgae, there are several species within this group that actively move: *Pseudonitzschia sp.* and *Bacillaria paxillifer* (the former name of this diatom is *Bacillaria paradoxa*, because of its unusual behaviour, Fig. 5) are good examples. *B. paxillifer* shows a remarkable form of gliding motility: Entire colonies of five to 30 cells expand and contract rhythmically and in coordination.²¹ Anomalously viscous mucilage excreted through a fissure that covers much of the cell length, may provide the means for the cell-to-cell attachment.²² Consequently, *Pseudonitzschia sp.* and *Bacillaria paradoxa* join *Ellerbeckia arenaria* as our candidates for bionanotribological investigations.

5. Technical Tribology

Biological and technical microsystems have many things in common. First of all, the mechanical interaction occurs at identical size and force scales.²³ In both types of systems, surface properties, e.g. wettability, nanostructure or surface chemistry have a strong impact on the performance of the system.

Micro- and nanotribology—considered as the mechanical interaction of moving bodies—is the science of friction, adhesion, lubrication and wear on the scale of micrometers to nanometers and the force scale of millinewtons to nanonewtons.

Some of the publications about nanoscale force measurements in diatoms (e.g. Refs [2, 8, 10, 11]) are indeed more than “just” nanoscale measurements, they even reach the single molecule level: Higgins and coworkers¹¹ report binding forces in the range of a few hundred piconewtons ($1 \text{ pN} = 10^{-12} \text{ N}$) for single adhesive strands protruding from the raphe of *C. australis*.

Biomicro- and nanotribology is a new interdisciplinary field of research combining methods and knowledge of physics, chemistry, mechanics and biology.

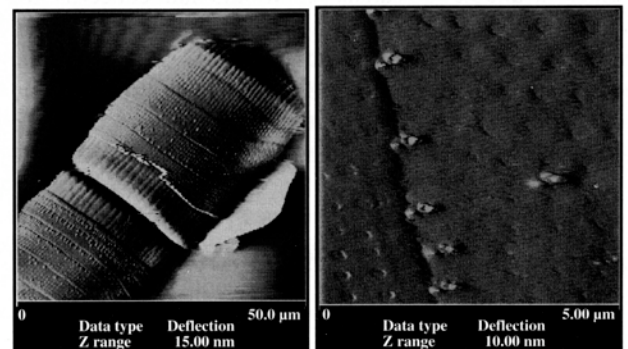


Fig. 4. Atomic force microscopy images (topography) of two interconnected diatom cells showing bead-like features, which might reduce friction. For detailed discussion see Gebeshuber et al. 2003. Left: Two cells of a yet unknown diatom species. Right: $5 \mu\text{m}$ zoom. © J. Microsc. Oxford.

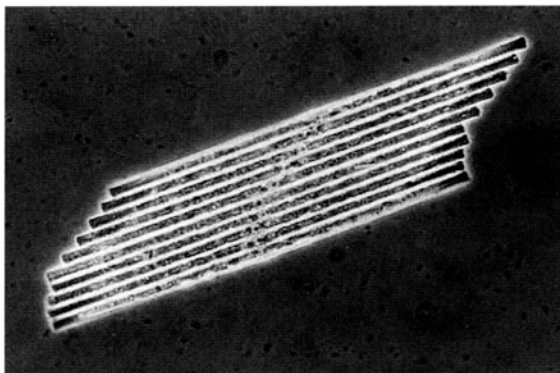


Fig. 5. A colony of ten *Bacillaria paxillifer* diatoms. The single cells are about 100 μm long. In motion, the cells glide along each other. We assume that biogenic lubricants protect the single cells from wear. © Wim van Egmond, Microscopy-UK.

5.1. Contact Mechanics

If two bodies contact each other in a point or a line, then the action of the compressive forces results in deformation. This has a strong impact on adhesion and friction. Contact mechanics represents a sophisticated synthesis of elasticity theory, fracture mechanics and surface science. Most of the contact models in tribology are based on the assumption of the contact of ideally smooth spheres. Recent models also incorporate the effects of roughness as well as the action of attractive forces inside the contact and in the vicinity of the contact radius. Since biological surfaces can be extremely flexible and soft, an intimate contact can be established. For a good overview on contact mechanics in tribology, see Ref. [24].

5.2. Viscoelasticity

The behaviour of a material is called viscoelastic if it combines flexible deformation according to Hooke's law ($F = -k \cdot x$) with Newtonian viscous flow. Newtonian viscous flow was first described by Newton in Principia in 1687.²⁵ It describes the simplest relation between shear stress and shear strain rate, namely that in which the shear stress is linearly proportional to the shear strain rate: $\tau = \eta \dot{\gamma}$. The parameter η is called the viscosity coefficient and may vary with the shearing rate. Viscoelasticity is characterized by the following features: relaxation, creep and hysteresis. Most, if not all biological tissues possess viscoelastic behaviour.²⁶

Subhash and co-workers performed a study of the indentation hardness and elastic properties of centric frustules of *Coscinodiscus concinnus* using nanoindentation.²⁷ These authors analysed more than one hundred indentations and found that the hardness varied between 0.001–0.189 GPa and the Young's modulus varied between 0.107–1.724 GPa. The Young's modulus values appear to be strongly dependent on the location of the indentation and the orientation of the frustule. In general, the frustule is stronger on the outer edge than inside.

5.3. Friction

Friction is an everyday experience. On one hand, friction is a desired property, and in fact necessary, for example for an insect to initiate motion. On the other hand, friction means loss of energy, and when friction is accompanied by wear, it also means damage and destruction.

An important concept in macroscale friction theory is the coefficient of friction, μ . The friction coefficient is defined as the relationship between the tangential (friction) force and the normal force. Note that only on the macroscale, this coefficient can be assigned a general value. On the micro- and nanoscale, the subtle influences of single contact points (asperities) can no longer be averaged due to the small dimensions and small normal forces.

Macroscale friction can be caused by mechanical interlock due to the roughness of the contacting surfaces. To maintain the motion of a body against the friction force, it is necessary to perform work. Not only does a moving body experience a friction force—force is also necessary to overcome inertia and static friction. It is necessary to differentiate between static, sliding and rolling friction. In sliding and rolling friction, wear is involved, and debris forms a third body.

Asperities on the surface of diatoms might serve to counteract friction, otherwise the cingula may not be pulled apart easily.

In 2500 BC the Egyptians discovered that their carriages slid better on damp sand and therefore poured water (or possibly an emulsion of olive oil) on their pathway!

The history of microfriction is much shorter. Friction measured on different size and force scales very often shows instabilities expressed in periodic stick/slip cycles. Squeaking doors or violin playing are examples of stick/slip on the macroscale. In the micro-world, stick/slips appear in mechanical and in biological systems. Even on the atomic scale, stick/slip phenomena are revealed by atomic force microscopy. However, many different mechanisms may come into play to construct friction forces and it is not yet established what mechanism predominates at what size scale.

Macro- and microtribological systems show a dependence of the friction force on the sliding velocity for dry as well as for lubricated systems.

5.4. Adhesion

Adhesion can be regarded as a state of minimum energy that is attained when two solids are brought into intimate contact. This means that a certain force is needed to separate the solids. Adhesion increases with decreasing roughness (two surfaces can be more effectively adhered the smoother they are), showing that adhesion has a distinct range of action. In addition to small roughness, soft and flexible materials can also show strong adhesion, since these materials physically accommodate the

roughness profile of the counter surface, leading to intimate contact.

A large proportion of diatom species are usually found attached to a diverse variety of surfaces. The adhesives they use have been studied by several groups (e.g. Refs [8, 9, 11, 28–32]). Some of these studies even reached the single molecule level¹¹ and chemical characterisation of the diatom adhesives is highly desirable. On the one hand, the adhesive industry can profit from new ideas (which are in fact not new but millions of years old), and on the other hand, knowledge of the diatom adhesives might promote the development of adhesive solvents for removal of undesirable organisms (e.g. in technical devices like tanks and pipelines as well as in biofouling of ships and marine structures).

The investigation of diatom adhesives at the molecular scale may result in innovations regarding optimized (bio)nanotechnologically constructed man-made materials, like adhesives and lubricants.

5.4.1. Molecular Forces in Adhesion

The finest scale of interaction is governed by molecular forces. To induce strong attraction, the spacing between the solids must be reduced less than about 10 nm.

In 1999, Smith and co-workers attempted to explain the molecular mechanistic origin of the toughness of natural adhesives, fibres and composites.³³ These authors mainly concentrated on the abalone shell, which is a composite of calcium carbonate plates sandwiched between organic material. This biomaterial, where the organic component comprises just a few per cent of the composite by weight, is 3000 times more fracture resistant than a single crystal of the pure mineral!³⁴ Natural materials are renowned for their strength and toughness. As another example: spider dragline silk has a breakage energy per unit weight two orders of magnitude greater than high tensile steel.³⁵

Adhesive force analyses of individual keratinous hairs of the Tokay gecko support the hypothesis that in this biological system adhesion operates by van der Waals forces. Van der Waals forces are extremely weak at greater than atomic distance gaps, and require intimate contact between the adhesive and the surface.³⁶

5.4.2. Electrostatic Forces

Bulk excess charges present on the surface induce the classical Coulomb attraction. This force vanishes after proper grounding of the samples.

The second contribution besides these charges arises from the electrostatic contact potential, resulting in the electrical double layer force. Unlike Coulomb attraction, this double-layer force remains constant after grounding. Most biological macromolecules are charged when surrounded by water, since the molecules expose weak acidic and basic functional groups.

5.4.3. Capillary Forces

Capillarity is closely connected to adhesion, cohesion and surface tension. A wetting liquid is pulled upwards in a capillary due to surface tension. In sliding systems, two surfaces are brought in close contact. The resulting slits and pores act as capillaries.

Of all the attractive forces in the micro-range, capillarity has the strongest impact provided that electrical excess charges can be neglected due to grounding. The liquid monolayers that are in direct contact with the solid are subject to electrical double-layer enforced ordering. Molecular forces act in the nano-Newton range. They are responsible for the mutual attraction or repulsion of liquid molecules and their interaction with the confining solids. Furthermore, blunt, ball-shaped probes (like the SILICON model system¹) detect capillary forces, while sharp, needle-like probes (like the tip of an atomic force microscope) penetrate the double layers and also experience molecular forces due to intimate contact with the solid.

5.5. Lubrication

Lubrication is one of the key aspects of micro- and nanotribology.³⁷ A lubricant is mainly used to keep two solids at a distance where the asperities are prevented from getting in direct mechanical contact with each other. This requires that the lubricant has to be sufficiently viscous in order for it not to be squeezed out of the contact. To describe lubrication effects at the macroscale, a Newtonian fluid model normally suffices. As the dimensions and forces decrease, nonlinear effects have to be included. Friction and adhesion forces with magnitudes lower than about 1 mN acting on contact areas in the micrometer range are strongly affected by the action of adsorbed liquids.

As the thickness of the lubricant decreases below about 10 nm, molecular influences become notable. Significantly altered physical properties are found in the range of a few monolayers (see e.g. Ref. [38]). The main effect in thin film lubrication is solidification.

Molecular forces are not only important for biological systems concerning adhesion (see Section 5.4.1.) but are also important in lubrication.

5.5.1. Water–Bulk Properties and Molecular Film Properties

All surfaces are covered by water, unless they are hydrophobic or dried. Water is of great importance for any known living being, since it influences the constitution of biological structures as the common solvent for all biological activities. Throughout the centuries, water has been the subject for intensive research.³⁹ Water is a small molecule with low viscosity. However, it is a dipole molecule which is able to form hydrogen bonds

to neighbouring water molecules or to solid surfaces. Water shows even in the bulk state many special properties and anomalies and has a high degree of short range order. Nature solves its lubrication problems with water as a base stock and biomolecules as additives. Therefore, detailed knowledge of water properties is important if we were to mimic biological lubrication.

To absorb water, a surface has to be able to keep the liquid. This means that the surface must have hydrophilic surface properties in order to be wetted. A hydrophilic surface is a polar surface while a hydrophobic surface is non-polar. Polar surfaces tend to build an aqueous double layer with distinctively different properties to those of bulk water. An example of water confinement in biological systems is the lipid bilayer membrane.

Continuum mechanics cannot be applied any more at very small distances of the separated bodies. Sophisticated simulation techniques have to be applied. The short-range forces in liquids (pertaining at the scale of a few nanometres) comprise van der Waals forces, electrostatic and ion correlation forces, solvation and structural forces, hydration and hydrophobic forces, polymer-mediated forces and thermal fluctuation forces. Some of these forces even switch from being attractive to repulsive or vice versa at some finite distance: in such cases, the potential energy minimum which determines the adhesion force or energy, occurs not at true molecular contact between the surfaces, but at some small distance farther out.⁴⁰

Short-range forces might be also relevant in the totally unexplored matter of exchange of materials through the diatom cell wall. The smallest pores in the diatom cell wall have diameters in the range of about 20 to 200 nm.

5.5.2. Solid Lubrication

Solid lubricants reduce friction because of particles which easily slide against each other. Examples are powders (dry graphite, Teflon®, Molybdenum disulfide, aluminium, copper, etc.) or ceramic particles. Solid lubricants are often used as additives for grease and they are utilised at thermally stressed locations.

A closed lubricant cycle is not possible in many cases, and therefore solid lubricants, which can be applied highly localised, have major advantages as opposed to fluid lubricants.

A possible way to obtain new solid-like lubricants involves careful selection of molecular properties leading to a robust lubrication film. Valuable clues about desirable molecular properties might very well arise from studies on natural lubricants.

5.6. Wear

Like adhesion and friction, wear can also be divided into macro-, micro- and nano-events. On the macroscale, repeated plastic deformation and the generation of surface

and subsurface failures and heat during friction lead to degradation of the material that is called wear. For example, microscale wear analysis is performed for hip-replacement materials.⁴¹ Wear on the atomic scale is accompanied by the formation of crystallographic defects like point defects or kinks.

Tribologists and diatomists are invited to combine their knowledge in bionanotribology, since fruitful technological innovations resulting from such synergistic endeavours are highly possible.

6. OUTLOOK

6.1. Diatom Bionanotribology

Nature solves its lubrication problems with water as a base stock and biomolecules as additives. The precise mechanisms differ, depending on the specific application, and thus e.g. the hip, the mouth, the eye, and the lungs all involve different, but related biomolecules.

Today, advances in physics and chemistry enable us to measure the adhesion, friction, stress and wear of biological structures on the micro- and nanoscale. Furthermore, the chemical composition and properties of natural adhesives and lubricants are accessible to chemical analysis.

We suggest *Pseudonitzschia sp.*, *B. paxillifer* and *E. arenaria* for detailed bionanotribological investigations. Current experiments comprise determination of the composition of the bead-like features (cf. Fig. 4), confocal microscopy combined with histochemical analysis of diatom mucilage, and techniques like mass and infrared spectrometry for organic compound identification on gliding surfaces. Furthermore, systematic analysis of diatom adhesives and lubricants to determine their strength and durability is highly desirable.

The adhesive and lubricant industry can profit from new ideas, and knowledge of the diatom adhesives might also promote the development of adhesive solvents for removal of undesirable organisms.

Diatoms cannot only provide ideas in the field of lubrication and adhesion.

One of the beauties of the diatoms is that there is a fantastic variation on a simple theme—the “Bauplan” of two valves and a series of girdle bands. The way in which the diatom organised (in evolutionary terms) the cell-wall to facilitate cell division inside a rigid box of silica brought with it special problems and it is these problems and the ways in which the diatom overcame them that can be of great interest to the tribologist!

However, tribology is just one field where biomimetic approaches originating from diatom research can innovate technology. Biological systems are highly controlled from the nanometer to the macroscopic levels, resulting in complex, hierarchical architectures that provide multifunctional properties that usually surpass those of analogous synthetically manufactured materials with similar phase compositions.⁴²

6.2. Bionanotechnology

Possible future applications of atomic force microscopy and spectroscopy techniques in biology, and especially in diatom research are manifold, interesting and challenging; e.g. watching cell division in real time at the nanoscale, finding out how diatoms produce their amorphous silica frustules, revealing what tricks they apply to generate strong adhesives or how their lubricants minimize friction in moving parts.

Biological materials are simultaneously “smart,” dynamic, complex, self-healing, and multifunctional, characteristics difficult to achieve in purely synthetic systems. Biomimetics, the use of biological principles in materials synthesis and assembly, may be a path for realizing nanotechnology, such as molecular and nanoscale electronics.⁴²

It is wonderful to dive deeper and deeper into the nanoworld, to watch biological processes at unprecedented resolution and to consider how their secrets might be applied in technological innovations. However, one should bear in mind that this focussed approach teaches us only about biomolecular interactions. Like all other organisms, diatoms are more than just an assemblage of simply interacting biomolecules. With their emerging complex properties, they can teach us about life itself. After all—to say it with A. N. Whitehead,⁴³ the English philosopher and mathematician—“physics has to be explained in terms of a generalized theory of the organism”!

Acknowledgments: ICG thanks P. K. Hansma from UCSB, who introduced her to AFM and provided the perfect environment to start her work with diatoms. What he can teach about doing science has no parallel. The authors thank A. M. Schmid for revealing the interesting mechanical properties and providing first samples of *E. arenaria* and R. Krisai for introducing us to their natural habitat. J. C. Weaver from UCSB helped in using the SEM, and J. H. Kindt from UCSB helped in the *Ellerbeckia* elongation experiments. Furthermore, the authors express gratitude for stimulating discussions with R. M. Crawford, F. Kinnen and J. Kreuzer. A special thank you goes to M. Scherge and S. Gorb, who with their book “Biological Micro- and Nanotribology—Nature’s solutions” reinforced our decision to work on diatom bionanotribology.

Partly, this work was funded from the “Austrian Kplus-Program” and has been carried out at the “Austrian Center of Competence for Tribology.”

References and Notes

1. M. Scherge and S. Gorb, Biological micro- and nanotribology. Nature’s solutions (NanoScience and Technology), Springer-Verlag, Berlin, Heidelberg (2001).
2. I. C. Gebeshuber, J. H. Kindt, J. B. Thompson, Y. DelAmo, H. Stachelberger, M. Brzezinski, G. D. Stucky, D. E. Morse, and P. K. Hansma, Atomic force microscopy study of living diatoms in ambient conditions. *J. Microsc. Oxf.* 212, 292 (2003).
3. M. Gross, Travels to the nanoworld—Miniature machinery in nature and technology. Perseus Publishing, Cambridge, MA (2001).
4. R. P. Feynman, There’s plenty of room at the bottom. In D. Gilbert, editor, Miniaturization, Reingold, New York (1961), pp. 282–296.
5. J. Parkinson and R. Gordon, Beyond micromachining: The potential of diatoms. *Trends Biotechnol.* 17, 190 (1999).
6. I. C. Gebeshuber, J. H. Kindt, J. B. Thompson, Y. DelAmo, M. Brzezinski, G. D. Stucky, D. E. Morse, and P. K. Hansma, Atomic force microscopy of diatoms *in vivo*, in Abstracts of the 15th North American Diatom Symposium, Pingree Park Campus, Colorado State University, (1999), p. 8.
7. S. A. Crawford, M. J. Higgins, P. Mulvaney, and R. Wetherbee, The nanostructure of the diatom frustule as revealed by atomic force and scanning electron microscopy. *J. Phycol.* 37, 543 (2001).
8. I. C. Gebeshuber, J. B. Thompson, Y. Del Amo, H. Stachelberger, and J. H. Kindt, *In vivo* nanoscale atomic force microscopy investigation of diatom adhesion properties. *Mat. Sci. Technol.* 18, 763 (2002).
9. M. J. Higgins, S. A. Crawford, P. Mulvaney, and R. Wetherbee. Characterization of the adhesive mucilages secreted by live diatom cells using atomic force microscopy. *Protist* 153, 25 (2002).
10. M. J. Higgins, J. E. Sader, P. Mulvaney, and R. Wetherbee, Probing the surface of living diatoms with atomic force microscopy: The nanostructure and nanomechanical properties of the mucilage layer. *J. Phycol.* 39, 722 (2003).
11. M. J. Higgins, P. Molino, P. Mulvaney, and R. Wetherbee, The structure and nanomechanical properties of the adhesive mucilage that mediates diatom-substratum adhesion and motility. *J. Phycol.* 39, 1181 (2003).
12. D. Rugar and P. K. Hansma, Atomic force microscopy. *Physics Today* 43, 23 (1990).
13. V. J. Morris, A. P. Gunning, and A. R. Kirby, Atomic force microscopy for biologists. World Scientific Publishing Company (1999).
14. D. M. Eigler and E. K. Schweizer, Positioning single atoms with a scanning tunneling microscope. *Nature* 344, 524 (1990).
15. M. F. Crommie, C. P. Lutz, and D. M. Eigler, Confinement of electrons to quantum corrals on a metal surface. *Science* 262, 218 (1993).
16. J. Landwehr and D. Goetz, *Nachwachsende Rohstoffe für die Chemie*, edited by Fachagentur Nachwachsende Rohstoffe e.V. Landwirtschaftsverlag, Münster (2003), p. 343.
17. R. Lauhanen, R. Kolpanen, T. Kuokkanen, S. Sarpola, and M. Lehtinen, The environmental effects of oils used in forest operations. *Teho Helsinki* (1998), Vol. 48, pp. 32–34.
18. K. J. Brown, K. Matson, and D. Taylor, New lubricating material for hydraulic turbine equipment. Proceedings Canadian Electrical Association Engineering and Operating Conference, Montreal (1993) pp. 1–20.
19. C. van den Hoek, D. Mann, and H. M. Jahns, *Algae: An introduction to phycology*. Cambridge University Press (1995).
20. F. E. Round, R. M. Crawford, and D. G. Mann, *Diatoms: Biology and morphology of the genera*. Cambridge University Press (1990).
21. M. R. M. Kapinga and R. Gordon, Cell motility rhythms in *Bacillaria paxillifer*. *Diatom Res.* 7, 221 (1992).
22. M. R. M. Kapinga and R. Gordon, Cell attachment in the motile colonial diatom *Bacillaria paxillifer*. *Diatom Res.* Vol. 7, 215 (1992).
23. I. Fujimasa, *Micromachines: A new era in mechanical engineering*. Oxford University Press (1997).
24. I. G. Goryacheva, *Contact mechanics in tribology (Solid mechanics and its applications)*, Kluwer Academic Publishers, The Netherlands (1998).
25. I. Newton, *The principia: Mathematical principles of natural philosophy (1687)*, reprint: University of California Press (1999).

26. Y. C. Fung, *Biomechanics: Mechanical properties of living tissues*, 2nd ed. Springer-Verlag, Berlin (1993).
27. G. Subhash, S. Yao, B. Bellinger, and M. R. Gretz, Investigation of mechanical properties of diatom frustules using nanoindentation. *J. Nanosci. Nanotech.* (2005, this issue).
28. Y. Wang, J. Lu, J. C. Mollet, M. R. Gretz, and K. D. Hoagland, Extracellular matrix assembly in diatoms (Bacillariophyceae). II. 2,6-dichlorobenzonitrile inhibition of motility and stalk production in *Achnanthes longipes*. *Plant Physiol.* 113, 1071 (1997).
29. Y. Wang, Y. Chen, C. Lavin, and M. R. Gretz, Extracellular matrix assembly in diatoms (Bacillariophyceae). IV. Ultrastructure of *Achnanthes longipes* and *Cymbella cistula* as revealed by high pressure freezing/freeze substitution and cryo-field emission scanning electron microscopy. *J. Phycol.* 36, 367 (2000).
30. B. A. Wustman, M. R. Gretz, and K. D. Hoagland, Extracellular matrix assembly in diatoms (Bacillariophyceae). I. A model of diatom adhesives based on chemical characterization and localization of polysaccharides from *Achnanthes longipes* and other diatoms. *Plant Physiol.* 113, 1059 (1997).
31. B. A. Wustman, J. Lind, R. Wetherbee, and M. R. Gretz, Extracellular matrix assembly in diatoms (Bacillariophyceae). III. Organization of fucoglucuronogalactans within the adhesive stalks of *Achnanthes longipes*. *Plant Physiol.* 116, 1431 (1998).
32. J. L. Lind, K. Heimann, E. A. Miller, C. van Vliet, N. J. Hoogenraad, and R. Wetherbee, Substratum adhesion and gliding in diatoms are mediated by extracellular proteoglycans. *Planta* 203, 213 (1997).
33. B. L. Smith, T. E. Schäffer, M. Viani, J. B. Thompson, N. A. Frederick, J. Kindt, A. Belcher, G. D. Stucky, D. E. Morse, and P. K. Hansma, Molecular mechanistic origin of the toughness of natural adhesives, fibres and composites. *Nature* 399, 761 (1999).
34. N. Watabe and K. M. Wilbur, (eds.): *The mechanisms of biomineralization in invertebrates and plants*. University of South Carolina Press, Columbia, SC (1976).
35. M. Hinman, Z. Dong, M. Xu, and R. V. Lewis, *Biomolecular materials*. Edited by C. Viney, S. T. Case, and J. H. Waite, Materials Research Soc., Pittsburgh (1993) pp. 25–34.
36. K. Autumn, Y. A. Liang, S. T. Hsieh, W. Zesch, W. P. Chan, T. W. Kenny, R. Fearing, and R. J. Full, Adhesive force of a single gecko foot-hair. *Nature* 405, 681 (2000).
37. S. M. Hsu and K. Zhang, Lubrication: Traditional to nanoscale films, in *micro/nanotribology and its applications*. Edited by B. Bhushan, Kluwer Academic Publishers, The Netherlands (1997), pp. 399–414.
38. H. Stoeri, R. Kleiner, W. S. M. Werner, R. Kolm, I. C. Gebeshuber, and C. Jögl, Characterisation of monomolecular lubricant films, *Proceedings 14th International Colloquium Tribology "Tribology and lubrication engineering"* (ed. W. J. Bartz), Technische Akademie Esslingen (2004), Vol III, pp. 1663–1666.
39. G. W. Robinson, S. B. Zhu, and M. W. Evans, *Water in biology, chemistry and physics: Experimental overviews and computational methodologies*, World Scientific Series in Contemporary Chemical Physics, World Scientific Publishing (1996), Vol. 9.
40. B. Bhushan, (editor): *Springer Handbook of Nanotechnology*. Springer Verlag, Berlin, Heidelberg (2004), pp. 543–563.
41. S. C. Scholes, A. Unsworth, R. M. Hall, and R. Scott, The effects of material combination and lubricant on the friction of total hip prostheses. *Wear* (2000), Vol. 241, pp. 209–213.
42. M. Sarikaya, *Nanomaterials assembly through biomimetics*. Eighth Foresight Conference on Molecular Nanotechnology (2000) <http://www.foresight.org/Conferences/>
43. A. N. Whitehead, *Science and the modern world*. Mentor, New York (1925).

Received: 8 March 2004. Revised/Accepted: 7 April 2004.

A.10 Micromechanics in biogenic hydrated silica: hinges and interlocking devices in diatoms

Gebeshuber I.C. and Crawford R.M.

J. Eng. Tribol. 220(J8), 787-796 (2006)

Abstract

Diatoms are single-celled organisms with rigid parts in relative motion at the micrometer scale and below. These biogenic hydrated silica structures have elaborate shapes, interlocking devices, and, in some cases, hinged structures. The silica shells of the diatoms experience various forces from the environment and also from the cell itself when it grows and divides, and the form of these micromechanical parts has been evolutionarily optimized during the last 150 million years or more, achieving mechanical stability. Linking structures of several diatom species such as *Aulacoseira*, *Corethron*, and *Ellerbeckia* are presented in high-resolution SEM images and their structure and presumed functions are correlated. Currently, the industry for micro- and nanoelectromechanical devices (MEMS and NEMS) puts great effort into investigating tribology on the micro- and nanometre scale. It is suggested that micro- and nanotribologists meet with diatomists to discuss future common research attempts regarding biomimetic ideas and approaches for novel and/or improved MEMS and NEMS with optimized tribological properties.

Micromechanics in biogenic hydrated silica: hinges and interlocking devices in diatoms

I C Gebeshuber^{1,2*} and R M Crawford³

¹Institut für Allgemeine Physik, Vienna University of Technology, Wien, Austria

²AC²T Austrian Center of Competence for Tribology, Wiener Neustadt, Austria

³Alfred-Wegener Institute for Polar and Marine Research, Bremerhaven, Germany

The manuscript was received on 3 November 2005 and was accepted after revision for publication on 10 August 2006.

DOI: 10.1243/13506501JET163

Abstract: Diatoms are single-celled organisms with rigid parts in relative motion at the micro-metre scale and below. These biogenic hydrated silica structures have elaborate shapes, interlocking devices, and, in some cases, hinged structures. The silica shells of the diatoms experience various forces from the environment and also from the cell itself when it grows and divides, and the form of these micromechanical parts has been evolutionarily optimized during the last 150 million years or more, achieving mechanical stability. Linking structures of several diatom species such as *Aulacoseira*, *Corethron*, and *Ellerbeckia* are presented in high-resolution SEM images and their structure and presumed functions are correlated. Currently, the industry for micro- and nanoelectromechanical devices (MEMS and NEMS) puts great effort into investigating tribology on the micro- and nanometre scale. It is suggested that micro- and nanotribologists meet with diatomists to discuss future common research attempts regarding biomimetic ideas and approaches for novel and/or improved MEMS and NEMS with optimized tribological properties.

Keywords: biotribology, diatom tribology, biogenic hydrated silica structures in relative motion

1 INTRODUCTION

Diatoms are single-celled organisms that generally multiply by cell division (see reference [1] for a general introduction). The oldest recorded diatom fossil dates back to 180 million years [2]. One of the best-known properties of the diatom cell is that it is contained in a shell of amorphous hydrated silica, $\text{SiO}_2 \cdot 2 \text{H}_2\text{O}$. The silica is biomineralized in the sense that it is produced by the organism, probably in a colloidal form and not incorporated from the environment. More than 50 different minerals are produced by organisms [3]. The biogenic glass of the diatoms is formed in exquisite detail even at the nanometre scale.

The cell wall of the naturally nanostructured diatoms is in essence composed of two halves that

overlap, as do the two halves of a Petri dish or a shoe box [Fig. 1(a)]. The parts of the silica box tightly fit into each other and protect the protoplast (i.e. the living protoplast including its membranes) from being twisted or squeezed. The silica box is of great relative strength [4], thus protective and transparent and thereby allowing light to pass through to the chloroplasts for photosynthesis. The pores of the silica box are thought to allow for material exchange with the environment [5]. During growth of the cell, the two halves are pushed away from each other as the protoplasm expands [Fig. 1(b)]. The silica parts also move against each other during cell division. After the nucleus divides, the cytoplasm pinches in two and results in two cells within the old cell wall with each lying up against one of the old walls [Figs 1(c) and (d)]. Within a membrane sac on the other side of each new cell, a new half of the wall (a valve, V) is then formed, each of them back to back with the other. Thereby, each of the two new cells has one old and one newly built valve. In many cases, the surfaces of these new valves are relatively

*Corresponding author: Institut für Allgemeine Physik, Vienna University of Technology, Technische Universität Wien, Wiedner Hauptstrasse 8-10/134, Wien A-1040, Austria. email: ille@iap.tuwien.ac.at or gebeshuber@iap.tuwien.ac.at

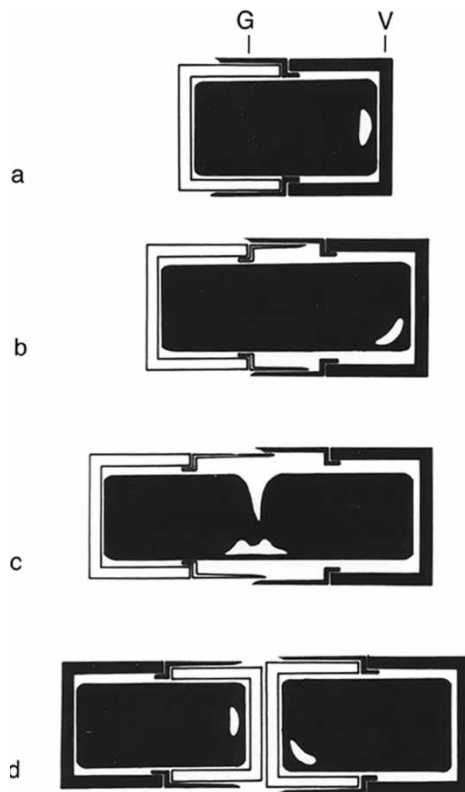


Fig. 1 Schematic of cell division in diatoms. (a) A single diatom cell, with two valves (V, one in black and one in white) and one series of girdle bands (G). (b) As the protoplasm expands during growth of the diatom, the two valves are pushed away from each other and an additional series of girdle bands are produced to accommodate the larger volume. (c) First the nucleus and then the cytoplasm divides to produce (d) two new cells. The new valves are formed, back-to-back with another. Each of the two new cells has one old and one newly built valve

smooth and when the walls are fully silicified, they are released from their membrane sac and the two new cells drift apart. Often, though, the valve surface is full of folds and spines but each component is always a discrete one within its single membrane sac until maturity when it is released from the vesicle. In addition to the valves, there are girdle bands (G) of silica surrounding the middle of the cell between the two valves on each cell and shown as one component on each valve in Fig. 1. These bands are to protect the protoplast during cell expansion before division [6]. The girdle bands are also produced in their own individual vesicles, but this will not concern us further here [1].

Diatoms occur both in freshwater and in seawater and may be attached to surfaces or freely floating. In

many cases, the diatoms form colonies. This has been perceived a device for slowing the sinking rate of the cell(s) in the water column [7], but it has recently been suggested as an anti-dispersion strategy [8]. Most of the diatom colonies are chains in which the single cells are connected end on end (valve to valve) like a string of pearls. Diatom colonies often comprise 30–50 cells. The valve-to-valve connection of the diatoms in a colony leaves the girdle band surface unaffected and able to function to accommodate cell expansion.

The cells manage to form these chains in one of two ways: either with biogenic adhesives connecting the single cells or via mechanical attachments. The adhesive material is produced by the cells through the sister or sibling valves and sticks them together or to a substratum. Such adhesives are common even in solitary species and can, for example, create problems through the fouling of the hulls of ships [9, 10]. Some of the diatom adhesives are very strong and reveal self-healing properties, i.e., broken adhesive bonds rebond when the adhesive is not stressed for a period exceeding a few seconds [11]. They might serve as templates for engineering novel underwater adhesives [11, 12]. The colony formation by adhesion will concern us no more here.

In the case of mechanical attachments between the single cells forming a chain, the cells produce linking structures that are integral with the valve and must, therefore, be formed within its membrane vesicle. In other words, the two sets of spines are formed simultaneously in the linking position. The sibling cells will remain in this relationship until, by some accident, the cells and/or the spines are broken. These mechanical linking structures are so well engineered and tight that the spines may remain interlocked even when the cells die, as can regularly be seen in specimens from diatom fossil deposits millions of years old [1]. Chain formation by linking structures must deal with two potentially destructive forces: one that threatens to pull the cells apart from one another and another that works to twist the chain. There is also the possibility of wear and abrasion of the interacting linking structures. Depending on the specific growth situations of the cells, the silica shells may be threatened by damage and wear, especially in turbulent inshore marine waters or in fast flowing streams and waterfalls. In the very nature of their formation, the valves and girdle bands cannot be replaced or restored once they are released from the membrane sacs in which they are formed and so they have evolved technologically interesting micromechanical solutions to such problems.

The following sections will present several examples of interlocking devices and hinges in diatoms. Historically interested readers might also

wish to read 'Art forms in nature' (1st edition 1899) [13] and 'On growth and form' (1st edition 1917) [14], especially chapter V on biomineralized structures and chapter VIII on form and mechanical efficiency.

2 HINGES AND INTERLOCKING DEVICES IN DIATOMS

It is known from the fossil record that colony formation by means of linking structures has a long history in the diatoms. Whereas linking by adhesives cannot be proved from fossil samples (since the adhesives disintegrated long ago), there are many examples of sister valves remaining attached through linking structures even in fossil deposits as many as 50 million years old. The diatoms are believed to have originated in the sea because the earliest deposits containing diatoms are marine [1]; what must have been a silica-rich environment seems to have favoured the development of extremely thick cell walls and the *Ellerbeckia* illustrated here is not exceptional with a cell wall thickness of 3–4 μm ; 0.1–0.2 μm is more usual for some modern planktonic species.

The linking structures formed by many of the diatom species common in these times were massive, but they were not simple (discussed subsequently). Nowhere a simple hook and loop arrangement is seen that one finds in a toy train coupling that has to permit sinusoidal movement as the train negotiates curves but does not normally have to deal with forces or moments that would twist the train. The linking arrangements in diatoms reduce the degrees of freedom, either to two as in the toy train or to one or even zero, as would be more likely in the turbulent ocean. The authors do not intend to review linking structures throughout the diatoms but to present instructive examples to illustrate some ways in which the diatom cell wall is equipped to deal with potentially destructive forces and moments.

For microelectromechanical systems (MEMS) and nanoelectromechanical systems (NEMS) technologies, macroscopic best practice in terms of, for example, lubrication and surface topography cannot be scaled down linearly. Effects of adhesion, stiction,* and contamination by third bodies, which are swamped by bulk continuum phenomena at the macroscale, become dominant at the micrometre length scale. Currently, the MEMS and NEMS

*Stiction refers to the tendency of read/write heads of hard disk drives to stick to the platters, preventing the disk from spinning up and possibly causing physical damage to the media [15]. The word is a combination of 'static' and 'friction'.

industry puts great effort into investigating tribology on the micro- and nanometre scale. Novel three-dimensional MEMS such as piezoelectric inkjet printer parts, accelerometers in cars for airbag deployment in collisions, gyroscopes used in modern cars to trigger dynamic stability control, disposable blood pressure sensors, or the several hundred thousands of digital micromirrors in a beamer would exhibit increased performance as soon as their tribology were optimized.

Diatoms already have well adapted and elaborate tribological properties on these scales and, therefore, can provide valuable ideas and templates for optimized MEMS and NEMS.

3 OBSERVATIONS

As a generalization, sibling valves of diatoms in a colony may either be joined at the centre of the valve face or at its margin. Good examples of the latter can be found in the plankton where organisms are free-floating in the lake or ocean. The genus[†] *Aulacoseira* (two sibling valves with T-shaped interconnections shown in Fig. 2), which is cylindrical with a discoid valve face, has a complete ring of spatulate spines, reducing the degrees of freedom of movement between the sibling valves to zero.

Similar spines are found along part of the margin of some species of the freshwater *Fragilaria* and in some genera of the marine Cymatosiraceae, all genera with somewhat oval or even spindle-shaped valves (see Fig. 3 for the elaborate spines between the two valves of the single cells). In the common marine genus *Skeletonema*, again a perfect cylinder, the marginal spines take a different form with a complex three-dimensional linkage. In all of these cases, there is no other structure on the valve face that links the cells together. In *Skeletonema* (see Fig. 4(a) for a colony of several cells and Fig. 4(b) for a zoom into the linking structures), there is a large space between the cells, that must be filled with seawater, as no organic material has ever been observed here. The authors propose that even in the most tightly bound siblings, e.g. *Aulacoseira*, water provides lubrication between interfacing structures of the two sibling valves. *Fragilaria* and *Cymatosira* would be intermediates in this respect.

[†]A genus (plural genera) is a grouping in the classification of organisms comprising one or more species. In the common biological nomenclature in the convention of Linnaeus, the name of an organism is composed of two parts – the binomial: its genus (always capitalized) and a species modifier. An example is *Homo sapiens*, the name for the human species that belongs to the genus *Homo*.

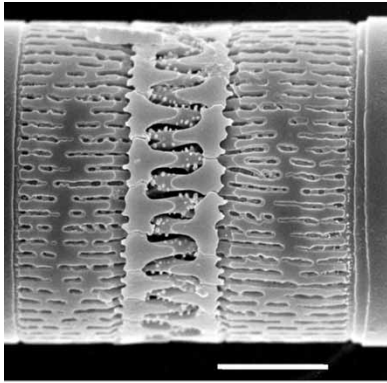


Fig. 2 Examples of linking sibling valves in the diatoms: in the freshwater genus *Aulacoseira*, sibling valves are often joined to form chains at the margin of the valve face by spatulate (T-shaped) spines, which, in some cases, seem to be able to allow the sibling valves to move apart a little, scale bar = 5 μm

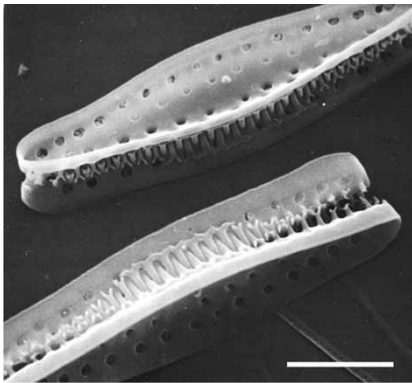


Fig. 3 In the genus *Cymatosira*, the cells also form chains but can live as single cells. The two valves of the single cells are connected via elaborated spines. Scale bar = 10 μm .

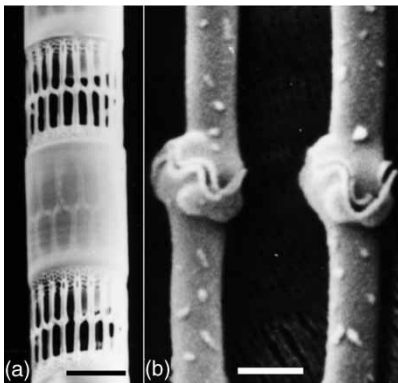


Fig. 4 In the common marine planktonic genus *Skeletonema*, the cells are held in chains by spines that maintain a wide gap between cells (a) and link by complex junctions of the spines (b). Scale bar, $a = 50 \mu\text{m}$, $b = 5 \mu\text{m}$

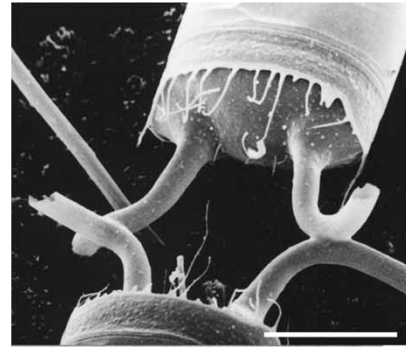


Fig. 5 The sibling valves of, perhaps, the most common marine planktonic diatom *Chaetoceros* are fused along part of their setae. Scale bar = 50 μm

Perhaps, the most common marine planktonic diatom genus is *Chaetoceros*, some species of which form chains and do so by fusion of the so-called setae between sibling valves. The seta is a kind of horn projecting out as a tube from the valve surface, usually one each at opposite ends of a slightly bipolar valve face and the fusion occurs close to, or a little distance from, the valve surface (Fig. 5). Because the setae grow out from the two sibling valves together, it is imagined that when they meet, the membrane sacs fuse with each other, allow the fusion of silica, and then, as the setae continue their different directions, become separated again; an example of the exquisite control that these organisms have. In all of these cases of chain formation, there exists the ability of the diatom to discontinue the chain by forming sibling valves that lack the linking structures [16], but this need not concern us further here.

If the diatoms from the fossil record are examined, it is apparent that much evolutionary experimentation took place in the early days when most of the diatoms were, at least fundamentally and approximately, radially symmetrical in valve view.* One of the experiments concerned linking sibling valves by means of a structure at the centre of the valve. *Syndetocystis* is a beautiful example (Fig. 6 shows the valve of one cell, the interconnection to the other cell, and a part of the second cell – the rest of that valve broke off sometime during the last 50 or so million years, Fig. 7 gives a detailed view of the linking structure). This diatom genus is heavily silicified and has a long tube at the centre of each valve that extends way beyond the valve and terminates in a two-armed clasp that loops around

*Note that the term 'radial symmetry' in biology is used differently than in engineering or mathematics. In the language of biology, organisms with radial symmetry may have body parts arranged in a regular, repeating pattern around a central axis (i.e. they are symmetric with respect to rotations of $2\pi/n$)

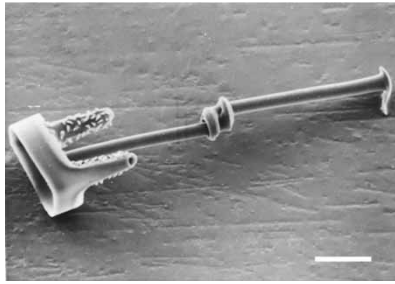


Fig. 6 In the fossil genus *Synetocystis*, the linking occurs by means of a structure at the centre of the valve. One of the valves has been broken and lost. At the apex of each spine is a loop that surrounds the shaft of the other spine. Scale bar = 20 μm

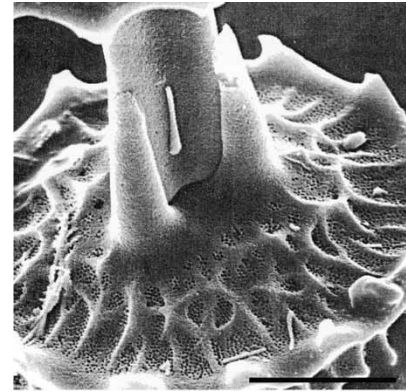


Fig. 9 The spine of *Trochosira* fits tightly inside three smaller spines from the other sibling. Scale bar = 50 μm

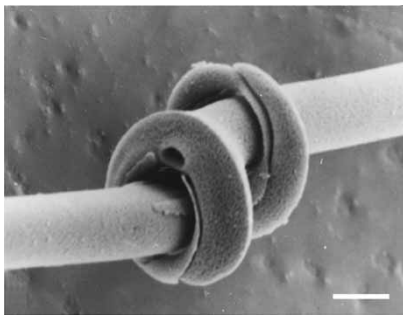


Fig. 7 A detail of the apex is shown. Scale bar = 5 μm

the tube from the sibling valve. By its very nature, each clasp is asymmetric and this asymmetry confers stability by preventing twisting of either valve with respect to its sibling.

Another fossil genus, *Trochosira*, has a different arrangement. A large fluted spine from one sibling (Fig. 8) fits tightly inside three smaller spines from the other sibling (Fig. 9). It is clear that twisting was

prevented, but it is not easy to understand how the valves stayed together.

A genus with a good fossil record and, unusually, with species living today in both marine and fresh-water habitats is *Ellerbeckia*. It has very closely linked sibling valves united by complex linking systems (Fig. 10). The valve margin of most species has very elaborate linking spines (Fig. 11), but there are also linking structures on the valve face, more or less towards the valve centre and usually radially orientated. Some examples are given in Figs 12 and 13 (the upper valves in both images are broken to expose the linking structures). In many species, one of the two sibling valves is a cameo form and the other intaglio, i.e. where the structure is either raised from or depressed into the valve surface, respectively. The two fit very closely with each other and may have the finest of detail on their surfaces – remember that they are formed in this relationship in their respective membrane sacs.

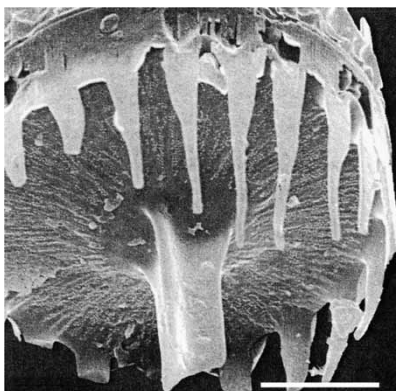


Fig. 8 In the fossil genus *Trochosira*, the linking occurs by means of a large fluted spine at the centre of the valve

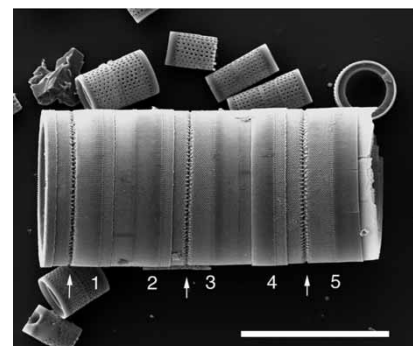


Fig. 10 A chain of what appears to be three cells of the fossil species *Ellerbeckia*. In reality, there are five cells (numbered) and the junctions between three sibling pairs are arrowed. Valves of *Aulacoseria* in the background. Scale bar = 10 μm

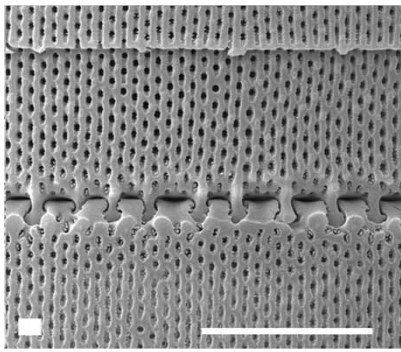


Fig. 11 A detail of the sibling junction rotated by 90°. Scale bar = 5 μm

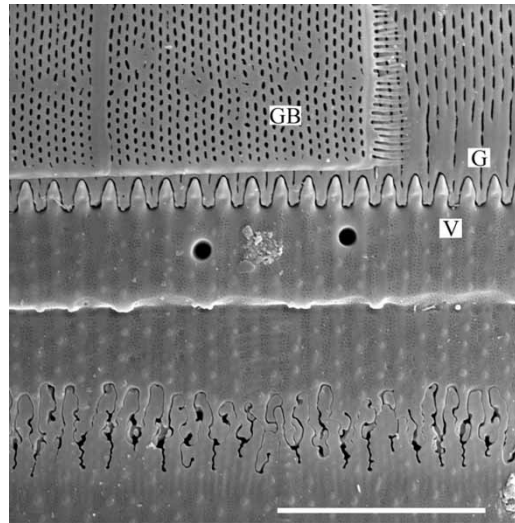


Fig. 14 Detail of another *Ellerbeckia* species with linking structures between valves below and interdigitating surfaces of valve edge (V) and girdle band (G) above. Also visible are the openings of two major tubes through the valve, the porous surface covering of the valve itself and the loose girdle band (GB). The linking structures can be seen at the broken edge of the valve in Fig. 13. Scale bar = 5 μm

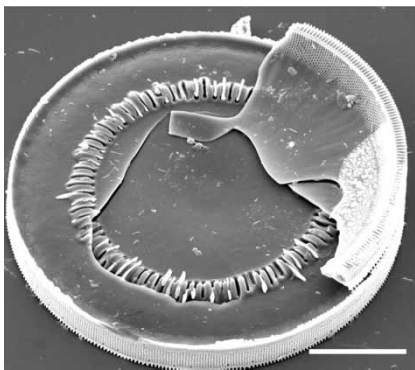


Fig. 12 A broken sibling pair of valves showing linking structures on the face of the valve. Scale bar = 20 μm

Figure 14 shows another species of *Ellerbeckia* with tightly interwoven linking structures.

At the end of chains of these two genera, one finds the so-called separation valves (Fig. 15). Formed as sibling pairs, they separate because they lack the firm linking structures on the valve margin and on

the valve face but, even here, there are cameo and intaglio structures that may be similar in form and orientation to the radial features.

It is easy to appreciate that there is no likelihood that the cells of a chain of *Ellerbeckia* will twist against

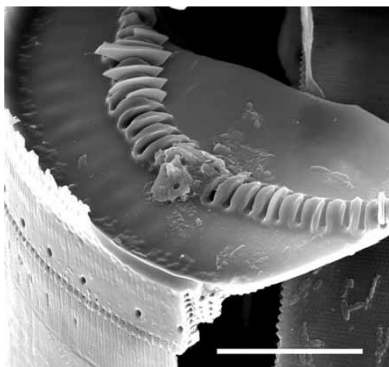


Fig. 13 Detail of another broken valve showing the intaglio slits into which the cameo ridges fit – some have broken and remain in the slits. Note the broken linking structures at the rim of the valve. Scale bar = 5 μm

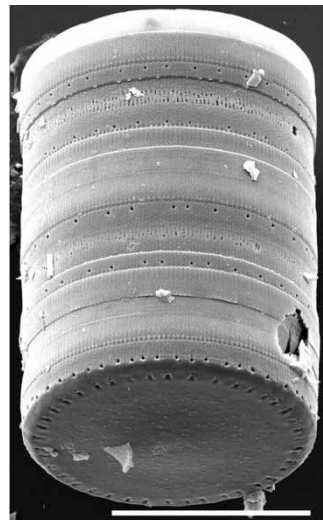


Fig. 15 A short chain with a separation valve, lacking the linking structures, at the near end. Scale bar = 25 μm

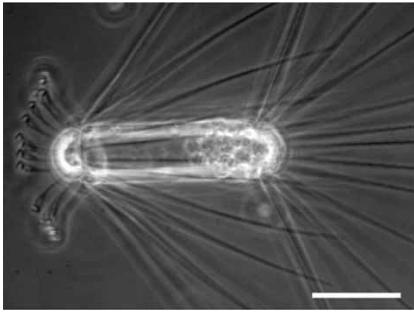


Fig. 16 A whole cell of the marine planktonic *Corethron* with two types of valves, one at either end of a long cylinder of girdle bands. The valve to the right has a radiating series of long spines. The valve to the left has long spines too, but also a crown of hooked spines. Scale bar = 50 μm

each other, yet this could be a problem for a less robust diatom. *Corethron* is a good example and something of an exception among diatoms. All three species have valves with movable parts and two of them exist as single cells. The cell in both of these species has two different valves. One has a set of long spines that are attached to the valve at a series of sockets on the rim of the hemispherical valve (Figs 16 to 18). The other valve also has a ring of similar spines, but alternating with them around the valve is a series of finer hooked spines (Fig. 16). Both series are inserted at their base in sockets as in the other valve. All spines can move to a degree in the socket, but the position in which they are found in the mature, independent cell is not where they are formed. The process of new valve formation in these diatoms is complicated and has been detailed in reference [6]. Put simply, the three sets of spines have to be formed along with the new valves, within, and protected by the cylinder of the two sets of girdle bands (Fig. 17). During the cell division cycle, the cell elongates greatly, forming very many girdle bands as it does so, thus creating a long space between the two sibling cells when they are complete. This space can accommodate the formation of the long spines. When the new cells are mature, they expand and pull the girdle cylinder away from the base of the spines and allow the spines to swing out to adopt their final position. In doing this, they move past a click-stop that prevents them moving too far back from their 'required' position. The whole structure is beautifully engineered in miniature but there is more. A function can be invoked for the long spines, not for hooking cells together in the marine plankton – their tiny barbs face the wrong way – but for keeping cells apart. This would be a strategy that could benefit a photosynthetic organism for which sinking out of the photic zone (i.e. the

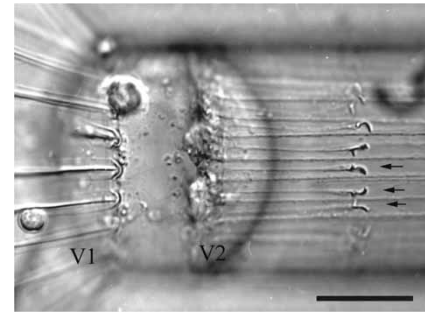


Fig. 17 A cell of *Corethron* with the old valve (V1) to the left showing the base of a number of long spines and the new valve (V2) to the right. Beneath the cylinder of the girdle bands, the tips of six hooked spines can be seen more or less regularly alternating with the long spines from both new valves. Note that the hooks are turned in different directions (arrows). Scale bar = 20 μm

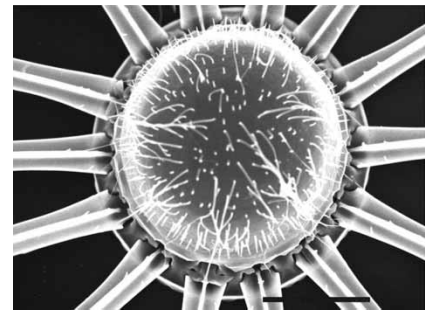


Fig. 18 Surface view of a valve similar to that in the right in Fig. 17, showing insertion of the long spines at the edge of the valve. Scale bar = 10 μm

surface zone of the sea or a lake having sufficient light penetration for photosynthesis) as marine snow* could be a problem. This hypothesis seems reasonable but what about the hooked spines? Figure 19 shows a number of spines in detail from *Corethron pennatum*. Careful inspection shows that the two surfaces of the spine are different and that there are left- and right-facing versions of the spines. On both species, the spines expand distally to form two hooks, the form of which is one of the distinguishing features of each species, and on each of the hooks, there is a series of small bead-like serrations. Without any proof, it is speculated that the function of these hooked spines is to lock the long

*In the deep ocean, marine snow is a continuous shower of mostly organic detritus falling from the upper layers of the water column. Its origin lies in activities within the productive photic zone.

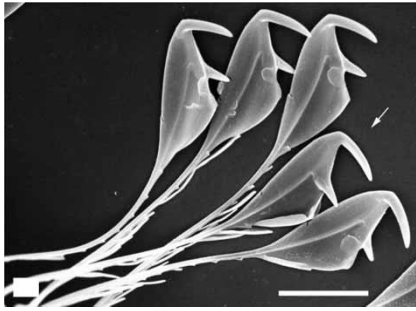


Fig. 19 Tips of five hooked spines. Note that on four of them, the second hook lies at the back and that the fifth (arrow) is, therefore, a mirror image of the others. Scale bar = 10 μm

spines in place beneath the girdle bands until, on maturity of the whole pair of sibling valves, the spines are allowed to swing out. It is thought [17] that the newly formed spines are spring-loaded within their sockets and that if they were released early, they would swing out and break the girdle bands. This would prevent further cell divisions. Some circumstantial evidence for this comes from light microscopy. Scanning electron microscopy shows that there are right- and left-facing versions of the hooked spines (Fig. 19). Using the inverted light microscope, the cell has been viewed from the end [6] and it appears that the direction in which the spines lie varies irregularly around the valve. However, one cannot be certain from scanning electron micrographs which way these are facing before being released from the girdle bands simply because it cannot be seen through the bands. Bearing in mind the dangers of twisting to the cell, this would seem to be in accord with the idea that, in which ever direction the cell is caused to twist, the hooked spines would remain in the locked position (Fig. 17). If they were all facing in the same direction, the entire arrangement might be vulnerable.

4 DISCUSSION

The diatoms are a remarkable group of organisms because they show a seemingly inexhaustible variation in the morphology of the cell wall and have a rich fossil record of evolutionary experimentation over more than 100 million years. Much of the evidence for the variation has inevitably been lost, but there is still an abundance of structure waiting to be understood. A more detailed review of the diatoms with respect to the principles outlined earlier will appear elsewhere, but here is considered the aspect of morphology as it relates to function.

There is much circumstantial evidence pointing to the likely function of this or that organelle,* because the diatoms have occupied so many of the available ecological niches. The most obvious of these is the tendency of some genera to form chains. Not every species in a given habitat forms chains, others have different thrival strategies, but many do so in the marine intertidal and shallow inshore waters typical of those in which the diatoms are thought to have evolved. Such situations are highly dispersive, and it can be supposed that the formation of chains is simply a means to avoid dispersal. During such periods when sea levels rose and the oceans deepened [18], the plankton developed less-heavily silicified cells able to remain suspended in the surface waters. Here, the environment is not so agitated but the dispersion out of the photic zone is a problem. Many organisms are taken permanently out of this zone in the form of aggregates commonly known as 'marine snow', but the two single-celled forms of *Corethron* appear to have a mechanism that must significantly reduce this danger. Most interesting is that the third species of the genus forms chains. This fact encourages us to ask how could a thrival strategy in related species of the same genus be so different? This cannot be answered at present but the genus, indeed the group as a whole, shows the kind of variation in morphology that the diatoms are capable of in response to the environment. The authors need to find a way to test some of these proposals. The responses on the part of the diatoms to the problem of forming colonies (essentially chains) have been appreciated for a number of years, but the realization that a number of these structures may have evolved to counter twisting of the chain is published here for the first time.

Finally, tribologists will wonder at the possibilities of erosion of the structure of the different wall components as they move tightly against one another. This is a subject that has received no attention in the diatoms because moving components have not been recognized as such and chains of cells have not been considered with respect to the forces acting on them. It was pointed out above that the wall components are formed by silicification within an organic membrane vesicle. The fate of the membrane, to the inside and to the outside of the component when the latter is completed, is a matter for debate, but it seems that the outer profile is lost. The wall thus comes to lie on the biological outside of the cell, and, if the diatom forms chains, there will be nothing between it and the sibling,

*An organelle is a structure which occurs in cells and which has a specialized function.

valve except the outside medium, water. If water is necessary to provide a lubricating cushion between the two siblings, then the authors might expect even the tightest fitting of species to show some way that water can get between the valve faces. It seems that all do so even if, as in *Ellerbeckia*, some very fine channels connect not the outside medium to the valve face but the protoplast itself.

It is suggested that micro- and nanotribologists meet with diatomists to discuss future common research attempts concerning micro- and nanomechanics of the silica structures, such as diatom wear studies. Diatoms are small, easy to cultivate, and because many of them are transparent, they are accessible to *in vivo* light microscopy techniques. Furthermore, some diatom species that stably adhere to a substratum are also accessible with atomic force microscopy techniques [11, 12, 19–24]. In addition, atomic force spectroscopy can yield important information on micro- and nanomechanical properties such as adhesion, viscoelasticity, hardness, and so on.

A real breakthrough in diatom tribology concerning the applicability to MEMS and NEMS requires basic understanding of the connection between structure and function of the silica walls and detailed knowledge about the chemical and physical properties at the interfaces. Furthermore, a generalization of the methods of controlled synthesis to new classes of monomers would tremendously strengthen nanotechnology [25, 26].

First publications concerning the tribology [11, 12, 19–24] and the nanotechnology [27, 28] of diatoms are already available in the literature and, hopefully, soon, there will be many more.

ACKNOWLEDGEMENTS

A part of this work has been funded by the Austrian Kplus-Program via the Austrian Center of Competence for Tribology, AC2T research GmbH, Wiener Neustadt.

The authors wish to thank K. Kaska for critically reading the manuscript and Pat Sims for kindly supplying Figs 6 to 9.

REFERENCES

- 1 Round, F. E., Crawford, R. M., and Mann, D. G. *Diatoms: biology and morphology of the genera*, 1990 (Cambridge University Press, Cambridge).
- 2 Rothpletz, A. Ueber die Flysh-Fucoiden und einige andere fossile Algen, sowie ueber liasische, Diatomeen fuehrende Hornschwamme. *Zeitschr. Deutsch. Geol. Ges.*, 1896, **48**, 910–914.
- 3 Mann, S. *Biomineralization*, 2002 (Oxford University Press, Oxford).
- 4 Hamm, C. E., Merkel, R., Springer, O., Jurkojc, P., Maier, C., Prechtel, K., and Smetacek, V. Architecture and material properties of diatom shells provide effective mechanical protection. *Nature*, 2003, **421**, 841–843.
- 5 Pickett-Heaps, J., Schmid, A.-M. M., and Edgar, L. A. The cell biology of diatom valve formation. In *Progress in phycological research* (Eds F. E. Round and D. J. Chapman), 1990, vol. 7, pp. 1–168 (Biopress, Bristol).
- 6 Crawford, R. M., and Hinz, F. The spines of the centric diatom *Corethron criophilum*: light microscopy of vegetative cell division. *Eur. J. Phycol.*, 1995, **30**, 95–105.
- 7 Tappan, H. and Loeblich, A. R. Jr. Evolution of the Oceanic plankton. *Earth-Sci. Rev.*, 1973, **9**, 207–240.
- 8 Crawford, R. M. Misleading perceptions – two illustrations of impediments to our understanding of behavioural diversity among planktonic diatoms. (Abstract). *Phycologist*, 2003, **64**, 4.
- 9 Higgins, M. J., Crawford, S. A., Mulvaney, P., and Wetherbee, R. The topography of soft, adhesive diatom ‘trails’ as observed by atomic force microscopy. *Biofouling*, 2000, **16**, 133–140.
- 10 Evans, L. V. and Hoagland, K. D. (Eds) *Algal biofouling (studies in environmental science)*, 1987 (Elsevier Publishing Company, Amsterdam).
- 11 Gebeshuber, I. C., Thompson, J. B., Del Amo, Y., Stachelberger, H., and Kindt, J. H. *In vivo* nanoscale atomic force microscopy investigation of diatom adhesion properties. *Mater. Sci. Technol.*, 2002, **18**, 763–766.
- 12 Gebeshuber, I. C., Kindt, J. H., Thompson, J. B., Del Amo, Y., Stachelberger, H., Brzezinski, M., Stucky, G. D., Morse, D. E., and Hansma P. K. Atomic force microscopy study of living diatoms in ambient conditions. *J. Microsc.*, 2003, **212**, 292–299.
- 13 Haeckel, E. *Art forms in nature*, 1974 (Dover Pictorial Archives, Dover Publications, New York).
- 14 Thompson, D. A. W. *On growth and form*, 1992 (Dover Publications, New York).
- 15 Mate, C. M. Molecular tribology of disk drives. *Tribol. Lett.*, 1998, **4**, 119–123.
- 16 Davey, M. C. and Crawford, R. M. Filament formation in the diatom *Melosira granulata*. *J. Phycol.*, 1986, **22**, 144–150.
- 17 Crawford, R. M., Hinz, F., and Honeywill, C. Three species of the diatom genus *Corethron* Castracane: structure, distribution and taxonomy. *Diatom Res.*, 1998, **13**, 1–28.
- 18 Sims, P. A., Mann, D. G., and Medlin, L. K. Evolution of the diatoms: insights from fossil, biological and molecular data. *Phycologia*, 2006, **45**, 361–402.
- 19 Crawford, S. A., Higgins, M. J., Mulvaney, P., and Wetherbee, R. The nanostructure of the diatom frustule as revealed by atomic force and scanning electron microscopy. *J. Phycol.*, 2001, **37**, 543–554.
- 20 Gebeshuber, I. C., Stachelberger, H., and Drack, M. Diatom bionanotribology – biological surfaces in relative motion: their design, friction, adhesion, lubrication and wear. *J. Nanosci. Nanotechnol.*, 2005, **5**(1), 79–87.

- 21 **Higgins, M. J., Crawford, S. A., Mulvaney, P., and Wetherbee, R.** Characterization of the adhesive mucilages secreted by live diatom cells using atomic force microscopy. *Protist*, 2002, **153**, 25–38.
- 22 **Higgins, M. J., Molino, P., Mulvaney, P., and Wetherbee, R.** The structure and nanomechanical properties of the adhesive mucilage that mediates diatom-substratum adhesion and motility. *J. Phycol.*, 2003, **39**, 1181–1193.
- 23 **Higgins, M. J., Sader, J. E., Mulvaney, P., and Wetherbee, R.** Probing the surface of living diatoms with atomic force microscopy: the nanostructure and nanomechanical properties of the mucilage layer. *J. Phycol.*, 2003, **39**, 722–734.
- 24 **Gebeshuber, I. C., Stachelberger, H., and Drack, M.** Diatom tribology. In *Life cycle tribology* (Eds D. Dowson, M. Priest, G. Dalmaz, and A. A. Lubrecht) Tribology and interface engineering series, Series Ed. B. J. Briscoe, 2005, vol. 48, pp. 365–370 (Elsevier, Amsterdam).
- 25 **Seeman, N. C. and Belcher, A. M.** Emulating biology: building nanostructures from the bottom up. *Proc. Natl. Acad. Sci.*, 2002, **99**, 6451–6455.
- 26 **Zhang, S.** Fabrication of novel biomaterials through molecular self-assembly. *Nat. Biotechnol.*, 2003, **21**(10), 1171–1178.
- 27 **Gebeshuber, I. C., Pauschitz, A., and Franek, F.** Biotribological model systems for emerging nanoscale technologies. Proceedings 2006 IEEE Conference on *Emerging technologies – nanoelectronics*, Singapore, 10–13 January 2006, pp. 396–400.
- 28 **Gordon, R., Sterrenburg, F. A. S., and Sandhage, K.** (Eds) Special issue on diatom nanotechnology. *J. Nanosci. Nanotechnol.*, 2005, **5**(1), 1–178.

Appendix B: Publication list

Journal articles

1. **Gebeshuber I.C.** and Drack M.
An attempt to reveal synergies between biology and engineering mechanics
J. Mech. Eng. Sci., in press, **invited article**
2. **Gebeshuber I.C.**
Biotribology inspires new technologies
Nano Today 2(5), 30-37, 2007
doi:10.1016/S1748-0132(07)70141-X, **invited article**
3. Lemell C., El-Said A.S., Meissl W., **Gebeshuber I.C.**, Trautmann C., Toulemonde M., Burgdörfer J. and Aumayr F.
On the nano-hillock formation induced by slow highly charged ions on insulator surfaces
Solid-State Electronics 51, 1398-1404, 2007
doi: 10.1016/j.sse.2007.06.016
4. El-Said A.S., Meissl W., Simon M.C., Crespo López-Urrutia J.R., **Gebeshuber I.C.**, Laimer J., Winter HP., Ullrich J. and Aumayr F.
Creation of surface nanostructures by irradiation with slow highly charged ions
Rad. Eff. Def. Solids 162, 467-472, 2007
doi: 10.1080/ 10420150701470803
5. El-Said A.S., Meissl W., Simon M.C., Crespo López-Urrutia J.R., Lemell C., Burgdörfer J., **Gebeshuber I.C.**, Winter HP., Ullrich J., Trautmann C., Toulemonde M., Aumayr F.
Potential energy threshold for nanohillock formation by impact of slow highly charged ions on a CaF₂(111) surface
Nucl. Instr. Meth. Phys. Res. B 258, 167-171, 2007
doi:10.1016/j.nimb.2006.12.142 [**Publication A8 in Appendix A**]
6. Gruenberger C., Ritter R., Aumayr F., Stachelberger H. and **Gebeshuber I.C.**
Algal biophysics: Euglena gracilis investigated by atomic force microscopy
Mat. Sci. Forum 555, 411-416, 2007
7. El-Said A.S., Meissl W., Simon M.C., Crespo López-Urrutia J.R., **Gebeshuber I.C.**, Lang M., Winter HP., Ullrich J. and Aumayr F.
Surface nanostructures induced by slow highly charged ions on CaF₂ single crystals
Nucl. Instr. Meth. Phys. Res. B 256, 346-349, 2007
doi:10.1016/j.nimb.2006.12.140 [**Publication A7 in Appendix A**]
8. Fürsatz M., Meissl W., Pleschko S., **Gebeshuber I.C.**, Stolterfoht N., Winter HP. and Aumayr F.
Charging and discharging of nano-capillaries during ion-guiding of multiply charged projectiles
J. Phys. Conf. Ser. 58, 319-322, 2007
9. Crawford R.M. and **Gebeshuber I.C.**
Harmony of beauty and expediency
Science First Hand 5(10), 30-36, 2006. Incl. Coverpage.

10. **Gebeshuber I.C.** and Crawford R.M.
Micromechanics in biogenic hydrated silica: hinges and interlocking devices in diatoms
J. Eng. Tribol. 220(J8), 787-796, 2006 [**Publication A10 in Appendix A**]
11. **Gebeshuber I.C.**
Bio-tribology and the operating environment (Discussion on D. Dowson and A. Neville)
J. Eng. Tribol. 220(J3), 333, 2006
12. **Gebeshuber I.C.**, Stachelberger H. and Drack M.
Diatom tribology
Life Cycle Tribology 48, 365-370, 2005
13. Kolm R., **Gebeshuber I.C.**, Kenesey E., Ecker A., Pauschitz A., Werner W.S.M., and Störi H.
Tribochemistry of mono molecular additive films on metal surfaces, investigated by XPS and HFRR
Life Cycle Tribology 48, 269-282, 2005
14. **Gebeshuber I.C.**, Stachelberger H. and Drack M.
Diatom bionanotribology - Biological surfaces in relative motion: their design, friction, adhesion, lubrication and wear
J. Nanosci. Nanotechnol. 5(1), 79-87, 2005. Incl. Coverpage.
[**Publication A9 in Appendix A**]
15. **Gebeshuber I.C.**, Kindt J.H., Thompson J.B., Del Amo Y., Stachelberger H., Brzezinski M., Stucky, G.D. Morse D.E. and Hansma P.K.
Atomic force microscopy study of living diatoms in ambient conditions
J. Microsc. 212, 292-299, 2003. Incl. Coverpage. [**Publication A3 in Appendix A**]
16. **Gebeshuber I.C.**, Cernusca S., Aumayr F. and Winter HP.
Nanosopic surface modification by slow ion bombardment
Int. J. Mass Spectrom. 229, 27-34, 2003 [**Publication A6 in Appendix A**]
17. **Gebeshuber I.C.**, Cernusca S., Aumayr F. and Winter HP.
Slow multicharged-ion induced nanodefects on monocrystalline insulator surfaces studied by UHV-AFM
Nucl. Instr. Meth. Phys. Res. B 205, 751-757, 2003 [**Publication A5 in Appendix A**]
18. **Gebeshuber I.C.**, Thompson J.B., Del Amo Y., Stachelberger H. and Kindt J.H.
In vivo nanoscale atomic force microscopy investigation of diatom adhesion properties
Mat. Sci. Technol. 18, 763-766, 2002 [**Publication A4 in Appendix A**]
19. Viani M.B., Pietrasanta L.I., Thompson J.B., Chand A., **Gebeshuber I.C.**, Kindt J.H., Richter M., Hansma H.G. and Hansma P.K.
Probing protein-protein interactions in real time
Nature Structural Biology 7, 644-647, 2000 [**Publication A2 in Appendix A**]
20. Petracchi D., **Gebeshuber I.C.**, DeFelice L.J. and Holden A.V.
Stochastic resonance in biological systems
Chaos, Solitons & Fractals 11, 1819-1822, 2000

21. **Gebeshuber I.C.**

The influence of stochastic behavior on the human threshold of hearing
Chaos, Solitons & Fractals 11, 1855-1868, 2000

22. Svrcek-Seiler W.A., **Gebeshuber I.C.**, Rattay F., Biro T. and Markum H.

Micromechanical models for the Brownian motion of hair cell stereocilia
J. Theor. Biol. 193, 623-630, 1998

23. Rattay F., **Gebeshuber I.C.**, Gitter A.H.

The auditory hair cell: a simple electric circuit model
J. Acoust. Soc. Am. 103, 1558-1565, 1998

Invited Book Chapters

1. **Gebeshuber I.C.**, Drack M., Aumayr F., Winter HP. and Franek F.

Scanning Probe Microscopy: From living cells to the subatomic range

In: Applied Scanning Probe Methods III: Characterization (NanoScience and Technology) (Eds. Bhushan B. and Fuchs H.)

Springer Berlin Heidelberg, ISBN 978-3-540-26909-0 (Print) 978-3-540-26910-6 (Online), 27-53, 2006. DOI 10.1007/3-540-26910-X_2 (**Publication A1 in Appendix A**)

2. **Gebeshuber I.C.**, Smith R.A.P., Aumayr F. and Winter HP.

Scanning Probe Microscopy across dimensions

In: From Cells to Proteins: Imaging Nature across Dimensions (Eds. Evangelista V., Barsanti L., Passarelli V. and Gualtieri P.)

NATO Security through Science Series, Sub-Series B: Physics and Biophysics, Vol. 3, Springer Netherlands, ISBN 978-1-4020-3614-9, 139-165, 2005

3. **Gebeshuber I.C.** and Rattay F.

Coding efficiency of inner hair cells at the threshold of hearing

In: Computational Models of Auditory Function (Eds. Greenberg S. und Slaney M.)

ISBN 90 5199 457 5, IOS Press, Amsterdam, NATO ASI Series A Vol. 312, 5-16, 2001

4. **Gebeshuber I.C.**, Mladenka A., Rattay F. and Svrcek-Seiler W.A.

Brownian motion and the ability to detect weak auditory signals

In: Chaos and Noise in Biology and Medicine (Eds. Barbi M. and Chillemi S.)

World Scientific Press, 230-237, 1999

Papers resulting from presentations at international conferences

1. **Gebeshuber I.C.**
Social, health and ethical implications of nanotechnology
Proc. 2nd Vienna International Conference Micro- and Nanotechnology - Viennano07
ISBN 978-3-901657-25-2 (book), ISBN 978-3-901657-27-6 (CD), 15-17, 2007
2. **Gebeshuber I.C.**, Smith R.A.P., El-Said A.S., Kaska K., Pleschko S., Gruenberger C., Winter HP. and Aumayr F.
UHV and ambient AFM investigations of silicon surfaces nanostructured with singly- and multiply-charged ions
Proc. VIII. Linz Winter Workshop "Advances in single molecule research for biology and nanoscience", Trauner Verlag Universität, Schriftenreihe Biophysik, Band 1, Eds: Hinterdorfer P., Schuetz G. and Pohl P., Linz, Austria, ISBN 3-85499-163-0, ISBN 978-3-85499-163-2, p. 117-122, 2006
3. **Gebeshuber I.C.**, Smith R.A.P., Fuersatz M., Kaska K., Pleschko S., Winter HP. and Aumayr F.
Nanostructuring surfaces with slow multiply charged ions
NanoSingapore2006, IEEE Conference on Emerging Technologies - Nanoelectronics, CD ROM, ISBN 0-7803-9358-9, 2006
4. **Gebeshuber I.C.**, Pauschitz A. and Franek F.
Biotribological model systems for emerging nano-scale technologies
NanoSingapore2006, IEEE Conference on Emerging Technologies - Nanoelectronics, CD ROM, ISBN 0-7803-9358-9, 2006
5. **Gebeshuber I.C.**, Smith R.A.P., Pleschko S., Gruenberger C., Kaska K., Fuersatz M., Winter H. and Aumayr F.
Nanostructuring surfaces with slow multiply charged ions
Proc. "Emerging Technologies - Nanoelectronics", IEEE Conference, ISBN 0-7803-9357-0, 324-327, 2006
6. **Gebeshuber I.C.**, Pauschitz A. and Franek F.
Biotribological model systems for emerging nano-scale technologies
Proc. "Emerging Technologies - Nanoelectronics", IEEE Conference, ISBN 0-7803-9357-0, 396-400, 2006
7. **Gebeshuber I.C.**, Stachelberger H., Drack M. and Franek F.
Biotribology at the micro- and nanoscale as exemplified by diatoms
Proc. 1st Vienna International Conference Micro-and Nano-Technology, March 9-11, 2005, Vienna, Austria, 135-140, 2005
8. Dörr N. and **Gebeshuber I.C.**
Schmierstoff-Grenzflächen-Wechselwirkungen in Tribosystemen
Z. Tribologie und Schmierungstechnik, 51. Jg., Heft 1/2004, expert-Verlag, Renningen, Germany, ISSN 0724-3472, 67-68, 2004

9. **Gebeshuber I.C.**, Stachelberger H. and Drack M.
Surfaces in relative motion: bionanotribological investigations
In: First International Industrial Conference Bionik 2004 (Eds. Boblan I. and Bannasch R.), Fortschr.-Ber. VDI Reihe 15 Nr. 249, VDI Verlag Düsseldorf, Germany, 2004. ISBN 3-18-324915-4, ISSN 0178-9589229-236, 229-236, 2004
10. Störi H., Kleiner R., Werner W.S.M., Kolm R., **Gebeshuber I.C.** and Jogl C.
Characterisation of monomolecular lubricant films
Proc. 14th International Colloquium Tribology, Technische Akademie Esslingen, Volume III, 1663-1666, January 13-15, 2004
11. Doerr N. and **Gebeshuber I.C.**
Schmierstoff-Grenzflächen Wechselwirkungen in Tribosystemen
Proc. 14th International Colloquium Tribology, Technische Akademie Esslingen, Volume I, 501-502, January 13-15, 2004
12. Kolm R., Kleiner R., **Gebeshuber I.C.**, Werner W. und Störi H.
Charakterisierung von monomolekularen Schmierstofffilmen
Proc. ÖTG Jahressymposium 2003, Vienna and Wiener Neustadt, Austria
13. Bleda-Maza de Lizana M., Brandt H., **Gebeshuber I.C.**, MacPherson M., Matsuguchi T. and Számádó S.
Does complexity always increase during major evolutionary transitions?
Proc. Santa Fe Institute Complex Systems Summer School 2003, Santa Fe, NM/USA
14. **Gebeshuber I.C.** and Rattay F.
Modeling the human hearing threshold curve for pure tones: the effects of stereociliary Brownian motion, endogenous transduction channel noise, stochasticity in neurotransmitter release and innervation density in various frequency bands
Proc. NATO ASI "Computational Hearing" (Eds. Greenberg S. and Slaney M.), 7-12, 1998
15. **Gebeshuber I.C.**, Pontes Pinto J., Naves Leao R., Mladenka A. and Rattay F.
Stochastic resonance in the inner ear: the effects of endogenous transduction channel noise and stereociliary thermal motions on the human hearing threshold in various frequency bands
ARGESIM Report No. 10: Proc. TU-BioMed Minisymposium 1998 "Brain Modelling" (Ed. Rattay F.), 40-44, 1998
16. **Gebeshuber I.C.**, Ratzer B. and Wild C.
Health care technology assessment in biomedical engineering: social science accompanying research
Med. Biol. Eng. Comput. 35(II), 1254, 1997
17. **Gebeshuber I.C.**, Ratzer B. and Wild C.
Sozialwissenschaftliche Begleitforschung biomedizinischer Projekte an der TU-Wien
TA-Datenbank-Nachrichten Nr. 2, 6. Jahrgang - Juli 1997, 37-41, 1997
18. Ratzer B., **Gebeshuber I.C.** and Wild C.
Biomedical Engineering: Social Science Accompanying Research
Annual Meeting of the International Society of Technology Assessment in Health Care 13, 47, 1997

19. **Gebeshuber I.C.**, Ratzer B. and Wild C.
Sozialwissenschaftliche Begleitung biomedizinischer Forschung
Soziale Technik 1, 12-15, 1997
20. **Gebeshuber I.C.** and Ratzer B.
Eine Sozialwissenschaftliche Begleitstudie von Projekten im Bereich Biomedizinischer Technik an der TU-Wien
Biomedizinische Technik 41(1), 580-581, 1996
21. **Gebeshuber I.C.**
The mechano-electric transduction in the inner ear
Biomedizinische Technik 41(1), 618-619, 1996

Papers submitted and in preparation:

Doerr N., Holzer D., Wanzenboeck H.D., Ecker A., Pauschitz A., Franek F. and **Gebeshuber I.C.**

Multi-method screening for the applicability of ionic liquids as sustainable lubricants
Advances in Tribology, **invited article**, submitted

Bogus A., **Gebeshuber I.C.**, Pauschitz A., Roy M. and Haubner R.

Micro- and nanomechanical properties of diamond films with various surface morphologies
submitted

Gebeshuber I.C.

Engineering at the interface revisited
J. Mech. Eng. Sci. 50th Anniversary Issue
invited article, submitted

El-Said A.S., Heller R., Meissl W., Ritter R., Facsko S., Lemell C., Solleder B., **Gebeshuber I.C.**, Betz G., Toulemonde M., Möller W., Burgdörfer J. and Aumayr F.
Creation of nano-hillocks on CaF₂ surfaces by slow highly charged ions
submitted

Hekele O., Goesselsberger C.G. and **Gebeshuber I.C.**

Nanodiagnosics performed on human red blood cells with the atomic force microscope
submitted

Hekele O., Goesselsberger C.G., Brandstetter M., Aumayr M., Sommer R. and **Gebeshuber I.C.**

Atomic force microscopy and spectroscopy study of the sporulation of Bacillus subtilis
submitted

Bogus A., **Gebeshuber I.C.**, Roy M., Polcar T., Cavaleiro A. and Franek F.

Nanotribology of Mo-Se-C films
in preparation

Bogus A., Aumeyr T., Vasko C.A., Doerr N., Werner W.S.M. and **Gebeshuber I.C.**

Isomer and oligomer specific lubrication investigated from the macro- to the nanoscale
J. Eng. Tribol., **invited article** in preparation

Gebeshuber I.C., Holzer D., Pieczetowski C.A., Goschke R. and Störi H.

Development of an atomic force microscope closed fluid cell for tribological investigations of large samples in chemically aggressive environments
J. Eng. Tribol., **invited article** in preparation

Jeronimidis G. and **Gebeshuber I.C.**

Review on Biomimetics (incl. Outlook)
J. Mech. Eng. Sci. 50th Anniversary Issue, **invited article** in preparation

Appendix C: Curriculum vitae

Title: Univ.-Ass. Dipl.-Ing. Dr. techn.

Date and Place of Birth: April 10, 1969, Bruck/Mur

Nationality: Austrian

Affiliation: Institut fuer Allgemeine Physik
Vienna University of Technology
Wiedner Hauptstrasse 8-10/134, A-1040 Wien
Phone: +43-1-5880113436, FAX: +43-1-58801-13499
E-mail: gebeshuber@iap.tuwien.ac.at



Education

1987-1998 Physics studies at Vienna University of Technology

1995 Diploma in Physics (with distinction)

1998 Ph.D. in Physics (with distinction)

Employment

10/1995-09/2000: Tutor, Vienna University of Technology

03/1998-06/1998: Scientific co-worker, Vienna University of Technology

07/1998-06/1999: PostDoc, Vienna University of Technology

02/1999: PostDoc, University of California Santa Barbara

06/1999-11/1999: PostDoc, University of California Santa Barbara

12/1999-12/1999: Scientific co-worker, Vienna University of Technology

01/2000-12/2002: PostDoc, Vienna University of Technology (100% until 09/2002, 50% from 10/2002)

01/2003-10/2006: Senior researcher and Project Manager, Austrian Center of Competence for Tribology, AC²T Research GesmbH, Wiener Neustadt (50%)

from 10/2007: Key researcher, Austrian Center of Competence for Tribology, AC²T Research GesmbH, Wiener Neustadt

from 10/2002: Univ.-Ass. at Institut fuer Allgemeine Physik (50% until 9/2006, 100% from 10/2006)

Research visits

- Foundation for Research and Technology Hellas, FO.R.T.H. Heraklion, Greece (09/97-10/97)
- Neuromorphic engineering, Telluride CO 81435, Colorado, USA (06/02-07/02)
- Research scholar at the Santa Fe Institute, New Mexico, USA (06/03-07/03)
- Physics Dept., University of California Santa Barbara, USA (several visits, 2000-03)
- Short term stays in Italy (CNR Pisa), England (Keele, Leeds), USA (Emory University Atlanta, UC Berkeley, UC Santa Barbara), Finland (Helsinki), France (École des Mines)

Current research interests

- Ion-Surface Interactions
- Tribology
- (Bio-)Nanotechnology
- Scanning Probe Microscopy

Team Member in Research Projects

- 08/2003-05/2006: FWF Project 16178 PHY
Nanometer-sized surface modifications on silicon produced by slow multiply charged ions
Principal Investigator F. Aumayr, TU Vienna
- 01/2000-12/2002: FWF Project 13543 PHY
UHV-AFM studies of nano-defect formation by slow multicharged ions at insulator surfaces
Principal Investigator F. Aumayr, TU Vienna
- 1998: Austrian Ministry of Science project
TU-BioMed - Coordination Model for Biomedical Research and Teaching regarding the specific framework given by the European Union
Principal Investigator F. Rattay, TU Vienna
- 1996-1998: Austrian Ministry of Science project
Medical Technology Assessment of (new) Biomedical Technologies
Principal Investigator C. Wild, Austrian Academy of Science

Research Project Management

- 10/2006-10/2009: **Project manager, Scientist in Charge, Gender Representative and Member of the Scientific Committee**
WEMESURF “Characterisation of wear mechanisms and surface functionalities with regard to life time prediction and quality criteria - from micro to the nano range”
6th framework EU Human Resources and Mobility activity, Marie Curie Research Training Network (RTN), Project volume 310 kEuro.
- 2005, 2006: **Austrian Project Manager**
Grain scale investigation into fretting contacts
Project with T. Dick and Prof. G. Cailletaud from the École National Supérieure des Mines de Paris, sponsored by ÖAD, Amadée Program (exchange with France)
- 01/2006-12/2009: **Deputy coordinator**
Production and Characterisation of Gas Phase Biomolecular Targets
JRA4 of the 6th framework Research Infrastructure Action: Integrated Infrastructure Initiative (I3) ITS LEIF “Ion Technology and Spectroscopy at Low Energy Ion Beam Facilities”, project volume ca. 100 000 Euro
- 01/2003-09/2006: **Project Manager**
Functional Surfaces
KPlus Strategic Research Project, project volume 544 000 Euro

Research Project Acquisition

- 05/2005-05/2006: **Principal Investigator**
Magnetic carbon?
Innovative Project 2005 Vienna University of Technology, project volume 47 600 Euro
- 10/1999-10/2000: **Principal Investigator**
Development of a Scanning Ion Conductance Microscope (SICM) in Combination with a Patch Clamp Device
Hochschuljubiläumsstiftung Project H-120/99, project volume 90 000 ATS
- 04/1999-04/2000: **Principal Investigator**
Development of a SICM for Technical and Biological Applications
Wiener Wirtschaft Technology Prize Project, project volume 100 000 ATS

Invited, plenary and keynote talks at International Conferences

1. Invited lecture

Geckos, white blood cells and diatoms: How natural micro- and nanotribological systems inspire emerging technologies

5th China International Symposium on Tribology, Beijing, China, 2008

2. Invited lecture

Bacilli, green algae, diatoms and red blood cells – how biology inspires novel materials in nanoarchitectural applications

7th EMRS Fall Meeting, Warsaw, Poland, 2008

3. Invited lecture

Geckoes, white blood cells and diatoms - how biology inspires novel dry, switchable and self-healing adhesives

2nd Leverhulme Trust Workshop ADHESINT, Sevilla, Spain, 2008

4. Invited lecture

Structural colours in biology and how these natural micro- and nanostructures inspire current technology

WIN Final European Workshop, Dresden, Germany, 2008

5. Invited lectures

Nanosciences at surfaces

Networking implications for women in nanosciences and nanotechnologies

WIN Workshop “Nanomaterials and Gender Aspects in Research and Technology”, Gothenburg, Sweden, 2007

6. Invited lecture

Structural colours in biology

ISCOM, Belgrade, Serbia, 2007

7. Invited lecture

Algae make glass and bacteria produce magnets. What materials science can learn from nature

Europäisches Forum Alpbach, Technologiegespräche, 2007

8. Invited plenary lecture

Science & Industry: Cooperation aspects

2nd Austrian Nanotechnology Cooperation Event, Wiener Neustadt, 2007

9. Invited plenary lecture

Social, health and ethical implications of nanotechnology

2nd Vienna International Conference Micro- and Nanotechnology - Viennano07, Vienna and Wiener Neustadt, 2007

10. Invited plenary lecture

Tribology of biomineralised structures

Principles of Biomineralisation, Bad Honnef, Germany, 2006

11. Invited plenary lecture

Networking implications for women in engineering

IIWE International Institute for Women in Engineering, Paris, France, 2006

12. Invited keynote lecture*Tribology in biology*4th International Colloquium Micro-Tribology'05, Karwica, Poland, 2005**13. Invited plenary lecture***Networking implications for women in engineering*

IIWE International Institute for Women in Engineering, Paris, France, 2005

14. Invited lecture*Scanning probe microscopy across dimensions*

NATO ASI "From cells to proteins: Imaging nature across dimensions", Pisa, Italy, 2004

Altogether I gave more than 70 oral presentations at conferences, meetings, workshops, etc.

Teaching experience

2007	Interactions with surfaces (134.114 PA)
2007	The origin of elements (134.160 VD)
2007	Grundlagen der Physik III (Basics of Physics III, 134.125 UE)
2007	Grundlagen der Physik II (Basics of Physics II, 134.110 UE)
2006	Grundlagen der Physik I (Basics of Physics I, 134.109 UE)
2004	Nanotechnology (134.146 VD) self-drafted lecture
2005	Introduction to Nanotechnology (134.152 VD) self-drafted lecture
2006	Introduction to Nanotechnology and Nanoanalytics (134.166 VO) self-drafted lecture
2007	Introduction to Nanotechnology (134.152 VD) self-drafted lecture
2004, 2006	Laborübungen III (Experimental Lab for Physicists III, 134.126 PR)
2003, 2005, 2007	Laborübungen II (Experimental Lab for Physicists II, 134.124 PR)
2003, 2005, 2007	Laborübungen I (Experimental Lab for Physicists I, 134.107 PR)
1995-2000	Tutor in Computer-Simulation (101.010)

Pupils and Students from Universities of Applied Sciences, doing an internship

- Gregor Gressenbauer, 2008 (European School Frankfurt)
AFM, XPS, nanotribology (two weeks in June 2008)
- Martina Aumayr (University of Applied Sciences Krems)
AFM, biotechnology (one month in August and September 2007)
- Daniel Alexander Pohoryles (École Lycée)
AFM, nanotribology (two weeks in July, August and September 2006)

Undergraduate students, doing the project work “Interactions with surfaces” (8 hours per week, for one semester):

- Mario Adam (physics engineering)
Development and construction of a photonic crystal lab experiment
- Franziska Stadlbauer (physics engineering)
Development and construction of a photonic crystal lab experiment
- Aaron Kaplan (computer science)
Nanotransmitters
- Dr. med. Michael Bauer (medicine)
Nanotransmitters
- Mathias Seidler (physics engineering)
Laser assisted polymer processing
- Lukas Süß (physics engineering)
UHV STM of HOPG bombarded with highly charged ions
- Sebastian Kropatschek (physics engineering)
SICM scanning LabView development
- Stefan Fossati (physics engineering)
targeted delivery, nanoparticles
- Monika Madl (materials science)
targeted delivery, nanoparticles
- Robin Glattauer (physics engineering)
targeted delivery, nanoparticles
- Johannes Srajer (physics engineering)
diatom tribology, FE modelling

- Christopher Andrew Vasko (physics engineering)
AFM investigation of isomer specific lubrication of tribologically relevant surfaces
- Anna Celarek (physics engineering)
Nanoflakes
- Markus Brandstetter (physics engineering)
AFM measurements on vegetative and sporulated Bacillus subtilis (2007)
- Matthias Schreitl (physics engineering, biology)
Investigating the click-stop mechanism in the diatom Corethron criophilum: optical and electron microscopy as well as micro-manipulation (2007)
- Matthias Willensdorfer (physics engineering, biology)
Investigating the click-stop mechanism in the diatom Corethron criophilum: optical and electron microscopy as well as micro-manipulation (2007)
- Markus Jahn (physics engineering)
Instrumentation and development of a scanning ion conductance microscope (2007)
- Hansjörg Jerabek (physics engineering)
Instrumentation and development of a scanning ion conductance microscope (2007)
- Winkler Hannes (physics engineering)
Instrumentation and development of a scanning ion conductance microscope (2007)
- Thomas Aumeyr (physics engineering)
AFM investigation of isomer specific lubrication of tribologically relevant surfaces (2007)
- Matthias Ikeda (physics engineering)
AFM investigation of isomer specific lubrication of tribologically relevant surfaces (2007)
- Donat Holzer (physics engineering)
AFM investigation of isomer specific lubrication of tribologically relevant surfaces (2007)
- Christoph Gösselsberger (physics engineering)
Bacillus subtilis sporulation (2007)
- Christoph Gösselsberger (physics engineering)
AFM force mapping on healthy and EPO red blood cells (2006)
- Cezary Pieczetowski (physics engineering)
Atomic Force Microscopy of nanostructured surfaces (2006)
- Robert Ritter (physics engineering)
AFM of Euglena gracilis (2006)
- Oliver Hekele (physics engineering)
AFM force mapping on healthy and EPO red blood cells (2006)

- Donat Holzer (physics engineering)
Development of an atomic force microscope closed fluid cell for tribological investigations of large samples in chemically aggressive environments (2005)
- Alexander Lurf (physics engineering)
MFM and nanomanipulation of magnetotactic bacteria (2005)
- Peter Oser (physics engineering)
MFM and nanomanipulation of magnetotactic bacteria (2005)
- Stefan Nagele (physics engineering)
AFM (2004)
- Danijel Dobožanov (physics engineering)
AFM (2004)
- Stefan Schraml (physics engineering)
SICM (2003)
- Perttu Niemela (biophysics)
Development of a scanning ion conductance microscope for technical and biological applications (2003)
- Gerald Richter (physics engineering)
Development of a scanning ion conductance microscope for technical and biological applications (2003)
- Manfred Schabernig (Lehramt Physik)
Omicron UHV AFM/STM Bedienungsanleitung (2000)

Summer students

- Summer 2006: Cezary Pieczetowski, financed by AC²T
- Summer 2005: Donat Holzer, financed by AC²T

IAESTE (International Association for the Exchange of Students for Technical Experience) students

- Summer 2006: Zahra Somani, United Kingdom
- Summer 2005: Farzy Tabari, Pakistan
- Summer 2003: Marco de Grazia, Italy

Diploma students

- Alexander Lurf (physics engineering)
AFM, XPS, SAM, tribology (in collaboration with the company CCI - Control Components Inc., from 2007)
- Robert Ritter (physics engineering)
Interacton of HCIs with SAMs / Magnetic carbon? (to finish 2008)
- Oliver Hekele (physics engineering)
Atomic force microscopy of Bacillus subtilis (2008)
- Clemens Grünberger (physics engineering)
Atomic force microscopy of the alga Euglena gracilis (with distinction, 2007)
- Manfred Schabernig (Lehramt student)
Rastersondenmethoden für die atomar aufgelöste Abbildung von Oberflächen (Scanning probe methods for atomically resolved surfaces) (2004)
- Stefan Schraml (physics engineering)
Setup and application of a scanning ion conductance microscope (2003)

Graduate Students (working for Dr. techn.)

- Agnieszka Bogus (physics, financed by Marie Curie RTN WEMESURF)
Isomer and oligomer specific monomolecular film lubrication investigated from the macro- to the nano range. Start 2007
- Davide Bianchi (physics, financed by Marie Curie RTN WEMESURF)
Characterization and analysis of surfaces in tribology through topographic methods. Start 2007

PostDoc

- Krystallia Psychogyiopoulos (chemistry, financed by Marie Curie RTN WEMESURF)
AFM, XPS

Popular Science / Outreach Activities

- **Gebeshuber I.C.**
Bionanotechnologie aus der Natur. Intelligente Materialien, Nanoroboter und vieles mehr!
University meets Public, VHS Meidling, Wien, 2008
- **Gebeshuber I.C.**
Schmetterlingsflügel, Pfauenfedern und Stoff, der die Farbe ändert, wenn Ihr ihn anhaucht - die neue Welt der Nanotechnologie
Museumsquartier, Wien, 2008
- **Gebeshuber I.C., Schmid H. and Aumayr F.**
Licht+Licht=Dunkelheit?
Yo!Tech 2007
- **Gebeshuber I.C.**
Bionanotechnologie aus der Natur. Intelligente Materialien, Nanoroboter u. v. m.!
Metalab, Wien, 2007
- **Gebeshuber I.C. and "B. Hupfauf"**
Bernd Hupfauf und 1 Ei gegen die Gravitation
ORF 1, Newton, 2007
- **Gebeshuber I.C., Jech M. and Franek F.**
Nanotechnologie und Tribologie
Dimensionen - Die Welt der Wissenschaft, ORF Ö1, 2007
- **Gebeshuber I.C. and Kerschbaum F.**
Gibt es Ausserirdische und kann die Nanotechnologie uns helfen, damit wir nie mehr Geschirr abwaschen müssen?
Rudi!Radiohund, Wien, 2007
- **Gebeshuber I.C.**
Die Physik der Wasserrutsche
Rudi!Radiohund, ORF Ö1, 2007
- **Gebeshuber I.C.**
Nanotechnologie für Körperbehinderte
Schulzentrum Ungargasse, Wien, 2007
- **Gebeshuber I.C.**
Bionanotechnologie aus der Natur. Intelligente Materialien, Nanoroboter und vieles mehr!
University meets Public, VHS Meidling, Wien, 2007
- **Gebeshuber I.C.**
Die Physikerin
Rudi!Radiohund, ORF Ö1, 2007
- **Gebeshuber I.C. and Bauer J.**
Chemische Elemente – Ausstellung
TU Wien, 2006

- Oberhummer H. und **Gebeshuber I.C.**
Astrophysik und Nanotechnologie
Ö1 “Von Tag zu Tag”, 2006
- Gebeshuber I.C. und Winter HP.
Von Metallen und Edelsteinen - und dem Robert mit der schönen Stimme.
Physik und Chemie - anschaulich präsentiert.
TU Wien, 2006
- **Gebeshuber I.C.**
Die Physik der Wasserrutsche
ORF 1, Newton, 2006
- **Gebeshuber I.C.** und Söllner E.
Von Metallen und Edelsteinen - und Schiffen, die auf unsichtbarem Gas dahingleiten.
Wunderbare Physik - anschaulich präsentiert.
Yo!Einstein, 2006
- **Gebeshuber I.C.**
Nanoroboter
Public lecture in tramway #2, 2006
- **Gebeshuber I.C.**
Bionanotechnologie aus der Natur. Intelligente Materialien, Nanoroboter und vieles mehr!
University meets Public, VHS Ottakring, 2006
- **Gebeshuber I.C.**
Warum auf der Nordhalbkugel die Winter kürzer und milder sind als auf der Südhalbkugel
Ö1, Wissen aktuell, 2005
- **Gebeshuber I.C.** and Bauer J.
Chemische Elemente – Ausstellung
Technische Universität Wien, 2005.
- **Gebeshuber I.C.**
Wie die Eier zu ihrer Form kommen
Ö1, Wissen aktuell, 2005
- **Gebeshuber I.C.**
Warum feuchte Steine dunkler sind als trockene
Ö1, Wissen aktuell, 2005
- **Gebeshuber I.C.**
Wissenschaftliche Lebensberatung: Was Sie immer schon über Naturwissenschaften wissen wollten.
Lange Nacht der Forschung, Wien, 2005
- **Gebeshuber I.C.**
Algen machen Glas und Bakterien erzeugen Magnete. Was die Materialwissenschaft von der Natur alles lernen kann.
University meets Public, VHS Simmering und VHS Liesing, 2003

Publicity

- *Experimentalphysikerin setzt sich für Frauenanliegen ein*
Der Standard, 5. 03. 2008, 18
- *Mentoring macht Mut*
TU frei.haus 10/2007, 13
- *Was Spaß macht am Technikerin/Naturwissenschaftlerin sein*
In: Forscherinnenbilder, TU-Wien, 2007
- *Die Hörschwelle als Wackeln des Eiffelturms*
Interview, Seibert P., Koryphäe 41 „Nanotechnologie“, 20-25, 2007
- *Haben Sie denn keine Kinderstube?*
Reiterer R., Kleine Zeitung, 22. 01. 2007, 10-11
- *Hartes und weiches C - Spannendes aus der Welt der Physik lockt Kinder an die Uni*
Wagner H., Kurier, 15. 01. 2007, 2
- *Physik studieren an der TU Wien*
TU Wien, 2006, 2007
- *Views from work*
w-fForte, 2006
- *On prime movers, macro and micro. Industry and Mother Nature have both developed highly efficient motors*
Kennedy S., Plant Services, 2006
- *Umgehe bewusst Regeln*
Aichinger H., Der Standard, 24./25. 06. 2006, 40
- *Begehrte Problemlöser. Österreichs Physiker: Schlechte Laborbedingungen, gute Jobaussichten*
Marot J., UNISTandard, 11. 05. 2006, 4

Education and Training of Physics Teachers

- **Gebeshuber I.C. (2008)**
Rastersondenmikroskopie
62. Fortbildungswoche für Lehrkräfte in Physik und Chemie an HS, AHS, BMS und BHS, Wien, 27.02.2008
- **Gebeshuber I.C. (2005)**
Nanotechnologie
59. Fortbildungswoche für Lehrkräfte in Physik und Chemie an HS, AHS, BMS und BHS, St. Pölten, 08.11. 2005

Honors and Awards

- *Expertin des Monats*
FEMtech, 2008
- *Winner of the Photo Competition*
Vienna University of Technology, 2006
- *Winner of the Innovative Project Initiative*
Vienna University of Technology, 2005
- *Winner of the Research Project Initiative*
Hochschuljubiläumsstiftung der Stadt Wien, 1999
- *Winner of the SUCCESS prize*
European Space Agency, 1999
- *Winner of the Wiener Wirtschaft Technology Prize*
Fonds 150 Years Vienna University of Technology, 1999
- *Winner of the first prize at the students competition*
ETH Zürich, 1996

Committee Positions

- *3rd Vienna International Conference Nanotechnology - Viennano09*
18. - 20. 03. 2009, Vienna & Wiener Neustadt, Austria
Member of the Scientific Committee
- *WEMESURF Summer School*
25. 08. - 05. 09. 2008, Semmering, Austria
Member of the Scientific Committee
- *1st International WiNET Symposium "Building blocks of life"*
14. - 21. 07. 2007, Hamburg, Germany
Member of the Scientific Committee
- *2nd Vienna International Conference Micro- and Nanotechnology - Viennano07*
14. - 16. 03. 2007, Vienna & Wiener Neustadt
Member of the Scientific Committee
- *WEMESURF Network meeting 02*
13. - 14. 03. 2007, Vienna, Austria
Member of the Scientific Committee
- *WEMESURF Marie Curie Research Training Network*
01. 11. 2006 - 31. 10. 2010
Scientist in Charge, Member of the Scientific Committee, Gender Officer

- *ECASIA '05*
11th European Conference on Applications of Surface and Interface Analysis
25. - 30. 09. 2005, Vienna, Austria
Member of the Scientific Committee
- *1st International Conference on Stochastic Resonance in Biological Systems*
5. - 9. 05. 1998, Arcidosso, Italy
Member of the Scientific Committee
- *NetMeeting2003*
Proteomics: A functional approach (NoE coordination meeting)
13. - 14. 02. 2003, Vienna, Austria
Organizer, Member of the Scientific Committee
- *Brain Modelling*
TU-BioMed Minisymposium
27. 02. 1998, Vienna, Austria
Member of the Organizing Committee, Member of the Scientific Committee
- *Neurophysik*
TU-BioMed Minisymposium
17. 04. 1996, Vienna, Austria
Member of the Organizing Committee, Member of the Scientific Committee

Editorial Board Memberships

- *Journal of Mechanical Engineering Science*
London, UK
Member of the Editorial Board (from 2006)
- *Chaos, Solitons and Fractals*
Special issue on stochastic resonance in biological systems
Elsevier, NL
Guest Editor (September 2000)

Other Scientific Community services

- *Strategic Education Development*
Vereinigung Österreichischer Industrieller (from 2006)
- *Public Relations Representative*
Faculty of Physics, Vienna University of Technology (from 2006)

Reviewing work (peer-reviewed journals, books)

- Biophysical Journal (from 1996)
- Central European Journal of Biology (from 2007)
- IEEE Transactions on Nanotechnology (from 2006)
- Journal of Microscopy (from 2008)
- Journal of Phycology (from 2003)
- Journal of Nano Research (from 2007)
- Materials and Manufacturing Processes (from 2007)
- Micron (from 2005)
- Journal of Mechanical Engineering Science (from 2005)
- Journal of Engineering Tribology (from 2006)
- “Scaling in Solid Mechanics”, Editor F.M. Borodich, Berlin, Springer, 2008

Acknowledgements

The habilitation is the highest academic qualification a person can achieve by their own pursuit in Austria and some other European and Asian countries. This habilitation thesis is part of the formal requirements for being awarded the *venia legendi*, the „permission for lecturing“. It is only because of friends and family, colleagues and supporting agencies I was able to proceed to the stage where I am now.

I want to thank my parents, for their continuous support, during my childhood, my school time and later.

And I want to thank the men in my life, Tony, Ernst, Frank and Mark.

A special thanks belongs to my African grey parrots and other animals that have supported me with their good spirits.

Professional support I got from my PhD thesis advisor DDDr. Frank Rattay, from my post-doctoral advisor Prof. Paul Hansma in Santa Barbara and from the colleagues here in Vienna who paved the way to my current stage: Prof. Fritz Aumayr and the late Prof. Hannspeter Winter, group leader and head of institute, who both, in their own, typical ways contributed enormously to my career. Thank you, Fritz, for giving me the freedom I need to do good work. I will never forget HPW's statement “Let me be your scientific home.” Furthermore, I want to thank Prof. Friedrich Franek and Dr. Andreas Pauschitz, CEOs of the Austrian Center of Competence for Tribology, for successful collaboration since 2003.

Prof. Herbert Stachelberger is to be held responsible for my “mutation” from being a computational scientist to an experimental physicist in 1999, by helping to raise money for my first scanning probe microscope. I wonder where I would be today without him!

Prof. Duncan Dowson provided me with my first editorial board position, Prof. Zygmunt Rymuza invited me for my first plenary lecture at a conference, the ETH Zürich, the European Space Agency, the Hochschuljubiläumsstiftung, the Vienna University of Technology and FEMtech awarded me prizes and honors, Prof. Herbert Störi appointed me scientist in charge for our EU TMR Network WEMESURF – all these actions promote my scientific self esteem and make me strong – Thank you!